UNIVERSITY OF CALIFORNIA

Santa Barbara

Synthesis, Characterization, and Electrochemical Properties of Metallophthalocyanines for Use in Energy Storage Applications

A dissertation submitted in partial satisfaction of the

requirements for the degree Doctor of Philosophy

in Chemistry

by

Madeline Peterson

Committee in charge:

Professor Gabriel Ménard, Chair

Professor Peter Ford

Professor Trevor Hayton

Professor Quyen Nguyen

Professor Lior Sepunaru

September 2021

The dissertation of Madeline Peterson is approved.

_____

Peter Ford

_____

Trevor Hayton

_____

Quyen Nguyen

_____

Lior Sepunaru

_____

Gabriel Ménard, Committee Chair

August 2021

Synthesis, Characterization, and Electrochemical Properties of Metallophthalocyanines for Use in Energy Storage Applications

by

Madeline Peterson

Acknowledgements

As is traditional, I first must thank my supervisor Gab Menard. Gab, thank you for giving me so much room to explore and shape my own projects. You had a bit more confidence in me than I ever did and for that I will always be grateful. I wouldn't have been able to explore so many different areas of chemistry without your support. Also, thank you always taking the joke well when I photoshopped your face onto different objects and made missing posters for you when you went on vacation. I hope one day I can be as good of an advisor as you. I would also like to thank my committee for all their help and guidance in shaping all the projects discussed here.

I want thank all of Gab lab for being excellent lab mates. It was a joy getting to work with you all and I'm so excited to see where you end up. I'm so sure you will all go on to do great things. In particular, I have to thank Camden Hunt and Megan Keener. Camden, thank you for all your chemistry help over the years and also for letting me move to Canada with you to work on my dream project. Megan, there is too much to say here so I'll just say I loved every Diet Coke run and rant session we had. I couldn't have done this without you.

To all of my brethren, I love you all and I would be remiss if I didn't thank you all for keeping me sane during the past five years (and honestly the whole time I've known you guys). Thank you all for letting me complain in the group chat and for always getting excited when I need you to. Truly the best friends I could ever ask for.

To Ben, thank you for always putting up with all of my antics and letting you ask you every out of left field question that enters my mind. You always allow me to be myself and I'm so happy we met at that party I definitely remember.

And finally, I would like to thank my family. Mom, Dad, Patrick, Susan, and Emily thank you for all of your support and love. Everything I accomplish is because of how you all shaped me as a person and your encouragement of my curiosity.

Vita Of Madeline Peterson
August 2021

EDUCATION

University of California- Santa Barbara — Santa Barbara, California

Jul 2016 –Present | Doctor of Philosophy- Inorganic Chemistry | *GPA: 3.96*

University of Iowa — Iowa City, Iowa

Aug 2012 – May 2016 | Bachelor of Science - Chemistry

RESEARCH AND PROFESSIONAL EXPERIENCE

Graduate Student Researcher- Ménard Laboratory — University of California- Santa Barbara
July 2016 – Present

Undergraduate Student Researcher- Messerle Laboratory — University of Iowa
Dec 2015 – May 2016

Undergraduate Student Researcher-Forbes Laboratory — University of Iowa
Dec 2013 – Dec 2015

Hands-On Photovoltaic Experience — National Renewable Energy Laboratory
July 2019

Nuclear Forensics Undergraduate Scholarship Program — Los Alamos National Laboratory
Jun 2015 – Dec 2015

Nuclear Forensics Undergraduate Summer School — University of Missouri, Columbia
Jun 2014 – Aug 2014

PRESENTATIONS & PUBLICATIONS

Peterson, M.; Ménard, G. UC Chemical Symposium, March 2021, Poster Presentation.

Peterson, M.; Hunt, C.; Wang, Z.; Heinrich, S.; Wu, G.; Ménard, G. " Synthesis, characterization, and electrochemical properties of a first-row metal phthalocyanine series" Dalton Trans., 2020, Advanced Article.

Hunt, C.; **Peterson, M.**; Anderson, C.; Chang, T.; Wu, G.; Scheiner, S.; Ménard, G. " Switchable Aromaticity in an Isostructural Mn Phthalocyanine Series Isolated in Five Separate Redox States" JACS 2019, 141, 6, 2604-2613.

Keener, M.; **Peterson, M**.; Hernández Sánchez, R.; Oswald, V. F.; Wu, G.; Ménard, G. "Towards Catalytic Ammonia Oxidation to Dinitrogen: A Synthetic Cycle by Using a Simple Manganese Complex." Chem. Eur. J. 2017, 23, 11479-11484.

Knight, AW; Eitrheim, ES; Nelson, AW; **Peterson, M**; McAlister, D; Forbes, TZ. "Trace-level extraction behavior of actinide elements by aliphatic alcohol extractants in mineral acids: insights into the trace solution chemistry of protactinium." *Solvent Extr. Ion Exc.* **2016**, *34*(6), 509-521.

Peterson, M. *Carbon nanomaterials as an extraction material for radionuclides*, Safety of Actinide Separation Processes (SACSESS), Warsaw, Poland, Apr 22-24, 2015. Poster.

FELLOWSHIPS AND AWARDS

Mellichamp Sustainability Fellowship
July-September 2019
Recognizes outstanding work mentoring undergraduate students in the Honor Organic Chemistry Lab Program

Dewolfe Excellence in Teaching Organic Chemistry
Recognizes outstanding work mentoring undergraduate students in the Honor Organic Chemistry Lab Program

OUTREACH

Graduate Students for Diversity in Science University of California- Santa Barbara
Oct 2016 – Present

Undergraduate Student Mentor University of California- Santa Barbara
Oct 2017 – Present

Abstract

Synthesis, Characterization, and Electrochemical Properties of Metallophthalocyanines for Use in Energy Storage Applications

by

Madeline Peterson

Phthalocyanines are a well-studied class of organic macrocycles with interesting photochemical and electrochemical properties that have applications in chemical sensing, energy storage, and solar energy conversion. We aim to correlate the identity of the metal center with the electronic properties and redox behavior of phthalocyanine complexes. We first describe the synthesis and characterization of a series of soluble first-row transition metal phthalocyanines complexes. This work focused on elucidating how the identity of the metal center shapes the electrochemical behavior of these complexes. Particular attention was paid to the role of axial ligation and its effects the phthalocyanines complexes' electrochemistry. It was found that axial ligation of the early transitions metal (V, Cr, Mn, and Fe) either through synthetic modification or solvent choice led to an increase in reversibility. While the late transition metals (Co, Ni, and Cu) demonstrated behavior consistent with adsorption onto the electrode surface which we attribute to their planarity. We proceeded to investigate in detail the interaction of a cobalt phthalocyanine complex with electrode surfaces using electrochemical techniques with the intention of forming electrochemically-modified surfaces.

We found that the adsorptive behavior of our cobalt complex could be controlled through axial interaction with O_2 and full surface modification was possible through repetitive cyclic voltammetry scanning.

We then aimed to correlate the solution-state electrochemical behavior of our metal phthalocyanine complex with their ability to function as charge carriers in a redox flow battery. A redox flow battery architecture with a conductive carbon additive was then used to compare the utility of our soluble metal phthalocyanine complexes with commercially available phthalocyanines complexes that demonstrate low solubility in most common solvents. It was found that the use of a conductive carbon additive allowed for the relatively insoluble phthalocyanine complexes to behave as effective charge carriers and we demonstrated that commercially available PcM complexes (PcVO, PcFe, and Pc Ni) could be used in this architecture with good efficiency metrics.

Finally, the optical and electronic properties of a manganese nitride phthalocyanine complex in both solution and thin films were investigated to determine its utility in organic electronics. It was found that while the complex displayed favorably red-shifted absorbance and energy levels however the excited-state lifetimes were short.

Table of Contents

List of Figures

List of Schemes

List of Tables

List of Symbols and Abbreviations

A	amp
Å	angstrom
Abs coeff	absorption coefficient
ACN	acetonitrile
AEM	anion exchange membrane
Anal. Calc.	analytical calculated
atm	atmosphere
Bu_4N	tetrabutylammonium
C_6D_6	deuterated benzene
CD_2Cl_2	deuterated dichloromethane
CV	cyclic voltammetry
d	day
DCE	1,2-dichloroethane
DCM	dichloromethane
DCM-d_2	deuterated dichloromethane
DFT	density functional theory
DMF	dimethylformamide
EPR	electron paramagnetic resonance
equiv	equivalent
Et	ethyl
^{EtO}Pc	1,4,8,11,15,18,22,25-Octaethoxyphthalocyanine

Fc	ferrocene
g	gram
h	hour
HOMO	highest occupied molecular orbital
HTM	hole transport material
Hz	hertz
I	current
I	isoindolic planes
J	joule
J	scalar coupling constant
K	degrees Kelvin
Kryptofix-222	2.2.2.-Cryptand
L	Liter
LMCT	ligand-to-metal charge transfer
LUMO	lowest unoccupied molecular orbital
m	meter
M	molar
MALDI	matrix-assisted laser desorption/ionization
Me	methyl
MeCN-d_3	deuterated acetonitrile
min	minute
mol	mole
MS	mass spectrometry

*n*BuLi	n-butyl lithium
NMR	nuclear magnetic resonance
OAc	acetate
^{o}C	degrees Celsius
OLEX^{2}	crystallography software
Pc	phthalocyanine
PcM	metallophthalocyanine
Ph	phenyl
POV-Ray	crystallography software
ppb	parts per billion
ppm	parts per million
PV	photovoltaic
r.t.	room temperature
SHELXTL	crystallography software
SOC	state of charge
T	temperature
t	time
T_1	relaxation time
TCSPC	time correlated single photon counting
THF	tetrahydrofuran
THF-d_8	deuterated tetrahydrofuran
TOF	time-of-flight
UV-Vis	ultraviolet-visible

V	volume
W	watt
XRD	x-ray diffraction
α	angle
β	angle
γ	angle
δ	chemical shift
ΔG	free energy
ΔH	enthalpy
ΔS	entropy
λ	wavelength
ν	frequency
π	pi orbital
σ	sigma orbital

Chapter 1: Introduction

1.1 U.S. Energy Production and Grid-Scale Energy Storage

1.1.1 Overview of U.S. Energy Production

With the rapid expansion of new and more efficient energy technologies[1], concerns over both mitigation of climate change[2], and creating a system robust to cyber attacks[3] the modernization of energy grids has become a top priority globally. This requires a shift in energy production from traditional fossil fuel-based systems to higher levels of renewable energy in order to expand the reach of distributed energy resources (DER), such as photovoltaics (PV), thus increasing grid security while limiting the damage done by climate change and CO_2 emissions. Contrary to this goal there is still a heavy reliance on fossil fuels and over the past decade global energy consumption has increased — growing by 2.3% in 2018, including high demand for fossil fuel based sources which accounted for 70% of the growth in demand.[4] Even after unexpected contraction of global energy demand, which fell by 4%, in 2020 the initial data for 2021 indicates a rebound of 4.6% pushing it above pre-pandemic levels.[5] This is combined with rising global emissions, increasing to a peak growth of 1.7% in 2018 with 33.1 Gt CO_2 emissions with the overall concentration of atmospheric CO_2 at a high of 412.5 ppm in 2020.[5] The largest CO_2 contributor globally is coal burning while the U.S. shows particularly high demand for natural gas — 2020 showing the biggest jump in U.S. consumption of natural gas since 1971.[4]

While the continued reliance on fossil fuels is daunting, renewable energy reached 29% of global electricity generation in 2020. Two-thirds of that growth come from solar and wind generation which are expected to grow by 18% and 17% respectively, the fastest increase on record since the 1970s.[5] A primary driver for this change is the sharp decrease in cost particularly for solar energy generation, which has already hit targets from the U.S. Department

of Energy 2020 SunShot program[6, 7] and are on track to achieve the 2030 SunShot goal of $0.03/kWh at the utility scale.[8]

The shift to a more modern grid is not trivial and requires an overhaul of current U.S. energy production to accommodate high levels of penetration from the fastest growing renewable energy sources, solar and wind. There is concern that renewable energy growth is not sufficient to drive down the share of fossil fuels to limit CO_2 emissions to the necessary levels.[9] One primary reason being these sources are variable generation (VG) sources meaning the amount of output depends on environmental conditions such as time of day, time of year, location, and weather. Estimates indicate the need for an 80% reduction in CO_2 emission by 2050 and the energy sector to be carbon-neutral by the end of this century to stabilize and mitigate the effects of global temperature increases.[10-12] There are several factors currently limiting the incorporation of more VG sources and shifting to a grid with higher levels of DER: a slow shift away from baseload generators with a minimum generation constraint; the need to ensure transmission interconnection between all major U.S. grids; strategies for inclusion of both VG renewables (e.g., wind and solar photovoltaics) and dispatchable renewables (e.g., hydroelectric); the curtailing of VG sources; and ramping up available energy storage to address the supply and demand mismatch of VG renewables.[11] These constraints highlight that a grid capable of sustaining high levels of renewable energy is both highly flexible and responsive with capabilities to monitor and shift energy output accordingly as VG output changes.[13, 14] One of the key points in the creation of a more flexible grid than is currently implemented is the need for a drastic increase in grid-scale energy storage in order to meet our renewable energy generation goals.[15]

1.1.2 Comparison of Technologies for U.S. Grid-Scale Energy Storage

While it is understood that more electrical energy storage (EES) is urgently needed, current integration is lacking. The U.S. has an annual generation capacity of 1100GW while the total storage capacity is only 24.2GW, meaning roughly 2.2% of energy generated in the U.S. is ever stored.[16-18] The vast majority of current storage capacity is both geographically concentrated[19] (with California implementing the most storage capacity in the U.S.) and technologically monolithic[12]. In order to better modernize our grid and increase our energy storage capabilities, we must expand and diversify our offerings of potential storage mediums. There are a variety of potential technologies able to fill this void: physical, mechanical, thermal, chemical, and electrochemical.[12] It is worth noting here that there is no one perfect energy storage medium and not every technology needs to serve every purpose— pumped hydroelectric storage is best served at large scales for bulk power management whereas lithium-ion batteries are well suited for consumer-scale energy storage.[20]

Therefore, it is worth looking at where there are technological gaps that must be filled to increase EES. One of the main problems facing the implementation of EES is that there are few technologies able to appropriately scale to levels suitable for bulk power management by utility companies. The only technologies currently deployed at this level are pumped hydroelectric and compressed air energy storage[12]; however, as they have specific geographical needs, their expansion of installed capacity to the necessary levels is limited. The most common energy storage implemented in the US currently, is pumped hydropower, which represents over 95% of the energy storage currently installed and is one of the most common options for long-duration energy storage.[16, 21] Pumped hydropower offers the potential for high capacity, high round-trip efficiency (70-80%), and relatively inexpensive energy storage ($20 kWh^{-1})[22, 23], however, there are concerns over future expansion as the technology requires

specific geographic sites for its installation[24]. This limitation prevents pumped hydropower storage from being used particularly in urban areas. This leaves a gap of utility scale stationary energy storage that must be filled by new technologies. Redox flow batteries (RFBs) are a promising solution for long-duration energy storage, due to their simple design, long life-times, relatively high round-trip efficiencies, and decoupled energy capacity and power.[25-28] RFBs offer similar round trip efficiencies (65-80%) and more geographic flexibility in comparison to pumped hydropower, however, they are limited by their relatively high costs ($40-200 kWh^{-1})[23]. Reducing the cost of RFBs is one of the most important ways of ensuring they are competitive as an energy storage technology.

1.1.3 Redox Flow Batteries

The focus on batteries capable of efficiently scaling to the utility-scale has increased interest in RFBs, a technology first proposed in Japan in the 1970s, that may be capable of meeting the needs detailed above.[25] Most commonly used commercially batteries (e.g., lithium-ion) have their electroactive components integrated into the electrode.[29] In RFBs, the energy storage and energy conversion are decoupled with the electroactive component, or charge carrier (CC), dissolved and stored in separate tanks until energy conversion (either charge or discharge) is needed, upon which it is passed through flow-field electrodes capable of transferring charge with an ionically conducting membrane separating the half-cells and allowing the migration of supporting electrolyte for charge balance (Fig. 1.1)

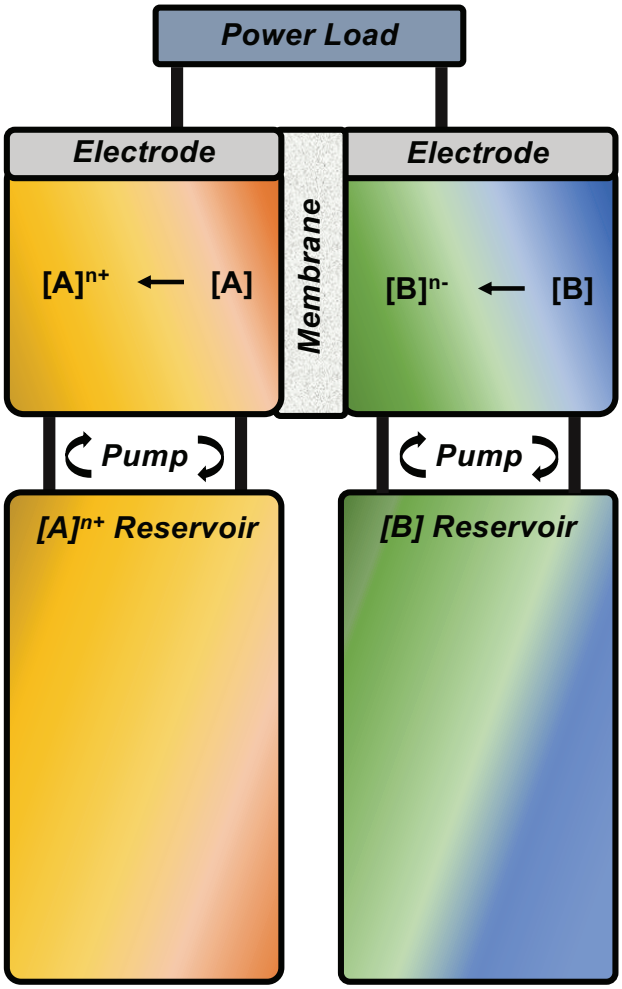

Figure 1.1: Diagram of an asymmetric RFB.

RFBs have several key advantages for application in stationary grid-scale energy storage: long lifetimes, fast response times, high power density, scalability, and the decoupling of energy density (dependent on tank size and CC concentration) and power density (dependent on electrode surface area and flow rate).[12, 25, 28, 30, 31] There are smaller installations of RFBs currently in use,[25, 32] but increasing widespread adoption of this technology requires addressing the following limitations: cost, crossover capacity fade, and low energy densities.[27, 33] One of the main targets of RFB research is currently focused on improving the energy density of RFBs,

which is controlled by the number of electrons transferred (n), the voltage of the cell (V_{cell}), the concentration of the CC (C_{CC}), and Faraday's constant (F) (Eqn. 1.1)

Eqn 1.1 $\hat{E}_{RFB} = 0.5nV_{cell}C_{cc}F$

Increasing the energy density is reliant upon careful selection of the solvent and design of the charge carrier. With respect to CC design, extensive work has been done on the synthesis and validation of a huge variety of compounds used, including: metal ions[34, 35], all organic[36], metal coordination complexes[37], redox active polymers[38], semi-solid[39], and lithium ion[40] for use as charge carrier. Many of these systems use asymmetric charge carriers (as shown in Fig. 1.1) where there are different CCs employed in each half-cell. This asymmetry requires ion-exchange membranes capable of maintaining charge balance while completely separating the catholyte and anolyte to prevent crossover between the CC tanks which leads to crossover capacity fade that accumulates to eventual cell death. Utilization of a bipolar species (a CC capable of being either oxidized or reduced, Fig. 1.2) can both eliminate crossover capacity fade as any CC that crosses the membrane can be regenerated on the next cycle while also allowing for less expensive porous membranes reducing the cost of RFBs in place of more traditional ion-exchange membranes.[27, 41]

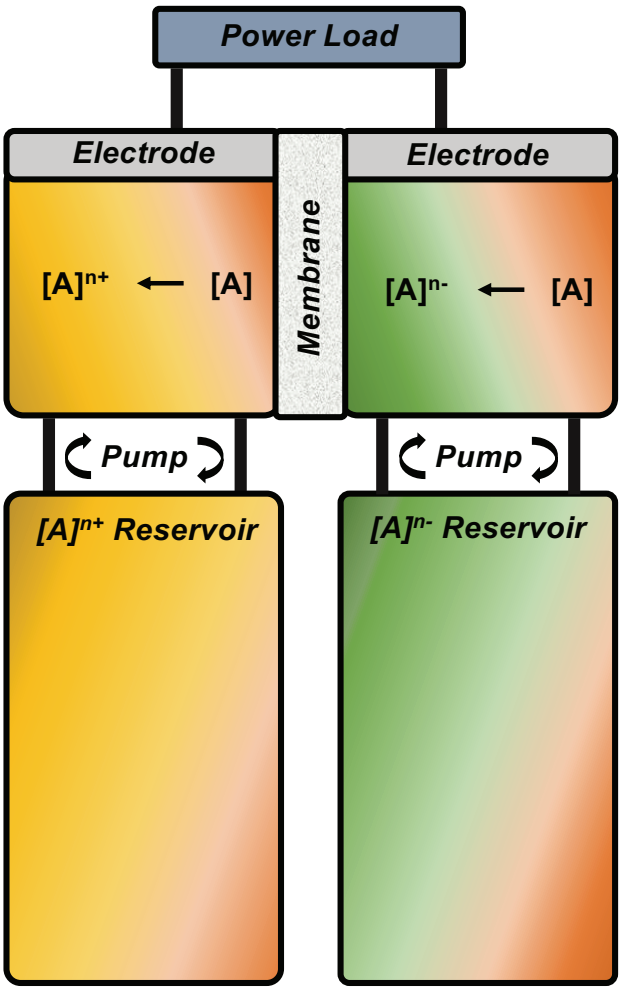

Figure 1.2: Diagram of a symmetric RFB using a bipolar CC.

Use of non-aqueous conditions can have major implications on the ability to increase energy density. Most RFBs use aqueous solutions which have been effective and may display high cell performance, low cost, and good stability.[34, 35] However, using aqueous solutions has its limitations, such as: relatively small electrochemical window (between -0.5 V and 1.25 V vs SHE on a carbon electrode)[42], limited solubility of potential CC, and relatively small operating temperature range.[12] To address these issues, non-aqueous RFBs have been extensively studied after first being proposed in 1984[43] with proponents touting larger solvent potential windows

leading to higher possible cell voltages, wider working temperature ranges, and the potential for higher CC solubilities leading to higher energy densities.[44] The working potentials of RFBs using non-aqueous solvents can be nearly double those using aqueous conditions ultimately leading to higher energy densities.[12] The use of non-aqueous conditions can offer the opportunity to use organic and organometallic complexes which have low solubility in water but have the potential for multiple redox events, tunability of their potential window, and potentially lower cost.[12]

While these advantages are promising, non-aqueous systems with organic CCs suffer from complex CC syntheses that increase CC cost and poor long-term stability. This has opened in the door to exploring other ways to circumvent needing high solubility of CC. One potential option is using hybrid RFBs that have one or more components that are not dissolved and instead may be precipitated out upon charge or discharge or remain undissolved throughout.[45] One of the most prominent of these are the semi-solid lithium flow batteries demonstrated by Chiang and co-workers.[39] Of particular relevance to this thesis are RFBs dependent on percolation networks where a charge carrier is mixed with an insoluble conductive carbon additive that essentially extends the electrode throughout solution allowing for charging and discharging to occur in a more diffuse fashion (Fig. 1.3).

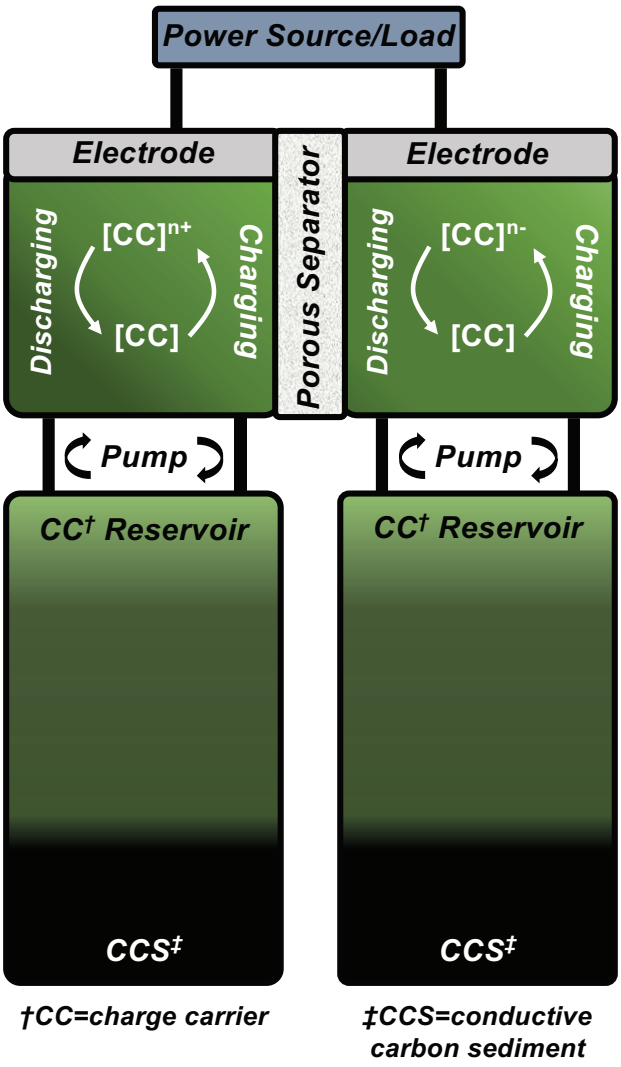

Figure 1.3: Diagram of an RFB utilizing a slurry-based system with a bipolar charge carrier and conductive carbon additive.

This architecture circumvents the solubility limits that typically plague RFBs while the conductive carbon additives allow for heterogenous electron transfer to be distributed throughout solution. Our group has previously shown this architecture to be successful for a substituted manganese nitride phthalocyanine[46] and wish to expand upon this work to demonstrate the advantages of this system for lower cost/higher energy density hybrid RFBs.

1.2 Phthalocyanines Synthesis and Properties

1.2.1 Overview

As discussed above, one area of interest is developing new, cost-effective charge carriers that can improve energy density. One such class of complexes may be phthalocyanines (Pcs) and their metalated derivatives (MPcs). Pcs are large macrocyclic ligands with four isoindole units linked by bridging nitrogen atoms and an internal circuit with a delocalized 18 e^- π system related to porphyrins that have been extensively studied since their discovery in the early 1900s due to their stability, capability to coordinated a wide variety of metals, electrochemical, and photochemical properties.[47, 48] Pcs well developed chemistry is in part due to their facile substitution on the macrocyclic ring (either peripherally as with R_1 or non-peripherally as with R_2 in Fig. 1.4) and the potential for tuning with both the choice of metal center (M in Fig. 1.4) and axial coordination of any metal in the central cavity (X in Fig. 1.4).

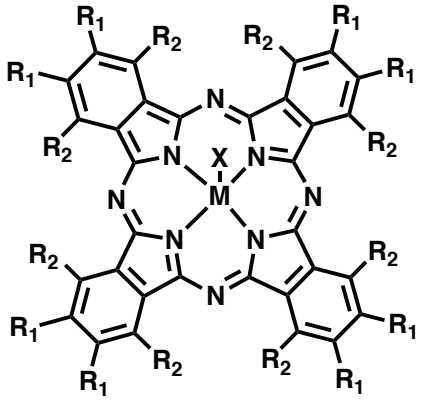

Metallophthalocyanine (MPc)

Figure 1.4: Structure of a substituted Pc macrocycle.

The effects of ring substitution[49-51] and the metal center[52, 53] on the chemical, electrochemical, and photophysical properties have been investigated. This variability in their properties has led Pcs to being a widely studied classes of organometallic compounds with proven applications

in catalysis[54, 55], chemical sensors[56-58], organic electronics[59], and solar cells[60-64]. To better understand the work detailed in this thesis, a brief overview of several important topics is presented here: Pc synthesis, their photochemical properties, as well as their electronic and electrochemical properties.

1.2.2 Synthesis and Substitution Patterns

Pc synthesis typically starts as a condensation of precursors to form a macrocyclic ring, often templated around a metal center. There are a wide variety of potential phthalocyanine precursors, with the most common being phthalonitrile (**1**), phthalic acid (**2**), phthalic anhydride (**3**), phthalimide (**4**), and diiminoisoindoline (**5**) (Fig. 1.5) with **1** being the most relevant precursor for laboratory scale syntheses.[65]

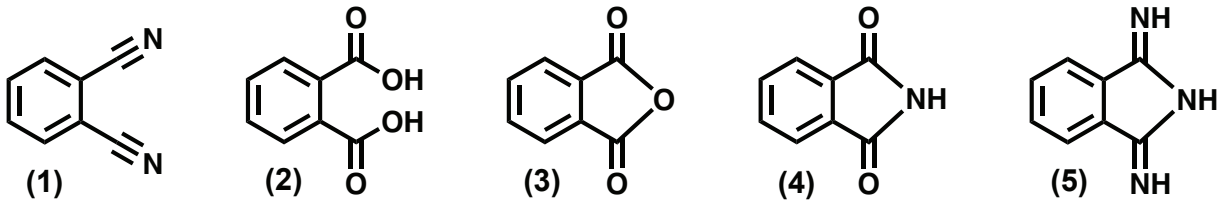

Figure 1.5: Structures of common Pc precursors.

The synthesis of symmetrically substituted phthalocyanines (that is phthalocyanines made from one precursor) is relatively straightforward and well explored[48] and typically requires a suitable precursor, base, and solvent (most often alcohols). The method most relevant to this work utilizes a phthalonitrile precursor and lithium metal to form the cyclized product with lithium in the central pocket ((**1**) in Scheme 1.1) which can then become the free pro-ligand upon the addition of hydrochloric acid ((**2**) in Scheme 1.1).

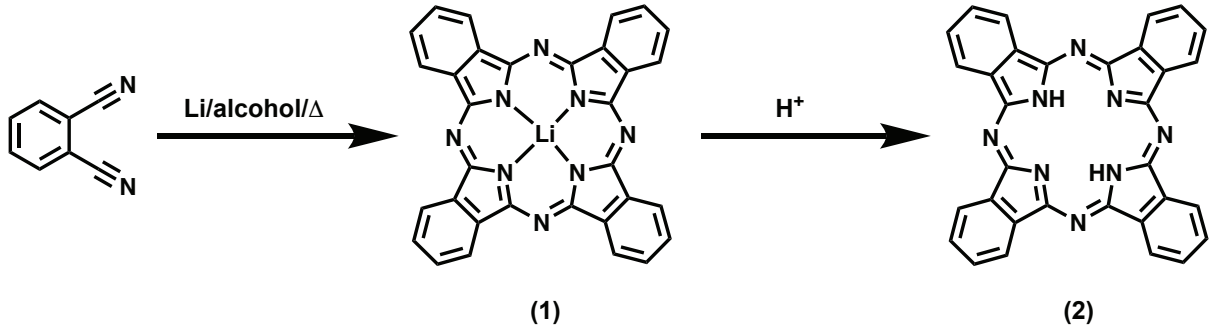

Scheme 1.1: Synthetic scheme for formation of a lithiated Pc (1) and a protonated Pc (2).

Either (**1**) or (**2**) can then be used to create other MPcs ((**3**) in Scheme 1.2) through a salt swap, done in a high boiling basic solvent such as DMF with a metal salt (typically metal halides or acetates).

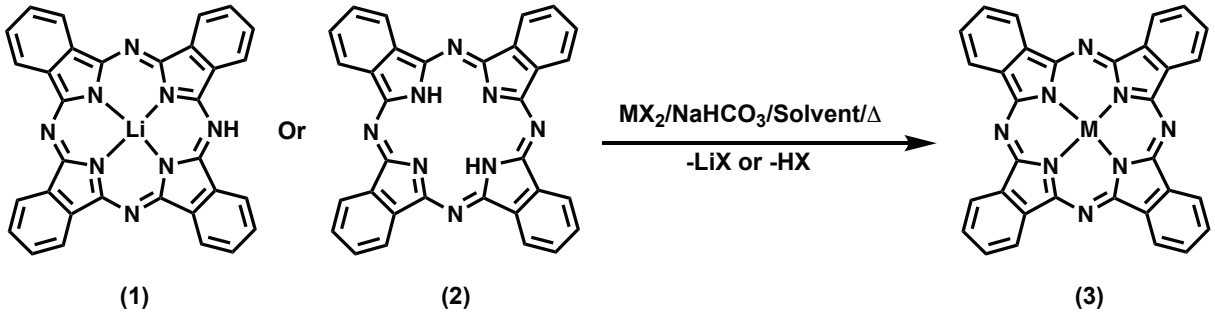

Scheme 1.2: Synthetic scheme for the metalation from either a lithiated or protonated Pc.

A general mechanism of the Pc formation is shown in Scheme 1.3. The elucidation of this mechanism was primarily achieved by the isolation and characterization of intermediates (A)[66], (B)[67], and (C)[68] and is thought to be primarily initiated by alkoxide ions formed in-situ through the reaction of alcohol and lithium metal.[48]

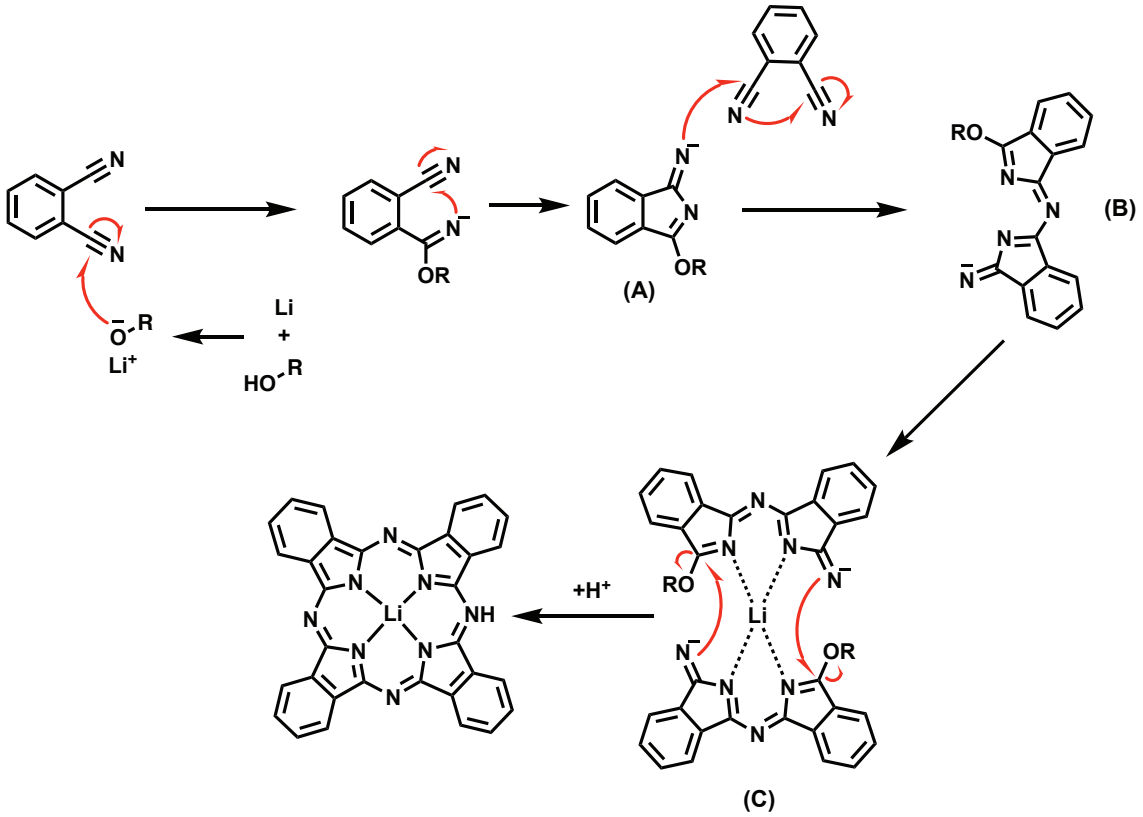

Scheme 1.3: Mechanism of formation for a Pc macrocycle using a lithium metal template.

While unsubstituted Pcs are industrially relevant, their planarity and strong intermolecular interactions render them mostly insoluble in typical solvents; therefore, the isoindole moieties are often substituted to enhance solubility. Typically, these functional groups are added to the precursor before the cyclization process detailed above in order to attempt to control the position and number of substituents. For symmetrical phthalocyanines, substitution usually occurs as either tetra-substituted (each precursor has one substituent) or octa-substituted (each precursor has two substituents). It is worth noting that substituents, particularly sulfate groups, can sometimes be added to the already formed Pc ring; however, these reactions can be difficult to control stoichiometrically and tend to yield a mixture of products.[65] This problem is also encountered for tetra-substituted Pcs where four constitutional isomers of varying symmetry

(C_{4h}, D_{2h}, C_{2v}, C_s) may be difficult to separate. The substituent chosen can have a profound effect on the properties[49, 69] with the options stretching from commonly used organic substituents in the case of alkyl[70], alkoxy[71], and phenyl[72] to the more exotic such as fullerenes[73], ferrocenes[74], and dendrimers[75]. In some instances, such as for use in dye-sensitized solar-cells where anchoring groups and push-pull molecular design can be advantageous[60-62], unsymmetrical Pcs are desired. This typically comes from mixing two precursors together in the conditions described above and allowing the formation of a statistical mixtures of products (Fig. 1.6) that then must be separated.

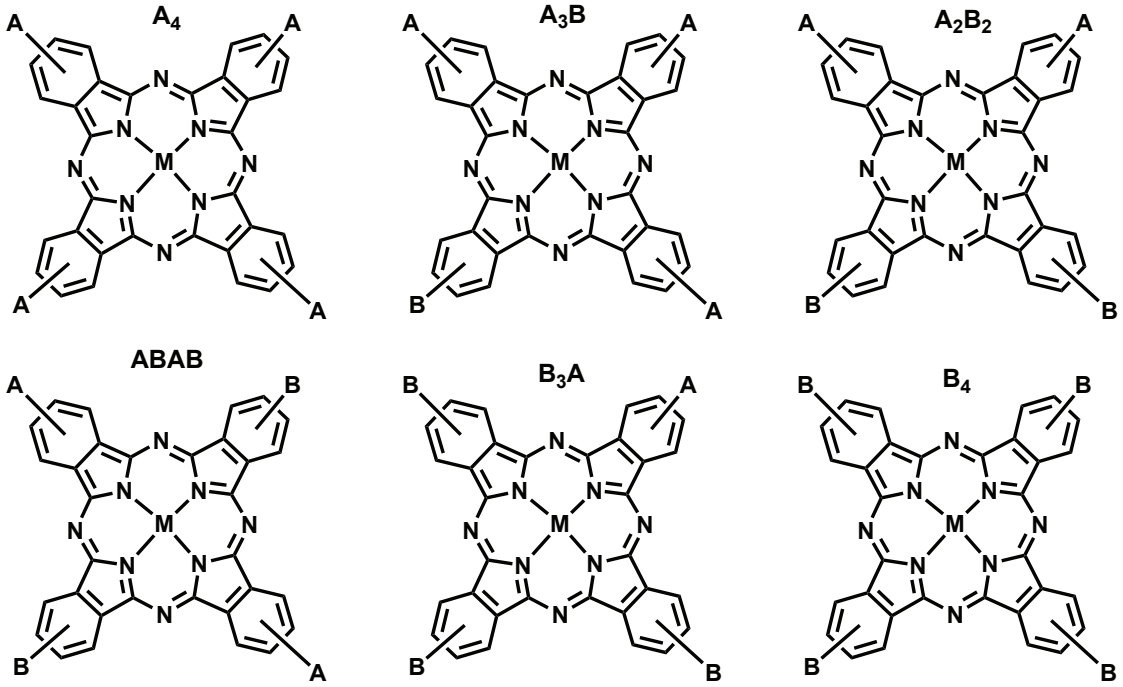

Figure 1.6: Structure of the potential isomers for unsymmetrical Pcs.

The wide variety of potential products yields a vast body of work on how best to prepare unsymmetrical Pcs and as such we will focus on the most relevant to this thesis: formation of

A_3B Pcs (Fig. 1.6) where only one isoindole subunit differs from the rest. Two main pathways are relevant: statistical condensation and the use of sub-phthalocyanine precursors.[76]

Statistical condensation in which two different precursors are mixed together in differing ratios (Scheme 1.4) is a commonly employed technique to form A_3B Pcs due to its experimental simplicity. This method as described by the title yields a statistical mixture of the different products shown in Fig. 1.6 which can be difficult to separate.

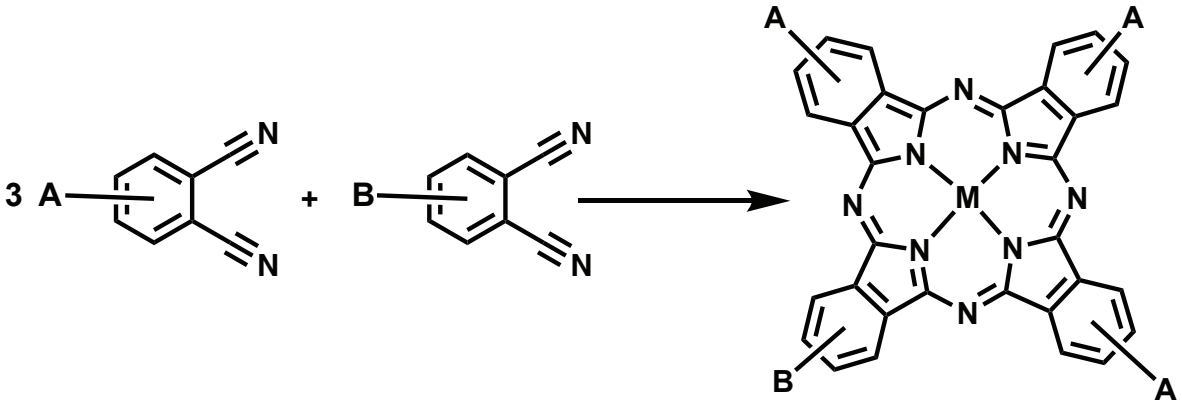

Scheme 1.4: General synthetic scheme for a statistical condensation.

There are two main consideration that must be made during these reactions that can help to determine the ratio of the products: the stoichiometry and the substituents on each precursor. The most typical stoichiometry used is a 3:1 ratio of A:B which yields a complex reaction mixture that is typically distributed as 33% A_4, 44% A_3B, and 23% of the remaining products[76] which can be separated using chromatography.[77-79] Higher ratios of A:B can be used to drive down the side product formation particularly when the B subunit is highly reactive leading to a separation of the A_3B from a product that is majority A_4.[80] The substituents on both the A and B subunits can also be used to drive the reaction towards the desired products. Using bulky substituents can also help ensure that a reaction between the A and B subunits occurs, as bulky

groups can prevent two A subunits from coming together; however, this does shift the ratio of products formed towards B subunit heavy products.[76, 81]

The second method uses the ring opening of a low-symmetry homolog of Pcs, the subphthalocyanine (Scheme 1.5), to form A_3B product.

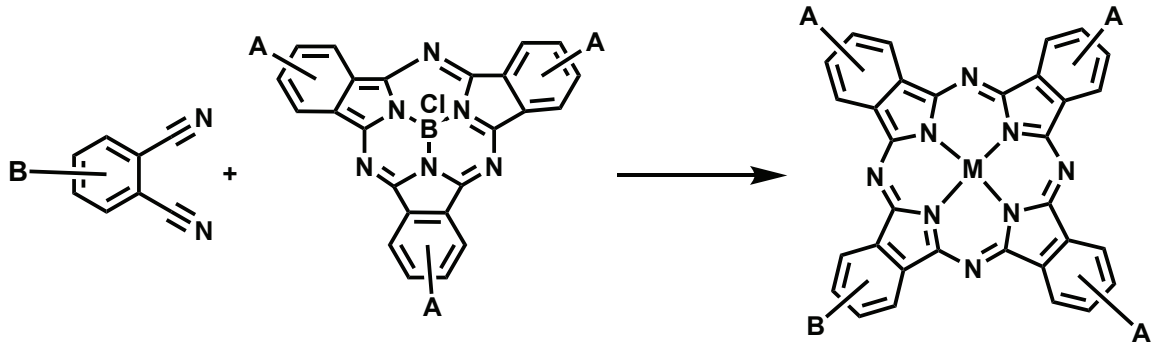

Scheme 1.5: General synthetic scheme for a subphthalocyanine ring opening.

This method can be highly selective given the correct conditions: addition of the desired metal salt, presence of a low reactivity phthalonitrile with a strong base (e.g. DBU), and sub phthalocyanines with no or electron-withdrawing substituents, and monomers with electron-donating substituents.[76, 82] If these conditions are not met, the resulting product is similar to that of the statistical condensation products.

1.2.3 Photochemistry of Phthalocyanines

1.2.3.1. Photochemistry Overview

A brief overview of some of the fundamentals of Pc photochemistry is given here so that the subsequent discussion of Pc electronic spectra and the discussion of the data in Chapter 5 are clear. A more thorough description of these phenomena and photochemistry generally can be found elsewhere.[83, 84]. Upon absorption of light, molecules can be excited and undergo an

electronic transition moving from a lower energy occupied orbital (the ground state) to a higher energy unoccupied orbital (the excited state). The main processes of excitation and emission for a Pc: absorbance (abs.), vibrational relaxation (VR), fluorescence (F), phosphorescence (P), internal conversion (IC), and intersystem crossing (ISC) are depicted in a simplified Jablonski diagram below (Fig. 1.7).

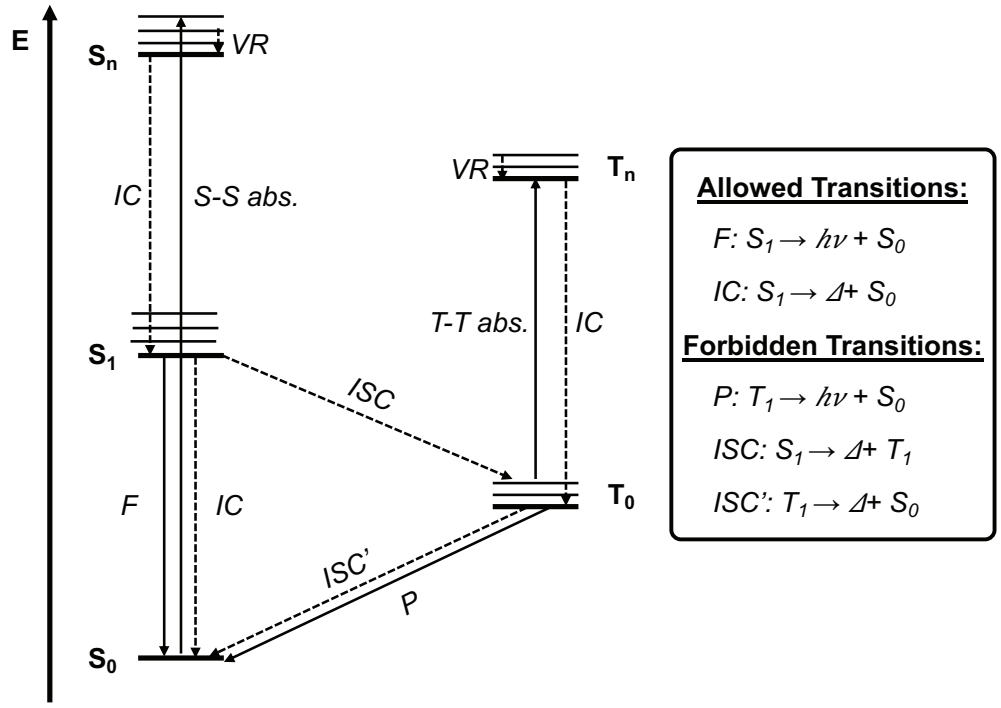

Figure 1.7: Jablonski diagram showing the pathways of excitation and emission in Pcs. Solid lines indicate radiative process and dashed lines indicated non-radiative processes.

In order to better understand this diagram, there are a few key points. First, these electronically excited states can affect both the energy of an electron as well as the spin of the system which can affect the decay processes. Electrons have individual spin angular ($m_s = \pm 1/2$) which in molecules add up to the total spin quantum number (S); in organic molecules such as Pcs electrons have a net pairing of spins, and their ground state is a singlet (S_0) where S =0. Upon

excitation with light, an electron can be moved from S_0 to an excited singlet state, S_n where n=1 is the lowest energy excited state. The excitation typically is not only an electronic excitation but rather a vibronic transition, that is a simultaneous electronic and vibrational transition. This occurs because electronic transitions are faster than nuclear motion as indicated by the Franck-Condon principle; therefore, what may have been the lowest energy vibrational mode for the ground state is often not for the excited state.[84]

The electron can then relax through two primary pathways: non-radiative (VR, IC) and radiative (F) decay. Non-radiative decay is the loss of vibrational energy either intramolecularly or intermolecularly which occurs both for VR and IC. The difference between the two is that VR is the transition between vibrational states of the same electronic state while IC is the transitional between vibrational state of different electronic states. Radiative decay is the emission of a photon during the transition between electronic excited states which occurs with the selection rule of $\Delta S = 0$ allowing for a transition between S_o and S_n. There is a relatively large gap between the rate constants of non-radiative decay (typically around 10^{12} s^{-1}) and radiative decay (maximally around 10^9 s^{-1}).[84] This difference in the rate constants leads to what is referred to as Kasha's rule which states that radiative decay occurs only in appreciable quantum yield from the lowest energy excited state in closed-shell organic molecules. There are exceptions to this rule, and it primarily depends on the energy difference between S_0 and the subsequent S_n states. As the energy gap between any two electronic states gets smaller, the vibrational overlap increases and so does the rate of non-radiative decay.[84] This can be seen experimentally is the shift between the absorption and emission, called the Stokes shift, that can give an idea of how much structural rearrangement occurs on excitation of a molecule. Pcs tends to be rigid and thus have small Stokes shifts.

In addition to transitions between singlet states, there are also transitions that occur with a change in spin leading to an excited triplet state (S = 1). While transitions between excited triplet states can be allowed as described above, a transition between singlet and triplet states (ISC in Fig. 1.7) is forbidden by the spin selection rule as $\Delta S=0$. Therefore, these transitions are often slower with the T_1 state being long lived. However, like singlet-singlet relaxation triplet-singlet relaxation will occur non-radiatively, with ISC crossing back to the ground state, or radiatively, with phosphorescence. The ratio of these transitions is dependent on the energy between them as well as the nature of the Pc and central metal being used, but in general the radiative decay is dependent on the extinction coefficient.[85] The exact balance of the decay processes can be found by looking at the quantum yields of the fluorescence and phosphorescence through steady-state measurement and the lifetimes of the excited states through time-resolved spectroscopy (such as time-correlated single photon counting in which as laser is used to induced the excited state and results in a histogram of the average lifetime for an excited state).[86]

1.2.3.2 Phthalocyanine Electronic Spectra

Pc's intense absorption of visible light, particularly in the red and NIR regions, contribute to their utility as dyes[87], in solar cell applications[61, 62, 88-90], non-linear optics[74, 91-93], and photodynamic therapy[94, 95] among other applications. In the discussion of Pc electronic spectra, the nomenclature comes from porphyrin spectroscopy and was defined by Platt with the B-band in porphyrins being strongly allowed and in the blue range while the Q-band being quasi-allowed.[96, 97] This terminology is used with Pcs as well as other analogues to keep consistency when discussing the spectra particularly since most of the work done on describing the electronic transitions of porphyrins also apply to Pcs.[97, 98] As a matter of general description,

Pcs show two absorption bands: the Q-band is observed at approximately 650-700 nm and the B-band (or Soret band) is observed at around 300-400 nm (Fig. 1.8).[85]

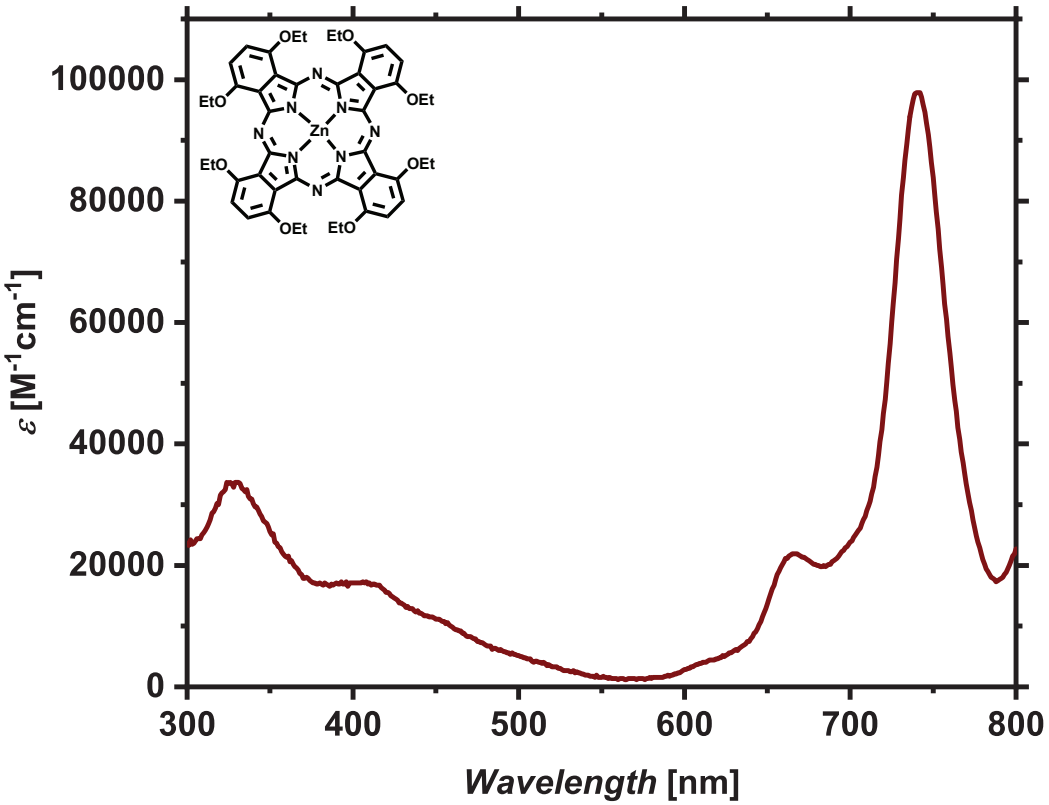

Figure 1.8: UV-vis spectrum of ^{OEt}PcZn in CH_2Cl_2 solution.

In Pcs, the absorption bands are narrow due to the rigidity of the phthalocyanine core causing the excited state structure to be similar to that of the ground state.[98] The spectra of Pcs show a marked shift from that of porphyrins with the Q-band increasing in intensity over the B-band, as well as a typical shift to lower energies for Pc absorption relative to porphyrins. These changes have been noted as resulting from the loss of degeneracy of the $1a_{1u}$ and $1a_{2u}$ HOMO orbitals when moving from porphyrins to Pcs allowing for the Q-band to shift lower energies and increase in intensity as predicted by Gouterman's four-orbital theory (Fig. 1.9).[98-100] The B-band in Pcs is actually best described at two separate bands (typically denoted a B1 and B2)

that are close enough in energy to be super imposed and indistinguishable in most solution state absorption spectra of transition metal Pc complexes as shown in Fig. 1.8.[99] In addition to these core properties, both the substitution of the Pc rings as well as the central metal atoms are known to have effects on the optical properties.

Computationally, it has been determined that the a_{1u} HOMO is primarily Pc based with its energy affected by the substituents while the $e_{g,}$ LUMO set mixes strongly with the metal and thus is affected by the identity of the central metal.[101, 102] Once a metal is coordinated to the Pc ring there is a shift in the ordering of the orbitals is dependent on the metal center which can have large effects on the optical properties. Metal centers can introduce new charge transfer (CT) bands into the absorption spectra typically between either 450-600nm or 700-1500nm[103] with these transitions coming from metal orbitals energetically between the a_{1u} and e_g sets that previously made up the Pc HOMO -LUMO gap (Fig. 1.9).[102]

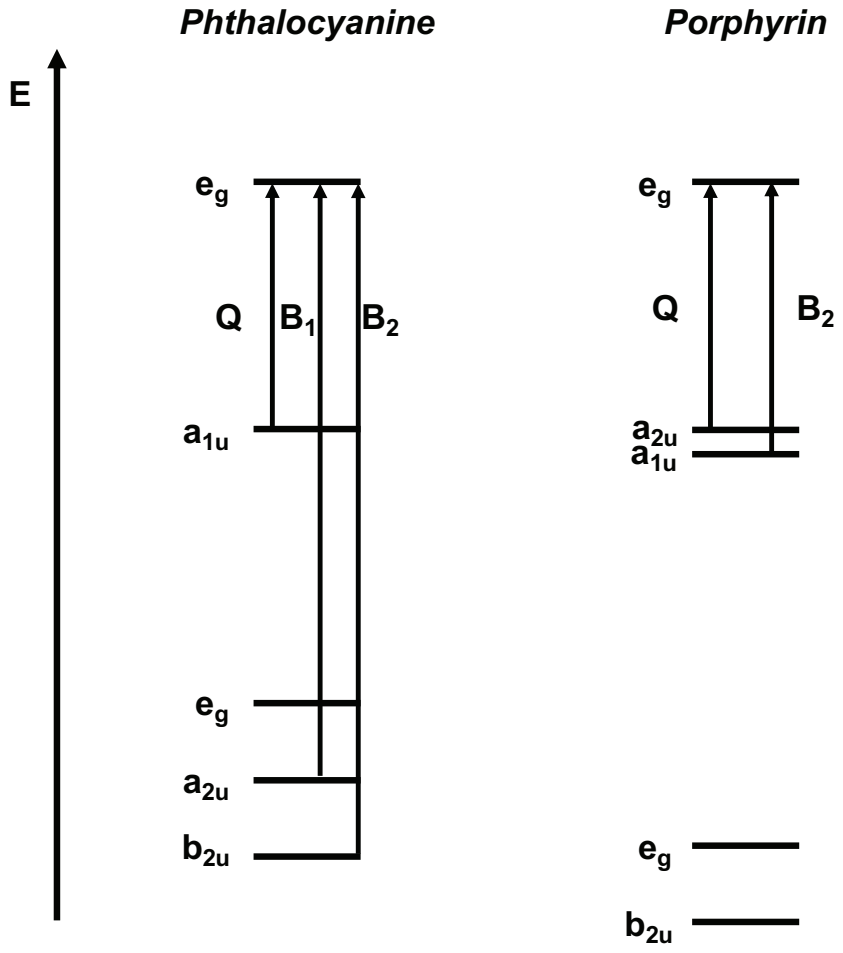

Figure 1.9: Predicted frontier orbitals in phthalocyanines and porphyrins based on Gouterman's work.

Here a distinction must be made between closed-shell and open-shell metals.[85] Closed-shell metals can show luminescence although this is more intense for main-group Pcs (e.g., MgPc, AlPc) than it is for first-row transition metals (e.g., ZnPc). The properties of Pc complexes with open-shell metals show a strong dependence on identity of the metal. In the case of diamagnetic 4d and 5d MPcs (e.g., RuPc, PtPc) intense phosphorescence is demonstrated.

First-row transition metals show more variability with some paramagnetic 3d metals (e.g., VOPc, CuPc) being able to luminesce while others (e.g. NiPc, CoPc) do not.[85]

The role of the substituents on Pc's electronic spectra has also been closely studied. A linear relationship between the number of positions substituted on a Pc ring and the magnitude of the shift in the Q-band for a given substituent has been idenified.[104] A systematic comparison of Pcs with electron-donating and -withdrawing groups has shown the identity, number, and position of substituents alter the levels of the HOMO and LUMO thus causing Q-band shifts[49, 105] In addition to shifting the Pc's energy levels, substituents can affect the photostability of complexes[106], aggregation propensity, and quantum yields.[51] Understanding the substituent effects described above provides a blueprint for how to use the type, number, and position of substituents to modify the electronic properties for a given application.

1.2.4 Phthalocyanine Electrochemistry

1.2.4.1 Redox Properties of Phthalocyanines

Much like with the photochemistry of phthalocyanines, the electrochemistry depends on a combination of the Pc core, chosen substituents, and any metal center chosen, thereby leading to a large variety in the potential redox properties. Phthalocyanine electrochemistry has been studied for almost every metallic and semi-metallic element on the periodic table and because of the breadth of the work, it is difficult to succinctly summarize all of it; therefore, the aim of this section is to highlight key components of Pc and MPc electrochemical behavior.[107] Often the discussion of Pc electrochemistry is divided between Pc rings with central elements that are non-redox active (e.g., H, Li, Zn) and those that are (e.g., Co, Fe, Mn) and that is how this section will be structured to try to disambiguate the Pc and metal redox properties.

Pc rings are typically assigned a doubly anionic charge denoted as Pc(-2) in their neutral state. Oxidation to Pc(-1) and Pc(0) correspond to the removal of the electrons from the a_{1u} HOMO while reduction to Pc(-3), Pc(-4), Pc(-5), and Pc(-6) corresponds to the addition of up to four electrons into the e_g LUMO set.[108] For ring-based redox chemistry, the first oxidation and reduction are separated by 1.5V, indicative of the energy difference between the HOMO and LUMO.[109] However, this value is based on a monomeric Pc complex, the ability to aggregate through spatial overlap of Pc ring's π-orbitals adds to the complexity of interpreting the redox chemistry. Cyclic voltammetry (CV) of Pc complexes (notably Zn and Si Pcs) demonstrated that oxidation is often stabilized by the formation of dimers and higher order aggregates due to charge delocalization.[109, 110] In contrast, aggregation showed little effect on the stability of the reduced species with Pc disaggregating due to increasing electrostatic reulsion.[109, 110] The choice of substituents, as well as their placement, can affect the redox process of the ring, shifting both the potentials of the oxidations and reductions as well as the gap between them.[50, 107]For redox inactive metals, ligand and metal redox are not entirely separate entities with the potentials for the ring oxidation and reduction being affected by the polarizing power of the central metal (defined at charge/ radius or ze/r) with smaller, more highly charge central metals making oxidation more difficult and reduction easier.[111] The difference between the oxidations and reductions is often changed when redox active transition metals are used with d-orbital energies falling between the HOMO and LUMO of the Pc ring.[109] It is also noted that the use of axially ligating species can change the electrochemistry of MPcs particularly with the ability to prevent aggregation, increase solubility, and stabilize metal-based redox events.[112, 113] One of the main advantages of MPcs is that they offer a site of tunability that expands the use of Pcs as electrocatalysts[114-117], electrochemically tunable

chromophores[118] and electrochemical sensors[119-121]. Often these applications rely on the interaction of MPc with surfaces and particularly electrode surfaces.

1.2.4.2 Phthalocyanine-functionalized Surfaces

While the limited solubility of Pcs is typically an issue for solution-based processes, it can be advantageous for functionalizing surfaces with Pcs. This modification has been done through a variety of methods, some of which are depicted below ((1) in Fig. 1.10).[55, 107, 122-124]

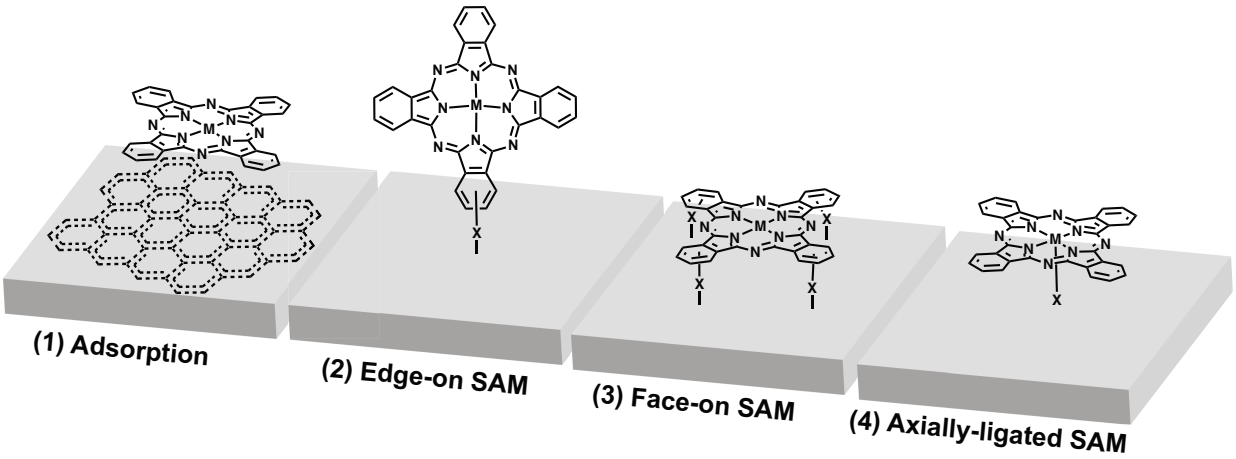

Figure 1.10: Methods of attached for Pcs to surfaces.

One of the most experimentally accessible methods has been the adsorption of Pcs onto a surface, typically a graphite or carbon-based surface, through spin-coating, drop-casting, or utilizing the Langmuir-Blodgett technique.[125-128] While adsorption yields Pcs bound to the surface through π-based ring interactions, more covalent interactions can be used through the addition of substituents (either on the ring or metal center) that are capable of bonding with the electrode surface ((2), (3), and (4) in Fig. 1.10). The most commonly used substituents in this case are sulfur containing ligand (alkylthio- arylthiol-, and other thiol-based substituents) interacting with a gold surface[122-124], although other methods such as polymeric Pcs with

cyano-groups interacting on gold[129], pyridine-linked TiO_2 srufaces[60], and carboxylic acids on ITO have been demonstrated[61, 78] among many others. Pc films can also be made through vapor deposition techniques such as physical vapor deposition and organic molecular beam epitaxy.[130] The last common method is electropolymerization of Pcs which can be synthesized by directly linking the benzene fragments, addition of Pcs to a polymer matrix, or formation of π-stacks of Pcs.[131, 132]

1.3 Scope of Dissertation

This dissertation primarily aims to understand transition metal phthalocyanines and their properties as they relate to fundamental electrochemistry, redox activity and grid-scale energy storage. We first detail the synthesis and characterization of a series of 3d transition metal phthalocyanines from vanadium to zinc (Chapter 2). The work primarily focuses on the difference in the electrochemistry of these compounds and ultimately finds a distinct link between axial ligation of the metal and reversible electrochemistry as well as differences between early and late transition metal complexes with the dividing line between early and late being iron. From this we discovered interesting adsorption and stripping behavior for our late transition metal complexes (^{OEt}PcCo, ^{OEt}PcNi, and ^{OEt}PcCu) on the electrode surface and sought to better understand the observed behavior (Chapter 3). We then selected representative compounds for the early (^{OEt}PcVO) and late (^{OEt}PcNi) transition metals and tested them as charge carriers in a slurry-based RFB setup previously published by our group to better understand the properties that are beneficial when utilizing slurry-based RFBs (Chapter 4).[46] Finally, we investigated the photochemical properties of our ^{OEt}PcMnN to determine how the manganese nitride moiety compares to other axially ligated metallophthalocyanines for use as a material in solar cells Chapter 5).

The work discussed in Chapter 2 was a collaborative effort which could not have been done without the hard work and talent of Camden Hunt, Zongheng Wang, and Shannon Heinrich. Both the author and Camden Hunt synthesized and characterized ^{OEt}PcVO, ^{OEt}PcMnCl, ^{OEt}PcMnN, ^{OEt}PcCo, ^{OEt}PcNi, ^{OEt}PcCu, and ^{OEt}PcZn. Shannon Heinrich synthesized and characterized ^{OEt}PcCr. Zongheng Wang synthesized and characterized ^{OEt}PcFe. The electrochemistry detailed in Chapter 2 was performed by the author and Camden Hunt. At the time of this writing, Chapter 2 has been published, Chapters 3 and 4 are being prepared as manuscripts, and more work is being done to determine the future of the project outlined in Chapter 5. The work in Chapter 2 is reproduced from the following reference with permission from the Royal Society of Chemistry.

Chapter 2: Peterson, M.; Hunt, C.; Wang, Z.; Heinrich, S. E.; Wu, G.; Ménard, G., Synthesis, characterization, and electrochemical properties of a first-row metal phthalocyanine series. *Dalton Transactions* 2020.

1.4 References

1. Romero Agüero, J.; Takayesu, E.; Novosel, D.; Masiello, R., Grid modernization: challenges and opportunities. *The Electricity Journal* **2017,** *30* (4), 1-6.

2. Yang, Z.; Zhang, J.; Kintner-Meyer, M. C. W.; Lu, X.; Choi, D.; Lemmon, J. P.; Liu, J., Electrochemical Energy Storage for Green Grid. *Chem. Rev.* **2011,** *111* (5), 3577-3613.

3. Mylrea, M.; Gourisetti, S. N. G. In *Blockchain: A path to grid modernization and cyber resiliency*, 2017 North American Power Symposium (NAPS), 17-19 Sept. 2017; 2017; pp 1-5.

4. Global Energy & CO2 Status Report 2019. IEA: Paris, 2019.

5. Global Energy Review 2021. IEA: Paris, 2021.

6. Ran Fu, D. F., Robert Margolis, Mike Woodhouse, and Kridten Ardani, U.S. Solar Photovoltaic System Cost Benchmark: Q1 2017. NREL, Ed. Department of Energy: Golden, CO, 2017.

7. W. Cole, B. F., P. Gagnon, J. Richards, Y. Sun, J. Zuboy, M. Woodhouse, R. Margolis, SunShot 2030 for Photovoltaics (PV): Envisioning a Low-cost PV Future NREL, Ed. Golden, CO, 2017.

8. The SunShot 2030 Goals. USDOE, Ed. Solar Energy Technologies Office: 2016.

9. Renewable capacity growth worldwide stalled in 2018 after two decades of strong expansion. IEA: 2019.

10. *EPA Analysis of the American Power Act in the 11th Congress*; USEPA: 2010.

11. Denholm, P.; Hand, M., Grid flexibility and storage required to achieve very high penetration of variable renewable electricity. *Energy Policy* **2011,** *39* (3), 1817-1830.

12. Gür, T. M., Review of electrical energy storage technologies, materials and systems: challenges and prospects for large-scale grid storage. *Energy & Environmental Science* **2018,** *11* (10), 2696-2767.

13. Mai, T. S., D.; Wiser, R.; Schneider, T., Renewable Electricity Futures Study Executive Summary. Laboratory, N. R. E., Ed. Golden, CO, 2012.

14. Aguero, J. R.; Khodaei, A., Grid Modernization, DER Integration & Utility Business Models - Trends & Challenges. *IEEE Power and Energy Magazine* **2018,** *16* (2), 112-121.

15. Al Shaqsi, A. Z.; Sopian, K.; Al-Hinai, A., Review of energy storage services, applications, limitations, and benefits. *Energy Reports* **2020**.

16. U.S. Energy Storage Factsheet. In *Center for Sustainable Systems*, University of Michigan, 2020; Vol. Pub. No. CSS15-17.

17. Tyra, B., Electric Power Monthly with Data for February 2021. Administration, U. S. E. I., Ed. Washington, DC, 2021.

18. Electric Power Annual 2019. Administration, U. S. E. I., Ed. Washington, DC, 2021.

19. Energy Storage Policy Summaries For The Global Energy Storage Database. Laboratory, S. N., Ed. 2019.

20. Abbas A. Akhil, G. H., Aileen B. Currier, Benjamin C. Kaun, Dan M. Rastler,Stella Bingqing Chen, Andrew L. Cotter, Dale T. Bradshaw, and William D. Gauntlett, DOE/EPRI Electricity Storage Handbook in Collaboration with NRECA. Laboratory, S. N., Ed. 2015.

21. Mai, T., Electric Sector Integration | Energy Analysis | NREL.

22. Pérez-Díaz, J. I.; Chazarra, M.; García-González, J.; Cavazzini, G.; Stoppato, A., Trends and challenges in the operation of pumped-storage hydropower plants. *Renewable and Sustainable Energy Reviews* **2015,** *44*, 767-784.

23. Sepulveda, N. A.; Jenkins, J. D.; Edington, A.; Mallapragada, D. S.; Lester, R. K., The design space for long-duration energy storage in decarbonized power systems. *Nature Energy* **2021,** *6* (5), 506-516.

24. Kaunda, C. S.; Kimambo, C. Z.; Nielsen, T. K., Hydropower in the Context of Sustainable Energy Supply: A Review of Technologies and Challenges. *ISRN Renewable Energy* **2012,** *2012*, 730631.

25. Doetsch, C.; Pohlig, A., 13 - The Use of Flow Batteries in Storing Electricity for National Grids. In *Future Energy (Third Edition)*, Letcher, T. M., Ed. Elsevier: 2020; pp 263-277.

26. Mongrid, K. V., V.; Alam, J.; Vartanian, C.; Sprenkle, V., 2020 Grid Energy Storage Technology Cost and Performance Assessment. DOE, Ed. 2020.

27. Prifti, H.; Parasuraman, A.; Winardi, S.; Lim, T. M.; Skyllas-Kazacos, M., Membranes for Redox Flow Battery Applications. *Membranes* **2012,** *2* (2), 275-306.

28. Weber, A. Z.; Mench, M. M.; Meyers, J. P.; Ross, P. N.; Gostick, J. T.; Liu, Q., Redox flow batteries: a review. *Journal of Applied Electrochemistry* **2011,** *41* (10), 1137.

29. Chen, T.; Jin, Y.; Lv, H.; Yang, A.; Liu, M.; Chen, B.; Xie, Y.; Chen, Q., Applications of Lithium-Ion Batteries in Grid-Scale Energy Storage Systems. *Transactions of Tianjin University* **2020,** *26* (3), 208-217.

30. Soloveichik, G. L., Flow Batteries: Current Status and Trends. *Chem. Rev.* **2015,** *115* (20), 11533-11558.

31. Alotto, P.; Guarnieri, M.; Moro, F., Redox flow batteries for the storage of renewable energy: A review. *Renewable and Sustainable Energy Reviews* **2014,** *29*, 325-335.

32. Sánchez-Díez, E.; Ventosa, E.; Guarnieri, M.; Trovò, A.; Flox, C.; Marcilla, R.; Soavi, F.; Mazur, P.; Aranzabe, E.; Ferret, R., Redox flow batteries: Status and perspective towards sustainable stationary energy storage. *Journal of Power Sources* **2021,** *481*, 228804.

33. Arenas, L. F.; Ponce de León, C.; Walsh, F. C., Engineering aspects of the design, construction and performance of modular redox flow batteries for energy storage. *Journal of Energy Storage* **2017,** *11*, 119-153.

34. Li, B.; Nie, Z.; Vijayakumar, M.; Li, G.; Liu, J.; Sprenkle, V.; Wang, W., Ambipolar zinc-polyiodide electrolyte for a high-energy density aqueous redox flow battery. *Nature Communications* **2015,** *6*, ncomms7303.

35. Li, L.; Kim, S.; Wang, W.; Vijayakumar, M.; Nie, Z.; Chen, B.; Zhang, J.; Xia, G.; Hu, J.; Graff, G.; Liu, J.; Yang, Z., A Stable Vanadium Redox-Flow Battery with High Energy Density for Large-Scale Energy Storage. *Advanced Energy Materials* **2011,** *1* (3), 394-400.

36. Duan, W.; Vemuri, R. S.; Milshtein, J. D.; Laramie, S.; Dmello, R. D.; Huang, J.; Zhang, L.; Hu, D.; Vijayakumar, M.; Wang, W.; Liu, J.; Darling, R. M.; Thompson, L.; Smith, K.; Moore, J. S.; Brushett, F. R.; Wei, X., A symmetric organic-based nonaqueous redox flow battery and its state of charge diagnostics by FTIR. *Journal of Materials Chemistry A* **2016,** *4* (15), 5448-5456.

37. Wang, H.; Sayed, S. Y.; Zhou, Y.; Olsen, B. C.; Luber, E. J.; Buriak, J. M., Water-soluble pH-switchable cobalt complexes for aqueous symmetric redox flow batteries. *Chemical Communications* **2020,** *56* (25), 3605-3608.

38. Nagarjuna, G.; Hui, J.; Cheng, K. J.; Lichtenstein, T.; Shen, M.; Moore, J. S.; Rodríguez-López, J., Impact of Redox-Active Polymer Molecular Weight on the Electrochemical Properties and Transport Across Porous Separators in Nonaqueous Solvents. *Journal of the American Chemical Society* **2014,** *136* (46), 16309-16316.

39. Duduta, M.; Ho, B.; Wood, V. C.; Limthongkul, P.; Brunini, V. E.; Carter, W. C.; Chiang, Y.-M., Semi-Solid Lithium Rechargeable Flow Battery. *Advanced Energy Materials* **2011,** *1* (4), 511-516.

40. Zhao, Y.; Ding, Y.; Song, J.; Li, G.; Dong, G.; Goodenough, J. B.; Yu, G., Sustainable Electrical Energy Storage through the Ferrocene/Ferrocenium Redox Reaction in Aprotic Electrolyte. *Angew. Chem. Int. Ed.* **2014,** *53* (41), 11036-11040.

41. Hendriks, K. H.; Robinson, S. G.; Braten, M. N.; Sevov, C. S.; Helms, B. A.; Sigman, M. S.; Minteer, S. D.; Sanford, M. S., High-Performance Oligomeric Catholytes for Effective Macromolecular Separation in Nonaqueous Redox Flow Batteries. *ACS Central Science* **2018,** *4* (2), 189-196.

42. Wang, W.; Luo, Q.; Li, B.; Wei, X.; Li, L.; Yang, Z., Recent Progress in Redox Flow Battery Research and Development. *Adv. Funct. Mater.* **2013,** *23* (8), 970-986.

43. Singh, P., Application of non-aqueous solvents to batteries. *Journal of Power Sources* **1984,** *11* (1), 135-142.

44. Gong, K.; Fang, Q.; Gu, S.; Li, S. F. Y.; Yan, Y., Nonaqueous redox-flow batteries: organic solvents, supporting electrolytes, and redox pairs. *Energy & Environmental Science* **2015,** *8* (12), 3515-3530.

45. Huang, Q.; Wang, Q., Next-Generation, High-Energy-Density Redox Flow Batteries. *ChemPlusChem* **2015,** *80* (2), 312-322.

46. Hunt, C.; Mattejat, M.; Anderson, C.; Sepunaru, L.; Ménard, G., Symmetric Phthalocyanine Charge Carrier for Dual Redox Flow Battery/Capacitor Applications. *ACS Applied Energy Materials* **2019,** *2* (8), 5391-5396.

47. Claessens, C. G.; Hahn, U.; Torres, T., Phthalocyanines: From outstanding electronic properties to emerging applications. *The Chemical Record* **2008,** *8* (2), 75-97.

48. McKeown, N. B., 98 - The Synthesis of Symmetrical Phthalocyanines. In *The Porphyrin Handbook*, Kadish, K. M.; Smith, K. M.; Guilard, R., Eds. Academic Press: Amsterdam, 2003; pp 61-124.

49. Kobayashi, N.; Ogata, H.; Nonaka, N.; Luk'yanets, E. A., Effect of Peripheral Substitution on the Electronic Absorption and Fluorescence Spectra of Metal-Free and Zinc Phthalocyanines. *Chemistry – A European Journal* **2003,** *9* (20), 5123-5134.

50. Li, R.; Zhang, X.; Zhu, P.; Ng, D. K. P.; Kobayashi, N.; Jiang, J., Electron-Donating or -Withdrawing Nature of Substituents Revealed by the Electrochemistry of Metal-Free Phthalocyanines. *Inorganic Chemistry* **2006,** *45* (5), 2327-2334.

51. Nyokong, T., Effects of substituents on the photochemical and photophysical properties of main group metal phthalocyanines. *Coord. Chem. Rev.* **2007,** *251* (13), 1707-1722.

52. Peterson, M.; Hunt, C.; Wang, Z.; Heinrich, S. E.; Wu, G.; Ménard, G., Synthesis, characterization, and electrochemical properties of a first-row metal phthalocyanine series. *DTr* **2020**.

53. Schlettwein, D.; Armstrong, N. R., Correlation of Frontier Orbital Positions and Conduction Type of Molecular Semiconductors As Derived from UPS in Combination with Electrical and Photoelectrochemical Experiments. *The Journal of Physical Chemistry* **1994,** *98* (45), 11771-11779.

54. Sorokin, A. B., Phthalocyanine Metal Complexes in Catalysis. *Chem. Rev.* **2013,** *113* (10), 8152-8191.

55. Zagal, J. H.; Griveau, S.; Silva, J. F.; Nyokong, T.; Bedioui, F., Metallophthalocyanine-based molecular materials as catalysts for electrochemical reactions. *Coord. Chem. Rev.* **2010,** *254* (23), 2755-2791.

56. Öztürk, Z. Z.; Kılınç, N.; Atilla, D.; Gürek, A. G.; Ahsen, V., Recent studies chemical sensors based on phthalocyanines. *J. Porphyrins Phthalocyanines* **2009,** *13* (11), 1179-1187.

57. Shoukat Ali, R. A.; Keshavayya, J.; Jagadisha, A. S.; Umesh, S. D., Copper (II) phthalocyanines: Electrode modification and sensing studies. *Materials Today: Proceedings* **2020**.

58. Zhou, R.; Josse, F.; Göpel, W.; Öztürk, Z. Z.; Bekaroğlu, Ö., Phthalocyanines as Sensitive Materials for Chemical Sensors. *Appl. Organomet. Chem.* **1996,** *10* (8), 557-577.

59. Melville, O. A.; Lessard, B. H.; Bender, T. P., Phthalocyanine-Based Organic Thin-Film Transistors: A Review of Recent Advances. *ACS Applied Materials & Interfaces* **2015,** *7* (24), 13105-13118.

60. Ikeuchi, T.; Agrawal, S.; Ezoe, M.; Mori, S.; Kimura, M., Enhanced Charge Separation Efficiency in Pyridine-Anchored Phthalocyanine-Sensitized Solar Cells by Linker Elongation. *Chemistry – An Asian Journal* **2015,** *10* (11), 2347-2351.

61. Urbani, M.; Ragoussi, M.-E.; Nazeeruddin, M. K.; Torres, T., Phthalocyanines for dye-sensitized solar cells. *Coord. Chem. Rev.* **2019,** *381*, 1-64.

62. Martín-Gomis, L.; Fernández-Lázaro, F.; Sastre-Santos, Á., Advances in phthalocyanine-sensitized solar cells (PcSSCs). *Journal of Materials Chemistry A* **2014,** *2* (38), 15672-15682.

63. Cheng, M.; Li, Y.; Safdari, M.; Chen, C.; Liu, P.; Kloo, L.; Sun, L., Efficient Perovskite Solar Cells Based on a Solution Processable Nickel(II) Phthalocyanine and Vanadium Oxide Integrated Hole Transport Layer. *Advanced Energy Materials* **2017,** *7* (14), 1602556.

64. Cho, K. T.; Cavazzini, M.; Rakstys, K.; Orlandi, S.; Paek, S.; Franckevičius, M.; Kanda, H.; Gegevičius, R.; Emmanuel, Q. V.; Pozzi, G.; Nazeeruddin, M. K., Perovskite Solar Cells: 18% Efficiency Using Zn(II) and Cu(II) Octakis(diarylamine)phthalocyanines as Hole-Transporting Materials. *ACS Applied Energy Materials* **2019,** *2* (9), 6195-6199.

65. Sharman, W. M.; Van Lier, J. E., 97 - Synthesis of Phthalocyanine Precursors. In *The Porphyrin Handbook*, Kadish, K. M.; Smith, K. M.; Guilard, R., Eds. Academic Press: Amsterdam, 2003; pp 1-60.

66. Chambrier, I. C., M. J., *J. Chem. Res. (S)* **1990**.

67. Oliver, S. W.; Smith, T. D., Oligomeric cyclization of dinitriles in the synthesis of phthalocyanines and related compounds: the role of the alkoxide anion. *Journal of the Chemical Society, Perkin Transactions 2* **1987,** (11), 1579-1582.

68. Hurley, T. J.; Robinson, M. A.; Trotz, S. I., Complexes derived from 1,3-diiminoisoindoline-containing ligands. II. Stepwise formation of nickel phthalocyanine. *Inorganic Chemistry* **1967,** *6* (2), 389-392.

69. Hanack, M.; Gül, A.; Hirsch, A.; Mandal, B. K.; Subramanian, L. R.; Witke, E., Synthesis and Characterization of Soluble Phthalocyanines: Structure-Property Relationship. *Molecular Crystals and Liquid Crystals Incorporating Nonlinear Optics* **1990,** *187* (1), 365-382.

70. Cook, M. J., 1,4,8,11,15,18,22,25-octasubstituted phthalocyanines: the contrasting effects of alkyl and alkoxy substituents on molecular self-assembly. *Journal of Materials Science: Materials in Electronics* **1994,** *5* (2), 117-128.

71. Gao, Y.; Chen, Y.; Li, R.; Bian, Y.; Li, X.; Jiang, J., Nonperipherally octa(butyloxy)-substituted phthalocyanine derivatives with good crystallinity: effects of metal-ligand coordination on the molecular structure, internal structure, and dimensions of self-assembled nanostructures. *Chemistry* **2009,** *15* (47), 13241-52.

72. Fukuda, T.; Homma, S.; Kobayashi, N., Deformed Phthalocyanines: Synthesis and Characterization of Zinc Phthalocyanines Bearing Phenyl Substituents at the 1-, 4-, 8-, 11-, 15-, 18-, 22-, and/or 25-Positions. *Chemistry – A European Journal* **2005,** *11* (18), 5205-5216.

73. Antonietta Loi, M.; Denk, P.; Hoppe, H.; Neugebauer, H.; Winder, C.; Meissner, D.; Brabec, C.; Serdar Sariciftci, N.; Gouloumis, A.; Vázquez, P.; Torres, T., Long-lived photoinduced charge separation for solar cell applications in phthalocyanine–fulleropyrrolidine dyad thin filmsElectronic supplementary information (ESI) available: plots of the refractive index, extinction coefficient and dielectric function of Pc-C60. See http://www.rsc.org/suppdata/jm/b2/b212621d. *Journal of Materials Chemistry* **2003,** *13* (4), 700-704.

74. González-Cabello, A.; Claessens, C. G.; Martin-Fuch, G.; Ledoux-Rack, I.; Vázquez, P.; Zyss, J.; Agulló-López, F.; Torres, T., Phthalocyanine-Ferrocene Dyads and Triads for Nonlinear Optics. *Synthetic Metals* **2003,** *137* (1), 1487-1488.

75. Li, W.-S.; Aida, T., Dendrimer Porphyrins and Phthalocyanines. *Chem. Rev.* **2009,** *109* (11), 6047-6076.

76. Rodriguez-Morgade, M. S. D. L. T., Gema; Torres, T., 99 - Design and Synthesis of Low-Symmetry Phthalocyanines and Related Systems. In *The Porphyrin Handbook*, Kadish, K. M.; Smith, K. M.; Guilard, R., Eds. Academic Press: Amsterdam, 2003; pp 125-160.

77. Cid, J.-J.; García-Iglesias, M.; Yum, J.-H.; Forneli, A.; Albero, J.; Martínez-Ferrero, E.; Vázquez, P.; Grätzel, M.; Nazeeruddin, M. K.; Palomares, E.; Torres, T., Structure–Function Relationships in Unsymmetrical Zinc Phthalocyanines for Dye-Sensitized Solar Cells. *Chemistry – A European Journal* **2009,** *15* (20), 5130-5137.

78. Giribabu, L.; Vijay Kumar, C.; Gopal Reddy, V.; Yella Reddy, P.; Srinivasa Rao, C.; Jang, S.-R.; Yum, J.-H.; Nazeeruddin, M. K.; Grätzel, M., Unsymmetrical alkoxy zinc phthalocyanine for sensitization of nanocrystalline TiO2 films. *Sol. Energy Mater. Sol. Cells* **2007,** *91* (17), 1611-1617.

79. do Nascimento, F. B.; Manieri, T. M.; Cerchiaro, G.; Ribeiro, A. O., Synthesis of unsymmetrical phthalocyanine derivatives and their interaction with mammary MCF7 cells. *Dyes and Pigments* **2013,** *99* (2), 316-322.

80. BAKBOORD, J. V.; COOK, M. J.; HAMURYUDAN, E., Non-uniformly substituted phthalocyanines and related compounds: alkylated tribenzo-imidazolo[4,5]-porphyrazines. *J. Porphyrins Phthalocyanines* **2000,** *04* (05), 510-517.

81. Rodríguez-Morgade, S.; Hanack, M., Synthesis, Separation and Characterization of the Structural Isomers of Octa-tert-Butylphthalocyanines and Dienophilic Phthalocyanine Derivatives. *Chemistry – A European Journal* **1997,** *3* (7), 1042-1051.

82. Weitemeyer, A.; Kliesch, H.; Woehrle, D., Unsymmetrically Substituted Phthalocyanine Derivatives via a Modified Ring Enlargement Reaction of

Unsubstituted Subphthalocyanine. *The Journal of Organic Chemistry* **1995,** *60* (15), 4900-4904.

83. Albini, A., *Photochemistry : past, present and future*. Heidelberg : Springer: Heidelberg, 2016.

84. Suppan, P.; Pasquier-Bird, A. M.; Chemistry, R. S. o., *Chemistry and Light*. Royal Society of Chemistry: 1994.

85. Ishii, K.; Kobayashi, N., 102 - The Photophysical Properties of Phthalocyanines and Related Compounds. In *The Porphyrin Handbook*, Kadish, K. M.; Smith, K. M.; Guilard, R., Eds. Academic Press: Amsterdam, 2003; pp 1-42.

86. Wahl, M. Time Correlated Single Photon Counting.

87. Dahlen, M. A., The Phthalocyanines A New Class of Synthetic Pigments and Dyes. *Industrial & Engineering Chemistry* **1939,** *31* (7), 839-847.

88. Balraju, P.; Kumar, M.; Roy, M. S.; Sharma, G. D., Dye sensitized solar cells (DSSCs) based on modified iron phthalocyanine nanostructured TiO2 electrode and PEDOT:PSS counter electrode. *Synthetic Metals* **2009,** *159* (13), 1325-1331.

89. Kimura, M.; Nomoto, H.; Suzuki, H.; Ikeuchi, T.; Matsuzaki, H.; Murakami, T. N.; Furube, A.; Masaki, N.; Griffith, M. J.; Mori, S., Molecular Design Rule of Phthalocyanine Dyes for Highly Efficient Near-IR Performance in Dye-Sensitized Solar Cells. *Chemistry – A European Journal* **2013,** *19* (23), 7496-7502.

90. Ragoussi, M.-E.; Ince, M.; Torres, T., Recent Advances in Phthalocyanine-Based Sensitizers for Dye-Sensitized Solar Cells. *Eur. J. Org. Chem.* **2013,** *2013* (29), 6475-6489.

91. Díaz-García, M. A., Nonlinear optical properties of phthalocyanines and related compounds. *J. Porphyrins Phthalocyanines* **2009,** *13* (04n05), 652-667.

92. Makhal, K.; Mathur, P.; Maurya, S.; Goswami, D., Extracting third order optical nonlinearities of Mn(III)-Phthalocyanine chloride using high repetition rate femtosecond pulses. *Journal of Applied Physics* **2017,** *121* (5), 053103.

93. Nwaji, N.; Mack, J.; Britton, J.; Nyokong, T., Synthesis, photophysical and nonlinear optical properties of a series of ball-type phthalocyanines in solution and thin films. *New J. Chem.* **2017,** *41* (5), 2020-2028.

94. Rais, D.; Toman, P.; Cerny, J.; Mensik, M.; Pfleger, J., Roles of octabutoxy substitution and J-aggregation in stabilization of the excited state in nickel phthalocyanine. *J. Phys. Chem. A* **2014,** *118* (29), 5419-26.

95. Rosenthal, I., PHTHALOCYANINES AS PHOTODYNAMIC SENSITIZERS*. *Photochemistry and Photobiology* **1991,** *53* (6), 859-870.

96. Platt, J. R., In *Radiation Biology*, Hollaender, A., Ed. McGraw-Hill: New York, 1956; Vol. III.

97. Gouterman, M., 1 - Optical Spectra and Electronic Structure of Porphyrins and Related Rings. In *The Porphyrins*, Dolphin, D., Ed. Academic Press: 1978; pp 1-165.

98. Isago, H., "Prototypical" Optical Absorption Spectra of Phthalocyanines and Their Theoretical Background. In *Optical Spectra of Phthalocyanines and Related Compounds: A Guide for Beginners*, Isago, H., Ed. Springer Japan: Tokyo, 2015; pp 21-40.

99. Mack, J.; Stillman, M. J., 103 - Electronic Structures of Metal Phthalocyanine and Porphyrin Complexes from Analysis of the UV–Visible Absorption and Magnetic Circular Dichroism Spectra and Molecular Orbital Calculations. In *The Porphyrin Handbook*, Kadish, K. M.; Smith, K. M.; Guilard, R., Eds. Academic Press: Amsterdam, 2003; pp 43-116.

100. FitzGerald, S. A photophysical study of novel silicon and zinc phthalocyanines. Durham University, Durham, U.K., 2002.

101. Liao, M.-S.; Kar, T.; Gorun, S. M.; Scheiner, S., Effects of Peripheral Substituents and Axial Ligands on the Electronic Structure and Properties of Iron Phthalocyanine. *Inorganic Chemistry* **2004,** *43* (22), 7151-7161.

102. Liao, M.-S.; Scheiner, S., Electronic structure and bonding in metal phthalocyanines, Metal=Fe, Co, Ni, Cu, Zn, Mg. *The Journal of Chemical Physics* **2001,** *114* (22), 9780-9791.

103. Lever, A. B. P.; Leznoff, C. C., Phthalocyanines: properties and applications. VCH: New York, NY, 1989; p 4 v.

104. Konami, H.; Hatano, M., Synthesis and Spectroscopic Properties of Zn(II) Mono-2-(t-butyl)phthalocyanine. *Chem. Lett.* **1988,** *17* (8), 1359-1362.

105. Kobayashi, N.; Sasaki, N.; Higashi, Y.; Osa, T., Regiospecific and Nonlinear Substituent Effects on the Electronic and Fluorescence Spectra of Phthalocyanines. *Inorganic Chemistry* **1995,** *34* (7), 1636-1637.

106. Maree, S. E.; Nyokong, T., Syntheses and photochemical properties of octasubstituted phthalocyaninato zinc complexes. *J. Porphyrins Phthalocyanines* **2001,** *5* (11), 782-792.

107. L'Her, M.; Pondaven, A., 104 - Electrochemistry of Phthalocyanines. In *The Porphyrin Handbook*, Kadish, K. M.; Smith, K. M.; Guilard, R., Eds. Academic Press: Amsterdam, 2003; pp 117-169.

108. Zhou, W.; Thompson, J. R.; Leznoff, C. C.; Leznoff, D. B., The Redox-Active Chromium Phthalocyanine System: Isolation of Five Oxidation States from Pc4−CrI to Pc2−CrIII. *Chemistry – A European Journal* **2017,** *23* (10), 2323-2331.

109. Lever, A. B. P.; Milaeva, E. R.; Speier, G., The Redox Chemistry of Metallophthalocyanines in Solution. In *Phthalocyanines: properties and applications*, VCH: New York, NY, 1989; pp 1-69.

110. DeWulf, D. W.; Leland, J. K.; Wheeler, B. L.; Bard, A. J.; Batzel, D. A.; Dininny, D. R.; Kenney, M., Isolation, spectroscopic properties, and electrochemical properties of two oligomeric silicon phthalocyanines. *Inorganic Chemistry* **1987,** *26* (2), 266-270.

111. Lever, A. B. P.; Minor, P. C., Electrochemistry of main-group phthalocyanines. *Inorganic Chemistry* **1981,** *20* (11), 4015-4017.

112. Lever, A. B. P.; Licoccia, S.; Magnell, K.; Minor, P. C.; Ramamurthy, P. *Mapping of the Energy Levels of Metallophthalocyanines via Electronic Spectroscopy, Electrochemsitry, and Photochemistry*; 1982; p 237.

113. Lever, A. B. P.; Wilshire, J. P., Electrochemistry of iron phthalocyanine complexes in nonaqueous solvents and the identification of five-coordinate iron(I) phthalocyanine derivatives. *Inorganic Chemistry* **1978,** *17* (5), 1145-1151.

114. Bedioui, F.; Griveau, S.; Nyokong, T.; John Appleby, A.; Caro, C. A.; Gulppi, M.; Ochoa, G.; Zagal, J. H., Tuning the redox properties of metalloporphyrin- and metallophthalocyanine-based molecular electrodes for the highest electrocatalytic activity in the oxidation of thiols. *Physical Chemistry Chemical Physics* **2007,** *9* (26), 3383-3396.

115. Wu, Y.; Jiang, Z.; Lu, X.; Liang, Y.; Wang, H., Domino electroreduction of CO2 to methanol on a molecular catalyst. *Natur* **2019,** *575* (7784), 639-642.

116. Zhang, X.; Wang, Y.; Gu, M.; Wang, M.; Zhang, Z.; Pan, W.; Jiang, Z.; Zheng, H.; Lucero, M.; Wang, H.; Sterbinsky, G. E.; Ma, Q.; Wang, Y.-G.; Feng,

Z.; Li, J.; Dai, H.; Liang, Y., Molecular engineering of dispersed nickel phthalocyanines on carbon nanotubes for selective CO2 reduction. *Nature Energy* **2020,** *5* (9), 684-692.

117. Zhong, J.-P.; Fan, Y.-J.; Wang, H.; Wang, R.-X.; Fan, L.-L.; Shen, X.-C.; Shi, Z.-J., Copper phthalocyanine functionalization of graphene nanosheets as support for platinum nanoparticles and their enhanced performance toward methanol oxidation. *Journal of Power Sources* **2013,** *242*, 208-215.

118. Işık Büyükekşi, S.; Karatay, A.; Orman, E. B.; Açar Selçuki, N.; Özkaya, A. R.; Salih, B.; Elmali, A.; Şengül, A., A novel AB3-type trimeric zinc(ii)-phthalocyanine as an electrochromic and optical limiting material. *DTr* **2020,** *49* (40), 14068-14080.

119. Mani, V.; Huang, S.-T.; Devasenathipathy, R.; Yang, T. C. K., Electropolymerization of cobalt tetraamino-phthalocyanine at reduced graphene oxide for electrochemical determination of cysteine and hydrazine. *RSC Advances* **2016,** *6* (44), 38463-38469.

120. Zuo, X.; Zhang, H.; Li, N., An electrochemical biosensor for determination of ascorbic acid by cobalt (II) phthalocyanine–multi-walled carbon nanotubes modified glassy carbon electrode. *Sensors and Actuators B: Chemical* **2012,** *161* (1), 1074-1079.

121. Akyüz, D.; Koca, A., An electrochemical sensor for the detection of pesticides based on the hybrid of manganese phthalocyanine and polyaniline. *Sensors and Actuators B: Chemical* **2019,** *283*, 848-856.

122. Agboola, B. O.; Ozoemena, K. I., Self-assembly and heterogeneous electron transfer properties of metallo-octacarboxyphthalocyanine complexes on gold electrode. *Physical Chemistry Chemical Physics* **2008,** *10* (17), 2399-2408.

123. Shokurov, A. V.; Yagodin, A. V.; Martynov, A. G.; Gorbunova, Y. G.; Selektor, S. L., Phthalocyanine Monolayers Self-Assembled Directly from its Thiobenzoyl Derivative. *ECS Journal of Solid State Science and Technology* **2020,** *9* (5), 051006.

124. Zhang, Y.; Ma, P.; Zhu, P.; Zhang, X.; Gao, Y.; Qi, D.; Bian, Y.; Kobayashi, N.; Jiang, J., 2,3,9,10,16,17,23,24-Octakis(hexylsulfonyl)phthalocyanines with good n-type semiconducting properties. Synthesis, spectroscopic, and electrochemical characteristics. *Journal of Materials Chemistry* **2011,** *21* (18), 6515-6524.

125. Schlettwein, D.; Yoshida, T., Electrochemical reduction of substituted cobalt phthalocyanines adsorbed on graphite. *J. Electroanal. Chem.* **1998,** *441* (1), 139-146.

126. Gan, P.; Foord, J. S.; Compton, R. G., Surface Modification of Boron-Doped Diamond with Microcrystalline Copper Phthalocyanine: Oxygen Reduction Catalysis. *ChemistryOpen* **2015,** *4* (5), 606-612.

127. Mho, S. i.; Ortiz, B.; Park, S. M.; Ingersoll, D.; Doddapaneni, N., Spectroelectrochemical Studies of Metallophthalocyanines Adsorbed on Electrode Surfaces. *Journal of The Electrochemical Society* **1995,** *142* (5), 1436-1441.

128. Mohammed, M. A.; Ottenbreit, P.; Prass, W.; Schnurpfeil, G.; Wöhrle, D., Langmuir-Blodgett films of phthalocyanine derivatives: mono- and multilayer films prepared from phthalocyanine derivatives containing polar and cationic substituents. *Thin Solid Films* **1992,** *213* (2), 285-294.

129. Lokesh, K. S.; De Wael, K.; Adriaens, A., Self-Assembled Supramolecular Array of Polymeric Phthalocyanine on Gold for the Determination of Hydrogen Peroxide. *Langmuir* **2010,** *26* (22), 17665-17673.

130. Schlettwein, D.; Jaeger, N. I.; Oekermann, T., Photoelectrochemical Reactions at Phthalocyanine Electrodes. In *The Porphyrin Handbook*, Kadish, K. M.; Smith, K. M.; Guilard, R., Eds. Academic Press: Amsterdam, 2003; pp 247-283.

131. Alpatova, N. M.; Ovsyannikova, E. V., Electropolymerization of Phthalocyanines. In *Electropolymerization*, 2010; pp 111-132.

132. Wohrle, D., Phthalocyanines in Polymer Phases. In *Phthalocyanines: properties and applications*, VCH: New York, NY, 1989; p 55.

Chapter 2: Synthesis, Characterization, and Electrochemical Properties of a First-row Transition Metal Phthalocyanine Series

2.1 Introduction

Grid-scale energy storage technologies are urgently needed in order to meet the demands of – and facilitate the transition to – installed and projected renewable energy sources. Redox-flow batteries (RFBs) are particularly attractive for grid-scale energy storage due to their inherently decoupled power and energy densities, providing modular power output and scalable total energy storage capacity which are key to the fluctuating demands of a renewable grid.[1] In addition to engineering challenges, recurring chemical issues impeding the development of commercial RFBs include the electrochemical stability, the solubility, and the cost of the charge carrier, the main redox-active molecule(s) comprising the battery. Phthalocyanines (Pcs) are a well-studied class of macrocycles that have found use in a variety of technologies, including semiconductors,[2, 3] sensors,[4-7] dyes/sensitizers,[8-11] catalysts,[12, 13] and energy storage applications.[14-16] In addition to their easy preparation, Pcs generally display good electrochemical stability and tuneable profiles.[17-19] Our group has recently explored the electronic structure of an octa-ethoxy substituted phthalocyanine Mn-nitride, **^{OEt}PcMnN** (^{OEt}Pc = 1,4,8,11,15,18,22,25-octaethoxy-Pc), as well as its switchable aromatic character controlled by its multiple ligand-borne redox events.[20] In a follow-up paper, we explored how this compound could be used as a symmetric charge carrier for RFB applications.[16] Herein, we expand this series to encompass most of the first-row metals (Scheme 2.1) and attempt to extract structural-electrochemical correlations which may lead to the design of robust charge carriers for RFB applications.

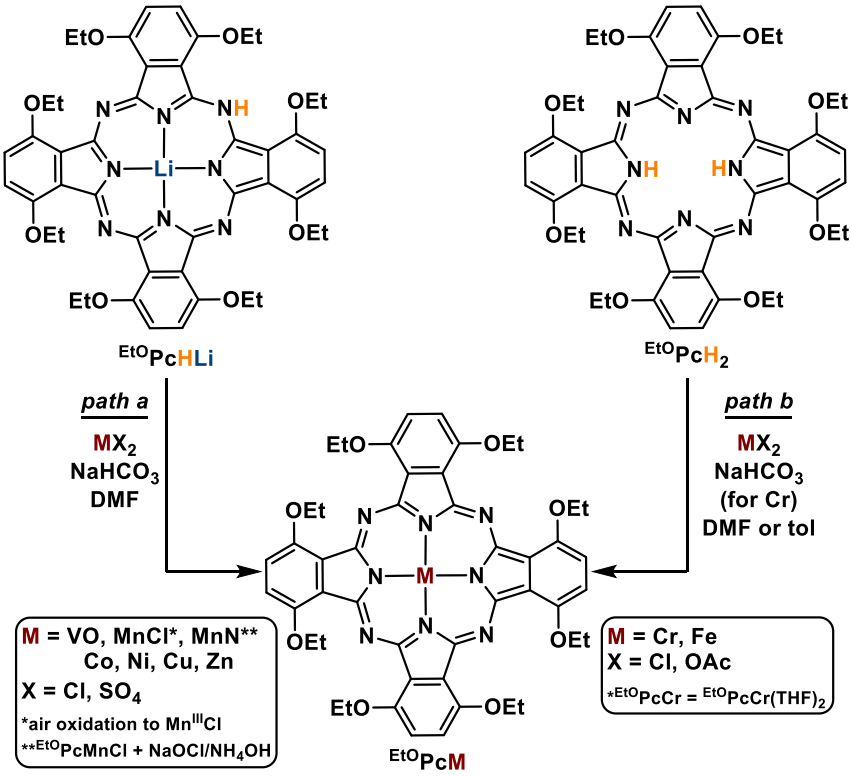

Scheme 2.1: General synthetic approach described in this paper to generate ^{EtO}PcM (M = VO, Cr, MnCl, MnN, Fe, Co, Ni, Cu, Zn) from ^{EtO}PcHLi (path a) or ^{EtO}PcH$_2$ (path b).

As part of this study, we believe we have identified a key pattern: Phthalocyanines with non-labile axial metal-ligand substituents appear to exhibit more reversible, well-defined electrochemistry when compared with their axially-bare counterparts, and do not appear to exhibit non-diffusional electrochemical plating responses. This pattern may provide an important design principle for the development of Pc species with reversible electrochemistry, for multiple applications, including energy storage.

2.2 Results and Discussion

2.2.1 Synthesis

The substituted ^{EtO}Pc ligand was originally reported by Rauchfuss and coworkers,[21] and we subsequently reported modified synthetic procedures to access both the protonated, **^{EtO}PcH$_2$**, and mono-lithiated, **^{EtO}PcHLi**, variants.[20] First-row metallophthalocyanines (**^{OEt}PcM**; M = VO, Cr, MnCl, MnN, Fe, Co, Ni, Cu, Zn) were accessed via two main synthetic routes using either **^{OEt}PcHLi** (path a) or ^{OEt}PcH$_2$ (path b) as outlined in Scheme 2.1. We note that **^{EtO}PcVO**, **^{EtO}PcNi**, and **^{EtO}PcCu** were previously reported by Rauchfuss,[21] but the first two were not structurally characterized,[22] and none were electrochemically characterized. For the purposes of this study, we resynthesized these compounds, as well as our reported congeners, **^{EtO}PcMnCl** and **^{EtO}PcMnN**,[20] and the new species, **^{EtO}PcCo** and **^{EtO}PcZn**, by heating a mixture of **^{EtO}PcHLi**, appropriate metal salt, and excess $NaHCO_3$ to 145 °C in dimethylformamide (DMF) for 4-20 h yielding dark green pure products after workup and recrystallization (Scheme 2.1, path a). The new compounds, **^{EtO}PcCr** and **^{EtO}PcFe**, were prepared from **^{EtO}PcH$_2$** using a similar methodology by mixing with the appropriate metal salt, excess $NaHCO_3$ for **^{EtO}PcCr**, and heating in either DMF (**^{EtO}PcCr**) or toluene (**^{EtO}PcFe**) under inert atmosphere for several hours, followed by purification (Scheme 2.1, path b; see Experimental Section). We note that the compounds described here may be synthesized following either route; however, the syntheses described here yield the highest amount of pure materials.

2.2.2 NMR Spectroscopy

Given their large aromatic circuits, NMR spectroscopy can be highly diagnostic for determining the electronic structure and ligand redox properties of metallophthalocyanines.[20] It can also be a useful tool in assessing the symmetry and possible spin-state of a given

compound with all compounds analysed by ^{1}H NMR spectroscopy in CD_2Cl_2 or $CDCl_3$. The starting ligand, **^{OEt}PcH$_2$**, displays an expected C_4-symmetric spectrum; however, the asymmetry in the related lithiated precursor, **^{EtO}PcHLi**, was assigned based on crystallographic studies (*vide infra*), as well as NMR spectroscopy where a series of overlapping triplets and quartets are observed in addition to a downfield shifted singlet at 14.75 ppm, due to the strong ring current provided by the Pc ring, integrating to one proton. Together, these data are consistent with a pseudo-C_{2v} symmetric molecule.

With the exceptions of the diamagnetic species, **^{OEt}PcM** (M = MnN, Ni, Zn) all other compounds (M = VO, Cr, MnCl, Fe, Co, Cu) displayed expected paramagnetically broadened and/or shifted ^{1}H NMR resonances. The S = ½ species, **^{OEt}PcVO**, **^{EtO}PcCo**, and **^{OEt}PcCu**, displayed broadened resonances, with only the **^{EtO}PcCo** resonances being additionally downfield shifted relative to the other two. The higher spin species (S > ½), **^{OEt}PcCr**, **^{OEt}PcMnCl**,[20] and **^{OEt}PcFe**, all displayed significantly broadened and shifted ^{1}H NMR resonances. While less broad than **^{OEt}PcCr** and **^{OEt}PcMnCl**, the resonances for **^{OEt}PcFe** displayed arene C–H resonances upfield at 3.44 ppm relative to the ethoxy peaks at 4.32 ppm (triplet) and 9.90 ppm (quartet).

2.2.3 ^{57}Fe Mössbauer Spectroscopy

The **^{OEt}PcFe** complex was further analysed by zero-field ^{57}Fe Mössbauer spectroscopy. The 90 K spectrum revealed a quadrupole doublet with an isomer shift value at δ = 0.33 mm s^{-1} and a quadrupole splitting value ($|\Delta E_Q|$) of 1.37 mm s^{-1} (Fig. 2.1).

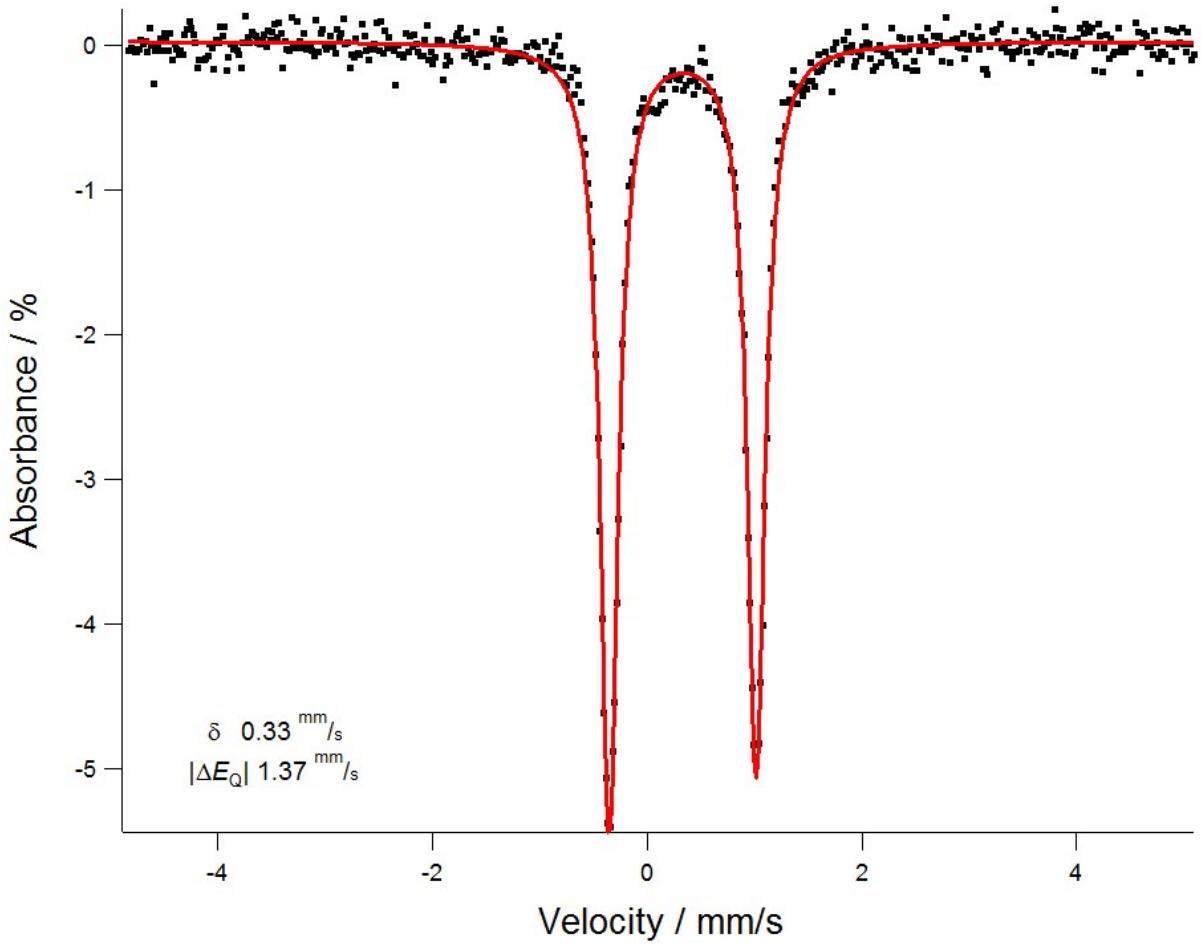

Figure 2.1: Zero-field ^{57}Fe Mössbauer spectrum of ^{EtO}PcFe, with isomer shift and quadrupole splitting values (lower left). Taken at 90 K.

These values are consistent with an expected intermediate spin (S = 1) square planar Fe center.[23] Our quadrupole splitting is roughly half of what would be expected by comparison with unsubstituted Pcs, which may be attributed to the electron donating ethoxy groups.[24, 25]

2.2.4 EPR Spectroscopy

EPR spectra were collected in dichloromethane (DCM) at 100 K for all non-integer, S = ½ species (**^{EtO}PcVO**, **^{EtO}PcCo**, **^{EtO}PcCu**). The EPR spectrum of **^{EtO}PcVO** revealed an expected axial signal ($g_{\parallel}$ = 2.020; $g_{\perp}$ = 1.920) with hyperfine coupling of the d^1 electron to the ^{51}V (I =

7/2) nucleus ($A_{\parallel}(^{51}V)$ = 174 G; $A_{\perp}(^{51}V)$ = 61 G), consistent with the single electron occupying the d_{xy} orbital (Fig. 2.2).[21, 26]

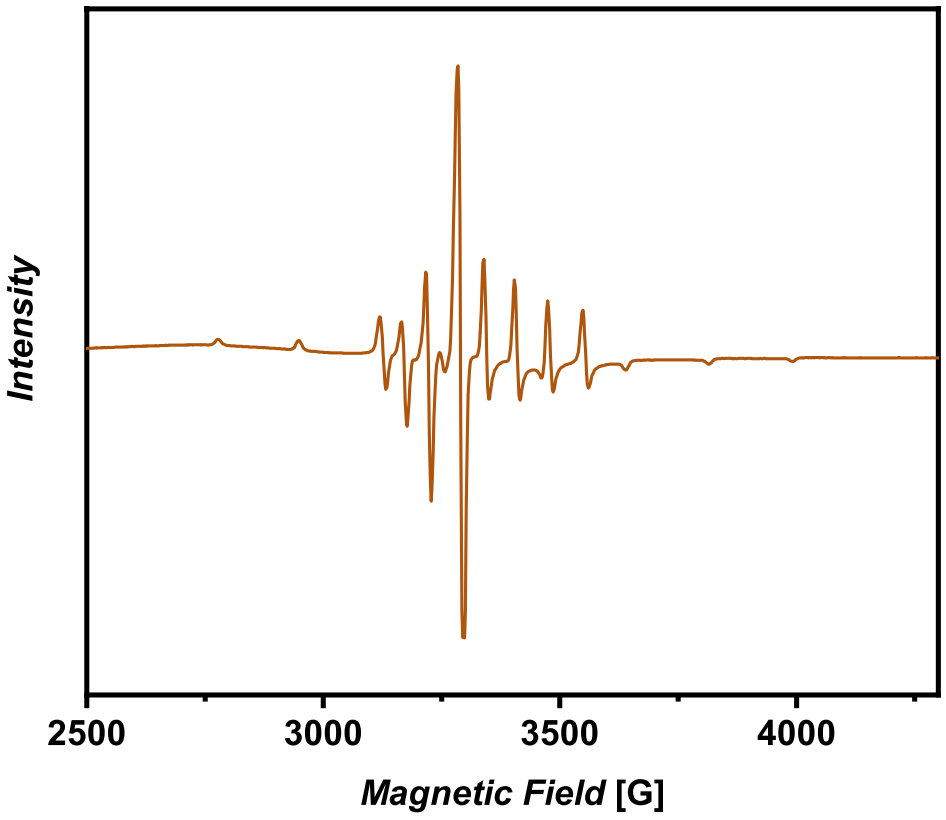

Figure 2.2: X-band EPR (ν = 9.302510 GHz) spectrum of ^{EtO}PcVO taken in CH_2Cl_2 at 100K.

^{EtO}PcCo shows a more complex spectrum likely indicative of its solvent dependence and air-sensitivity previously observed in PcCo EPR spectra.[27-31] Our spectrum (Fig. 2.3) resembles one reported by Zwart and van Wolput's featuring superimposed PcCo and PcCo(O_2) features.[30] The resonance at g = 2.009 may suggest the formation of an oxygen adduct,

^{EtO}PcCo(O_2),[30] with superimposed axial signals for **^{EtO}PcCo** at $g_{\perp}$ = 2.150 ($A_{\perp}$ (^{59}Co) = 69 G; I(^{59}Co) = 7/2) and $g_{\parallel}$ = 1.98 ($A_{\parallel}$(^{59}Co) = 116 G; I(^{59}Co) = 7/2).[32]

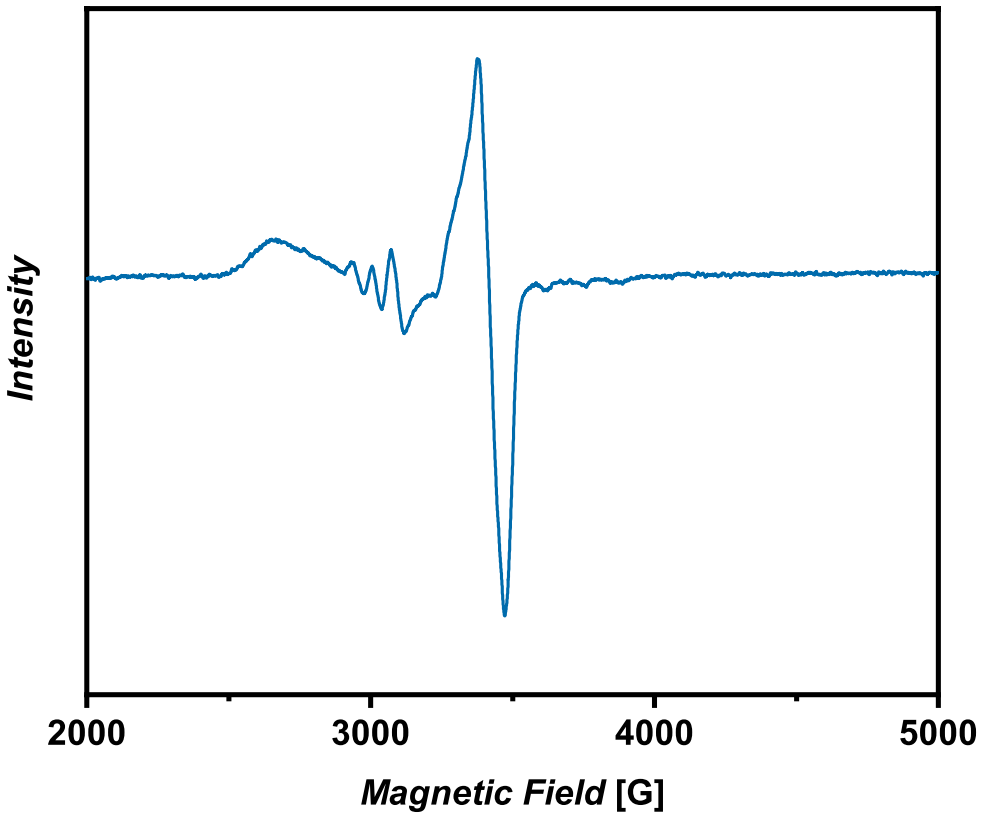

Figure 2.3: X-band EPR (ν = 9.606425 GHz) spectrum of ^{EtO}PcCo taken in CH_2Cl_2 at 100K.

Lastly, the spectrum for **^{EtO}PcCu** displays an axial signal ($g_{\parallel}$ =2.043; $g_{\perp}$ = 2.178) with significant hyperfine coupling to the spin active nuclei, ^{63}Cu (69%, I = 3/2) and ^{65}Cu (31%, I = 3/2), along the perpendicular direction ($A_{\perp}$(^{63}Cu, ^{65}Cu) = 205 G) expected from a lone electron in the $d_{x^2-y^2}$ orbital. Some unresolved superhyperfine to the ^{14}N (I = 1) nuclei is also apparent (Fig. 2.4).[21, 33]

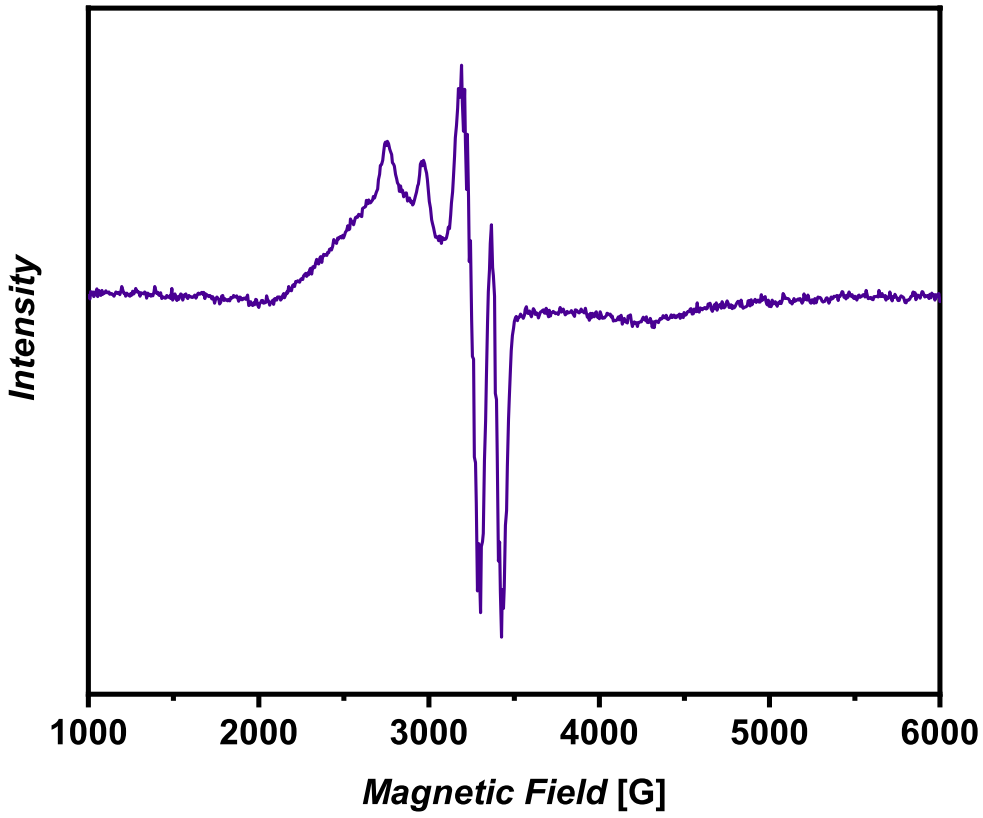

Figure 2.4: X-band EPR(v = 9.292836 GHz) spectrum of ^{EtO}PcCu taken in CH_2Cl_2 at 100K.

2.2.5 UV-Vis Spectroscopy

The electronic spectra of metallophthalocyanines and related macrocycles have been extensively studied over the past several decades both experimentally and theoretically.[34-44] Gouterman's four-orbital model has been widely applied to explain the strongest absorption bands emerging from nominally D_{4h}-symmetric porphyrin or Pc π-based $a_{1u}\rightarrow 2e_g$ (HOMO→LUMO) and higher energy $a_{2u}\rightarrow 2e_g$ (HOMO(-1)→LUMO) absorptions termed Q and B (Soret) bands, respectively. Open-shell species, such as the ones synthesized here, can

give rise to additional charge-transfer (CT) bands as a result of the metal 3d orbitals lying between the Pc HOMO and LUMO. Scheiner and others have studied such systems computationally,[42-44] and found that the a_{1u} HOMO is purely Pc π-based and that its energy is largely unaffected by the identity of the metal, whereas the $2e_g$ LUMO mixes more extensively with the metal orbitals, although not in a predictable linear fashion along the first-row metals. The UV-Vis spectra for all complexes synthesized here were collected in DCM and the absorption spectra of the first-row complexes are shown in Fig. 2.5.

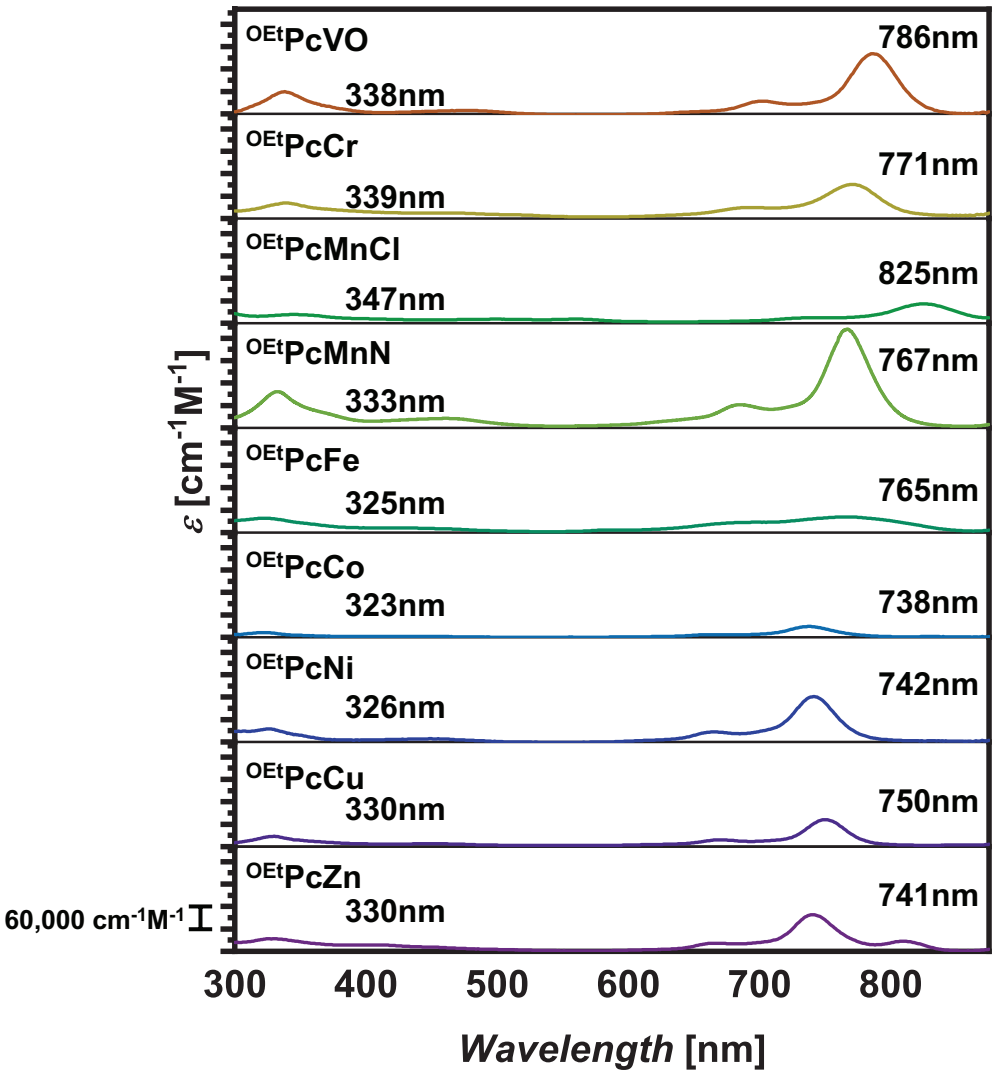

Figure 2.5: UV-vis spectra of metallophthalocyanines in DCM. Soret and Q-band λ_{max} values are labelled. Y-axis scaling: each large tick mark = 60,000 cm^{-1} M^{-1}.

Scheiner and Liao's calculated Q band energies for unsubstituted PcM complexes (M = Fe^{II}, Co^{II}, Ni^{II}, Cu^{II}, Zn^{II}) revealed a general decrease in energy (redshift) with increasing M atomic number,[42] mostly mimicking observed experimental data.[37] Our values do not follow this general trend, with **^{OEt}PcFe** and **^{OEt}PcZn** being outliers. A closer look at the M^{II} series only (**^{OEt}PcCr**, **^{OEt}PcFe**, **^{OEt}PcCo**, **^{OEt}PcNi**, **^{OEt}PcCu**, **^{OEt}PcZn**), reveals a general *blueshift* in the Q peak from **^{OEt}PcCr** (771 nm) to **^{OEt}PcCo** (738 nm), but no observable trend from **^{OEt}PcCo** to **^{OEt}PcZn** (Fig. 2.5). A look at the entire series, however, does reveal a general blueshift in Q band energy from **^{OEt}PcVO** to **^{OEt}PcCo** – with **^{OEt}PcMnCl** as an outlier – indicating that the Q band is mostly unaffected by the metal oxidation state, but could be responsive to tuning through axial substitution as has been shown previously.[45] We note also that **^{EtO}PcFe** displays a broadened Q band, possibly due to the closely overlapping Pc a_{1u} and Fe 3d frontier orbitals giving rise to underlying CT bands.[36, 42] While this data was collected under air-free conditions it may also be possible that our **^{EtO}PcFe** was erroneously exposed to oxygen leading to a u-oxo species with a mixture of Fe(II) and Fe(III) centers creating the broadening. Further experimentation is needed to determine the exact cause. We also note that in the spectrum of **^{EtO}PcZn** there is an additional red-shifted band that is most likely due to J-aggregation.[46, 47] The lack of a pronounced trend in Q band energy is of little concern as this is often observed in PcM series.[48] Similarly, we also note the lack of any discernible trend in Soret band energies in our series.

2.2.6 Structural Characterization

With the exception of ^{EtO}**PcZn**, all complexes were structurally characterized by single crystal X-ray diffraction (XRD) studies. The partial solid-state structures of all first-row metal complexes are shown in Fig. 2.6. While PcM complexes are generally planar,[18, 49-52] we observe significant Pc ring distortions in each complex, with ^{EtO}**PcCr** being the least distorted (Fig. 2.6). While axial metal-ligand mono-substitution typically leads to domed Pc structures,[51, 53-56] *ortho*-substituted isoindole rings cause saddling of the Pc ligand.[57-60] Dihedral angles between mean isoindole planes and the central N_4 plane (defined as the plane generated by the four pyrrolic metal-bound N atoms, Fig. 2.6c), or between adjacent or

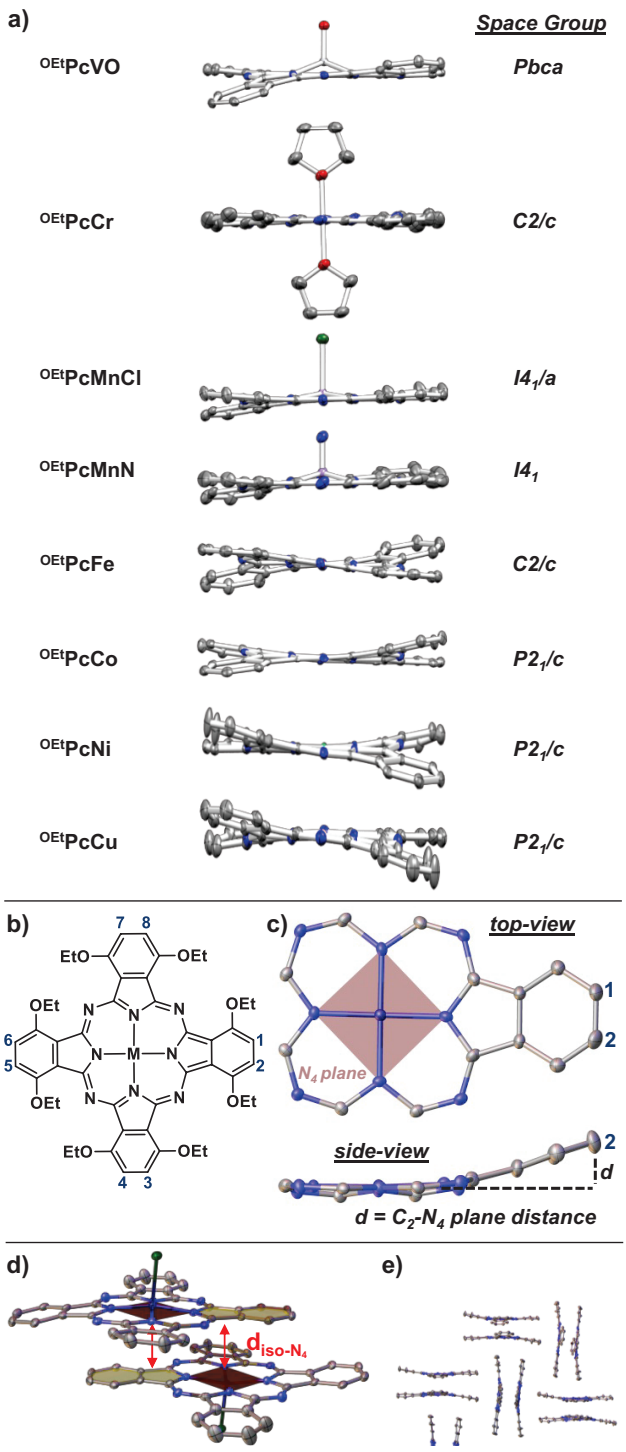

Fig. 2.6 a) Truncated solid-state molecular structures obtained by XRD studies of the metallophthallocyanine series C_x-N_4 distance (d) measurement used (bottom), shown

using C_2 in this example. d) Depiction of the isoindole-N_4 plane distances used to calculate d_{iso}-N_4. e) Representative herringbone extended structure shown with ^{EtO}PcCu.

opposite isoindole rings, are typically used to assess the degree of distortion in substituted PcM complexes.[57-61] However, significant information may be lost in using this assessment, such as the twisting of the isoindole rings relative to the N_4 plane,[20] making comparisons across a series difficult. Therefore, to compare the distortion throughout our **^{EtO}PcM** series, including both axially and non-axially substituted complexes, we used a simple model to assess the level of distortion by comparing the lateral deviation of the peripheral C atoms (labelled C_1-C_8; Fig. 2.6b) to the mean N_4 plane common to each complex (Fig. 2.6b-c, Table 2.1).

Compd.	|*d*| (C_1–N_4)	|*d*| (C_2–N_4)	|*d*| (C_3–N_4)	|*d*| (C_4–N_4)	|*d*| (C_5–N_4)	|*d*| (C_6–N_4)	|*d*| (C_7–N_4)	|*d*| (C_8–N_4)	d_{avg}	M–N_4 dist.	|dihed.$_1$|	|dihed.$_2$|	|dihed.$_{avg}$|	$d_{iso\text{-}N4}$
^{OEt}PcH$_2$	*0.779*	*0.704*	*0.687*	*0.477*	*0.013*	*0.076*	*0.217*	*0.177*	*0.391*	*N/A*	*11.4*	*13.6*	*12.5*	*3.376*
^{OEt}PcLiH	*0.114*	*0.064*	*0.898*	*0.804*	*0.752*	*0.574*	*0.037*	*0.123*	*0.421*	*0.077*	*12.9*	*12.3*	*12.6*	*3.398*
^{OEt}PcVO	*1.243*	*1.321*	*0.171*	*0.083*	*0.130*	*0.112*	*0.496*	*0.581*	*0.517*	*0.557*	*15.2*	*9.0*	*12.1*	*3.266*
^{OEt}PcCr	*0.276 (0.425)*	*0.245 (0.203)*	*0.236 (0.024)*	*0.051 (0.036)*	*0.276 (0.425)*	*0.245 (0.203)*	*0.236 (0.024)*	*0.051 (0.036)*	*0.202 (0.172)*	*0 (0)*	*0 (0)*	*0 (0)*	*0 (0)*	*N/A*
^{OEt}PcMnCl	*0.651*	*0.616*	*0.253*	*0.245*	*0.126*	*0.180*	*0.252*	*0.335*	*0.332*	*0.260*	*6.6*	*7.5*	*7.1*	*3.372*
^{OEt}PcMnN	*0.389 (0.225)*	*0.298 (0.262)*	*0.156 (0.616)*	*0.074 (0.622)*	*0.443 (0.393)*	*0.559 (0.247)*	*0.919 (0.063)*	*0.926 (0.135)*	*0.471 (0.320)*	*0.402 (0.407)*	*11.0 (7.9)*	*10.5 (6.9)*	*10.8 (7.4)*	*3.296*
^{OEt}PcFe	*0.162*	*0.162*	*1.250*	*1.244*	*1.244*	*1.250*	*0.162*	*0.162*	*0.705*	*0*	*17.5*	*17.5*	*17.5*	*3.265*
^{OEt}PcFe*	*0.109*	*0.350*	*0.256*	*0.243*	*0.109*	*0.350*	*0.256*	*0.243*	*0.240*	*0*	*0*	*0*	*0*	*N/A*
^{OEt}PcCo	*0.888*	*0.699*	*0.847*	*0.800*	*0.390*	*0.172*	*0.058*	*0.008*	*0.483*	*0.018*	*18.8*	*9.7*	*14.3*	*3.332*
^{OEt}PcNi	*0.347*	*0.110*	*0.002*	*0.031*	*0.699*	*0.602*	*0.786*	*0.742*	*0.415*	*0.009*	*15.4*	*9.7*	*12.6*	*3.401*
^{OEt}PcCu	*0.782*	*0.812*	*0.666*	*0.779*	*0.030*	*0.070*	*0.134*	*0.329*	*0.450*	*0.024*	*9.6*	*15.7*	*12.7*	*3.380*

Table 2.1: Calculated peripheral C_x-to-N_4 distances (x = 1-8) as shown in Fig. 2 of the paper with N_4 defined as the plane created by the four inner pyrrolic nitrogen atoms in the Pc macrocycle. For unit cells containing multiple ^{EtO}PcM molecules, the second set of values are shown in parentheses. All d values are in Å and all dihedral angles in degrees (°).

The C_x–N_4 plane distances, labelled d (x = 1-8; Fig. 2.6c), are tabulated and the absolute averages presented alongside the absolute averages of the conventional dihedral angles (taken

from opposite isoindole rings) in Table 2.1. As will be described below, we observed that the distortions described seemed to arise mostly from crystal packing, often attributed to substituent and/or co-crystalized solvent effects in the Pc literature[51]; therefore, this analysis should only be used as a qualitative comparison between the various solid-state structures. As a starting point, the solid-state structure of the protonated ligand (**^{EtO}PcH$_2$**) revealed a significant amount of distortion as evidenced by some d values approaching 0.8 Å, with an average of 0.391 Å (Table 2.2), likely resulting from the *ortho*-ethoxy group substitutions. The compound does not adopt a distinct saddled or domed structure and is best described as a mixed nonplanar conformation.[51] The axially substituted complexes, **^{EtO}PcVO**, **^{EtO}PcMnCl**, and **^{EtO}PcMnN**,[20] contain some of the most distorted Pc rings with some d values as high as approximately 1.3 Å. Of this series, **^{EtO}PcVO** has the highest d_{avg} (0.517 Å), followed by **^{EtO}PcMnN** (0.471 Å) and **^{EtO}PcMnCl** (0.332 Å). The same trend is observed for the M–N_4 distances (Table 2.2).[56, 62] This trend matches the π-donating ability and multiple bonding character of the axial ligands, with increasingly donating/bonding (O^{2-}, N^{3-}) ligands leading to more pronounced puckering of the metal out of the N_4 plane. Again, for these axially substituted species, none adopted distinct domed structures often observed for axially substituted systems instead showing twisting associated with the ethoxy groups.[20, 21, 51] Lastly, we note that for the symmetrically substituted **^{EtO}PcCr** complex bearing two axially coordinated THF molecules, the molecule is the least distorted of our entire series (d_{avg} = 0.172-0.202 Å). In contrast to the other structures, the extended packing structure revealed that the THF molecules provided more separation between distinct **^{EtO}PcCr** fragments, allowing the molecule to adopt a more planar structure and suggesting that packing effects likely play a significant role in the extent of the distortions observed in all complexes.

Compound	d_{avg}	$\lvert dihedral_{avg} \rvert$	$M–N_4$ distance	d_{iso-N4}
$^{OEt}PcH_2$	0.391	12.5	N/A	3.376
$^{OEt}PcLiH$	0.421	12.6	0.077	3.398
$^{OEt}PcVO$	0.517	12.1	0.557	3.266
$^{OEt}PcCr$	0.202 (0.172)	0 (0)	0 (0)	N/A
$^{OEt}PcMnCl$	0.332	7.1	0.260	3.372
$^{OEt}PcMnN$	0.471 (0.320)	10.8 (7.4)	0.402 (0.407)	3.296
$^{OEt}PcFe$	0.705	17.5	0	3.265
$^{OEt}PcFe^{*}$	0.240	0	0	N/A
$^{OEt}PcCo$	0.483	14.3	0.018	3.332
$^{OEt}PcNi$	0.415	12.6	0.009	3.401
$^{OEt}PcCu$	0.450	12.7	0.024	3.380

Table 2.2 Comparison of structural metrics across the phthalocyanine series. Average d values (d_{avg} in Å) and dihedral angles ($dihedral_{avg}$ in °) are calculated from the values in Table 2.3 (see experimental section), with d values obtained as shown in Fig. 2b-c and dihedrals obtained from opposite isoindole planes. The M–N_4 distances (Å) represent the degree of metal puckering out of the N_4 plane. The diso-N_4 (in Å) values represent the distance between the isoindole and N_4 planes of stacked PcM species as shown in Fig. 2d. Values in parentheses are from a second molecule in the same unit cell.

For the later metal compounds (**^{EtO}PcFe**, **^{EtO}PcCo**, **^{EtO}PcNi**, **^{EtO}PcCu**), there were few, if any, trends observable. While in one instance, **^{EtO}PcFe** may appear to be the most distorted of the entire series (d_{avg} = 0.705 Å), a second crystal structure, **^{EtO}PcFe***, was obtained and is more in line with the remainder of this series (d_{avg} = 0.240 Å) indicating again the significant role of crystal packing (Table 2.2). While both **^{EtO}PcFe** and **^{EtO}PcFe*** crystallized in the same space group (*C2/c*), we note that **^{EtO}PcFe*** is the only compound in the series where two O atoms from ethoxy groups of adjacent molecules were pointing directly at the Fe center ($d_{Fe–O}$ = 2.507 Å). In all other molecules of the series, except **^{EtO}PcCr**, an isoindole ring hovered directly above a M center or the bare N_4 plane (in **^{EtO}PcH$_2$**) forming distinct sandwich structures, where axial metal ligands, if present, were trans-disposed (Fig. 2.6d). The isoindole-N_4 distances ($d_{iso\text{-}N4}$) were measured and ranged from 3.265-3.401 Å with no clear trend along the series (Table 2.2). Together, most of these sandwich structures adopted the familiar herringbone arrangement in the extended structure (Fig. 2.6e) viewed, for example, along the *100* planes in the *P2$_1$/c* symmetric complexes (**^{EtO}PcH$_2$**, **^{EtO}PcHLi**, **^{EtO}PcCo**, **^{EtO}PcNi**, **^{EtO}PcCu**). Complexes **^{EtO}PcVO** and **^{EtO}PcCr** adopted more complex zigzag structures, whereas **^{EtO}PcFe** packed in sheets, and neither of these displayed herringbone patterns.

2.2.7 Cyclic Voltammetry

As described in the introduction, our interest in synthesizing this series of first-row **^{EtO}PcM** complexes was to determine their structural-electronic properties and extract possible design criteria for robust Pc-based RFB charge carriers. In our previous work studying **^{EtO}PcMnN**, we isolated and fully characterized a total of four charged states, **[^{EtO}PcMnN]^{n}** (n = +2, +1, −1, −2), in addition to the neutral form (n = 0), and characterized the redox events as ligand-borne.[20] This species displayed clean, quasi-reversible electrochemical events by cyclic

voltammetry (CV) which, in a later report, we found also translated to long-term electrochemical stability suitable for symmetric charge carrier applications.[16] While electrochemical reversibility on the CV timescale does not immediately translate to charge carrier stability,[63] irreversibility on the CV timescale would almost certainly lead to poor charge carrier performance.[64] In this section, we studied the electrochemical profiles of our species in an attempt to correlate structural to electrochemical properties and stability with the goal of proposing possible design criteria for stable Pc-based charge carriers. All complexes were studied by CV using $[Bu_4N][PF_6]$ as supporting electrolyte and referenced to the ferrocene/ferrocenium (Fc/Fc^+) redox couple. CVs of all compounds were taken in DCM with some also collected in coordinating solvents, such as acetonitrile (ACN) and THF, for reasons described below (Fig. 2.7).

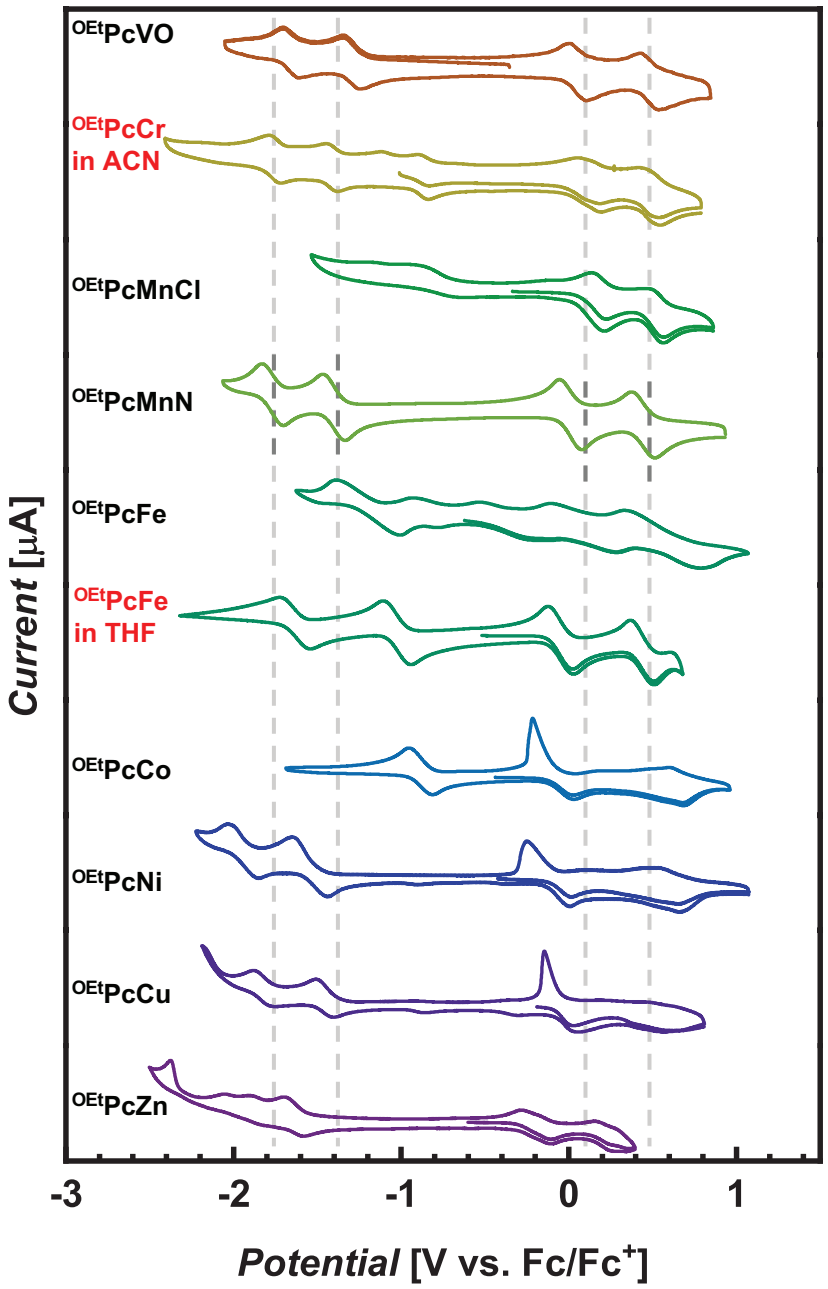

Figure 2.7: CVs of the metallophthalocyanines (concentrations range from 0.43 to 0.60 mM) series in DCM (unless otherwise specified) with 0.1 M [Bu_4N][PF_6] supporting electrolyte at a scan rate of 0.5 V/s. A 3 mm diameter glassy carbon working electrode, a

Pt wire counter electrode, and a Pt wire pseudo-reference electrode were used. All CVs were internally referenced to the Fc/Fc^+ redox couple.

All CVs shown here are compared to the CV for **[^{EtO}PcMnN]^n** with ligand-borne redox events with the formal reduction potentials ($E_{1/2}$) (n): −1.75 V (*−2/−1*), −1.38 V (*−1/0*), 0.02 V (*0/+1*), and 0.45 V (*+1/+2*) (black dashed lines, Fig. 3, Table 2.3).[20] Noticeably, the CV for **^{EtO}PcVO** is analogous to **^{EtO}PcMnN**, but with anodically shifted redox events at −1.66 V, −1.29 V, 0.06 V, and 0.48 V, which we assign to the corresponding ligand-based redox couples. Similar to **^{EtO}PcMnN**, we propose that the vanadyl unit in **^{EtO}PcVO** acts as a redox-innocent cap providing access to mostly ligand-based quasi-reversible redox events.[20]

Compound	$E_{1/2}$ (1st ox.) ($E_{p,a}$; $E_{p,c}$)	$E_{1/2}$ (2nd ox.) ($E_{p,a}$; $E_{p,c}$)	$E_{1/2}$ (1st red.) ($E_{p,a}$; $E_{p,c}$)	$E_{1/2}$ (2nd red.) ($E_{p,a}$; $E_{p,c}$)	$E_{1/2}$ (3rd red.) ($E_{p,a}$; $E_{p,c}$)
^{OEt}PcH$_2$	*−0.08 (0.02; −0.18)*	-	*−1.42 (−1.34; −1.49)*	*−1.76 (−1.69; −1.83)*	-
^{OEt}PcLiH	*−0.15 (−0.13; −0.19)*	*0.25 (0.27; 0.23)*	*−1.49 (−1.43; −1.54)*	-	-
^{OEt}PcVO	*0.06 (0.11; 0.01)*	*0.48 (0.53; 0.43)*	*−1.29 (−1.24; −1.34)*	*−1.66 (−1.61; −1.71)*	-
^{OEt}PcCr (in ACN)	*0.13 (0.19; 0.06)*	*0.48 (0.54; 0.42)*	*−0.88 (−0.91; −0.84)*	*−1.42 (−1.45; −1.38)*	*−1.75 (−1.78; −1.72)*
^{OEt}PcMnCl	*0.18 (0.21; 0.14)*	*0.52 (0.56; 0.48)*	-	-	-
^{OEt}PcMnN	*0.01 (0.08; −0.06)*	*0.44 (0.51; 0.37)*	*−1.40 (−1.33; −1.47)*	*−1.77 (−1.70; −1.83)*	-
^{OEt}PcFe (in DCM)	*0.08 (0.28; −0.11)*	*0.56 (0.79; 0.33)*	*−1.20 (−1.01; −1.39)*	-	-
^{OEt}PcFe (in THF)	*−0.06 (0.02; −0.13)*	*0.44 (0.51; 0.37)*	*−1.02 (−0.94; −1.11)*	*−1.64 (−1.54; −1.73)*	-

^{OEt}PcCo	*−0.10* *(0.03; −0.22)*	*0.64* *(0.68; 0.60)*	*−0.88* *(−0.81; −0.95)*	-	-
^{OEt}PcNi	*−0.12* *(0.01; −0.25)*	*0.62* *(0.68; 0.56)*	*−1.55* *(−1.44; −1.65)*	*−1.94* *(−1.85; −2.02)*	-
^{OEt}PcCu	*−0.05* *(0.05; −0.15)*	-	*−1.46* *(−1.40; −1.51)*	*−1.83* *(−1.77; −1.88)*	-

Table 2.3: Peak potentials for all compounds as found in their individual voltammograms using the experimental conditions described in the experimental section.

We observed interesting parallels in the next three compounds of the series: **^{EtO}PcCr**, **^{EtO}PcMnCl**, and **^{EtO}PcFe**. In particular, in DCM, all revealed poorly defined redox events, especially on the reductive side, possibly due to axial ligand lability – THF in **^{EtO}PcCr** or Cl^- in **^{EtO}PcMnCl** – and/or reaction with the DCM solvent (Fig. 2.7). For **^{EtO}PcCr** and **^{EtO}PcFe**, this is contrasted to their CVs in coordinating solvents, such as ACN or THF (Fig. 2.7). While the CV of **^{EtO}PcCr** was taken in both THF (Fig. 2.8 (b)) and ACN (Fig. 2.8 (c)), the limited electrochemical window of the former prevented a full analysis of all redox events.

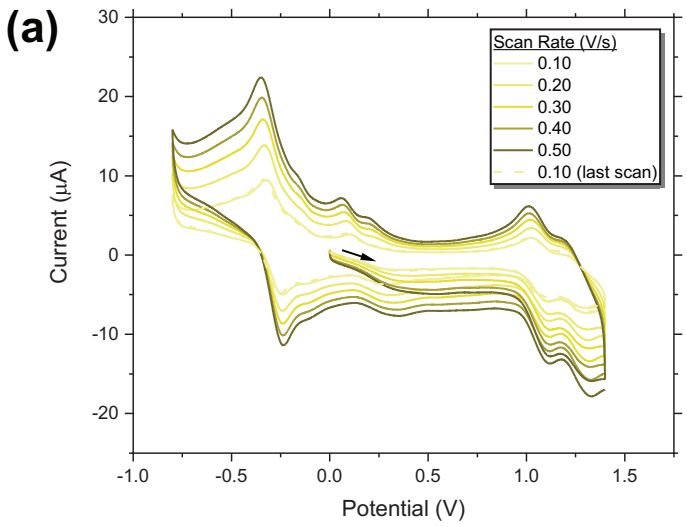
(a)
Scan Rate (V/s)
0.10
0.20
0.30
0.40
0.50
0.10 (last scan)
Current (μA)
Potential (V)

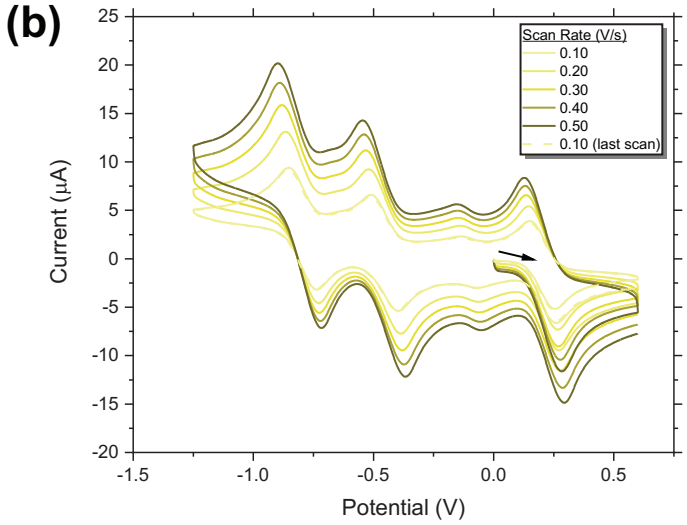
(b)
Scan Rate (V/s)
0.10
0.20
0.30
0.40
0.50
0.10 (last scan)
Current (μA)
Potential (V)

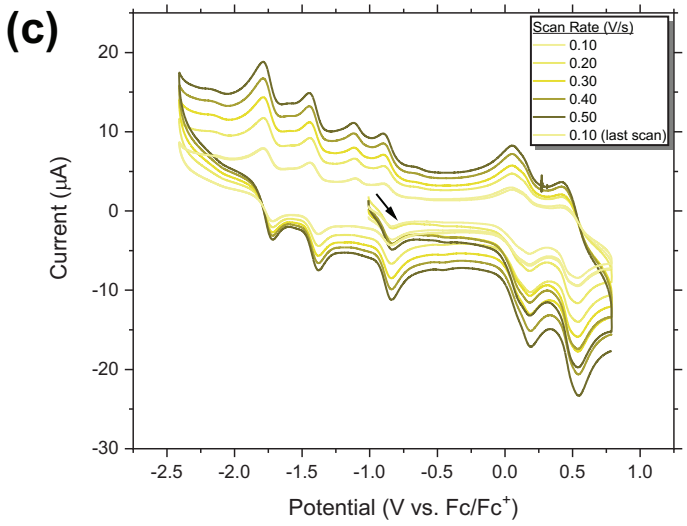
(c)
Scan Rate (V/s)
0.10
0.20
0.30
0.40
0.50
0.10 (last scan)
Current (μA)
Potential (V vs. Fc/Fc+)

Figure 2.8: CVs of ^{EtO}PcCr at varying scan rates (inset) with the arrow indicating initial scan direction in (a) DCM (b) THF (c) ACN. See experimental section for individual data and experimental conditions.

Taken in ACN, the CV revealed three quasi-reversible reductions ($E_{1/2}$ = −0.88, −1.42 and −1.75 V) and two quasi-reversible oxidations ($E_{1/2}$ = 0.13 and 0.48 V) (Fig. 2.8 (c), Table 2.3). While these events cannot be definitely assigned as either ring- or metal-centered, a comparison to literature would suggest that one of the oxidations is metal-centered and most reductions are ligand-centered.[65] Regardless, coordinating solvents clearly play a significant role in generating more quasi-reversible redox events on the CV timescale, likely due to maintained axial coordination and reduced aggregation, compared to a non-coordinating solvent, such as DCM (Fig. 2.8 (a)). A similar pattern is observed with ^{OEt}**PcFe** where the CV in DCM displayed a series of unassigned irreversible events, in stark contrast to the four clean quasi-reversible redox events (two reductions, two oxidations) in THF at $E_{1/2}$ values of −1.64, −1.03, −0.05, and 0.44 V (Fig. 2.9 (b), Table 2.3).

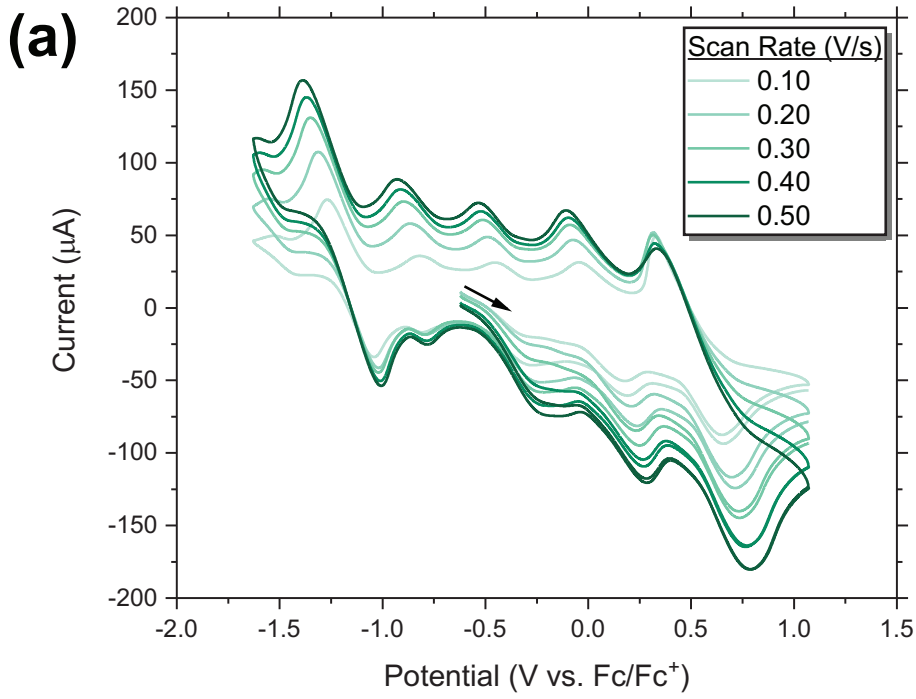
(a)
Scan Rate (V/s)
0.10
0.20
0.30
0.40
0.50
Current (μA)
Potential (V vs. Fc/Fc+)

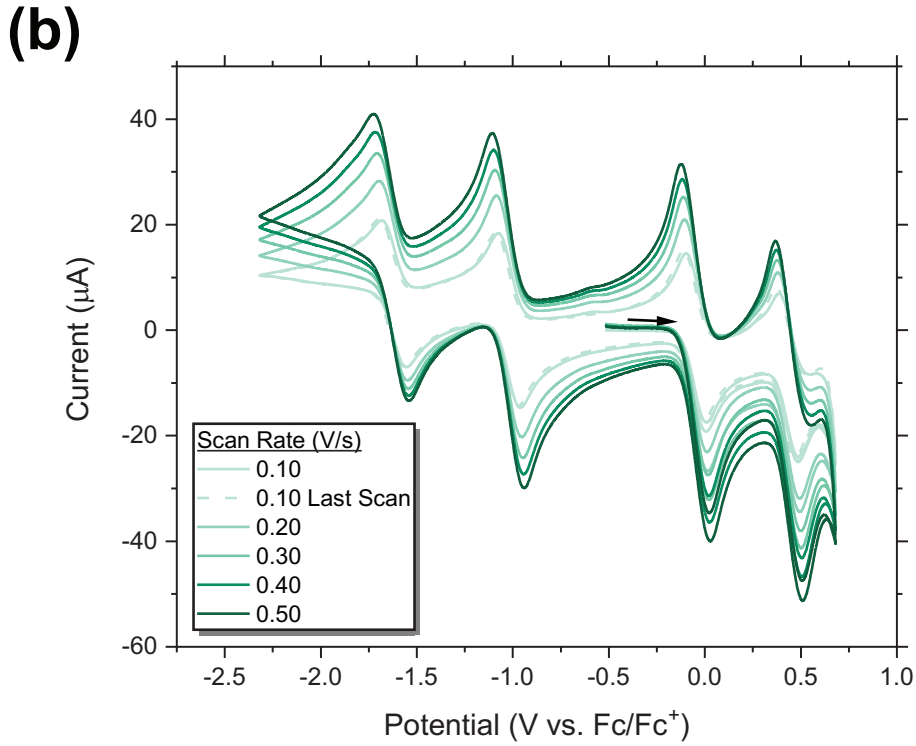
(b)
Scan Rate (V/s)
0.10
0.10 Last Scan
0.20
0.30
0.40
0.50
Current (μA)
Potential (V vs. Fc/Fc+)

Figure 2.9: CVs of ^{EtO}PcFe at varying scan rates (inset) with the arrow indicating initial scan direction in (a) DCM (b) THF. See experimental section for individual data and experimental conditions.

While the solid-state structure of ^{OEt}**PcFe** revealed no Fe-bound THF molecules, in contrast to ^{OEt}**PcCr** (Fig. 2.6a), $PcFe^{II}$ species are known to bind axial ligands,[66, 67] especially strong field ones. Given that the CV was acquired in THF, it is likely that at least weak coordination may act to stabilize the redox events, particularly compared to DCM (Fig. 2.9 (a)). We note that the two assigned oxidation events for ^{OEt}**PcFe** ($E_{1/2}$ = −0.05, 0.44 V) are remarkably similar to those for ^{EtO}**PcMnN** ($E_{1/2}$ = 0.02, 0.45 V) and may suggest ligand-borne oxidation events, supporting Scheiner's calculations.[42] In contrast, the reductive events for ^{OEt}**PcFe** ($E_{1/2}$ = −1.64, −1.03 V) are significantly different than for ^{EtO}**PcMnN** ($E_{1/2}$ = −1.75, −1.38 V) and are consistent with metal-borne vs. ligand-borne reduction events, respectively, consistent with both experimental[66] and Scheiner's theoretical results.[42] The following set of compounds, ^{EtO}**PcCo**, ^{EtO}**PcNi**, and ^{EtO}**PcCu**, each display relatively sharp, non-diffusional events at similar potentials – E_p = 0.22, −0.25, and −0.15 V, respectively – which appear only after scanning to the outermost second oxidation events at approximately 0.7 V (Fig. 2.7, Table 2.3). These sharp, Gaussian-shaped current peaks are tentatively assigned as adsorptive stripping events resulting from the oxidatively induced adsorption of the compounds onto the electrode surface.[68-71] We further propose that the absence of available axial metal-ligand coordination for ^{EtO}**PcCo** in DCM, as well as the inability for coordination to ^{EtO}**PcNi** and ^{EtO}**PcCu** due to filled d_z^2 orbitals, likely facilitate the interaction of the metallophthalocyanines with the electrode surface. The metal-free ^{EtO}**PcH$_2$** also displays this phenomenon in further support of our assessment (Fig. 2.10).

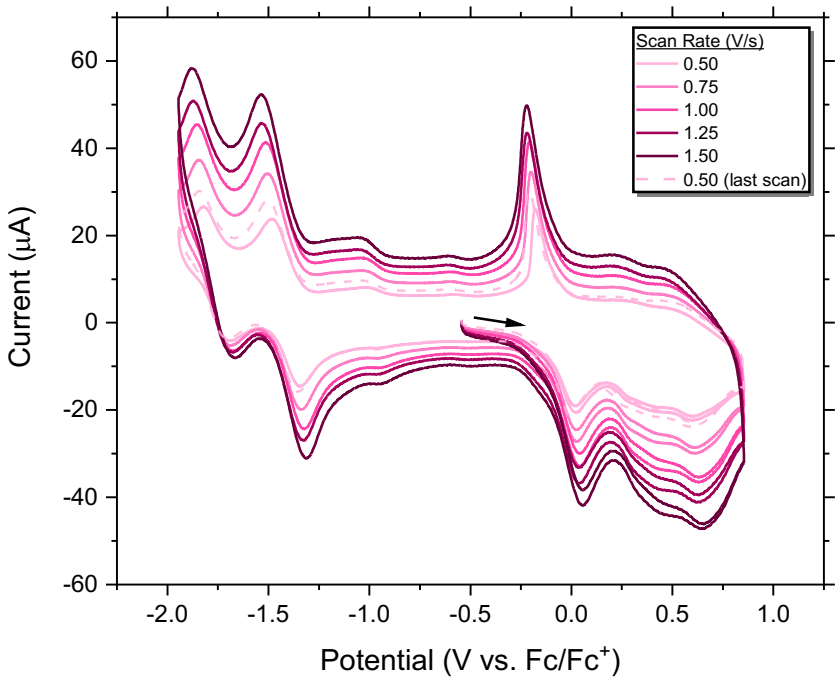

Figure 2.10: CVs of $^{EtO}PcH_2$ at varying scan rates (inset) with the arrow indicating initial scan direction. Experimental conditions: Taken in DCM with 0.53 mM of $^{EtO}PcH_2$, 0.1 M of $[Bu_4N][PF_6]$, 3 mm diameter glassy carbon working electrode, Pt wire counter electrode, and Pt wire pseudo-reference electrode. Internally referenced to Fc/Fc^+.

Such Pc-carbon surface interactions are well precedented and have been exploited for many applications.[13, 72-74] While these interactions are typically ascribed to Pc-surface π—π interactions,[73] we observed that our **^{EtO}PcCo** required the most polishing between scans, suggesting a possible metal-based contribution to surface adsorption. On the reductive side, a quasi-reversible event for **^{EtO}PcCo** is observed at $E_{1/2}$ = −0.88 V, similar to **^{EtO}PcFe** ($E_{1/2}$ = −1.03 V), and is assigned as a metal-based reduction event consistent with DFT studies.[42] This reduction event is also noticeably shifted from the two quasi-reversible reduction events observed in **^{EtO}PcNi** ($E_{1/2}$ = −1.94, −1.55 V) and **^{EtO}PcCu** ($E_{1/2}$ = −1.83, −1.46 V) which are

very similar to those observed in **^{EtO}PcMn3** and support predicted ligand-based redox events (Table 2.2, Fig. 2.7).[20, 42]

The last compound in our series, the structurally uncharacterized **^{OEt}PcZn**, exhibited two quasi-reversible oxidations at $E_{1/2}$ = −0.19, 0.20 V, as well as a quasi-reversible reduction event at $E_{1/2}$ = −1.64 V, all of which would necessarily be ligand-borne. Additionally, this reduction was followed by two irreversible reduction ($E_{p,c}$ = −1.90, −2.06 V), as well as a final reductive event (E_p = −2.38 V) resulting in a sharp irreversible response which is likely due to reaction with the DCM solvent. Unlike, in the other late metal Pcs described above, adsorption to the electrode surface did not seem to occur with **^{OEt}PcZn**. In the absence of structural characterization, we cannot definitively state why **^{OEt}PcZn** does not adsorb onto the electrode surface; however, we note that most published PcZn species contain axially coordinated solvent molecules[51, 75], which is further supported by a cursory search of the Cambridge Crystallographic Data Center. Given **^{OEt}PcZn** was synthesized in DMF, it is possible that some coordinating solvent molecules remain.

Correlating our electrochemical and structural data for this series of compounds, we can propose that non-labile axial metal-ligand coordination (**^{EtO}PcVO**, **^{EtO}PcMnN**) is optimal for generating clean, quasi-reversible electrochemical events. In the case of **^{EtO}PcMnN**, we have shown that such electrochemical properties translated to excellent charge carrier stability.[16] The poor reductive stability of **^{EtO}PcMnCl** suggested possible chloride lability. In the absence of a strongly bound ligand, the electrochemical properties of our species were drastically improved by the presence of a coordinating solvent, such as THF or ACN, when such a species was capable of binding the solvent (**^{EtO}PcCr**, **^{EtO}PcFe**). For the later metals, **^{EtO}PcCo**, **^{EtO}PcNi**, and **^{EtO}PcCu**, our structural data indicated the absence of axial metal-ligand

coordination (Fig. 2.6a) which clearly translated to pronounced electrode adsorption events in DCM (Fig. 2.7), also observed for ^{EtO}**PcH$_2$**. Axial ligands likely play a significant role in preventing aggregation and stacking at the electrode, as shown most significantly in the solid-state structure of ^{EtO}**PcCr**, where individual molecules are the most spaced apart. While some compounds known to adsorb onto electrodes have been tested as potential charge carriers with some degree of success,[63] we believe that this characteristic is likely not beneficial for long-term RFB cycling (> 1,000 cycles) due to possible incomplete desorption from cycle to cycle which may lead to poorer electrode kinetics.[68]

2.3 Summary

In this chapter, we described the synthesis and characterization of a series of substituted metallophthalocyanines, ^{EtO}**PcM** (**M** = VO, Cr, Fe, Co, Ni, Cu, Zn), as well as their lithiated and protonated precursors (**M** = HLi, H_2). All complexes were structurally characterized (except ^{EtO}**PcZn**) and their electrochemical properties interrogated. Depending on the nature of M, the electrochemical results revealed both ligand- and metal-borne redox events which were correlated to previous experimental and theoretical results. Structural correlations were also drawn wherein the late metal species (^{EtO}**PcCo**, ^{EtO}**PcNi**, ^{EtO}**PcCu**) with no axial metal-ligand coordination revealed pronounced electrode adsorption events which could hinder their applications as stable charge carriers for RFB applications. In contrast, species with non-labile axial groups (^{EtO}**PcVO** and ^{EtO}**PcMnN**) revealed clean, quasi-reversible electrochemical profiles. The use of coordinating solvents was also found to significantly improve the reversibility of the redox processes for ^{EtO}**PcCr** and ^{EtO}**PcFe**, likely preventing their aggregation onto the electrode surfaces. We are currently investigating the use of these compounds as potential charge carriers for RFB applications.

2.4 Experimental Section

Techniques and Reagents. All air-free manipulations were performed under an atmosphere of dry, oxygen-free N_2 within an MBraun glovebox (MBRAUN UNIlab Pro SP Eco equipped with a −40°C freezer), or by standard Schlenk techniques. Pentane, hexanes, benzene, diethyl ether, DCM, and THF (inhibitor-free) were dried and degassed on an MBraun Solvent Purification System and stored over activated 4 Å molecular sieves. All other solvents (chloroform, DMF) were degassed by freeze-pump-thaw and stored on activated 4 Å molecular sieves prior to use. Metal salts ($VOSO_4 \cdot 5H_2O$, $CrCl_2$, $Fe(OAc)_2$, $CoCl_2 \cdot 6H_2O$, $NiCl_2 \cdot 6H_2O$, $CuCl_2$, and $ZnCl_2$) were purchased from Strem Chemicals, Li metal, 2,3-dicyanohydroquinone from Acros Organics, and ethyl iodide from Alfa Aesar and all were used without further purification. All other reagents were obtained from Sigma-Aldrich, Fisher Scientific, or VWR and used without further purification. **^{EtO}PcMnCl** and **^{EtO}PcMnN** were synthesized following our previous report.[20] Celite® and 4 Å molecular sieves were dried at 250 °C under dynamic vacuum (<0.1 Torr) for 24 h prior to use.

Spectroscopic Measurements. NMR spectra were obtained on an Agilent Technologies 400 MHz spectrometer, or a Varian 600 MHz spectrometer, and referenced to residual solvent. Chemical shifts (δ) are recorded in ppm and the coupling constants are in Hz. J-Young air-tight adaptors were used for air- and water-sensitive compounds. Perpendicular-mode X-band EPR spectra were collected on a Bruker EMX EPR spectrometer equipped with an Oxford ESR 900 liquid helium cryostat. All EPR samples contained roughly 1 mg of material and data acquisition collected at 100 K in frozen DCM or THF. It should be noted that a small residual free radical signal is commonly observed in PcM complexes.[18] UV-Vis spectra were collected on a Shimadzu UV-2401PC spectrophotometer. All measurements were performed on

recrystallized product. All stock solutions and dilutions were prepared by mass. Zero-field ^{57}Fe Mössbauer spectroscopy was performed using a SEE Co Model W304 resonant gamma-ray spectrometer (activity = 50 mCi +/- 10%), ^{57}Co/Rh source (manufactured by Ritverc) equipped with a Janis Research Model SVT-400 cryostat system. The source linewidth is < 0.12 mm/s for the outermost lines of a 25 micron alpha-Fe foil standard. Isomer shifts are referenced to alpha-Fe foil at room temperature. Samples were prepared using approximately 30 mg of powdered material and measured at 100 K unless otherwise noted. Data was fitted using a custom Igor Pro (Wavemetrics) macro package developed by the Betley group at Harvard University.

X-ray Crystallography. Data was collected on a Bruker KAPPA APEX II diffractometer equipped with an APEX II CCD detector using a TRIUMPH monochromator with a Mo Kα X-ray source (α = 0.71073 Å). The crystals were mounted on a cryoloop under Paratone-N oil, and all data were collected at 100 K using an Oxford nitrogen gas cryostream system. A hemisphere of data was collected using ω scans with 0.5° frame widths. Data collection and cell parameter determination were conducted using the SMART program. Integration of the data frames and final cell parameter refinement were performed using SAINT software. Absorption correction of the data was carried out using SADABS. Structure determination was done using direct or Patterson methods and difference Fourier techniques. All hydrogen atom positions were idealized and rode on the atom of attachment. Structure solution, refinement, graphics, and creation of publication materials were performed using SHELXTL or OLEX^2.

Electrochemical Measurements. CV was performed on a CH Instruments 630E Electrochemical Analysis Potentiostat. Unless otherwise noted, the working electrode was a 3mm diameter glassy carbon (CH Instruments) and was cleaned prior to each experiment by

sequentially polishing with a gradient of 1.0 μm, 0.3 μm, and 0.05 μm alumina (CH Instruments) on a cloth pad, followed by rinsing with distilled water and acetone. The Pt wire pseudo-reference and counter electrodes were rinsed with distilled water and acetone and heated white-hot with a butane torch. All measurements were performed on recrystallized product and referenced to the Fc/Fc^+ redox couple unless otherwise stated.

3,6-Diethoxyphthalonitrile. 3,6-Diethoxyphthalonitrile was synthesized using a modified literature procedure.[20, 21] A mixture of 2,3-dicyanohydroquinone (5.20 g, 33.4 mmol, 1 equiv) and K_2CO_3 (5.00 g, 36 mmol, 1.1 equiv) in 125 mL of wet acetone was sparged with N_2 or Ar for 30 minutes then heated to reflux. Ethyl iodide (13 mL, 162 mmol, 5 equiv) was then added dropwise to the mixture. The yellow slurry was stirred under reflux for 48 h. After cooling, the yellow solid was filtered on a glass frit and subsequently transferred to a mortar and pestle where it was ground into a powder. The powder was reintroduced to the glass frit and washed successively with 500 mL of H_2O, 150 mL of EtOH, and 150 mL of Et_2O. The product was collected and dried under reduced pressure for 24 h, affording a white powder. Additional product could be recovered by evaporation of the eluent after the wash, and this additional product was similarly washed with H_2O, EtOH, and Et_2O. Yield: 5.154 g (73.4%). ^{1}H NMR (600 MHz, CD_2Cl_2): δ 7.21 (s, 2H, C_6H_2.), 4.16 (q, J = 7.0 Hz, 4H, O$CH_2$$CH_3$), 1.48 (t, J = 7.0 Hz, 6H, OCH_2CH_3).

^{EtO}PcHLi. This compound was synthesized following our previously reported procedure.[20] Single crystals suitable for XRD studies were obtained by vapor diffusion of Et_2O into a concentrated solution of the product in DCM. ^{1}H NMR (600 MHz, CD_2Cl_2): δ 14.75 (s, 1H, NH), 7.57-7.52 (m, 8H, C_6H_2), 4.97-4.89 (m, 16H, O$CH_2$$CH_3$), 1.82-1.75 (m, 24H, OCH_2CH_3).

λ_{max} (ε) = 723 nm (66,552 M^{-1} cm^{-1}), 783 nm (76,897 M^{-1} cm^{-1}). MS (MALDI-TOF): Calculated 873.18(M^+) Found 873.40 (M^+).

$^{EtO}PcH_2$. This compound was synthesized using a modified literature procedure.[20, 21] **^{EtO}PcHLi** (1.00 g, 0.98 mmol, 1 equiv) was slurried in 50 mL of H_2O in a flask and 5 mL HCl (12.1 M, excess) was added dropwise over the course of 5 mins, changing the green slurry to a purple solution. The progress of the reaction was monitored by ^{1}H NMR spectroscopy every 24 h, with a small aliquot of solution removed and neutralized with excess bicarbonate, before filtering over a plug Celite®/glass wool, leaving a dark green pad that was washed with excess water and then extracted with CH_2Cl_2, resulting in a forest green eluent that was reduced to dryness and subsequently dissolved in CD_2Cl_2 for analysis. The product was neutralized with $NaHCO_3$ (20.000 g, 238 mmol, excess) once a conversion > 95% was observed by NMR spectroscopy (after roughly 48 h). The produce was collected by filtration and washed with 500 mL H_2O, 250 mL EtOH, and 150 mL of Et_2O, resulting in a dark green powder that was dried under reduced pressure. Yield: 0.857 g (86.0%). Single crystals suitable for XRD studies were obtained by vapor diffusion of Et_2O into a concentrated solution of the product in DCM. ^{1}H NMR (600 MHz, CD_2Cl_2): δ 7.66 (s, 8H, *C_6H_2*), 4.92 (q, *J* = 7.0 Hz, 16H, O*CH_2*CH_3), 1.81 (t, *J* = 7.0 Hz, 24H, OCH_2*CH_3*), 0.23 (s, 2H, *NH*). λ_{max} (ε) = 770 nm (102,222 M^{-1} cm^{-1}). MS (MALDI-TOF): Calculated 866.38(M^+) Found 866.38 (M^+).

$^{EtO}PcVO$. This compound was synthesized using a modified literature procedure.[21] Under an inert atmosphere, **^{EtO}PcHLi** (0.200 g, 0.23 mmol, 1 equiv), $VOSO_4 \cdot 5H_2O$ (0.200 g, 0.79 mmol, excess), and $NaHCO_3$ (0.200 g, 2.3 mmol, excess) were combined in a round-bottom flask with 15 mL of DMF, and the resulting mixture was heated to 145 °C for 4 h. H_2O (100 mL) was then added and the solution was stirred for 15 mins, and subsequently filtered through a glass

frit, leaving a dark green solid. The solid was washed successively with 150 mL of H_2O, 50 mL of EtOH, and 50 mL of Et_2O and subsequently collected and dried under reduced pressure. Yield: 0.090 g (42.2%). Single crystals suitable for XRD studies were obtained by vapor diffusion of Et_2O into a concentrated solution of the product in DCM. ^{1}H NMR (600 MHz, CD_2Cl_2): δ 8.53 (bs, *C_6H_2*), 5.03 (bs, O*CH_2*CH_3), 1.86 (bs, OCH_2*CH_3*). λ_{max} (ε) = 786 nm (160,930 M^{-1} cm^{-1}). MS (MALDI-TOF): Calculated 931.30 (M^+) Found 932.39 ($M\text{-}H^+$).

^{EtO}PcCr. Under an inert atmosphere, **^{EtO}PcH$_2$** (0.50 g, 0.58 mmol, 1.0 equiv), $CrCl_2$ (0.080 g, 0.65 mmol, 1.1 equiv), and $NaHCO_3$ (0.242 g, 2.9 mmol, 5 equiv) were slurried in 30 mL of DMF in a thick-walled pressure vessel and heated to 100 °C for 5 h, resulting in a dark blue solution. After cooling, the mixture was filtered under inert atmosphere and the solid was extracted with THF. The combined filtrate was collected and dried under vacuum at 100 °C. The product was then purified by layered recrystallization using THF/isooctane at −35 °C. Yield: 0.260 g (49.0%). Single crystals suitable for XRD studies were obtained by vapor diffusion of 2,2,4-trimethylpentane into a concentrated solution of the product in THF. ^{1}H NMR (600 MHz, CD_2Cl_2): δ 6.46-6.19 (bm), δ 1.89 (bs), δ -3.56 (bs). λ_{max} (ε) = 771 nm (91,412 M^{-1} cm^{-1}). MS (MALDI-TOF): Calculated 916.30 (M^+) Found 917.39 (M^+).

^{EtO}PcFe. Under an inert atmosphere, **^{EtO}PcH$_2$** (1.00 g, 1.15 mmol, 1 equiv) and $Fe(OAc)_2$ (0.24 g, 1.38 mmol, 1.2 equiv) were slurried in 15 mL of toluene and heated to reflux for 24 h resulting in a dark green solution. After cooling, all volatiles were removed under reduced pressure, yielding a dark green powder. The crude product was transferred to a glass frit and washed with 25 mL of pentane and 25 mL of EtO_2. The resulting dark green filter was extracted with 50 mL of DCM and the filtrate was reduced to an estimated 10 mL under reduced pressure, and layered with pentane (10mL) at room temperature. Yield: 0.840 g (75.8%). Single crystals

suitable for XRD studies were obtained by vapor diffusion of hexanes into a concentrated solution of the product in benzene at room temperature. ^{1}H NMR (600 MHz, CD_2Cl_2): δ 9.90 (q, *J* = 7 Hz, 16H, O*CH*$_2$CH$_3$), 4.32 (t, *J* = 7 Hz, 24H, OCH$_2$*CH*$_3$), 3.44 (s, 8H, *C*$_6$*H*$_2$). λ_{max} (ε) = 765 nm (41,868 M^{-1} cm^{-1}). MS (MALDI-TOF): Calculated 920.29 (M^+) Found 920.40 (M^+).

EtOPcCo. Under an inert atmosphere, **EtOPcHLi** (0.200 g, 0.23 mmol, 1 equiv), $CoCl_2 \cdot 6H_2O$ (0.200 g, 0.84 mmol, excess), and $NaHCO_3$ (0.200 g, 2.3 mmol, excess) were combined in a round-bottom flask with 15 mL of DMF, and the resulting mixture was heated to 145 °C for 4 h. H_2O (100 mL) was then added and the solution was stirred for 15 mins, and subsequently filtered through a glass frit, leaving a dark green solid. The solid was washed successively with 150 mL of H_2O, 10 mL of EtOH, and 25 mL of Et_2O and subsequently collected and dried under reduced pressure. Yield: 0.204 g (96%). Single crystals suitable for XRD studies were obtained by vapor diffusion of pentane into a concentrated solution of the product in DCM, or by slow evaporation from EtOH. ^{1}H NMR (600 MHz, CD_2Cl_2): δ 9.89 (bs, *C*$_6$*H*$_2$), 7.30 (bs, O*CH*$_2$CH$_3$), 3.39 (bs, OCH$_2$*CH*$_3$). λ_{max} (ε) = 738 nm (28,793 M^{-1} cm^{-1}). MS (MALDI-TOF): Calculated 923.29 (M^+) Found 923.40 (M^+).

EtOPcNi. This compound was synthesized using a modified literature procedure.[21] In air, **EtOPcHLi** (0.208 g, 0.24 mmol, 1 equiv), $NiCl_2 \cdot 6H_2O$ (0.200 g, 0.84 mmol, excess), and $NaHCO_3$ (0.200 g, 2.3 mmol, excess) were combined in a round-bottom flask with 15 mL of DMF, and the resulting mixture was heated to 145 °C for 4 h. H_2O (100 mL) was then added and the solution was stirred for 15 mins, and subsequently filtered through a glass frit, leaving a dark green solid. The solid was washed successively with 150 mL of H_2O, 50 mL of EtOH, and 50 mL of Et_2O and subsequently collected and dried under reduced pressure. Yield: 0.230

g (>100% (excluding co-crystallized CH_2Cl_2); 88.24% (including co-crystallized CH_2Cl_2)). Single crystals suitable for XRD studies were obtained by vapor diffusion of Et_2O into a concentrated solution of the product in DCM. ^{1}H NMR (600 MHz, CD_2Cl_2): δ 7.54 (s, 8H, *C_6H_2*), 4.83 (q, *J* = 7.0 Hz, 16H, O*CH_2*CH_3), 1.75 (t, *J* = 7.0 Hz, 24H, OCH_2*CH_3*). λ_{max} (ε) = 742 nm (121276.6 M^{-1} cm^{-1}). MS (MALDI-TOF): Calculated 922.29 (M^+) Found 923.40 (M-H^+).

^{EtO}PcCu. This compound was synthesized using a modified literature procedure.[21] Under an inert atmosphere, **^{EtO}PcHLi** (0.207 g, 0.24 mmol, 1 equiv), $CuCl_2$ (0.161 g, 1.20 mmol, 5 equiv), and $NaHCO_3$ (0.107 g, 1.27 mmol, 5.3 equiv) were combined in a round-bottom flask with 10 mL of DMF, and the resulting mixture was heated to 165 °C for 20 h. H_2O (80 mL) was then added and the solution was stirred for 30 mins, and subsequently filtered through a glass frit, leaving a dark green solid. The solid was washed successively with 100 mL of H_2O and 20 mL of EtOH and subsequently collected and dried under reduced pressure. Yield: 0.091 g (41.4%). Single crystals suitable for XRD studies were obtained by vapor diffusion of hexanes into a concentrated solution of the product in DCM, or by slow evaporation from EtOH. ^{1}H NMR (600 MHz, CD_2Cl_2): δ 4.58 (bs, 16H), δ 1.61 (bs, 24H). λ_{max} (ε) = 750 nm (72,421 M^{-1} cm^{-1}). MS (MALDI-TOF): Calculated 927.29 (M^+) Found 927.40 (M^+).

^{EtO}PcZn. This compound was synthesized using a modified literature procedure.[21] Under an inert atmosphere, **^{EtO}PcHLi** (0.2174 g, 0.25 mmol, 1 equiv), $ZnCl_2$ (0.1813 g, 1.33 mmol, 5.3 equiv), and $NaHCO_3$ (0.1223 g, 1.46 mmol, 5.8 equiv) were combined in a round-bottom flask with 20 mL of DMF, and the resulting mixture was heated to 165 °C for 20 h. H_2O (80 mL) was then added and the solution was stirred for 30 mins, and subsequently filtered through a glass frit, leaving a dark green solid. The solid was washed successively with 100 mL of H_2O

and 20 mL of EtOH and subsequently collected and dried under reduced pressure. High purity product could be recrystallized by vapor diffusion of hexanes into a concentrated DCM solution of the product. Yield: 0.091 g (22.1%). ^{1}H NMR (600 MHz, $CDCl_3$): δ 7.62 (s, 8H, *C_6H_2*), 5.04 (q, *J* = 7.0 Hz, 16H, O*CH_2*CH_3), 1.74 (t, *J* = 7.0 Hz, 24H, OCH_2*CH_3*). λ_{max} (ε) = 742 nm (121276.6 M^{-1} cm^{-1}). λ_{max} (ε) = 741 nm (97,885 M^{-1} cm^{-1}). MS (MALDI-TOF): Calculated 929.30 (M^+) Found 930.37 ($M\text{-}H^+$).

2.5 References

1. Soloveichik, G. L., Flow Batteries: Current Status and Trends. *Chem. Rev.* **2015,** *115* (20), 11533-11558.

2. Turek, P.; Petit, P.; Andre, J. J.; Simon, J.; Even, R.; Boudjema, B.; Guillaud, G.; Maitrot, M., A new series of molecular semiconductors: phthalocyanine radicals. *Journal of the American Chemical Society* **1987,** *109* (17), 5119-5122.

3. Eley, D. D., Phthalocyanines as Semiconductors. *Natur* **1948,** *162* (4125), 819-819.

4. Bouvet, M., Phthalocyanine-based field-effect transistors as gas sensors. *Analytical and Bioanalytical Chemistry* **2006,** *384* (2), 366-373.

5. Janata, J., Chemical sensors. *Analytical Chemistry* **1992,** *64* (12), 196-219.

6. Öztürk, Z. Z.; Kılınç, N.; Atilla, D.; Gürek, A. G.; Ahsen, V., Recent studies chemical sensors based on phthalocyanines. *J. Porphyrins Phthalocyanines* **2009,** *13* (11), 1179-1187.

7. Zhou, R.; Josse, F.; Göpel, W.; Öztürk, Z. Z.; Bekaroğlu, Ö., Phthalocyanines as Sensitive Materials for Chemical Sensors. *Appl. Organomet. Chem.* **1996,** *10* (8), 557-577.

8. Grätzel, M., Dye-sensitized solar cells. *Journal of Photochemistry and Photobiology C: Photochemistry Reviews* **2003,** *4* (2), 145-153.

9. Ragoussi, M.-E.; Ince, M.; Torres, T., Recent Advances in Phthalocyanine-Based Sensitizers for Dye-Sensitized Solar Cells. *Eur. J. Org. Chem.* **2013,** *2013* (29), 6475-6489.

10. Rosenthal , I., Phthalocyanines as Photodynamic Sensitizers. *Photochemistry and Photobiology* **1991,** *53* (6), 859-870.

11. Dahlen, M. A., The Phthalocyanines A New Class of Synthetic Pigments and Dyes. *Industrial & Engineering Chemistry* **1939,** *31* (7), 839-847.

12. Sorokin, A. B., Phthalocyanine Metal Complexes in Catalysis. *Chem. Rev.* **2013,** *113* (10), 8152-8191.

13. Zagal, J. H.; Griveau, S.; Silva, J. F.; Nyokong, T.; Bedioui, F., Metallophthalocyanine-based molecular materials as catalysts for electrochemical reactions. *Coord. Chem. Rev.* **2010,** *254* (23), 2755-2791.

14. Yamaki, J. i.; Yamaji, A., Phthalocyanine Cathode Materials for Secondary Lithium Cells. *J. Electrochem. Soc.* **1982,** *129* (1), 5-9.

15. Oni, J.; Ozoemena, K. I., Phthalocyanines in batteries and supercapacitors. *J. Porphyrins Phthalocyanines* **2012,** *16* (07n08), 754-760.

16. Hunt, C.; Mattejat, M.; Anderson, C.; Sepunaru, L.; Ménard, G., Symmetric Phthalocyanine Charge Carrier for Dual Redox Flow Battery/Capacitor Applications. *ACS Appl. Energy Mater.* **2019,** *2*, 5391-5396.

17. Laurs, H.; Heiland, G., Electrical and optical properties of phthalocyanine films. *Thin Solid Films* **1987,** *149* (2), 129-142.

18. Leznoff, C. C.; Lever, A. B. P., *Phthalocyanines: Properties and Applications*. Wiley VCH: New York, NY, 1989.

19. McKeown, N. B.; B, M. K. N., *Phthalocyanine Materials: Synthesis, Structure and Function*. Cambridge University Press: 1998.

20. Hunt, C.; Peterson, M.; Anderson, C.; Chang, T.; Wu, G.; Scheiner, S.; Ménard, G., Switchable Aromaticity in an Isostructural Mn Phthalocyanine Series Isolated in Five Separate Redox States. *J. Am. Chem. Soc.* **2019,** *141* (6), 2604-2613.

21. Contakes, S. M.; Beatty, S. T.; Dailey, K. K.; Rauchfuss, T. B.; Fenske, D., π-Complexes of Phthalocyanines and Metallophthalocyanines. *Organometallics* **2000,** *19* (23), 4767-4774.

22. Lin, M.-J.; Wang, J.-D.; Chen, N.-S., Crystal Structure of Octaethyloxyphthalocyaninato Copper, the Overlap Affect on the Ring Skeleton Distortion. *Z. Anorg. Allg. Chem.* **2005,** *631* (8), 1352-1354.

23. Evans, D. F., 400. The determination of the paramagnetic susceptibility of substances in solution by nuclear magnetic resonance. *J. Chem. Soc.* **1959,** (0), 2003-2005.

24. Dale, B. W.; Williams, R. J. P.; Edwards, P. R.; Johnson, C. E., Mössbauer spectra of compounds containing iron(II) in strong-field tetragonal environments. *Transactions of the Faraday Society* **1968,** *64* (0), 620-629.

25. Bell, N. A.; Brooks, J. S.; Robinson, J. K.; Thorpe, S. C., Variable-temperature 57Fe Mössbauer studies of the α and β phases of iron phthalocyanine. *J. Chem. Soc., Faraday Trans.* **1998,** *94* (20), 3155-3159.

26. Assour, J. M.; Goldmacher, J.; Harrison, S. E., Electron Spin Resonance of Vanadyl Phthalocyanine. *J. Chem. Phys.* **1965,** *43* (1), 159-165.

27. Assour, J. M.; Kahn, W. K., Electron Spin Resonance of α- and β-Cobalt Phthalocyanine1a. *Journal of the American Chemical Society* **1965,** *87* (2), 207-212.

28. Assour, J. M., Solvent Effects on the Spin Resonance Spectra of Cobalt Phthalocyanine. *J. Am. Chem. Soc.* **1965,** *87* (21), 4701-4706.

29. Roberts, E. M.; Koski, W. S., Electron Spin Resonance of Copper Phthalocyanine. *J. Am. Chem. Soc.* **1961,** *83* (8), 1865-1867.

30. Zwart, J.; van Wolput, J. H. M. C., An E.S.R. study of the reaction of cobalt phthalocyanines with ammonia and dioxygen. *J. Mol. Catal.* **1979,** *5* (1), 51-64.

31. Lever, A. B. P.; Minor, P. C., Solvent dependence of phthalocyanine redox equilibria. *Advances in Molecular Relaxation and Interaction Processes* **1980,** *18* (2), 115-126.

32. Ozarowski, A.; Lee, H. M.; Balch, A. L., Crystal Environments Probed by EPR Spectroscopy. Variations in the EPR Spectra of CoII(octaethylporphyrin) Doped in Crystalline Diamagnetic Hosts and a Reassessment of the Electronic Structure of Four-Coordinate Cobalt(II). *J. Am. Chem. Soc.* **2003,** *125* (41), 12606-12614.

33. Abkowitz, M.; Monahan, A. R., ESR and electronic spectral investigation of the self-association of phthalocyanine dyes in solution. *J. Chem. Phys.* **1973,** *58* (6), 2281-2287.

34. Gouterman, M., Spectra of porphyrins. *Journal of Molecular Spectroscopy* **1961,** *6*, 138-163.

35. Gouterman, M., 1 - Optical Spectra and Electronic Structure of Porphyrins and Related Rings. In *The Porphyrins*, Dolphin, D., Ed. Academic Press: New York, 1978; Vol. III, pp 1-165.

36. Lever, A. B. P.; Pickens, S. R.; Minor, P. C.; Licoccia, S.; Ramaswamy, B. S.; Magnell, K., Charge-transfer spectra of metallophthalocyanines: correlation with electrode potentials. *Journal of the American Chemical Society* **1981,** *103* (23), 6800-6806.

37. Minor, P. C.; Gouterman, M.; Lever, A. B. P., Electronic spectra of phthalocyanine radical anions and cations. *Inorg. Chem.* **1985,** *24* (12), 1894-1900.

38. Ceulemans, A.; Oldenhof, W.; Gorller-Walrand, C.; Vanquickenborne, L. G., Gouterman's "four-orbital" model and the MCD spectra of high-symmetry metalloporphyrins. *Journal of the American Chemical Society* **1986,** *108* (6), 1155-1163.

39. Ghosh, A.; Gassman, P. G.; Almloef, J., Substituent Effects in Porphyrazines and Phthalocyanines. *Journal of the American Chemical Society* **1994,** *116* (5), 1932-1940.

40. Day, P. N.; Wang, Z.; Pachter, R., Calculation of the structure and absorption spectra of phthalocyanines in the gas-phase and in solution. *Journal of Molecular Structure: THEOCHEM* **1998,** *455* (1), 33-50.

41. P. Piet, D.; Danovich, D.; Zuilhof, H.; J. R. Sudhölter, E., Ionization potentials of porphyrins and phthalocyanines. A comparative benchmark study of fast improvements of Koopman's Theorem. *Journal of the Chemical Society, Perkin Transactions 2* **1999,** (8), 1653-1662.

42. Liao, M.-S.; Scheiner, S., Electronic structure and bonding in metal phthalocyanines, Metal=Fe, Co, Ni, Cu, Zn, Mg. *The Journal of Chemical Physics* **2001,** *114* (22), 9780-9791.

43. Liao, M.-S.; Kar, T.; Gorun, S. M.; Scheiner, S., Effects of Peripheral Substituents and Axial Ligands on the Electronic Structure and Properties of Iron Phthalocyanine. *Inorganic Chemistry* **2004,** *43* (22), 7151-7161.

44. De Lile, J. R.; Heine, T.; Zhou, S., Electronic structure and oxygen reduction on tunable [Ti(IV)Pc]2+ and Ti(II)Pc titanyl-phthalocyanines: A quantum chemical prediction. *Computational Materials Science* **2017,** *129*, 24-36.

45. Barthel, M.; Dini, D.; Vagin, S.; Hanack, M., An Easy Route for the Synthesis of New Axially Substituted Titanium(IV) Phthalocyanines. *Eur. J. Org. Chem.* **2002,** *2002* (22), 3756-3762.

46. Muthukumar, P.; Kim, H.-S.; Ku, K.-S.; Park, J. H.; Son, Y.-A., Synthesis, characterization and aggregation and fluorescence properties of novel highly soluble zinc phthalocyanines bearing tetrakis-4-(3-(piperidin-1-yl)phenoxy) with tetra and dodecachloro substituents. *Fibers and Polymers* **2016,** *17* (4), 553-559.

47. Hestand, N. J.; Spano, F. C., Expanded Theory of H- and J-Molecular Aggregates: The Effects of Vibronic Coupling and Intermolecular Charge Transfer. *Chem. Rev.* **2018,** *118* (15), 7069-7163.

48. Lever, A. B. P., The Phthalocyanines. In *Advances in Inorganic Chemistry and Radiochemistry*, Emeléus, H. J.; Sharpe, A. G., Eds. Academic Press: 1965; Vol. 7, pp 27-114.

49. Robertson, J. M.; Woodward, I., 37. An X-ray study of the phthalocyanines. Part III. Quantitative structure determination of nickel phthalocyanine. *Journal of the Chemical Society (Resumed)* **1937,** (0), 219-230.

50. Gardberg, A. S.; Doan, P. E.; Hoffman, B. M.; Ibers, J. A., Singly and Doubly Oxidized Phthalocyanine (pc) Rings: [Cu(pc)(ReO4)] and [Cu(pc)(ReO4)2]. *Angew. Chem. Int. Ed.* **2001,** *40* (1), 244-246.

51. Engel, M. K., 122 - Single-Crystal Structures of Phthalocyanine Complexes and Related Macrocycles. In *The Porphyrin Handbook*, Kadish, K. M.; Smith, K. M.; Guilard, R., Eds. Academic Press: Amsterdam, 2003; pp 1-242.

52. Cissell, J. A.; Vaid, T. P.; DiPasquale, A. G.; Rheingold, A. L., Germanium Phthalocyanine, GePc, and the Reduced Complexes SiPc(pyridine)2 and GePc(pyridine)2 Containing Antiaromatic π-Electron Circuits. *Inorganic Chemistry* **2007,** *46* (19), 7713-7715.

53. Konarev, D. V.; Kuzmin, A. V.; Faraonov, M. A.; Ishikawa, M.; Khasanov, S. S.; Nakano, Y.; Otsuka, A.; Yamochi, H.; Saito, G.; Lyubovskaya, R. N., Synthesis, Structures, and Properties of Crystalline Salts with Radical Anions of Metal-Containing and Metal-Free Phthalocyanines. *Chem. Eur. J.* **2015,** *21* (3), 1014-1028.

54. Wong, E. W. Y.; Walsby, C. J.; Storr, T.; Leznoff, D. B., Phthalocyanine as a Chemically Inert, Redox-Active Ligand: Structural and Electronic Properties of a Nb(IV)-Oxo Complex Incorporating a Highly Reduced Phthalocyanine(4−) Anion. *Inorganic Chemistry* **2010,** *49* (7), 3343-3350.

55. Wong, E. W. Y.; Leznoff, D. B., Synthesis and structural characterization of a magnesium phthalocyanine(3–) anion. *J. Porphyrins Phthalocyanines* **2012,** *16* (01), 154-162.

56. Ziolo, R. F.; Griffiths, C. H.; Troup, J. M., Crystal structure of vanadyl phthalocyanine, phase II. *J. Chem. Soc., Dalton Trans.* **1980,** (11), 2300-2302.

57. Chambrier, I.; J. Cook, M.; T. Wood, P., Conformationally stressed phthalocyanines: the non-planarity of the 1,4,8,11,15,18,22,25-octaisopentyl derivative. *Chem. Commun.* **2000,** (21), 2133-2134.

58. Kobayashi, N.; Fukuda, T.; Ueno, K.; Ogino, H., Extremely Non-Planar Phthalocyanines with Saddle or Helical Conformation: Synthesis and Structural Characterizations. *Journal of the American Chemical Society* **2001,** *123* (43), 10740-10741.

59. Mack, J.; Kobayashi, N., Low Symmetry Phthalocyanines and Their Analogues. *Chem. Rev.* **2011,** *111* (2), 281-321.

60. Fukuda, T.; Homma, S.; Kobayashi, N., Deformed Phthalocyanines: Synthesis and Characterization of Zinc Phthalocyanines Bearing Phenyl Substituents at the 1-, 4-, 8-, 11-, 15-, 18-, 22-, and/or 25-Positions. *Chem. Eur. J.* **2005,** *11* (18), 5205-5216.

61. Zhou, W.; Platel, R. H.; Teixeira Tasso, T.; Furuyama, T.; Kobayashi, N.; Leznoff, D. B., Reducing zirconium(iv) phthalocyanines and the structure of a Pc4-Zr complex. *Dalton Trans.* **2015,** *44* (31), 13955-13961.

62. Dar, T. A.; Tomar, R.; Mian, R. M.; Sankar, M.; Maurya, M. R., Vanadyl β-tetrabromoporphyrin: synthesis, crystal structure and its use as an efficient and selective catalyst for olefin epoxidation in aqueous medium. *RSC Advances* **2019,** *9* (18), 10405-10413.

63. Wang, H.; Sayed, S. Y.; Zhou, Y.; Olsen, B. C.; Luber, E. J.; Buriak, J. M., Water-soluble pH-switchable cobalt complexes for aqueous symmetric redox flow batteries. *Chemical Communications* **2020,** *56* (25), 3605-3608.

64. Wang, H.; Sayed, S. Y.; Luber, E. J.; Olsen, B. C.; Shirurkar, S. M.; Venkatakrishnan, S.; Tefashe, U. M.; Farquhar, A. K.; Smotkin, E. S.; McCreery, R.

L.; Buriak, J. M., Redox Flow Batteries: How to Determine Electrochemical Kinetic Parameters. *ACS Nano* **2020,** *14* (3), 2575-2584.

65. Zhou, W.; Thompson, J. R.; Leznoff, C. C.; Leznoff, D. B., The Redox-Active Chromium Phthalocyanine System: Isolation of Five Oxidation States from Pc4−CrI to Pc2−CrIII. *Chem. Eur. J.* **2017,** *23* (10), 2323-2331.

66. Lever, A. B. P.; Wilshire, J. P., Electrochemistry of iron phthalocyanine complexes in nonaqueous solvents and the identification of five-coordinate iron(I) phthalocyanine derivatives. *Inorg. Chem.* **1978,** *17* (5), 1145-1151.

67. Konarev, D. V.; Kuzmin, A. V.; Simonov, S. V.; Khasanov, S. S.; Lyubovskaya, R. N., Structure and optical properties of fullerene C60 complex with dipyridinated iron(II) phthalocyanine [Fe(II)Pc(C5H5N)2]·C60·4C6H4Cl2: First structure of bisaxially coordinated iron(II) phthalocyanine complex with acetonitrile Fe(II)Pc(CH3CN)2. *J. Porphyrins Phthalocyanines* **2014,** *18* (01n02), 87-93.

68. Compton, R. G.; Banks, C. E., *Understanding Voltammetry*. 2nd ed.; Imperial College Press: London, 2011.

69. Ma, W.; Wu, J.; Shen, C.; Tang, H.; Pan, M., Nickel phthalocyanine-tetrasulfonic acid as a promoter of methanol electro-oxidation on Pt/C catalyst. *J. Appl. Electrochem.* **2008,** *38* (6), 875-879.

70. Komorsky-Lovrić, Š., Voltammetry of microcrystals of cobalt and manganese phthalocyanines. *J. Electroanal. Chem.* **1995,** *397* (1), 211-215.

71. Zhong, J.-P.; Fan, Y.-J.; Wang, H.; Wang, R.-X.; Fan, L.-L.; Shen, X.-C.; Shi, Z.-J., Copper phthalocyanine functionalization of graphene nanosheets as support for platinum nanoparticles and their enhanced performance toward methanol oxidation. *J. Power Sources* **2013,** *242*, 208-215.

72. Korfhage, K. M.; Ravichandran, K.; Baldwin, R. P., Phthalocyanine-containing chemically modified electrodes for electrochemical detection in liquid chromatography/flow injection systems. *Anal. Chem.* **1984,** *56* (8), 1514-1517.

73. Mho, S.-i., Spectroelectrochemical Studies of Metallophthalocyanines Adsorbed on Electrode Surfaces. *J. Electrochem. Soc.* **1995,** *142* (5), 1436.

74. Zuo, X.; Zhang, H.; Li, N., An electrochemical biosensor for determination of ascorbic acid by cobalt (II) phthalocyanine–multi-walled carbon nanotubes modified glassy carbon electrode. *Sensors and Actuators B: Chemical* **2012,** *161* (1), 1074-1079.

75. Li, X.; He, X.; Chen, Y.; Fan, X.; Zeng, Q., Solid-state supramolecular chemistry of zinc tetraphenylporphyrin and zinc phthalocyanine with bis(pyridyl) ligands. *Journal of Molecular Structure* **2011,** *1002* (1), 145-150.

Chapter 3: Characterization of the Electrodeposition Behavior of a Cobalt Phthalocyanine Complex

3.1 Introduction

Phthalocyanines (Pcs) and their metalated analogues (MPcs) are a class of compounds that have demonstrated a high degree of versatility in their applications being used as dyes and pigments[1, 2], sensitizers in solar cells[3-12], molecular catalysts[13-17], and electrochemical sensors[18-21]. The ease of structural modification leading to the tuning of material properties, such as photochemical and electrochemical behavior, for Pcs has been a leading reason for their wide-spread utility with both the metal center identity[22, 23] and that of the substituents[24, 25] being significant. Of particular relevance are Pc-modified surfaces, which have been extensively studied for use in fuel cells[26-28], as electrochemical sensors[29-31] and as electrocatalysts[32-34]. Surface modification can be achieved through several experimental methods. Vacuum deposition has been used with unsubstituted Pcs[35, 36], offering precise control over the Pc film thickness and surface coverage; however, this method is limited to unsubstituted Pcs due to decomposition of substituted Pc macrocycles. For substituted Pcs solution processing of the Pc and electrode surface is preferred. Tethering the covalent attachment of a Pc to a surface through either its ring or axial substituents can create uniform self-assembled monolayers (SAMs) at the surface and has the advantage of stable dative interactions forming the basis of attachment; however, this method requires substituents capable of bonding to the surface thus limiting the scope of applicable Pcs.[23] The most common Pc-modified surfaces are carbon electrodes which typically rely on spontaneous formation of π-stacked Pc layers at the electrode surface enabling modification with a wide variety of substituted Pcs.[37] Finally, electrodeposition can be performed by repetitive scanning of a cyclic voltammogram allowing for the Pc to build up at the electrode surface.[38, 39] The ability of MPc complexes to functionalize electrodes through electrodeposition, particularly cobalt and iron

phthalocyanines, has been exploited in electrochemical sensing application.[40-42] A variety of PcCo complexes have been shown to engage in both oxidatively induced electrodeposition[41] and electropolymerization[43] . Previous work by our group[44] showed that octa-ethoxy substituted Pc complexes with late transition metals — **^{OEt}PcCo**, **^{OEt}PcNi**, and **^{OEt}PcCu** (**^{OEt}Pc** = 1,4,8,11,15,18,22,25-octaethoxy-Pc) — show interaction with the electrode surface upon oxidation in dichloromethane (DCM). Similar features with transient oxidative adsorption have been reported for other Pcs with oxygen-bearing substituents[45, 46] and the conditions of film formation have been shown to affect the electrochemical sensing ability of these modified electrodes[39]. Herein we describe the use of electrochemical methods to study the **^{OEt}PcCo** interaction with electrode surfaces to better understand the factors influencing the adsorption behavior and how this may be beneficial to the creation of modified electrode surfaces.

3.2 Results and Discussion

3.2.1 Fundamental Electrochemistry

As discussed in Chapter 2, the CV of **^{OEt}PcCo** shows one quasi-reversible reduction ($E_{1/2}$ = -0.88 V) that is metal based in character ($Co^{II} \rightarrow Co^{I}$) as well as two oxidative peaks $E_{1/2}$ = -0.10 V and 0.64 V) assigned to Pc oxidation ($Pc^{2-} \rightarrow Pc^{1-}$ and $Pc^{1-} \rightarrow Pc^{0}$). Comparing the effect of scan rate on the features reveals distinct changes between slow (5 mVs^{-1}, Fig. 3.1 (a)) and fast (750 mVs^{-1}, Fig. 3.1 (b)) scan rates. The first oxidation has a sharp return feature indicative of a non-diffusional response that broadens and decreases in its intensity relative to the other peaks as scan rate increases. The second oxidation appears surface bound at slow scan rates with a small peak to peak separation (17 mV) while at faster scan rates the second oxidation broadens with the return feature becoming difficult to distinguish. The reductive peak appears quasi-reversible and diffusional with a ratio of the cathodic peak current ($I_{p,c}$) to the anodic

peak current ($I_{p,a}$) being close to unity at slow scan rates while at faster scan rates the forward scan shows a broadening and an increase in the ratio of $I_{p,c}$ to $I_{p,a}$ to 2, indicating a more complex electron transfer mechanism.[46, 47] It is worth noting that the ring-based reductions of Pcs often show more reversibility than the oxidations due to the tendency of oxidized Pc species to aggregate; however, it is possible that in this case the oxidative adsorption is complicating the reductive events reversibiltiy.[48]

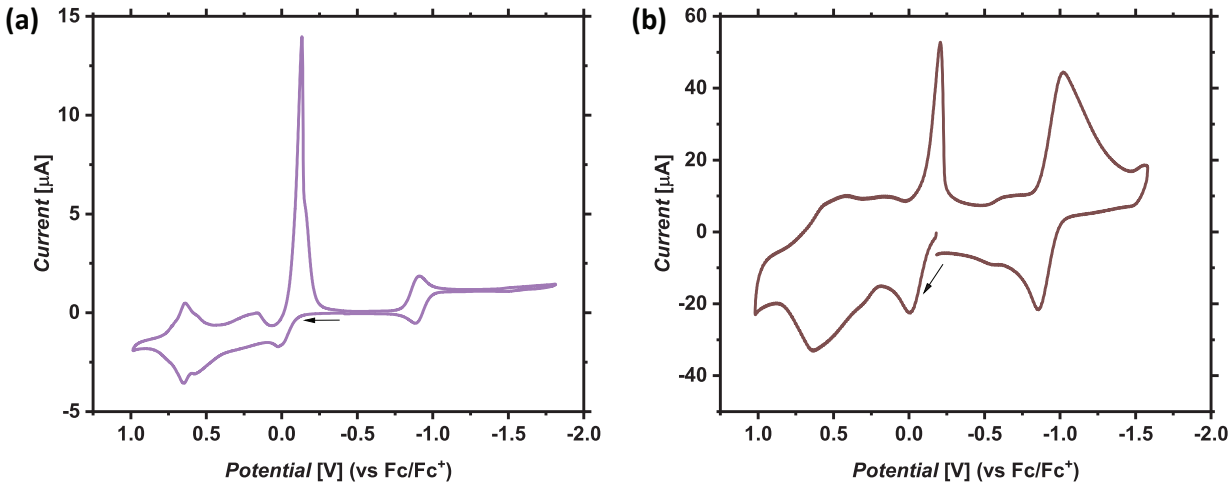

Figure 3.1: CV of ^{OEt}PcCo at (a) 0.005 V/s at a concentration of 0.52 mM in DCM (b) 0.750 V/s at a concentration of 0.58mM in DCM under N2 atmosphere with [NBu_4][PF_6] (0.1 M) supporting electrolyte, a 3 mm glassy carbon working electrode, Pt wire counter electrode, and a Pt wire pseudo-reference electrode. Internally referenced to ferrocene.

Variable scan rate data of **^{OEt}PcCo** in DCM (Fig. 3.2 (a)) was collected and investigated using the Randles-Ševčík equation. Due to the adsorptive nature of the first oxidation, a linear relationship between the peak current and the scan rate is expected. Instead, a linear relationship between the peak current and the square root of the scan rate is observed, as well as a non-zero intercept for the **[^{OEt}PcCo]$^+$ / [^{OEt}PcCo]** redox couple (Fig. 3.2 (b)). While this

is unexpected for a surface bound event, previous reports[45] have indicated similar dependence for other Pcs showing electrode adsorption. The interaction of ^{OEt}**PcCo** with the electrode surface were also investigated to determine both the diffusion coefficient (D) and the heterogeneous charge-transfer rate coefficient (k_0) through use of Randles-Ševčík[49] (Fig. 3.2 (b)) and Nicholson plots[50, 51] (Fig. 3.2 (c)) respectively.

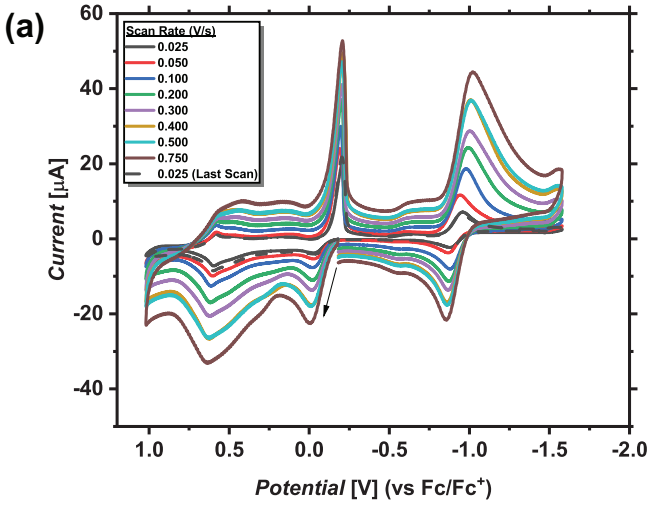
(a)
Scan Rate (V/s)
0.025
0.050
0.100
0.200
0.300
0.400
0.500
0.750
0.025 (Last Scan)
Current [μA]
Potential [V] (vs Fc/Fc+)

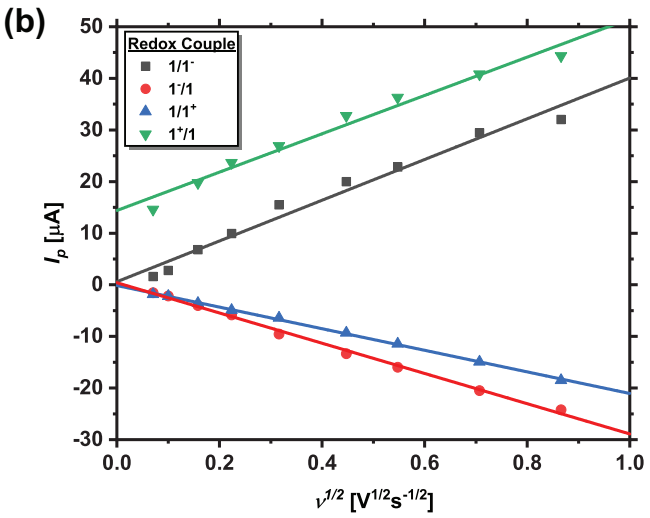
(b)
Redox Couple
1/1-
1-/1
1/1+
1+/1
Ip [μA]
ν1/2 [V1/2s-1/2]

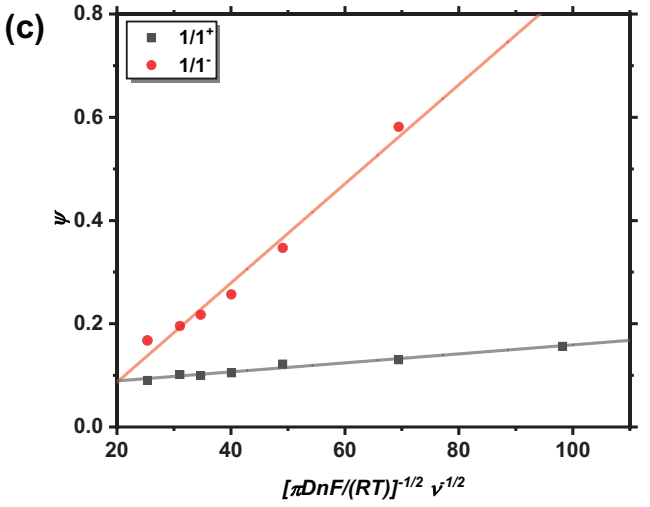
(c)
1/1+
1/1-
ψ
[πDnF/(RT)]-1/2 ν1/2

Figure 3.2: Fundamental electrochemical data. (a) Variable scan rate CV of ^{OEt}PcCo in DCM (0.58 mM) with [NBu_4][PF_6] (0.1 M) supporting electrolyte and using a 3 mm diameter glassy carbon working electrode, Pt wire counter electrode, and Pt wire pseudo-reference electrode. Internally referenced to ferrocene. (b) Randles-Ševčík plot for each redox event in ^{OEt}PcCo. (c) Nicholson plot for each redox event in ^{OEt}PcCo. See experimental section for fitting details.

The diffusion coefficient for each redox event as well the heterogeneous rate transfer coefficient match with literature values[52-54] (Table 3.1). These results indicate that there may be contributions of both adsorption and diffusional effects which have been reported before[45].

Species	**$D_{Randles-Ševčík}$ (cm^2 s^{-1})**	
[^{OEt}PcCo]$^+$	$2.33x10^{-5}$	
[^{OEt}PcCo]	$1.69x10^{-5}$	
[^{OEt}PcCo]$^-$	$1.45x10^{-5}$	
Redox Couple	**$E_{1/2}$ (V)**	**$k_{0\text{-Nicholson}}$ (cm s^{-1})**
[^{OEt}PcCo]⇌[^{OEt}PcCo]$^+$+e^-	-0.11	0.0008
[^{OEt}PcCo]+e^-⇌[^{OEt}PcCo]$^-$	-1.00	0.0096

Table 3.1: Relevant experimental physical parameters (D, k_0, and $E_{1/2}$) for ^{OEt}PcCo on a glassy working electrode. Full fitting data can be found in Tables 3.3 and 3.4.

To further probe the adsorption behavior, we tested the effect of electrode composition by changing from a glassy carbon to a platinum disk working electrode, collecting the variable scan rate data (Fig.3.3 (a)) and determining D (Fig. 3.3 (b)) and k_0 (Fig. 3.3 (c)).

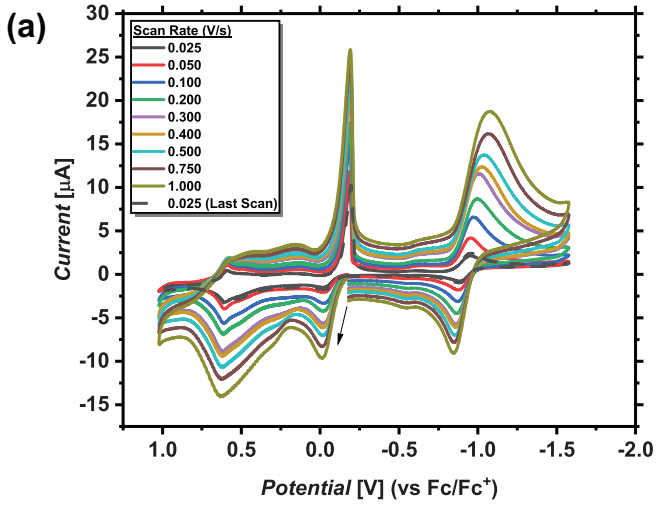
(a)
Scan Rate (V/s)
0.025
0.050
0.100
0.200
0.300
0.400
0.500
0.750
1.000
0.025 (Last Scan)
Current [μA]
Potential [V] (vs Fc/Fc+)

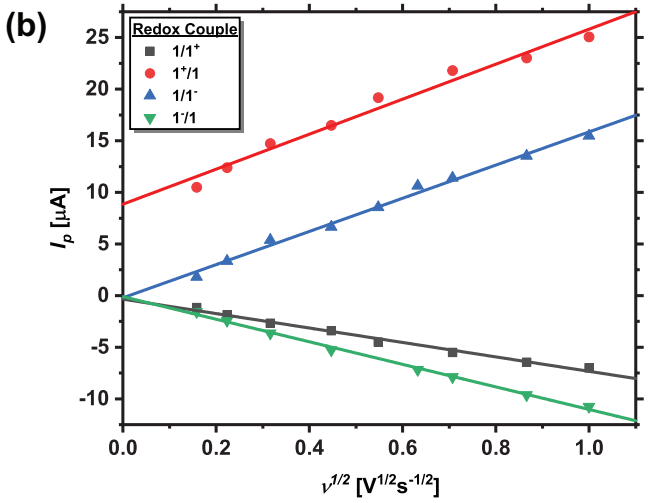
(b)
Redox Couple
1/1+
1+/1
1/1-
1-/1
Ip [μA]
ν1/2 [V1/2s-1/2]

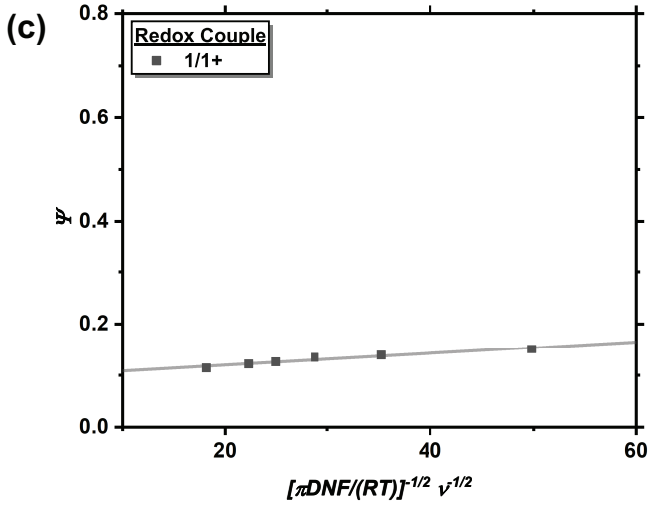
(c)
Redox Couple
1/1+
Ψ
[πDNF/(RT)]-1/2 ν1/2

Figure 3.3: Fundamental electrochemical data. (a) Variable scan rate CV of ^{OEt}PcCo in DCM (0.58 mM) with [NBu_4][PF_6] (0.1 M) supporting electrolyte and using a 1.5 mm diameter Pt disk working electrode, Pt wire counter electrode, and Pt wire pseudo-reference electrode. Internally referenced to ferrocene. (b) Randles-Ševčík plot for each redox event in ^{OEt}PcCo. (c) Nicholson plot for ^{OEt}PcCo. Fitting data can be found in the experimental section in Tables 3.3 and 3.4

Use of a platinum disk working electrode shows a similar response to that of the glassy carbon working electrode. The values for D are similar for all redox events and the values for k_0 are similar for the oxidative events however the k_0 for the reductive event on the Pt disk electrode was unable to be determined using the Nicholson method tehrefor it is not reported here (Table 3.2).

Species	**$D_{Randles-Ševčík}$ (cm^2 s^{-1})**	
$[^{OEt}PcCo]^+$	$3.68x10^{-5}$	
$[^{OEt}PcCo]$	$1.96x10^{-5}$	
$[^{OEt}PcCo]^-$	$1.51x10^{-5}$	
Redox Couple	**$E_{1/2}$ (V)**	**$k_{0\text{-Nicholson}}$ (cm s^{-1})**
$[^{OEt}PcCo] \rightleftharpoons [^{OEt}PcCo]^+ + e^-$	-0.10	0.0011
$[^{OEt}PcCo] + e^- \rightleftharpoons [^{OEt}PcCo]^-$	-0.94	-

Table 3.2: Relevant experimental physical parameters (D, k_0, and $E_{1/2}$) for ^{OEt}PcCo on Pt disk electrode. Full fitting data can be found in the experimental section in Tables 3.5 and 3.6.

Pcs have been shown to form π-π interactions one different carbon-based and metallic surfaces, however, the strength of the interactions depends on the surface identity.[39, 55, 56] These results indicate that the electrochemically induced interaction between the electrode and **^{OEt}PcCo** is similar for both the glassy carbon and platinum disk electrodes perhaps indicating that the adsorption response is primarily a function of the interaction between adjacent **^{OEt}PcCo** molecules. To investigate this we tested the effect of atmosphere on the electrochemical behavior as cobalt phthalocyanines are known axially ligate O_2.[57] This is reflected through the loss of the adsorption behavior in the CV of **^{OEt}PcCo** under an air atmosphere (Fig. 3.4 and Fig. 3.5(a)) with isolation of the first oxidation shows a more diffusional shape than was observed under N_2 atmosphere.

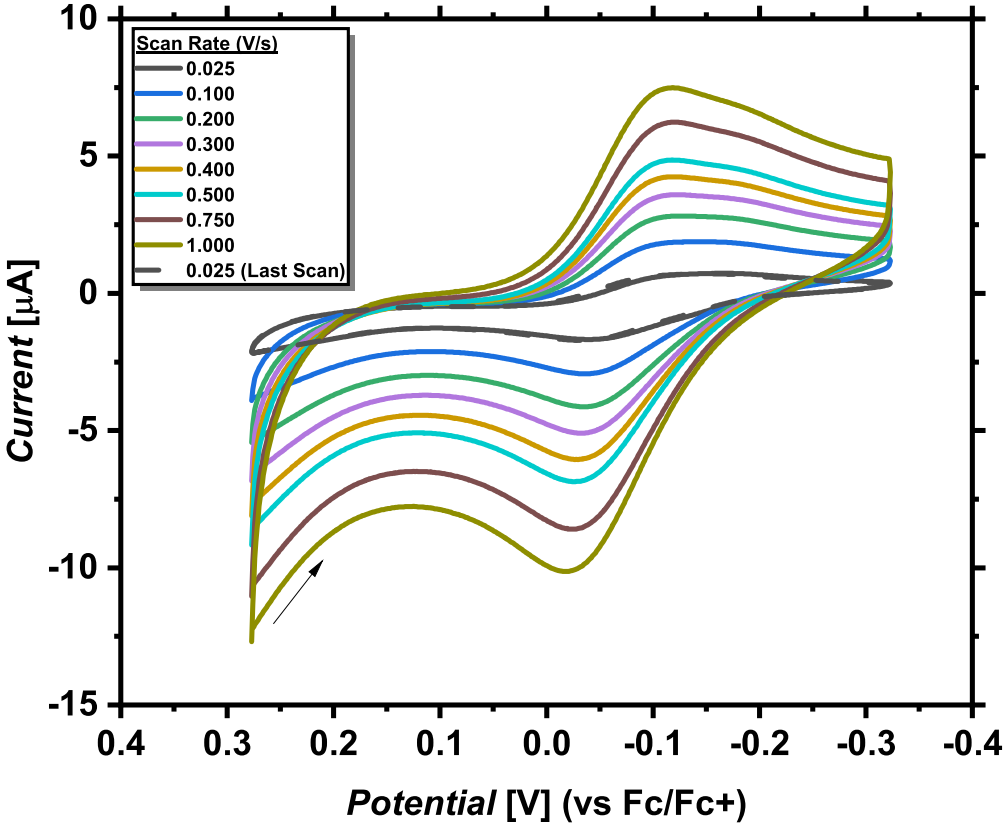

Figure 3.4: Variable scan rate CV the first oxidation of ^{OEt}PcCo (0.61 mM) in DCM under air atmosphere with [NBu_4][PF_6] (0. 1M) supporting electrolyte, a 3 mm glassy carbon working electrode, Pt wire counter electrode, and a Pt wire pseudo-reference electrode. Internally referenced to ferrocene.

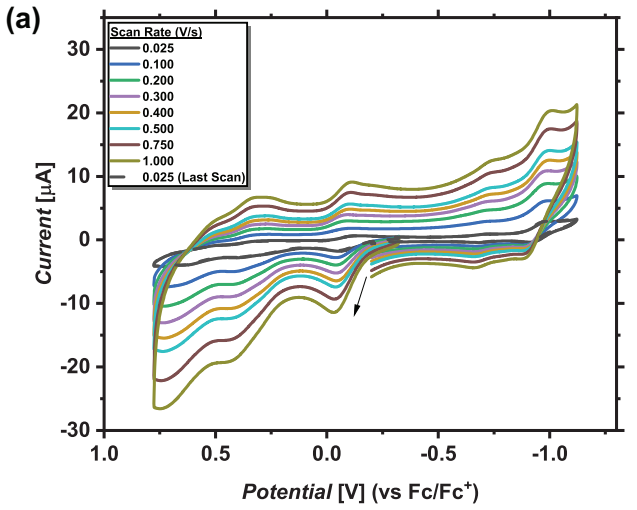
(a)
Scan Rate (V/s)
0.025
0.100
0.200
0.300
0.400
0.500
0.750
1.000
0.025 (Last Scan)
Current [μA]
Potential [V] (vs Fc/Fc+)

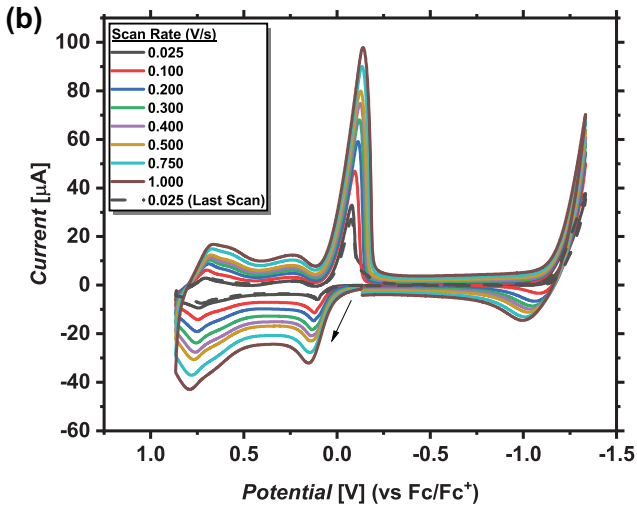
(b)
Scan Rate (V/s)
0.025
0.100
0.200
0.300
0.400
0.500
0.750
1.000
0.025 (Last Scan)
Current [μA]
Potential [V] (vs Fc/Fc+)

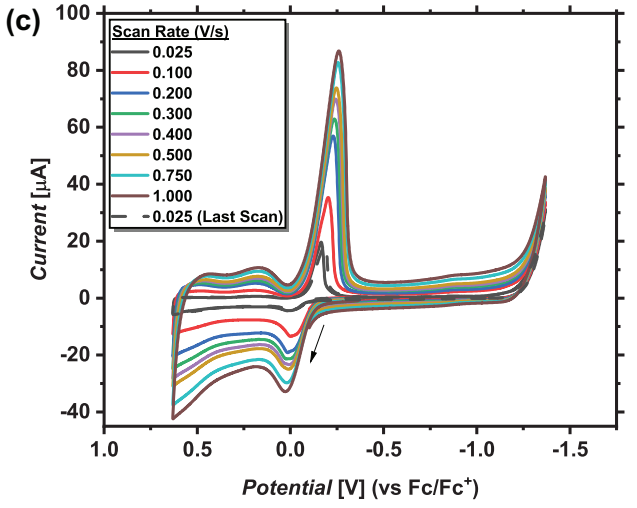
(c)
Scan Rate (V/s)
0.025
0.100
0.200
0.300
0.400
0.500
0.750
1.000
0.025 (Last Scan)
Current [μA]
Potential [V] (vs Fc/Fc+)

Figure 3.5: Variable scan rate CV of (a) ^{OEt}PcCo (0.61 mM) (b) ^{OEt}PcNi (0.61 mM) (c) ^{OEt}PcCu (0.69 mM) in DCM under air atmosphere with [NBu_4][PF_6] (0.1 M) supporting electrolyte, a 3 mm glassy carbon working electrode, Pt wire counter electrode, and a Pt wire pseudo-reference electrode. Internally referenced to ferrocene.

The coordination of O_2 axially may offer an explanation as to the reason for the change in peak shape as the axially coordination prevents **^{OEt}PcCo** π-stacking interactions. To further confirm, the CVs of **^{OEt}PcNi** (Fig. 3.5 (b)) and **^{OEt}PcCu** (Fig. 3.5 (c)), which exhibit the same adsorption response[44] but do not show a tendency to form O_2-coordinated complexes, were taken in air. Both complexes showed the adsorption features in inert and air atmospheres demonstrating that axial ligation is detrimental to the intermolecular interaction necessary for film formation.

3.2.2 Electrochemical Film Formation

To further probe film formation, the effect of electrochemical conditions was tested through two methods: repetitive scanning of the CV and pre-conditioning of the electrode at an oxidative potential followed linear sweep voltammetry (LSV). Electrolytic deposition is typically achieved through potentiodynamic methods by repetitive cycling of the potential over a CV; however, potentiostatic measurements have also been employed by holding at a specific potential for a known length of time.[41, 42] A solution of **^{OEt}PcCo** in DCM with [Bu_4N][PF_6] was cycled between +1 V to -2 V vs Fc/Fc^+ at 0.5 V s^{-1} during 500 potential cycles (Fig. 3.6).

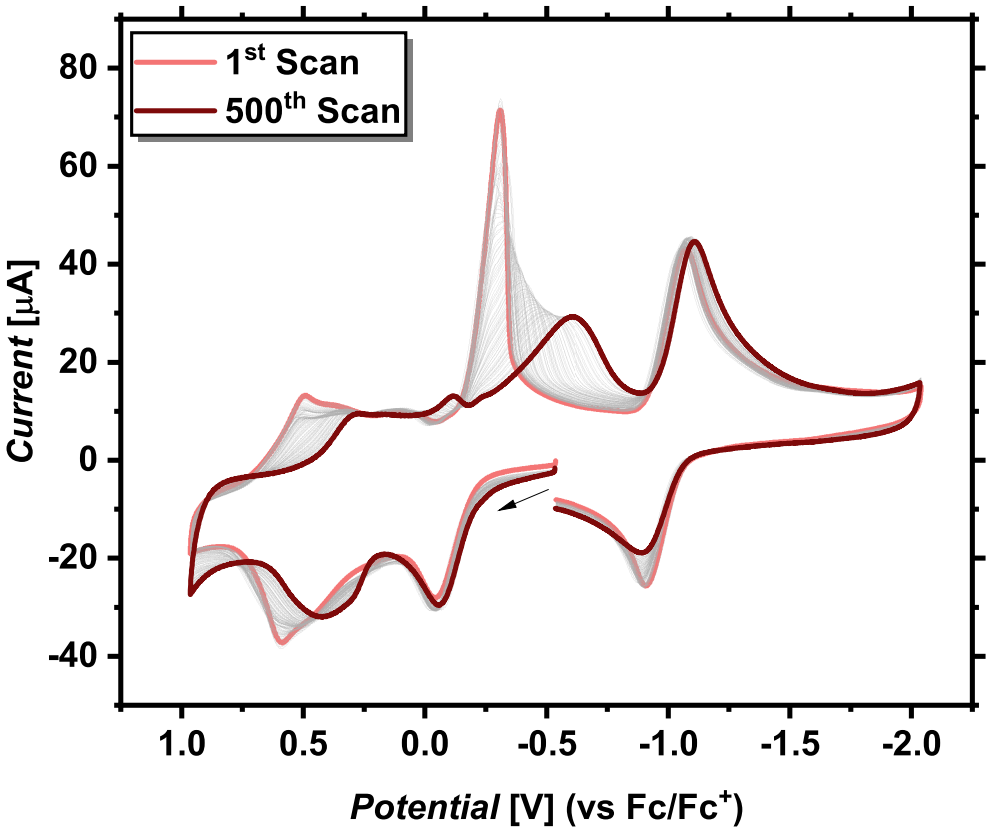

Figure 3.6: Every fifth scan of a multi-sweep CV of ^{OEt}PcCo (0.95 mM) of at 0.5 V/s with $[NBu_4][PF_6]$ (0.1 M) supporting electrolyte and using a 3 mm diameter glassy carbon working electrode, Pt wire counter electrode, and Pt wire pseudo-reference electrode. Internally referenced to ferrocene.

Over the course of the potential cycling the reduction peak at -1.0 V remained stable although the reverse wave did not show a decrease in the peak current over the course of the experiment. The cathodic wave of the first oxidative peak shifts by 0.3 V to a more negative potential with concurrent broadening over the course of the experiment. Similar peak broadening and shifts to more negative potentials are seen for the second oxidative event. **^{OEt}PcCo** demonstrates

both a shift in peak potential as well as the peak broadening, similar to what has been observed for electrodeposition of thiophene substituted Pcs, indicating this is indeed electrodeposition.[42]

Due to the seemingly oxidatively induced nature of the deposition process, LSV with a pre-conditioning step at an oxidative potential was employed to compare with the results obtained by potential cycling of the CV. Different pre-conditioning times were used to elucidate the effects of the oxidative potential hold. With no pre-conditioning applied to the electrode, variable scan rate LSV shows one distinct oxidative peak with a lower peak current than what is observed in the variable scan rate CV in addition to a more diffusional peak shape across all scan rates(Fig. 3.7(a))

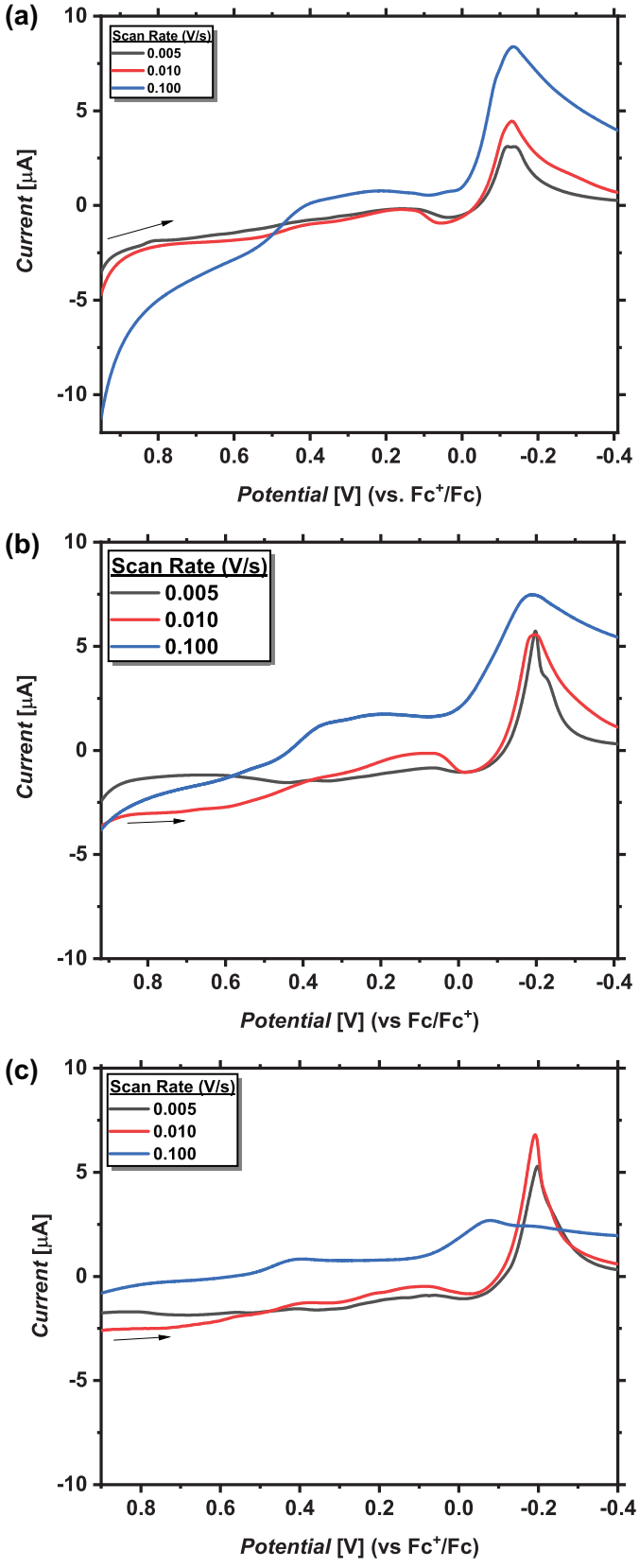
(a)
Scan Rate (V/s)
0.005
0.010
0.100
Current [μA]
Potential [V] (vs. Fc+/Fc)
(b)
Scan Rate (V/s)
0.005
0.010
0.100
Current [μA]
Potential [V] (vs Fc/Fc+)
(c)
Scan Rate (V/s)
0.005
0.010
0.100
Current [μA]
Potential [V] (vs Fc+/Fc)

Figure 3.7: Variable scan rate linear sweep voltammetry of ^{OEt}PcCo (0.56 mM) in DCM under N_2 atmosphere with [NBu_4][PF_6] (0.1 M) supporting electrolyte, a 3 mm glassy carbon working electrode, Pt wire counter electrode, and a Pt wire pseudo-reference electrode. Internally referenced to ferrocene. Preconditioning at 0.9 V for (a) 0 seconds (b) 10 seconds (c) 60 seconds.

Pre-conditioning time for 10 seconds at 0.9 V (Fig. 3.7 (b)) shows a sharp non-diffusional response with a shoulder at a scan rate of 5 mVs^{-1}. Increasing the scan rate to 10 mVs^{-1} and 100 mVs^{-1} shows peak broadening with the shoulder disappearing. A longer pre-conditioning time of 60 seconds at 0.9 V (Fig.3.7 (c)) shows a sharp non-diffusional response at both 5mVs^{-1} and 10 mVs^{-1} while at 100 mVs^{-1} the voltammogram has flattened with two new peaks appearing at more positive potentials. At slower scan rates (5 and 10 mVs^{-1}) the peak current increased with increasing pre-conditioning time while at a faster scan rate (100 mVs^{-1}) the peak current decreases with increasing scan rate (Fig. 3.8 (a)), consistent with what is observed during the potential cycling of the CV in which the oxidative peak current decreases over time. Widening the window reveals a current spike occurs at a potential similar to that of the reduction of **^{OEt}PcCo** for both 10 second and 60 second pre-conditioning times (Fig. 3.8 (b)), suggesting cathodic stripping of the **^{OEt}PcCo** that was deposited during pre-conditioning.

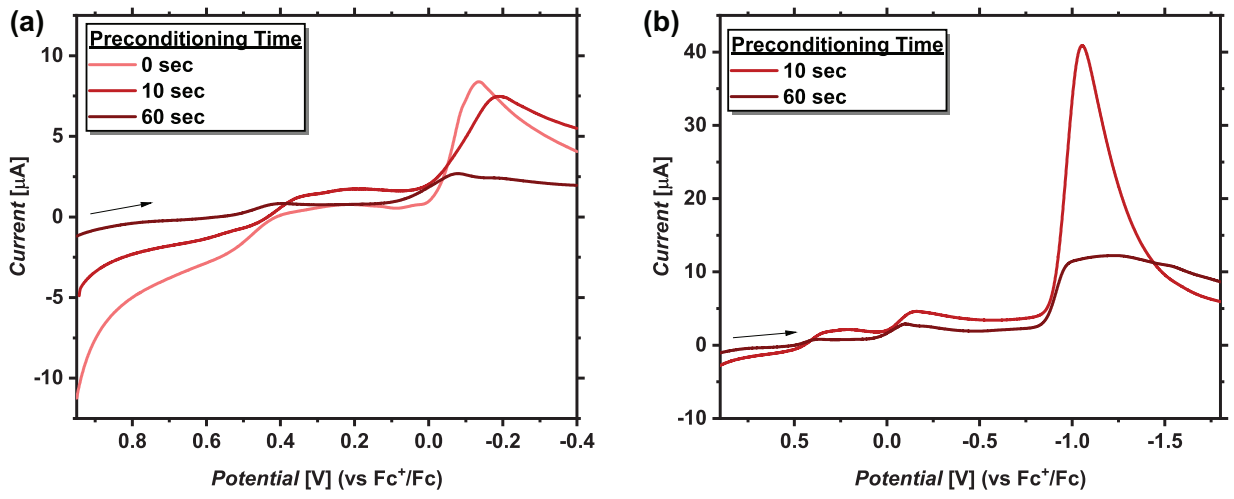

Figure 3.8: Comparison of linear sweep voltammetry of ^{OEt}PcCo (0.56 mM) with electrode preconditioning for different durations at 0.9 V with a scan rate of 0.100 V/s in DCM under N_2 atmosphere with [NBu_4][PF_6] (0.1 M) supporting electrolyte, a 3mm glassy carbon working electrode, Pt wire counter electrode, and a Pt wire pseudo-reference electrode. Internally referenced to ferrocene. Full data can be found in the experimental section.

Interestingly, the effect of scan rate after 60 seconds of pre-conditioning (Fig. 3.9) a similar trend to that shown in Fig. 3.6 is observed. At 5 mV s^{-1} and 10 mV s^{-1} a voltammogram similar what is observed in slow scan rates of the CV in Fig. 3.1 (a). While at scan rates above 100 mVs^{-1} two oxidative peaks that appear diffusional are seen and a spike is current response is seen beginning at -0.8 V

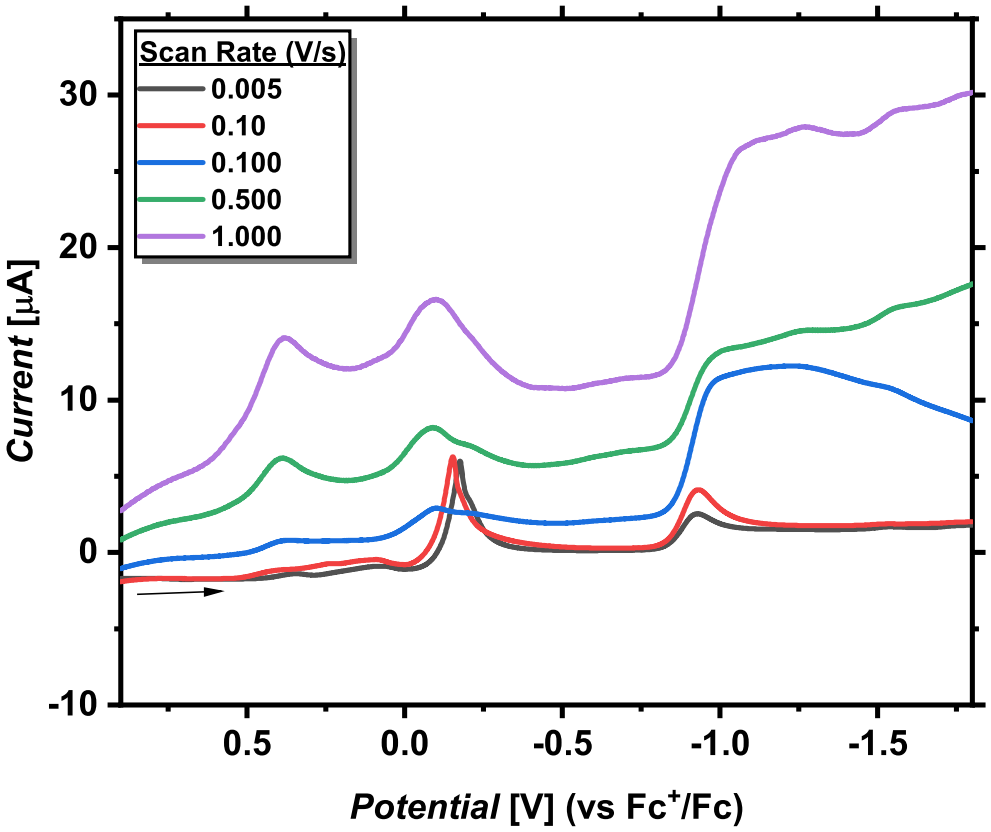

Figure 3.9: Variable scan rate linear sweep voltammetry with electrode preconditioning for 60 seconds at 0.9 V of ^{OEt}PcCo (0.50 mM) in DCM under N_2 atmosphere with $[NBu_4][PF_6]$ (0.1 M) supporting electrolyte, a 3mm glassy carbon working electrode, Pt wire counter electrode, and a Pt wire pseudo-reference electrode. Internally referenced to ferrocene.

This is a shift from the results obtained using potential cycling of the CV which showed no minimal changes in the reductive peak over the course of 500 sequential scans. Longer pre-conditioning time increase the coverage of the electrode surface with a layer of ^{OEt}PcCo that is unable to be fully removed on the timescale of the LSV experiment. The LSV results suggest

that the formation of a fully functionalized electrode can be achieved through pre-conditioning at oxidative potentials, offering a method of controlling film thickness through modification of the pre-conditioning times.

3.3 Summary

The fundamental electrochemical behavior of ^{OEt}PcCo and its implications on electrochemical film formation has been described here. Analysis of variable scan rate data showed that the adsorption behavior of **^{OEt}PcCo** is similar on both glassy carbon and platinum disk electrodes. The effect of oxygen was also tested, showing that in complexes capable of coordinating O_2, like **^{OEt}PcCo**, adsorption was impeded while in complexes that are not known to coordinate O_2, **^{OEt}PcNi** and **^{OEt}PcCu**, adsorption proceeded. Electrochemical film formation of **^{OEt}PcCo** on a glassy carbon electrode surface was then done both potentiodynamically and potentiostatically. These results showed that pre-conditioning the electrode surface by holding it at an oxidative potential was more effective for creation of ^{OEt}PcCo films, however, these results warrant further exploration as it is unclear whether this is the result of electrodeposition forming π-stacked films or a more complex electropolymerization reaction in which the ethoxy substituents participate. Raman and impedance spectroscopy of electrochemically formed films may help to elucidate this question. Testing of **^{OEt}PcCo** films and their ability to function as electrochemical sense as a function of the electrochemical parameters of formation also warrants further investigation.

3.4 Experimental

3.4.1 General Considerations

Techniques and Reagents. All air-free manipulations were performed under an atmosphere of dry, oxygen-free N_2 within an MBraun glovebox (MBRAUN UNIlab Pro SP Eco equipped

with a −40°C freezer), or by standard Schlenk techniques. Pentane, hexanes, benzene, diethyl ether, DCM, and THF (inhibitor-free) were dried and degassed on an MBraun Solvent Purification System and stored over activated 4 Å molecular sieves. All other solvents (chloroform, DMF) were degassed by freeze-pump-thaw and stored on activated 4 Å molecular sieves prior to use. Metal salts ($CoCl_2 \cdot 6H_2O$, $NiCl_2 \cdot 6H_2O$, and $CuCl_2$) were purchased from Strem Chemicals, Li metal, 2,3-dicyanohydroquinone from Acros Organics, and ethyl iodide from Alfa Aesar and all were used without further purification. All other reagents were obtained from Sigma-Aldrich, Fisher Scientific, or VWR and used without further purification. **^{EtO}PcCo**, **^{OEt}PcNi**, and **^{EtO}PcCu** were synthesized following our previous report.[58] Celite® and 4 Å molecular sieves were dried at 250 °C under dynamic vacuum (<0.1 Torr) for 24 h prior to use.

Electrochemical Measurements. CV was performed on a CH Instruments 630E Electrochemical Analysis Potentiostat. The working electrode was cleaned prior to each scan by sequentially polishing with a gradient of 1.0 μm, 0.3 μm, and 0.05 μm alumina (CH Instruments) on a cloth pad, followed by rinsing with distilled water and acetone. The Pt wire pseudo-reference and counter electrodes were rinsed with distilled water and acetone and heated white-hot with a butane torch. All measurements were performed on recrystallized product and referenced to the Fc/Fc^+ redox couple unless otherwise stated.

3.4.2 Syntheses

3,6-Diethoxyphthalonitrile. 3,6-Diethoxyphthalonitrile was synthesized using a modified literature procedure.[59, 60] A mixture of 2,3-dicyanohydroquinone (15.198 g, 94.9 mmol, 1 equiv) and K_2CO_3 (16.100 g, 116.5 mmol, 1.2 equiv) in 200 mL of wet acetone was sparged with N_2 for 20 minutes then heated to reflux under N_2. Ethyl iodide (13 mL, 479.8 mmol, 5.1

equiv) was then added dropwise to the mixture. The yellow slurry was stirred under reflux for 30 h. After cooling, 100mL of H_2O was added and stirred for 10 minutes. The slurry was filtered over a glass frit and washed successively with 500 mL of H_2O, 150 mL of EtOH, and 150 mL of Et_2O. The product was collected and dried under reduced pressure for 24 h, affording a white powder. Additional product could be recovered by evaporation of the eluent after the wash, and this additional product was similarly washed with H_2O, EtOH, and Et_2O. Yield: 11.659 g (56.8%). ^{1}H NMR (600 MHz, $CDCl_3$): δ 7.21 (s, 2H, *C_6H_2*.), 4.16 (q, *J* = 7.0 Hz, 4H, O*CH_2*CH_3), 1.48 (t, *J* = 7.0 Hz, 6H, OCH_2*CH_3*).

^{EtO}PcHLi. This compound was synthesized following our previously reported procedure.[60] Single crystals suitable for XRD studies were obtained by vapor diffusion of Et_2O into a concentrated solution of the product in DCM. ^{1}H NMR (600 MHz, CD_2Cl_2): δ 14.75 (s, 1H, NH), 7.57-7.52 (m, 8H, *C_6H_2*), 4.97-4.89 (m, 16H, O*CH_2*CH_3), 1.82-1.75 (m, 24H, OCH_2*CH_3*). λ_{max} (ε) = 723 nm (66,552 M^{-1} cm^{-1}), 783 nm (76,897 M^{-1} cm^{-1}). MS (MALDI-TOF): Calculated 873.18(M^+) Found 873.40 (M^+).

^{EtO}PcCo. In a nitrogen glovebox, ^{EtO}PcHLi (0.200 g, 0.23 mmol, 1 equiv), $CoCl_2$ (0.200 g, 0.84 mmol, excess), and $NaHCO_3$ (0.200 g, 2.3 mmol, excess) were combined in a pressure vessel with 15 mL of DMF and sealed with a Teflon cap. The resulting mixture was placed in a preheated oil bath at 165 °C for 4 h. The pressure vessel was then returned to the glovebox and opened under inert atmosphere. The mixture was filtered over a frit. The solid was washed successively with 150 mL of H_2O, 10 mL of EtOH, and 25 mL of Et_2O and subsequently collected and dried under reduced pressure. Yield: 0.204 g (96%). ^{1}H NMR (600 MHz, CD_2Cl_2): δ 9.89 (bs, *C_6H_2*), 7.30 (bs, O*CH_2*CH_3), 3.39 (bs, OCH_2*CH_3*). λ_{max} (ε) = 738 nm. MS (MALDI-TOF): Calculated 923.29 (M^+) Found 923.40 (M^+).

^{EtO}PcNi. In a nitrogen glovebox, ^{EtO}PcHLi (0.208 g, 0.24 mmol, 1 equiv), $NiCl_2 \cdot 6H_2O$ (0.200 g, 0.84 mmol, excess), and $NaHCO_3$ (0.200 g, 2.3 mmol, excess) were combined in a pressure vessel with 15 mL of DMF and sealed with a Teflon cap. The resulting mixture was placed in a preheated oil bath at 165 °C for 4 h. The pressure vessel was then returned to the glovebox and opened under inert atmosphere. The mixture was filtered over a frit. The solid was washed successively with 150 mL of H_2O, 10 mL of EtOH, and 25 mL of Et_2O and subsequently collected and dried under reduced pressure. Yield: 0.230 g (>100% (excluding co-crystallized CH_2Cl_2); 88.24% (including co-crystallized CH_2Cl_2)). ^{1}H NMR (600 MHz, CD_2Cl_2): δ 7.54 (s, 8H, C_6H_2), 4.83 (q, J = 7.0 Hz, 16H, O$CH_2$$CH_3$), 1.75 (t, J = 7.0 Hz, 24H, OCH$_2$$CH_3$). λ_{max} (ε) = 742 nm. MS (MALDI-TOF): Calculated 922.29 (M^+) Found 923.40 ($M\text{-}H^+$).

^{EtO}PcCu. In a nitrogen glovebox, ^{EtO}PcHLi (0.207 g, 0.24 mmol, 1 equiv), $CuCl_2$ (0.161 g, 1.20 mmol, 5 equiv), and $NaHCO_3$ (0.107 g, 1.27 mmol, 5.3 equiv) were combined in a pressure with 10 mL of DMF, and the resulting mixture was heated to 165 °C for 20 h. H_2O (80 mL) was then added and the solution was stirred for 30 mins, and subsequently filtered through a glass frit, leaving a dark green solid. The solid was washed successively with 100 mL of H_2O and 20 mL of EtOH and subsequently collected and dried under reduced pressure. Yield: 0.091 g (41.4%). ^{1}H NMR (600 MHz, CD_2Cl_2): δ 4.58 (bs, 16H), δ 1.61 (bs, 24H). λ_{max} (ε) = 750 nm. MS (MALDI-TOF): Calculated 927.29 (M^+) Found 927.40 (M^+).

3.4.3 Electrochemistry Data

Redox Couple	Slope ($As^{1/2}V^{-1/2}$)	R^2	Diffusion Coefficient (cm^2s^{-1})
1/1+	2.10E-05	0.999	7.47E-06
1+/1	3.71E-05	0.976	2.33E-05

1/1-	3.95E-05	0.976	2.64E-05
1-/1	2.93E-05	0.997	1.45E-05

Table 3.3: Data for the Randles-Ševčík fitting of ^{OEt}PcCo with a 3mm GC working electrode.

^{OEt}PcCo Redox Couple	Slope	R^2
1/1+	0.0008	0.972
1/1-	0.0096	0.980

Table 3.4: Data for the Nicholson analysis fitting of ^{OEt}PcCo with a 3mm GC working electrode.

Redox Couple	Slope ($As^{1/2}V^{-1/2}$)	R^2	Diffusion Coefficient (cm^2s^{-1})
1/1+	6.99E-06	0.988	6.21E-06
1+/1	1.70E-05	0.978	3.68E-05
1/1-	1.61E-05	0.992	3.30E-05
1-/1	1.09E-05	0.996	1.51E-05

Table 3.5: Data for the Randles-Ševčík fitting of ^{OEt}PcCo with a 1.5mm diameter Pt disk working electrode.

^{OEt}PcCo Redox Couple	Slope	R^2
1/1+	0.0011	0.946

1/1-	0.0156	0.976

Table 3.6: Data for the Nicholson analysis fitting of ^{OEt}PcCo with a 1.5mm diameter Pt disk working electrode.

3.5 References

1. Dahlen, M. A., The Phthalocyanines A New Class of Synthetic Pigments and Dyes. *Industrial & Engineering Chemistry* **1939,** *31* (7), 839-847.

2. Topuz, B. B.; Gündüz, G.; Mavis, B.; Çolak, Ü., Synthesis and characterization of copper phthalocyanine and tetracarboxamide copper phthalocyanine deposited mica-titania pigments. *Dyes and Pigments* **2013,** *96* (1), 31-37.

3. Yanagi, H.; Chen, S.; Lee, P. A.; Nebesny, K. W.; Armstrong, N. R.; Fujishima, A., Dye-Sensitizing Effect of TiOPc Thin Film on n-TiO2 (001) Surface. *The Journal of Physical Chemistry* **1996,** *100* (13), 5447-5451.

4. Giribabu, L.; Vijay Kumar, C.; Gopal Reddy, V.; Yella Reddy, P.; Srinivasa Rao, C.; Jang, S.-R.; Yum, J.-H.; Nazeeruddin, M. K.; Grätzel, M., Unsymmetrical alkoxy zinc phthalocyanine for sensitization of nanocrystalline TiO2 films. *Sol. Energy Mater. Sol. Cells* **2007,** *91* (17), 1611-1617.

5. Imahori, H.; Umeyama, T.; Ito, S., Large π-Aromatic Molecules as Potential Sensitizers for Highly Efficient Dye-Sensitized Solar Cells. *Acc. Chem. Res.* **2009,** *42* (11), 1809-1818.

6. Cid, J.-J.; García-Iglesias, M.; Yum, J.-H.; Forneli, A.; Albero, J.; Martínez-Ferrero, E.; Vázquez, P.; Grätzel, M.; Nazeeruddin, M. K.; Palomares, E.; Torres, T., Structure–Function Relationships in Unsymmetrical Zinc Phthalocyanines for Dye-Sensitized Solar Cells. *Chemistry – A European Journal* **2009,** *15* (20), 5130-5137.

7. Balraju, P.; Kumar, M.; Roy, M. S.; Sharma, G. D., Dye sensitized solar cells (DSSCs) based on modified iron phthalocyanine nanostructured TiO2 electrode and PEDOT:PSS counter electrode. *Synthetic Metals* **2009,** *159* (13), 1325-1331.

8. Ragoussi, M.-E.; Ince, M.; Torres, T., Recent Advances in Phthalocyanine-Based Sensitizers for Dye-Sensitized Solar Cells. *Eur. J. Org. Chem.* **2013,** *2013* (29), 6475-6489.

9. Kimura, M.; Nomoto, H.; Suzuki, H.; Ikeuchi, T.; Matsuzaki, H.; Murakami, T. N.; Furube, A.; Masaki, N.; Griffith, M. J.; Mori, S., Molecular Design Rule of Phthalocyanine Dyes for Highly Efficient Near-IR Performance in Dye-Sensitized Solar Cells. *Chemistry – A European Journal* **2013,** *19* (23), 7496-7502.

10. Martín-Gomis, L.; Fernández-Lázaro, F.; Sastre-Santos, Á., Advances in phthalocyanine-sensitized solar cells (PcSSCs). *Journal of Materials Chemistry A* **2014,** *2* (38), 15672-15682.

11. Ikeuchi, T.; Agrawal, S.; Ezoe, M.; Mori, S.; Kimura, M., Enhanced Charge Separation Efficiency in Pyridine-Anchored Phthalocyanine-Sensitized Solar Cells by Linker Elongation. *Chemistry – An Asian Journal* **2015,** *10* (11), 2347-2351.

12. Urbani, M.; Ragoussi, M.-E.; Nazeeruddin, M. K.; Torres, T., Phthalocyanines for dye-sensitized solar cells. *Coord. Chem. Rev.* **2019,** *381*, 1-64.

13. Loas, A.; Gerdes, R.; Zhang, Y.; Gorun, S. M., Broadening the reactivity spectrum of a phthalocyanine catalyst while suppressing its nucleophilic, electrophilic and radical degradation pathways. *Dalton Trans* **2011,** *40* (19), 5162-5.

14. Ma, W.; Wu, J.; Shen, C.; Tang, H.; Pan, M., Nickel phthalocyanine-tetrasulfonic acid as a promoter of methanol electro-oxidation on Pt/C catalyst. *Journal of Applied Electrochemistry* **2008,** *38* (6), 875-879.

15. Wu, Y.; Jiang, Z.; Lu, X.; Liang, Y.; Wang, H., Domino electroreduction of CO2 to methanol on a molecular catalyst. *Natur* **2019,** *575* (7784), 639-642.

16. Zagal, J. H.; Griveau, S.; Silva, J. F.; Nyokong, T.; Bedioui, F., Metallophthalocyanine-based molecular materials as catalysts for electrochemical reactions. *Coord. Chem. Rev.* **2010,** *254* (23), 2755-2791.

17. Zhang, X.; Wang, Y.; Gu, M.; Wang, M.; Zhang, Z.; Pan, W.; Jiang, Z.; Zheng, H.; Lucero, M.; Wang, H.; Sterbinsky, G. E.; Ma, Q.; Wang, Y.-G.; Feng, Z.; Li, J.; Dai, H.; Liang, Y., Molecular engineering of dispersed nickel phthalocyanines on carbon nanotubes for selective CO2 reduction. *Nature Energy* **2020,** *5* (9), 684-692.

18. Akyüz, D.; Koca, A., An electrochemical sensor for the detection of pesticides based on the hybrid of manganese phthalocyanine and polyaniline. *Sensors and Actuators B: Chemical* **2019,** *283*, 848-856.

19. Kalimuthu, P.; Sivanesan, A.; John, S. A., Fabrication of optochemical and electrochemical sensors using thin films of porphyrin and phthalocyanine derivatives. *Journal of Chemical Sciences* **2012,** *124* (6), 1315-1325.

20. Vanoni, C. R.; Winiarski, J. P.; Nagurniak, G. R.; Magosso, H. A.; Jost, C. L., A Novel Electrochemical Sensor Based on Silsesquioxane/Nickel (II) Phthalocyanine for the Determination of Sulfanilamide in Clinical and Drug Samples. *Electroanalysis* **2019,** *31* (5), 867-875.

21. Zuo, X.; Zhang, H.; Li, N., An electrochemical biosensor for determination of ascorbic acid by cobalt (II) phthalocyanine–multi-walled carbon nanotubes modified glassy carbon electrode. *Sensors and Actuators B: Chemical* **2012,** *161* (1), 1074-1079.

22. Mho, S. i.; Ortiz, B.; Park, S. M.; Ingersoll, D.; Doddapaneni, N., Spectroelectrochemical Studies of Metallophthalocyanines Adsorbed on Electrode Surfaces. *Journal of The Electrochemical Society* **1995,** *142* (5), 1436-1441.

23. Bedioui, F.; Griveau, S.; Nyokong, T.; John Appleby, A.; Caro, C. A.; Gulppi, M.; Ochoa, G.; Zagal, J. H., Tuning the redox properties of metalloporphyrin- and metallophthalocyanine-based molecular electrodes for the highest electrocatalytic activity in the oxidation of thiols. *Physical Chemistry Chemical Physics* **2007,** *9* (26), 3383-3396.

24. Kobayashi, N.; Ogata, H.; Nonaka, N.; Luk'yanets, E. A., Effect of Peripheral Substitution on the Electronic Absorption and Fluorescence Spectra of Metal-Free and Zinc Phthalocyanines. *Chemistry – A European Journal* **2003,** *9* (20), 5123-5134.

25. Li, R.; Zhang, X.; Zhu, P.; Ng, D. K. P.; Kobayashi, N.; Jiang, J., Electron-Donating or -Withdrawing Nature of Substituents Revealed by the Electrochemistry of Metal-Free Phthalocyanines. *Inorganic Chemistry* **2006,** *45* (5), 2327-2334.

26. Zhang, H.; Zhang, S.; Wang, Y.; Si, J.; Chen, Y.; Zhuang, L.; Chen, S., Boosting the Performance of Iron-Phthalocyanine as Cathode Electrocatalyst for Alkaline Polymer Fuel Cells Through Edge-Closed Conjugation. *ACS Applied Materials & Interfaces* **2018,** *10* (34), 28664-28671.

27. Jasinski, R., Cobalt Phthalocyanine as a Fuel Cell Cathode. *Journal of The Electrochemical Society* **1965,** *112* (5), 526.

28. Dursun, S.; Yazici, M. S., Mixed Carbon-Graphene Supports for Cobalt (II) Phthalocyanine as Fuel Cell Cathode. *ECS Journal of Solid State Science and Technology* **2020,** *9* (4), 041008.

29. Balan, I.; David, I. G.; David, V.; Stoica, A.-I.; Mihailciuc, C.; Stamatin, I.; Ciucu, A. A., Electrocatalytic voltammetric determination of guanine at a cobalt phthalocyanine modified carbon nanotubes paste electrode. *J. Electroanal. Chem.* **2011,** *654* (1), 8-12.

30. Lu, S.; Hummel, M.; Kang, S.; Gu, Z., Selective Voltammetric Determination of Nitrite Using Cobalt Phthalocyanine Modified on Multiwalled Carbon Nanotubes. *Journal of The Electrochemical Society* **2020,** *167* (4), 046515.

31. de Holanda, L. F.; Ribeiro, F. W. P.; Sousa, C. P.; da Silva Casciano, P. N.; de Lima-Neto, P.; Correia, A. N., Multi-walled carbon nanotubes–cobalt phthalocyanine modified electrode for electroanalytical determination of acetaminophen. *J. Electroanal. Chem.* **2016,** *772*, 9-16.

32. Cruz Moraes, F.; Cabral, M. F.; Machado, S. A. S.; Mascaro, L. H., Electrocatalytic Behavior of Glassy Carbon Electrodes Modified with Multiwalled Carbon Nanotubes and Cobalt Phthalocyanine for Selective Analysis of Dopamine in Presence of Ascorbic Acid. *Electroanalysis* **2008,** *20* (8), 851-857.

33. González-Gaitán, C.; Ruiz-Rosas, R.; Morallón, E.; Cazorla-Amorós, D., Relevance of the Interaction between the M-Phthalocyanines and Carbon Nanotubes in the Electroactivity toward ORR. *Langmuir* **2017,** *33* (43), 11945-11955.

34. Praats, R.; Käärik, M.; Kikas, A.; Kisand, V.; Aruväli, J.; Paiste, P.; Merisalu, M.; Sarapuu, A.; Leis, J.; Sammelselg, V.; Douglin, J. C.; Dekel, D. R.; Tammeveski, K., Electroreduction of oxygen on cobalt phthalocyanine-modified carbide-derived carbon/carbon nanotube composite catalysts. *J. Solid State Electrochem.* **2021,** *25* (1), 57-71.

35. Laurs, H.; Heiland, G., Electrical and optical properties of phthalocyanine films. *Thin Solid Films* **1987,** *149* (2), 129-142.

36. Yang, G.; Wang, Y.-L.; Xu, J.-J.; Lei, H.-W.; Chen, C.; Shan, H.-Q.; Liu, X.-Y.; Xu, Z.-X.; Fang, G.-J., A facile molecularly engineered copper (II) phthalocyanine as hole transport material for planar perovskite solar cells with enhanced performance and stability. *Nano Energy* **2017,** *31*, 322-330.

37. Mho, S.-i., Spectroelectrochemical Studies of Metallophthalocyanines Adsorbed on Electrode Surfaces. *Journal of The Electrochemical Society* **1995,** *142* (5), 1436.

38. Demir, E.; Silah, H.; Uslu, B., Phthalocyanine Modified Electrodes in Electrochemical Analysis. *Crit. Rev. Anal. Chem.* **2020**, 1-37.

39. Martin, C. S.; Gouveia-Caridade, C.; Crespilho, F. N.; Constantino, C. J. L.; Brett, C. M. A., Iron Phthalocyanine Electrodeposited Films: Characterization and Influence on Dopamine Oxidation. *The Journal of Physical Chemistry C* **2016,** *120* (29), 15698-15706.

40. Chohan, S.; Booysen, I. N.; Mambanda, A., Cobalt β-tetra(3-oxyflavone/2-(2-oxyphenyl)benzoxazole)phthalocyanines and their carbon nanotube conjugates: Formation, characterization and dopamine electrocatalysis. *Polyhedron* **2015,** *102*, 284-292.

41. Erdoğmuş, A.; Booysen, I. N.; Nyokong, T., Synthesis and electrochemical properties of new tetra substituted cobalt phthalocyanine complexes, and their application in electrode modification for the electrocatalysis of l-cysteine. *Synthetic Metals* **2011,** *161* (3), 241-250.

42. Osmanbaş, Ö. A.; Koca, A.; Özçeşmeci, İ.; Okur, A. İ.; Gül, A., Voltammetric, spectroelectrochemical, and electrocatalytic properties of thiol-derivatized phthalocyanines. *Electrochim. Acta* **2008,** *53* (15), 4969-4980.

43. Bayrak, R.; Akçay, H. T.; Bıyıklıoğlu, Z.; Değirmencioğlu, İ., Substituted phthalocyanines and their electropolymerization properties. *Synthetic Metals* **2016,** *220*, 643-652.

44. Peterson, M.; Hunt, C.; Wang, Z.; Heinrich, S. E.; Wu, G.; Ménard, G., Synthesis, characterization, and electrochemical properties of a first-row metal phthalocyanine series. *DTr* **2020,** *49* (45), 16268-16277.

45. Blakemore, J. D.; Hull, J. F.; Crabtree, R. H.; Brudvig, G. W., Aqueous speciation and electrochemical properties of a water-soluble manganese phthalocyanine complex. *DTr* **2012,** *41* (25), 7681-7688.

46. Sakamoto, K.; Ohno, E., Electrochemical characterization of soluble cobalt phthalocyanine derivatives. *Dyes and Pigments* **1998,** *37* (4), 291-306.

47. Nicholson, R. S.; Shain, I., Theory of Stationary Electrode Polarography. Single Scan and Cyclic Methods Applied to Reversible, Irreversible, and Kinetic Systems. *Analytical Chemistry* **1964,** *36* (4), 706-723.

48. Lever, A. B. P.; Milaeva, E. R.; Speier, G., The Redox Chemistry of Metallophthalocyanines in Solution. In *Phthalocyanines: properties and applications*, VCH: New York, NY, 1989; pp 1-69.

49. Zanello, P.; Royal Society of, C., *Inorganic electrochemistry : theory, practice and applications*. Royal Society of Chemistry: Cambridge, 2003.

50. Lavagnini, I.; Antiochia, R.; Magno, F., An Extended Method for the Practical Evaluation of the Standard Rate Constant from Cyclic Voltammetric Data. *Electroanalysis* **2004,** *16* (6), 505-506.

51. Nicholson, R. S., Theory and Application of Cyclic Voltammetry for Measurement of Electrode Reaction Kinetics. *Analytical Chemistry* **1965,** *37* (11), 1351-1355.

52. DeWulf, D. W.; Leland, J. K.; Wheeler, B. L.; Bard, A. J.; Batzel, D. A.; Dininny, D. R.; Kenney, M., Isolation, spectroscopic properties, and electrochemical properties of two oligomeric silicon phthalocyanines. *Inorganic Chemistry* **1987,** *26* (2), 266-270.

53. Yu, B.; Lever, A. B. P.; Swaddle, T. W., Electrochemistry of Metal Phthalocyanines in Organic Solvents at Variable Pressure. *Inorganic Chemistry* **2004,** *43* (14), 4496-4504.

54. Hunt, C.; Mattejat, M.; Anderson, C.; Sepunaru, L.; Ménard, G., Symmetric Phthalocyanine Charge Carrier for Dual Redox Flow Battery/Capacitor Applications. *ACS Applied Energy Materials* **2019,** *2* (8), 5391-5396.

55. Niu, T.; Si, N.; Zhou, D.; Zhou, M., Submolecular Imaging of Parallel Offset π–π Stacking in Nonplanar Phthalocyanine Bilayers. *The Journal of Physical Chemistry C* **2019,** *123* (12), 7178-7184.

56. Zhang, X.-F.; Shao, X., π–π binding ability of different carbon nano-materials with aromatic phthalocyanine molecules: Comparison between graphene, graphene oxide and carbon nanotubes. *Journal of Photochemistry and Photobiology A: Chemistry* **2014,** *278*, 69-74.

57. Zwart, J.; van Wolput, J. H. M. C., An E.S.R. study of the reaction of cobalt phthalocyanines with ammonia and dioxygen. *J. Mol. Catal.* **1979,** *5* (1), 51-64.

58. Peterson, M.; Hunt, C.; Wang, Z.; Heinrich, S. E.; Wu, G.; Ménard, G., Synthesis, characterization, and electrochemical properties of a first-row metal phthalocyanine series. *DTr* **2020**.

59. Contakes, S. M.; Beatty, S. T.; Dailey, K. K.; Rauchfuss, T. B.; Fenske, D., π-Complexes of Phthalocyanines and Metallophthalocyanines. *Organometallics* **2000,** *19* (23), 4767-4774.

60. Hunt, C.; Peterson, M.; Anderson, C.; Chang, T.; Wu, G.; Scheiner, S.; Ménard, G., Switchable Aromaticity in an Isostructural Mn Phthalocyanine Series Isolated in Five Separate Redox States. *J. Am. Chem. Soc.* **2019,** *141* (6), 2604-2613.

Chapter 4: Comparison of Differently Substituted Metallophthalocyanine Complexes for Use as Charge Carriers in a Slurry-based Redox Flow Battery

4.1 Introduction

Declining costs of renewable energy sources (i.e., solar), as well as targets projecting the need to drastically shift energy production away from fossil fuels to combat climate change have exploded interest in increasing the penetration of renewable energy sources in our grids; however, their inherent intermittency is a limiting factor in their continued growth.[1-4] Ambitious targets require modernization of our energy grid to appropriately deal with the issues associated with intermittent power sources. The creation and installation of new grid-scale electrical energy storage (EES) allows for the shift of renewable energy output during high production to times of high demand with high efficiency, high flexibility, and low cost. Redox flow batteries (RFBs) are often cited as one exciting technology meeting all of these goals for this application.[5-7] RFBs utilize dissolved charge-carriers that can be charged during times of high energy production by flowing past electrodes, stored separately in their charged states, and discharged by flowing back past the electrodes during times of high energy demand. This flow-based architecture has several advantages namely: simple design, long lifetimes, scalability, and decoupled energy density (dependent on tank size and charge-carrier concentration) and power density (dependent on flow rate and electrode surface area).[7] While small grid-scale installations of RFBs exist, there are several barriers to wide-spread adoption as a utility: cost, crossover capacity fade, and low energy density.[8]

To improve on these problems, several key parameters have been identified: moving to non-aqueous solvents, utilization of bipolar charge-carriers, and slurry-based RFB system.[9-12] In aqueous systems, the electrochemical window of water can limit the potential energy density of the system. Thus, moving towards cheap, non-toxic organic solvents presents an opportunity to increase the working electrochemical window, thereby increasing the energy density.[9, 10]

Bipolar charge-carrier molecules capable of being both oxidized and reduced, minimize crossover capacity fade, as well as the cost associated with expensive membranes needed to keep asymmetric charge carriers separated.[12] Slurry-based systems remove the need for soluble charge-carriers which can improve synthetic ease while also maintaining fast charge/discharge kinetics and improving energy density.[11]

Metal phthalocyanines (Pcs) have many desirable properties to address the problems presented. Pcs are macrocyclic compounds that are chemically robust, tunable through both peripheral substitution and metal coordination in the central cavity, and exhibit a wide variety of chemical and physical properties.[13, 14] Previously, we reported the use of ^{OEt}PcMnN as a charge carrier in both solution state cycling, as well as in the slurry-state by combining it with a conductive carbon additive, ketjen black (KB), in a hybrid RFB/capacitor system.[11] We also detailed the synthesis and characterization of a series of first-row transition metal **^{OEt}PcM** complexes (^{OEt}Pc = 1,4,8,11,15,18,22,25-octaethoxyphthalocyanine, M= VO, Cr, MnCl, MnN, Fe, Co, Ni, Cu, Zn) which indicated a tentative correlation between metal center identity and axial coordination with electrochemical behavior, described in Chapters 2-3.[15] From this series we identified several main candidates as potential charge carriers due to their interesting electrochemical profiles as well as synthetic simplicity, electrochemical reversibility (**^{OEt}PcVO**), and potentially advantageous Pc-surface interactions (**^{OEt}PcNi**). This design allowed us to circumvent the low solubility of Pcs in organic solvents – one of their main drawbacks – and to better understand the dynamics at play between the conductive carbon additive and the charge carriers. Additionally, it allowed us to elucidate the fact that full dissolution of the charge carrier was not necessary and to expand our charge carriers to commercially available, unsubstituted MPcs (**PcVO**, **PcFe**, and **PcNi**) to demonstrate cost

effective use of this system. Herein, we present a comparison of a series of metallophthalocyanines for validation as charge carriers in a slurry based RFB system, including the use of commercially available MPcs charge carriers.

4.2 Electrochemistry

Our initial investigation into a series of first-row **^{OEt}PcM** complexes revealed a correlation between metal center identity, axial coordination, and electrochemical behavior.[15] Therefor, we selected two common solvents used in non-aqueous RFBs,[10] dimethylformamide (DMF) and acetonitrile (ACN), to test the electrochemical behavior and stability of our ^{OEt}PcM complexes with the aim of elucidating solvent effects. We repetitively scanned the CV of **^{OEt}PcVO** and **^{OEt}PcNi** in ACN and DMF as well as DCM which we have previously used as our solvent for our electrochemical measurements[11, 15] (Fig. 4.1)

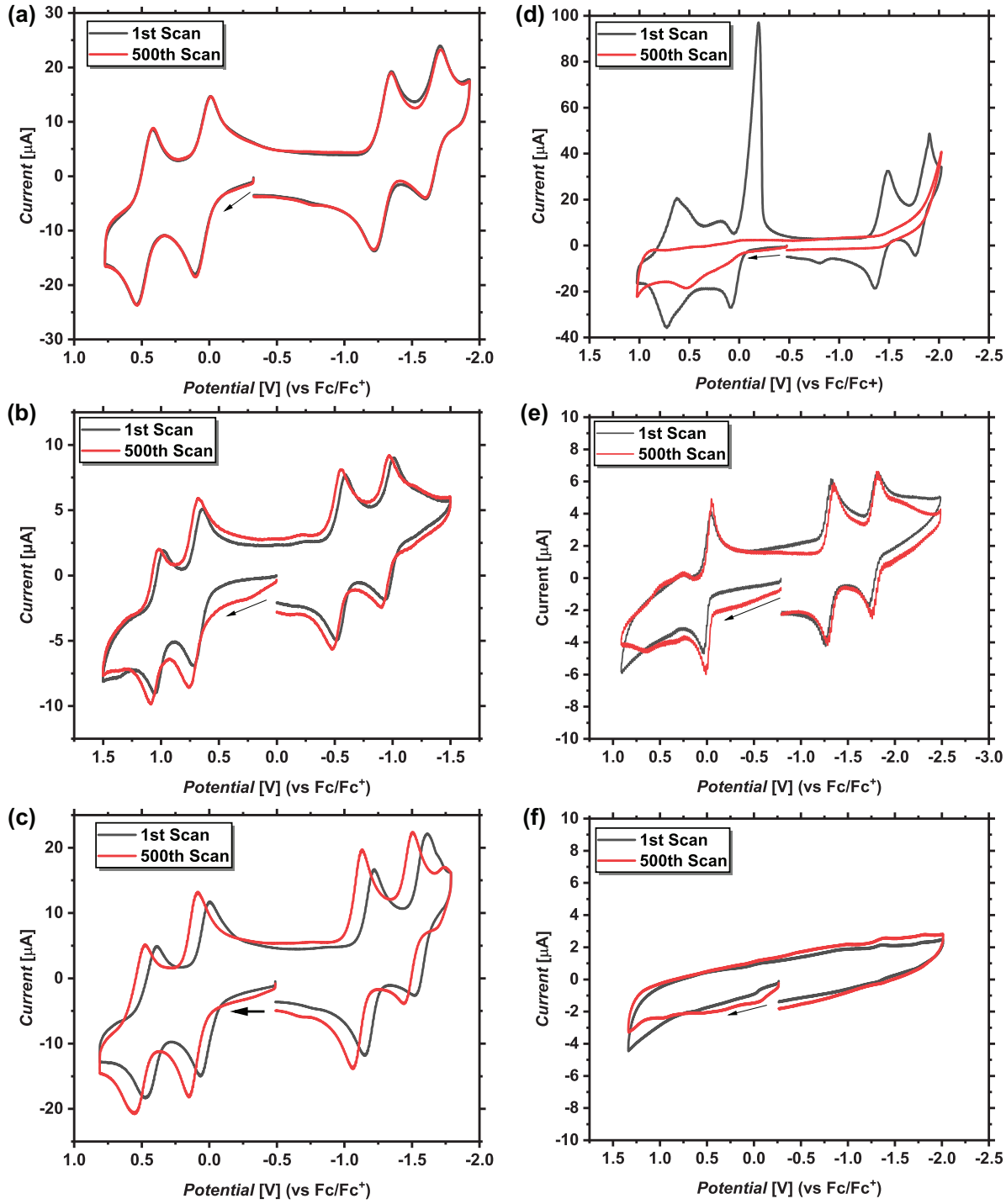

Figure 4.1: Multi-sweep CV at 0.5 V/s with $[NBu_4][PF_6]$ (0.1 M) supporting electrolyte and using a 3 mm diameter glassy carbon working electrode, Pt wire counter electrode, and Pt wire pseudo-reference electrode. Internally referenced to ferrocene. With the

following *OEtPcM* concentrations: (a) ^{OEt}PcVO in DCM (0.49mM) (b) ^{OEt}PcVO in DMF (0.52 mM) (c) ^{OEt}PcVO in ACN (0.49 mM) (d) ^{OEt}PcNi in DCM (0.54 mM) (e) ^{OEt}PcNi in DMF (0.5 2mM) (f) ^{OEt}PcNi in ACN (0.52 mM).

It is worth noting that the solubility of these complexes is high in chlorinated solvents such as chloroform or DCM, as well as more coordinating solvents such as DMF, but is lower in solvents such as ACN or tetrahydrofuran. Both complexes fully dissolve in DCM while the **^{OEt}PcVO** was sparingly soluble in both ACN and DMF and ^{OEt}PcNi was sparingly soluble in DMF and mostly insoluble in ACN. For **^{OEt}PcVO**, only minor shifts between the 1st and 500th scans appear in each solvent, which we attribute to shifts in the Pt wire pseudo-reference over the course of the experiment, matching with our previous results with **^{OEt}PcMnN** indicating that the capping axial ligands add extra stability. For the **^{OEt}PcNi**, the picture is a bit more complex with the scans in DMF showing little change while in DCM the peaks completely disappear over the course of the experiment. We posit that is this due to the formation of an increasingly thick layer of **^{OEt}PcNi** adsorbed to the electrode surface essentially forming an *in-situ* Pc-functionalized electrode.[16] Interestingly, this behavior is seen for both a Pt disk as well as a GC disk working electrode indicating this behavior of the **^{OEt}PcNi** is generalizable to many different surfaces (Fig. 4.2).

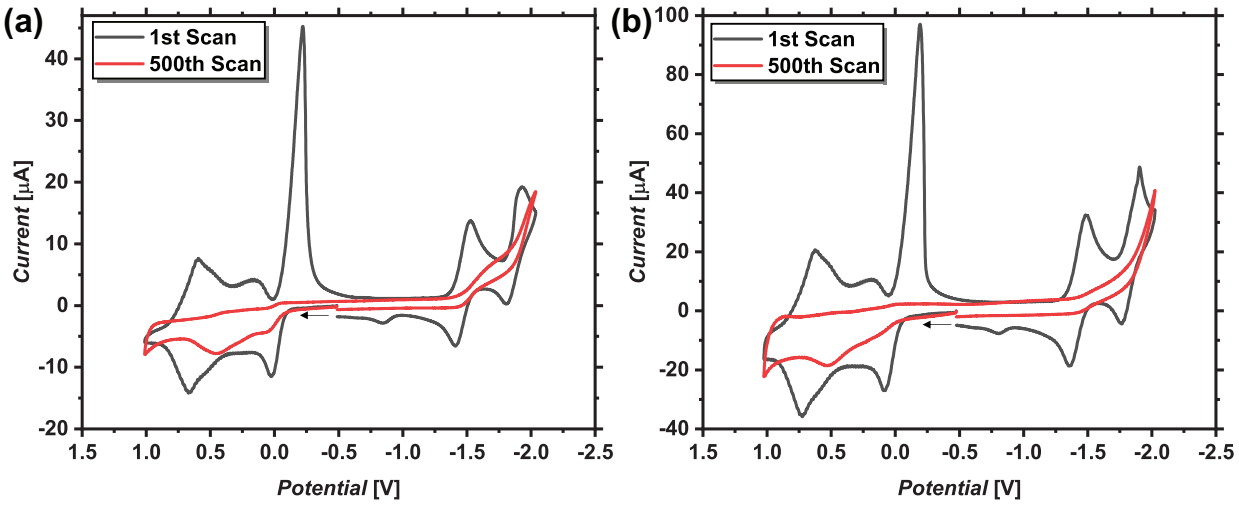

Figure 4.2: Multi-sweep CV at 0.5 V/s with $[NBu_4][PF_6]$ (0.1 M) supporting electrolyte, 0.54 mM ^{OEt}PcNi in DCM, using Pt wire counter electrode, and a Pt wire pseudo-reference electrode. Internally referenced to ferrocene. With the following working electrodes: (a) 1.5mm Pt disk electrode (b) 3mm glassy carbon.

Further study of this unique behavior can be seen in Chapter 3. This does further support the idea that in a less coordinating solvent such as DCM, intermolecular interactions between **^{OEt}PcNi** dominate and control the observed electrochemistry while in more coordinating solvents such as DMF there is a change in solvation that prevents these strong intermolecular interactions leading to better defined electrochemistry thus affecting its behavior as a charge carrier.

We continued our assessment of **^{OEt}PcVO** and **^{OEt}PcNi** as charge carriers by measuring key physical parameters that impact their utility: diffusion coefficients (D), heterogeneous rate transfer coefficients (k_0), and thermodynamic stability. D was investigated using the Randles-Ševčík equation (Eqn 4.1) for a reversible event.

Eqn 4.1: $I_p = 268600n^{3/2}AD^{1/2}Cv^{1/2}$

The variable scan rate data was then used to determine k_0 through use of Nicholson's[17] kinetic parameters and Lavagini's[18] numerical interpretation of Nicholson's working curve (Eqn 4.2)

Eqn 4.2: $\Psi = (-0.6288 + 0.0021\chi)/(1-0.017\chi) = k_0[\pi D n \nu F/(RT)]^{-1/2}$

The variable scan rate data as well as the Randles-Ševčík and Nicholson plots for **^{OEt}PcVO** can be found in Fig. 4.3. DCM was selected as the solvent for these experiments due to the higher solubility **^{OEt}PcVO** in DC relative to the other solvents.

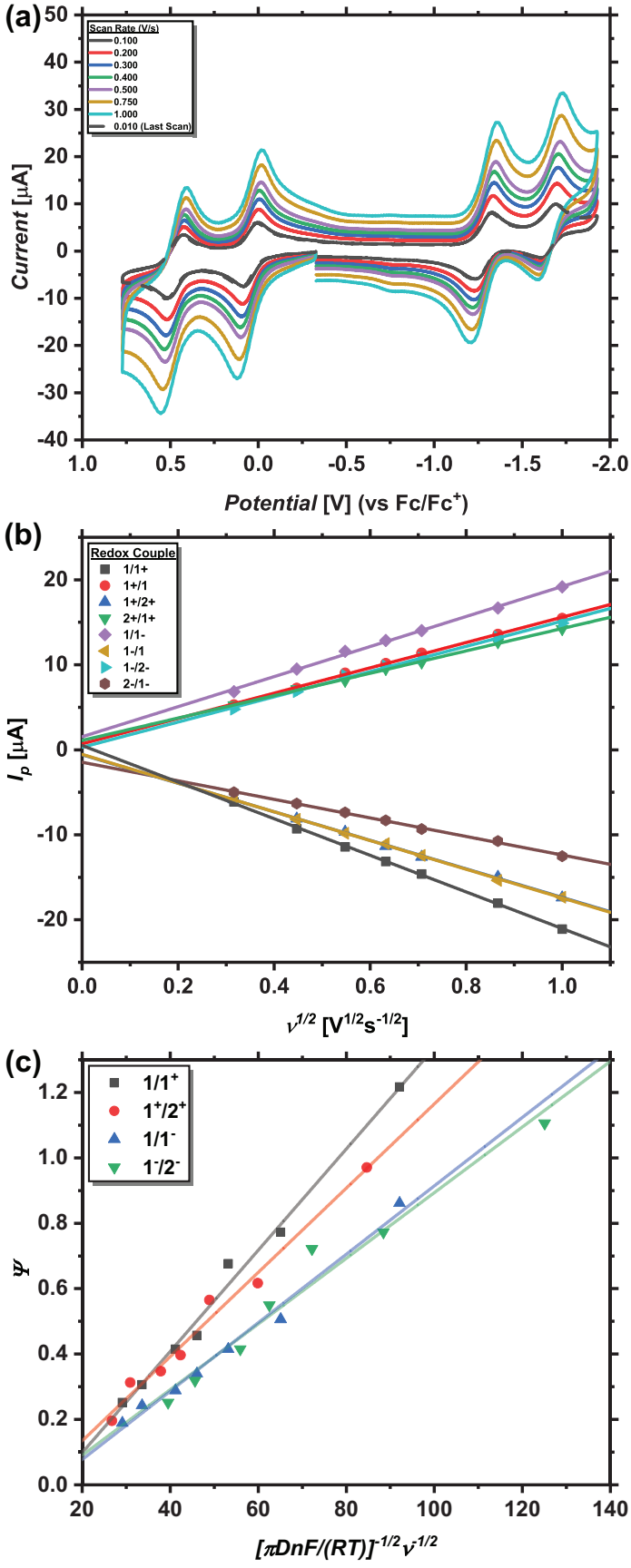
(a)
Scan Rate (V/s)
0.100
0.200
0.300
0.400
0.500
0.750
1.000
0.010 (Last Scan)
Current [μA]
Potential [V] (vs Fc/Fc+)
(b)
Redox Couple
1/1+
1+/1
1+/2+
2+/1+
1/1-
1-/1
1-/2-
2-/1-
Ip [μA]
ν1/2 [V1/2s-1/2]
(c)
1/1+
1+/2+
1/1-
1-/2-
χ
[πDnF/(RT)]-1/2ν1/2

Figure 4.3: Fundamental electrochemical data. (a) Variable scan rate CV of ^{OEt}PcVO in DCM (0.49mM) with [NBu_4][PF_6] (0.1M) supporting electrolyte and using a 3 mm diameter glassy carbon working electrode, Pt wire counter electrode, and Pt wire pseudo-reference electrode. Internally referenced to ferrocene. (b) Randles-Ševčík plot for each redox event in ^{OEt}PcVO. (c) Nicholson plot for each redox event in ^{OEt}PcVO. See Tables 4.3, 4.5, and 4.7 for fitting data.

The variable scan rate data as well as the Randles-Ševčík and Nicholson plots for **^{OEt}PcNi** can be found in Fig. 4.4. For the **^{OEt}PcNi** the lack of solubility in ACN and the lack of reversibility for the oxidations in DCM limited us to using the values from the quasi-reversible data in DMF to measure D and k_0.

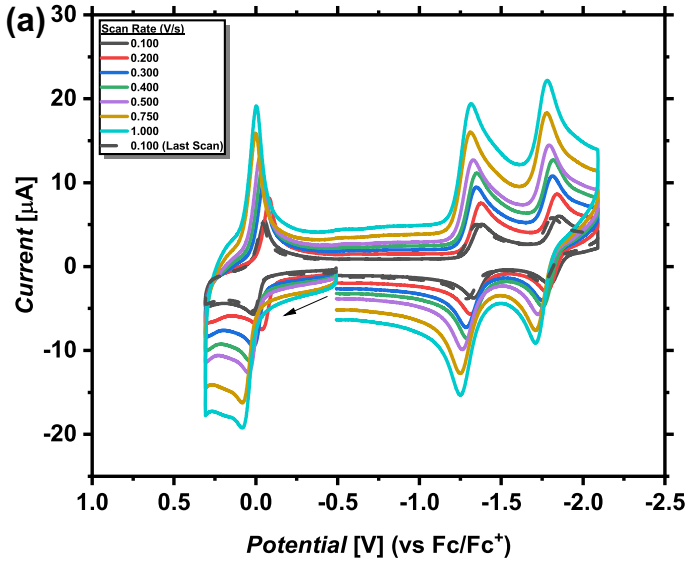
(a)
Scan Rate (V/s)
0.100
0.200
0.300
0.400
0.500
0.750
1.000
0.100 (Last Scan)
Current [μA]
Potential [V] (vs Fc/Fc+)

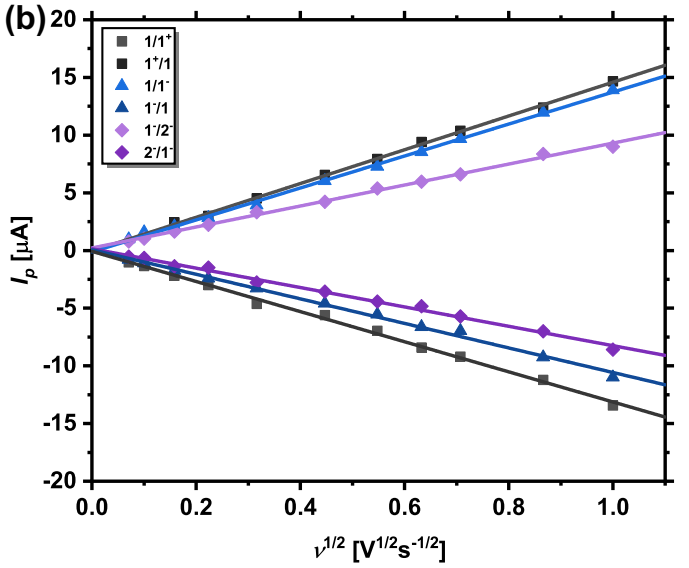
(b)
1/1+
1+/1
1/1-
1-/1
1-/2-
2-/1-
Ip [μA]
ν1/2 [V1/2s-1/2]

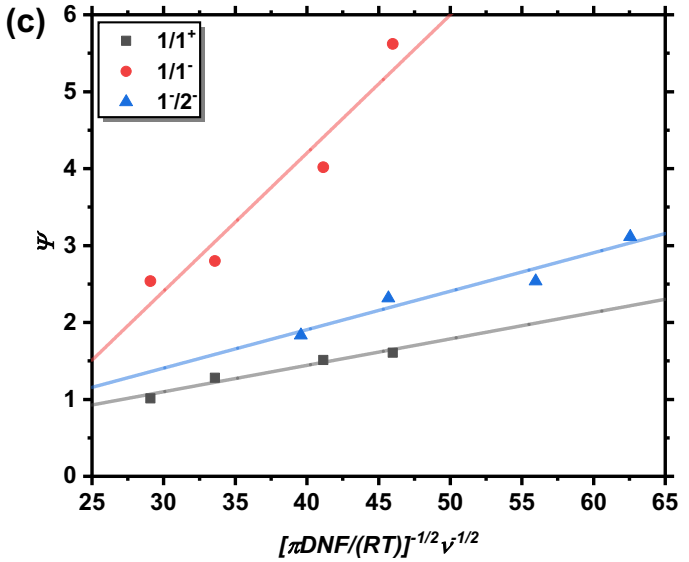
(c)
1/1+
1/1-
1-/2-
Ψ
[πDNF/(RT)]-1/2ν-1/2

Figure 4.*4*: Fundamental electrochemical data. (a) Variable scan rate CV of ^{OEt}PcNi in DMF (0.31mM) with [NBu_4][PF_6] (0.1M) supporting electrolyte and using a 3mm diameter glassy carbon working electrode, Pt wire counter electrode, and Pt wire pseudo-reference electrode. Internally referenced to ferrocene. (b) Randles-Ševčík plot for each redox event in ^{OEt}PcNi. (c) Nicholson plot for each redox event in ^{OEt}PcNi. See Tables 4.4, 4.6, and 4.8 for full fitting data.

The calculated values of D and k_0 for both **^{OEt}PcVO** and **^{OEt}PcNi** are shown in Table 4.1. The values of D and k_0 for both compounds are similar to other published Pcs[19, 20] and are sufficient for use as a charge carrier[21]. In addition to the favorable values of D and k_0, both offer wide voltage gaps with **^{OEt}PcNi** showing a one-electron transfer with a gap of 1.3 V while **^{OEt}PcVO** offers a two-electron transfer with a gap of 2.1 V.

Species	**$D_{Randles-Ševčík}$ (cm^2 s^{-1})**	
$[^{OEt}PcVO]^{2+}$	$3.72x10^{-6}$	
$[^{OEt}PcVO]^{+}$	$5.39x10^{-6}$	
$[^{OEt}PcVO]$	$8.28x10^{-6}$	
$[^{OEt}PcVO]^{-}$	$5.39x10^{-6}$	
$[^{OEt}PcVO]^{2-}$	$2.54x10^{-6}$	
$[^{OEt}PcNi]^{+}$	$1.14x10^{-5}$	
$[^{OEt}PcNi]$	$9.64x10^{-6}$	
$[^{OEt}PcNi]^{-}$	$5.23x10^{-6}$	
$[^{OEt}PcNi]^{2-}$	$3.76x10^{-6}$	
Redox Couple	**$E_{1/2}$ (V)**	**$k_{0\text{-Nicholson}}$ (cm s^{-1})**
$[^{OEt}PcVO]^{+} \rightleftharpoons [^{OEt}PcVO]^{2+} + e^{-}$	0.48	0.012

$[^{OEt}PcVO] \rightleftharpoons [^{OEt}PcVO]^{+} + e^{-}$	0.05	0.015
$[^{OEt}PcVO] + e^{-} \rightleftharpoons [^{OEt}PcVO]^{-}$	-1.28	0.010
$[^{OEt}PcVO]^{-} + e^{-} \rightleftharpoons [^{OEt}PcVO]^{2-}$	-1.65	0.010
$[^{OEt}PcNi] \rightleftharpoons [^{OEt}PcNi]^{+} + e^{-}$	-0.02	0.180
$[^{OEt}PcNi] + e^{-} \rightleftharpoons [^{OEt}PcNi]^{-}$	-1.32	0.050
$[^{OEt}PcNi]^{-} + e^{-} \rightleftharpoons [^{OEt}PcNi]^{2-}$	-1.79	0.034

Table 4.1: Relevant experimental physical parameters (D, k_0, and $E_{1/2}$) for ^{OEt}PcVO and ^{OEt}PcNi.

While the majority values for D and k_0 are similar to published results, the k_0 value for oxidation of **^{OEt}PcNi** is higher than expected, in addition to this discrepancy, the behavior of the oxidative peak **^{is}** not the same at all scan rates. While **^{OEt}PcVO** shows similar electrochemical behavior for all scan rates tested and maintains its quasi-reversibility (Fig. 4.5 (a)), **^{OEt}PcNi** shows a change in behavior at scan rates below 25 mV/s (Fig. 4.5 (b)). At a scan rate of 10 mV/s the cathodic wave of the first oxidation shows both the expected feature (at -0.05 V) and a new feature at a more negative potential (-0.14 V). Upon lowering the scan rate to 5mV/s there return feature seen at higher scan rates disappears and the return feature is now at -0.13 V.

(a)

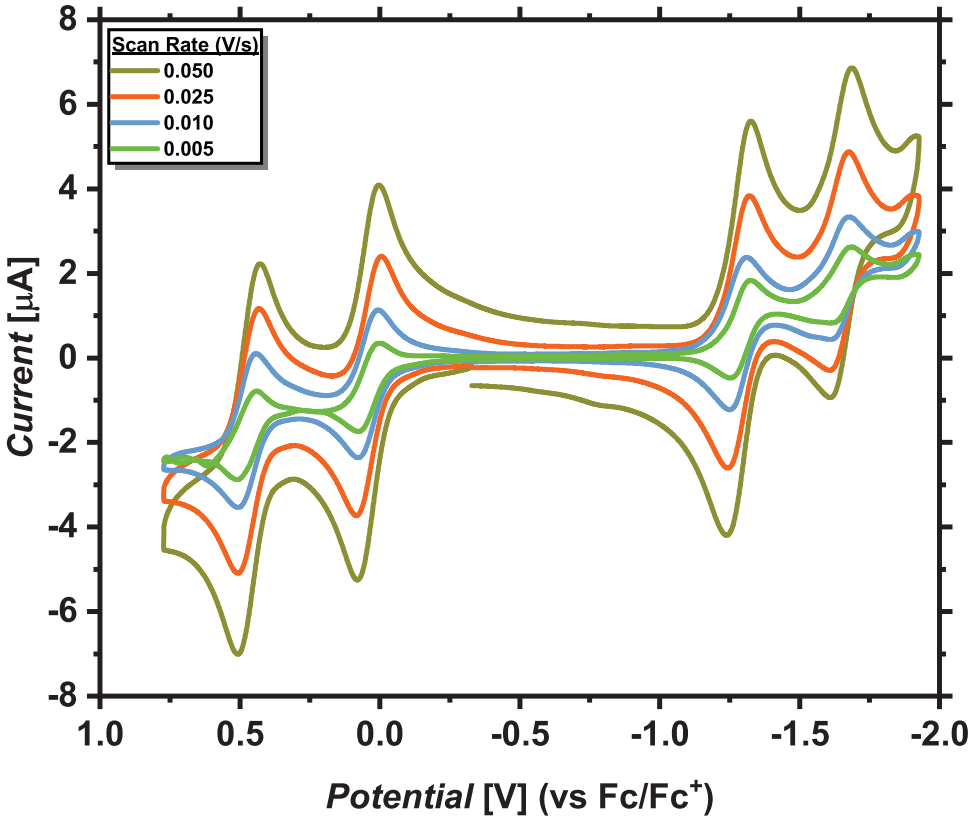
Scan Rate (V/s)
0.050
0.025
0.010
0.005
Current [μA]
Potential [V] (vs Fc/Fc+)

(b)

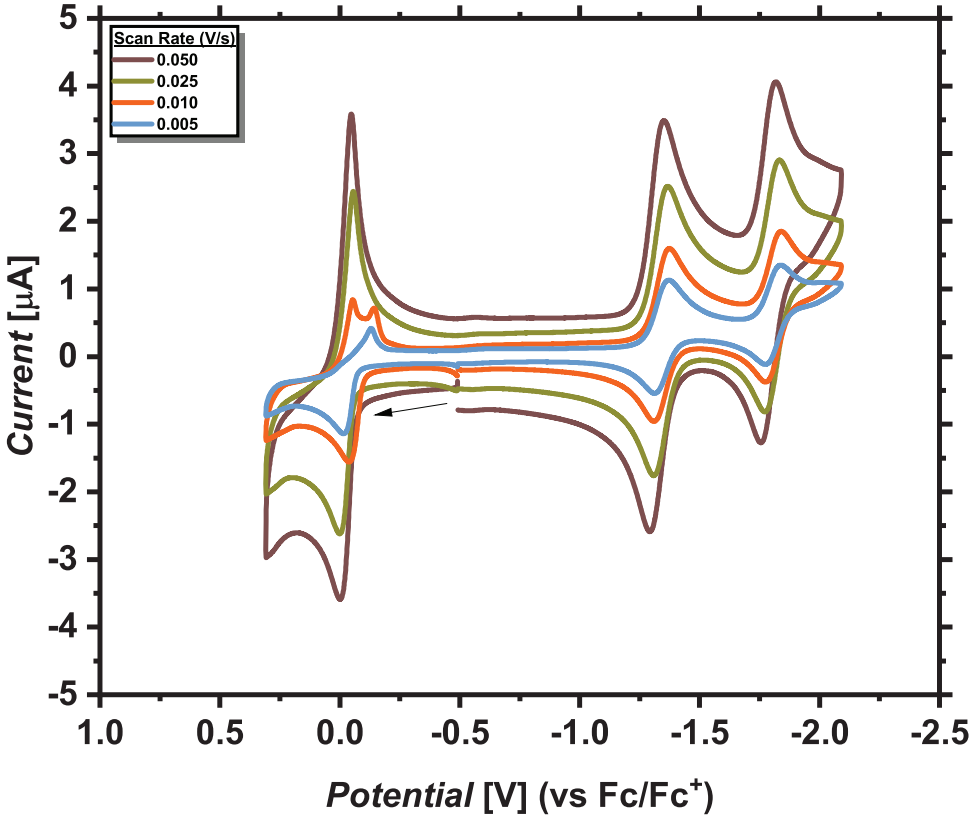
Scan Rate (V/s)
0.050
0.025
0.010
0.005
Current [μA]
Potential [V] (vs Fc/Fc+)

Figure 4.5: Variable scan rate CV of ^{OEt}PcVO (0.31mM) in DCM with [NBu_4][PF_6] (0.1M) supporting electrolyte, a 3mm glassy carbon working electrode, Pt wire counter electrode, and a Pt wire pseudo-reference electrode. Internally referenced to ferrocene.

PcNi complexes are not known to display axial ligation or a shift in their electrochemical behavior in coordinating solvents[22] with both the reductions and oxidation assigned to ring-based events. There is some discussion around the oxidation of PcNi complexes being due to the Ni^{II}/Ni^{III} couple[23, 24] and evidence that excitation-induced axial coordination of PcNi complexes occurs.[25] Therefor, the origin of this shifting behavior of **^{OEt}PcNi** both in coordinating media and at slower scan rates and its connection to the discrepancy in the value k_0 of warrants further investigation With this electrochemical data, we then moved to studying the solution-state cycling behavior for both these complexes.

4.3 Solution-State Cycling

Solvent choice in RFBs can have an effect on their efficacy; therefore, we selected two solvents common in non-aqueous RFBs, DMF and ACN, which both have favorable properties for RFB applications.[10] For a charge carrier such as **^{OEt}PcVO** with five available redox state the galvanostatic cycling curves would be expected to show two potential plateaus[12], however, **^{OEt}PcVO** in both DMF and ACN have complex curve features with no distinct plateaus. These features better match that of a suspension of Pc particles throughout solution which was observed at higher concentrations of **^{OEt}PcMnN** previously.[11] This difference between the charge-discharge features observed for **^{OEt}PcMnN** and **^{OEt}PcVO** could be in part due to the lower solubility of **^{OEt}PcVO** in both DMF and ACN which prevents fully dissolution even at low concentrations.

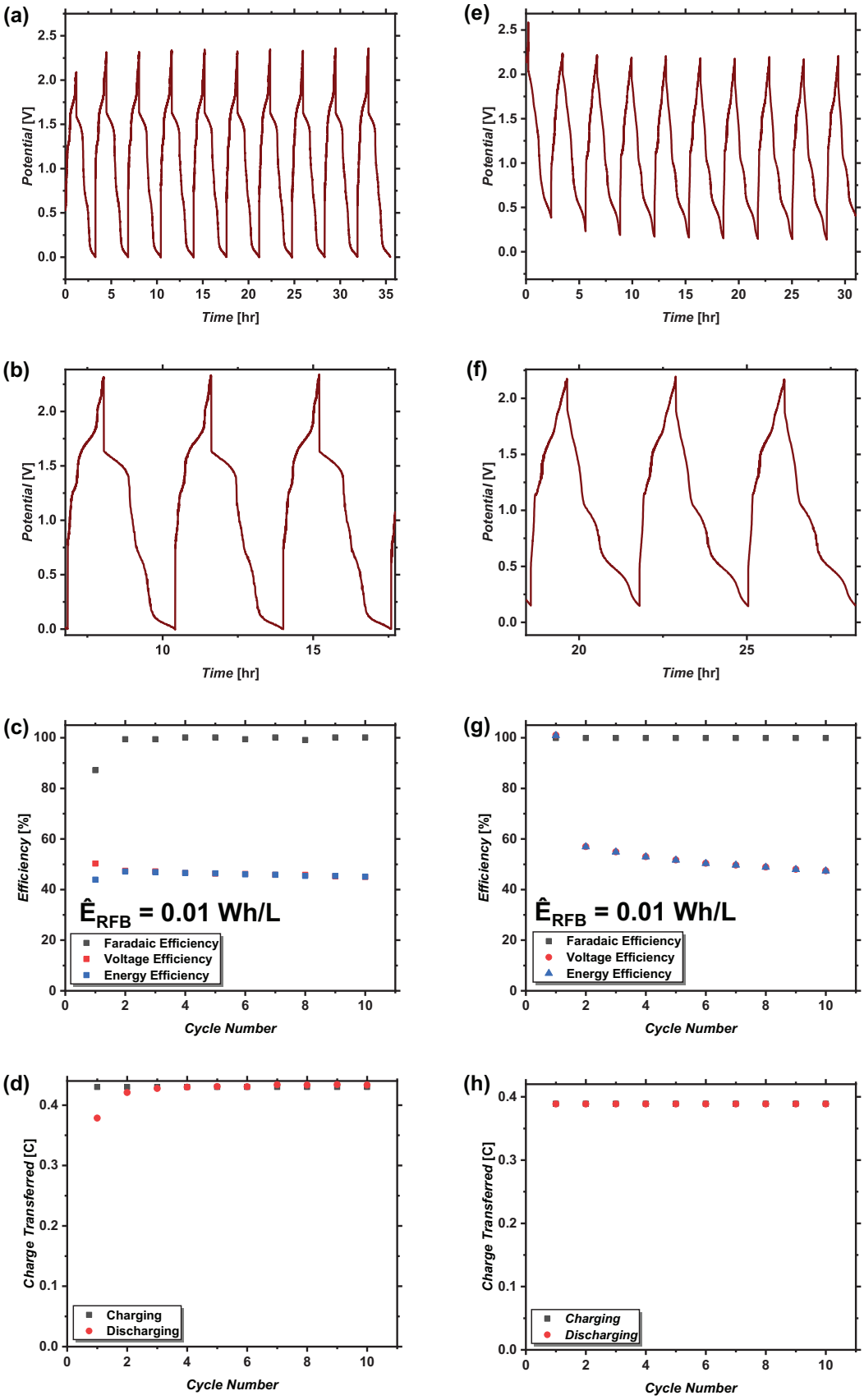
(a)
Potential [V]
Time [hr]
(e)
Potential [V]
Time [hr]
(b)
Potential [V]
Time [hr]
(f)
Potential [V]
Time [hr]
(c)
Efficiency [%]
Ê_RFB = 0.01 Wh/L
Faradaic Efficiency
Voltage Efficiency
Energy Efficiency
Cycle Number
(g)
Efficiency [%]
Ê_RFB = 0.01 Wh/L
Faradaic Efficiency
Voltage Efficiency
Energy Efficiency
Cycle Number
(d)
Charge Transferred [C]
Charging
Discharging
Cycle Number
(h)
Charge Transferred [C]
Charging
Discharging
Cycle Number

Figure 4.6: (a, b) Galvanostatic, two-electrode charge-discharge curves of ^{OEt}PcVO(0.60mM). Taken in a glass-fritted H-cell in DMF (5mL per compartment) with [Bu$_4$N][PF$_6$] (0.2M), coiled Pt working electrode, and coiled Pt counter electrode. 100µA charge, -50µA discharge over 10 cycles. (c) Efficiency metrics of ^{OEt}PcVO solution-state cycling in DMF. Energy density inset over legend. (d) Charge transferred from a galvanostatic cycling of ^{OEt}PcVO in DMF. (e, f) Galvanostatic, two-electrode charge-discharge curves of ^{OEt}PcVO(0.54mM). Taken in a glass-fritted H-cell in ACN (5mL per compartment) with [Bu$_4$N][PF$_6$] (0.2M), coiled Pt working electrode, and coiled Pt counter electrode. 100µA charge, -50µA discharge over 10 cycles. (g) Efficiency metrics of ^{OEt}PcVO solution-state cycling in ACN. Energy density inset over legend. (h) Charge Transferred from a galvanostatic cycling of ^{OEt}PcVO in ACN.

Aggregation of **^{OEt}PcVO** in both solvents explains the complex charge-discharge features. Evidence for this explanation is seen in the analysis of solutions used in the working electrode (WE) and counter electrode (CE) compartments after cycling (Fig. 4.7).

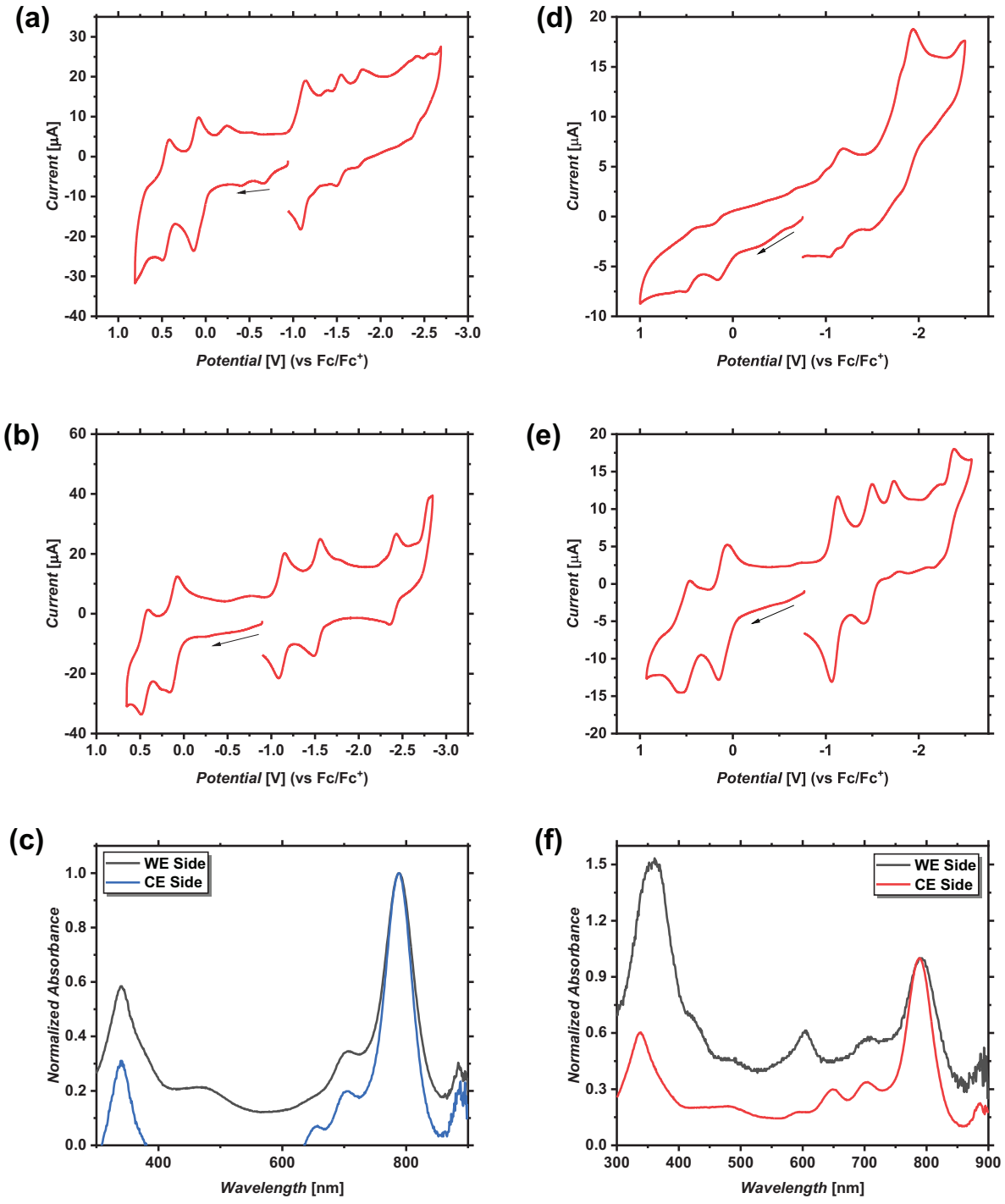

Figure 4.7: (a) CV at 0.5 V/s of the ^{OEt}PcVO WE compartment after cycling in DMF using a 3mm GC working electrode, Pt wire counter electrode, and a Pt wire pseudo-reference

electrode. Internally referenced to ferrocene. (b) CV at 0.5 V/s of the ^{OEt}PcVO CE compartment after cycling in DMF using a 3mm GC working electrode, Pt wire counter electrode, and a Pt wire pseudo-reference electrode. Internally referenced to ferrocene. (c) UV-vis of both the WE and CE compartment after cycling of ^{OEt}PcVO in DMF under Ar atmosphere. The solution using for cycling were diluted with DCM to achieve concentrations suitable for UV-vis analysis. (d) CV at 0.5 V/s of the ^{OEt}PcVO WE compartment after cycling in ACN using a 3mm GC working electrode, Pt wire counter electrode, and a Pt wire pseudo-reference electrode. Internally referenced to ferrocene. (b) CV at 0.5 V/s of the ^{OEt}PcVO CE compartment after cycling in ACN using a 3mm GC working electrode, Pt wire counter electrode, and a Pt wire pseudo-reference electrode. Internally referenced to ferrocene. (c) UV-vis of both the WE and CE compartment after cycling of ^{OEt}PcVO in ACN under Ar atmosphere. The solution using for cycling were diluted with DCM to achieve concentrations suitable for UV-vis analysis.

After cycling **^{OEt}PcVO** in DMF the CV of the WE compartment shows new features particularly on the reductive side and the UV-vis shows an increase in the baseline absorbance and a broadening of the Q-band, behavior consistent with aggregation.[16, 19, 22] Analysis of the solutions used for cycling of **^{OEt}PcVO** in ACN also show signs of aggregation. The CV of the WE compartment shows minimal current response at the potentials expected, indicating that much of the **^{OEt}PcVO** is no longer dissolved. The UV-vis of the WE compartment shows an increase in absorption over all wavelengths, a broadening of the Q-band, and a change in the relative intensities of the B-band and Q-band all indicative of aggregation.[16] It appears that the cell is not able to fully discharge leaving features consistent with an oxidized species. However, this aggregation does not appear to affect the Faradaic efficiency with both DMF

and ACN showing values above 98% excluding the first cycle in DMF (we attributed this lowered Faradaic efficiency with a breakdown of some of the larger aggregates slowly dissolving into solution). Both DMF and ACN show fade in their voltage efficiency over the first 10 cycles with DMF showing a 2% fade from 47 to 45% and ACN showing a 10% fade from 57 to 47%. We attribute the low voltage efficiency to the un-optimized charge and discharge rates and the fade to cell polarization due to the aggregation of ^{OEt}**PcVO**. The Faradaic capacity (the total charge transferred on discharge relative to the initial discharge) does not show any fade over the 10 cycles.

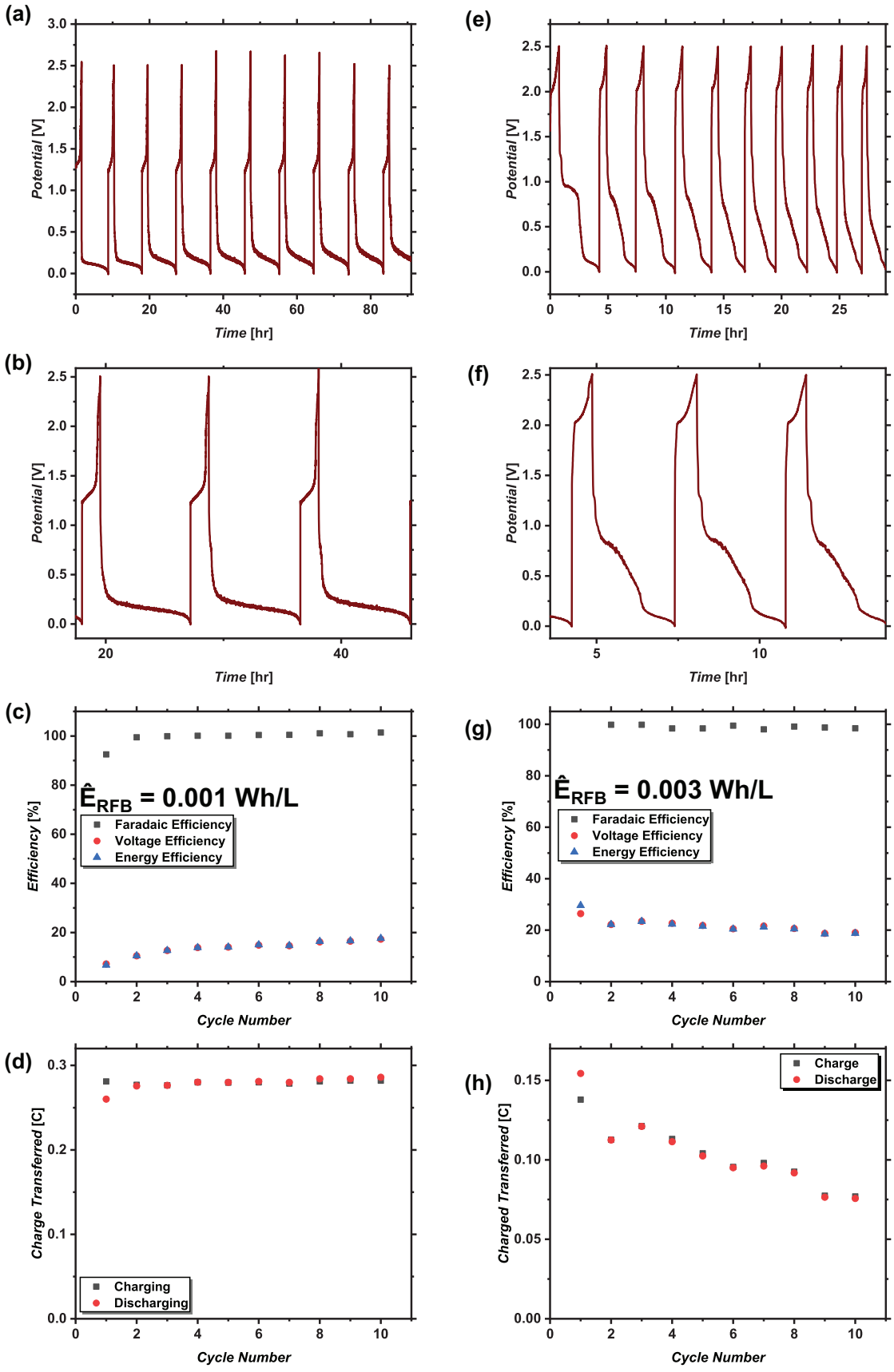
(a)
Potential [V]
Time [hr]
(e)
Potential [V]
Time [hr]
(b)
Potential [V]
Time [hr]
(f)
Potential [V]
Time [hr]
(c)
Ê_RFB = 0.001 Wh/L
Faradaic Efficiency
Voltage Efficiency
Energy Efficiency
Efficiency [%]
Cycle Number
(g)
Ê_RFB = 0.003 Wh/L
Faradaic Efficiency
Voltage Efficiency
Energy Efficiency
Efficiency [%]
Cycle Number
(d)
Charge Transferred [C]
Charging
Discharging
Cycle Number
(h)
Charge
Discharge
Charged Transferred [C]
Cycle Number

Figure 4.8: (a, b) Galvanostatic, two-electrode charge-discharge curves of ^{OEt}PcNi (0.20 mM). Taken in a glass-fritted H-cell in DMF (5mL per compartment) with [Bu_4N][PF_6] (0.2 M), coiled Pt working electrode, and coiled Pt counter electrode. 50 µA charge, -10 µA discharge over 10 cycles. (c) Efficiency metrics of ^{OEt}PcNi solution-state cycling in DMF. Energy density inset over legend. (d) Charge transferred from a galvanostatic cycling of ^{OEt}PcNi in DMF. (e, f) Galvanostatic, two-electrode charge-discharge curves of ^{OEt}PcNi (0.54 mM). Taken in a glass-fritted H-cell in ACN (5mL per compartment) with [Bu_4N][PF_6] (0.2 M), coiled Pt working electrode, and coiled Pt counter electrode. 50 µA charge, -12. 5µA discharge over 10 cycles. (g) Efficiency metrics of ^{OEt}PcNi solution-state cycling in ACN. Energy density inset over legend. (h) Charge transferred from a galvanostatic cycling of ^{OEt}PcNi in ACN.

^{OEt}PcNi also retains good Faradaic efficiencies (>98% over all cycles) for both DMF and ACN: however, the voltage efficiency and energy efficiency are low. In DMF the voltage efficiency shows an increase of 10% from to 17% over the 10 cycles and the Faradaic capacity shows and increase of 11% as well. Analysis of the WE and CE compartments show little aggregation after cycling in DMF in either the CV or UV-vis (Fig. 4.9) leading us low voltage efficiency to the low concentration of **^{OEt}PcNi,** with the slow dissolution of more **^{OEt}PcNi** overtime leading to the increases in efficiencies and capacities seen.

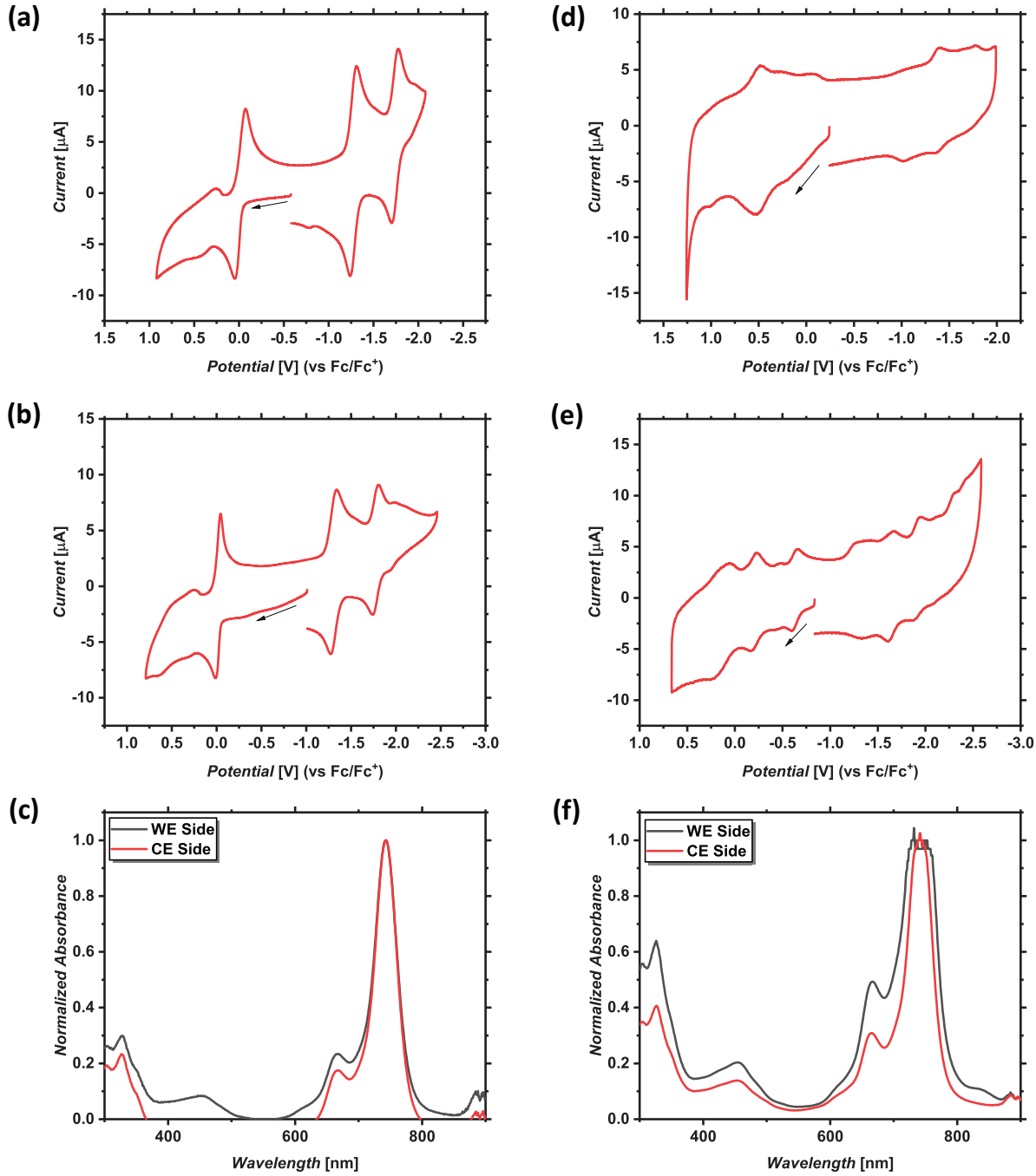

Figure 4.9: (a) CV at 0.5 V/s of the ^{OEt}PcNi WE compartment after cycling in DMF using a 3mm GC working electrode, Pt wire counter electrode, and a Pt wire pseudo-reference electrode. Internally referenced to ferrocene. (b) CV at 0.5 V/s of the ^{OEt}PcNi CE

compartment after cycling in DMF using a 3mm GC working electrode, Pt wire counter electrode, and a Pt wire pseudo-reference electrode. Internally referenced to ferrocene. (c) UV-vis of both the WE and CE compartment after cycling of ^{OEt}PcNi in DMF under Ar atmosphere. The solution using for cycling were diluted with DCM to achieve concentrations suitable for UV-vis analysis. (d) CV at 0.5 V/s of the ^{OEt}PcNi WE compartment after cycling in ACN using a 3mm GC working electrode, Pt wire counter electrode, and a Pt wire pseudo-reference electrode. Internally referenced to ferrocene. (b) CV at 0.5 V/s of the ^{OEt}PcNi CE compartment after cycling in ACN using a 3mm GC working electrode, Pt wire counter electrode, and a Pt wire pseudo-reference electrode. Internally referenced to ferrocene. (c) UV-vis of both the WE and CE compartment after cycling of ^{OEt}PcNi in ACN under Ar atmosphere. The solution using for cycling were diluted with DCM to achieve concentrations suitable for UV-vis analysis.

In ACN, **^{OEt}PcNi** appears to be unstable with the voltage efficiency decreasing from 26% to 19% and the Faradaic capacity decreasing by 50% over 10 cycles. After cycling the UV-vis of the solutions from the WE and CE compartments is consistent with that of our published spectrum for **^{OEt}PcNi**[15]; however, there was material plated onto the glass of both the WE and CE compartments. Washing the H-cell with DCM and taking the UV-vis of the resulting solution shows spectra consistent with an aggregated species (Fig. 4.10).[26]

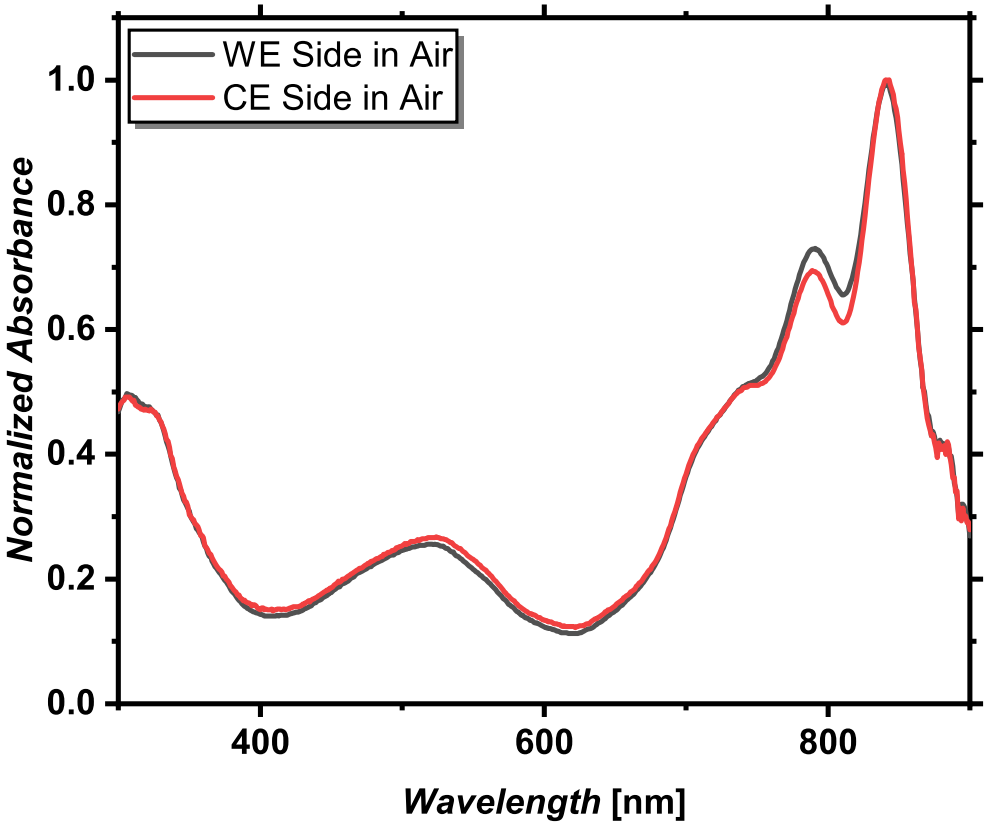

Figure 4.10: UV-vis of both the WE and CE compartment after cycling of ^{OEt}PcNi in ACN under air atmosphere. The solution using for cycling were diluted with DCM to achieve concentrations suitable for UV-vis analysis.

Additionally, the CV of both compartments shows new peaks, again indicative of aggregation. While the solution-state results clearly exclude these compounds from being suitable as charge carriers alone due to their low solubility, it is worth utilizing them in conjunction with a conductive carbon additive to try and overcome these shortcomings.

4.4 Slurry-State Cycling

Since conductive carbon surface area and charge transfer properties can be sensitive to processing conditions, we began our investigation by first performing a cycling experiment with a slurry of KB and ACN utilizing the same voltage cutoff used in the solution state cycling experiments above. This experiment showed a capacitive relationship during charge and discharge as well as excellent Faradaic efficiency (>98%), voltage efficiency (64%), and Faradaic capacity retention.

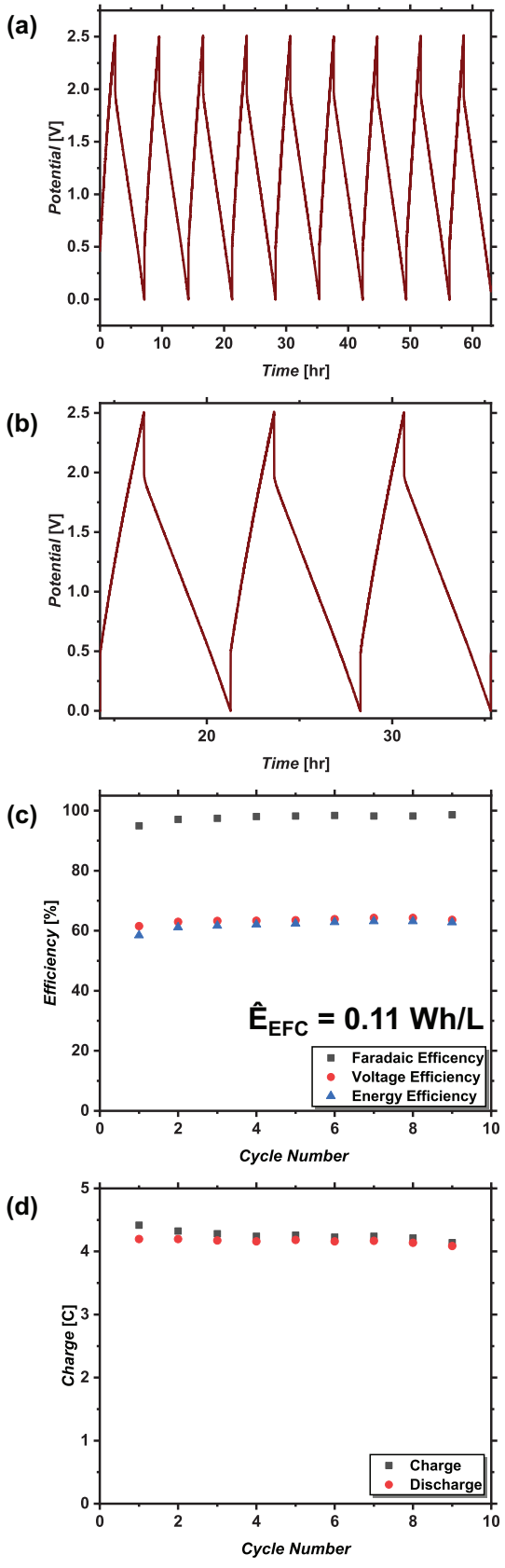
(a)
Potential [V]
Time [hr]
(b)
Potential [V]
Time [hr]
(c)
Efficiency [%]
Ê_EFC = 0.11 Wh/L
Faradaic Efficency
Voltage Efficiency
Energy Efficiency
Cycle Number
(d)
Charge [C]
Charge
Discharge
Cycle Number

Figure 4.11: (a) Galvanostatic, two-electrode charge-discharge curves of a KB slurry (b) Selected charge-discharge curves of a galvanostatically charged KB slurry (c) Efficiency metrics of a galvanostatically charged KB slurry. Energy density inset over legend. (d) Charge transferred from a galvanostatically charged KB slurry. Conditions: taken in a glass-fritted H-cell in ACN (5mL per compartment) with $[Bu_4N][PF_6]$ (0.2 M) with 51.4 mg of KB per compartment, coiled Pt working electrode, and coiled Pt counter electrode. 500 µA charge, -250 µA discharge over 10 cycles.

From these experimental charge-discharge curves, we were also able to determine the amount of charge transferred — 4.1 C for every 51.4 mg KB used — that could then be used in subsequent experiments to estimate the contribution of the KB to the capacity of these hybrid systems. With this basis for the charge delivered by KB we then began to cycle our Pc complexes as slurries with KB.

Galvanostatic cycling of a ^{OEt}**PcVO** and KB slurry in ACN shows good Faradaic efficiency (> 98%), excluding the first cycle, while it demonstrates significant fade in both the voltage efficiency (decreasing from 53% to 38% over 20 cycles) and the Faradaic capacity (decreasing by 31% over 20 cycles) (Figure 4.12 (d))

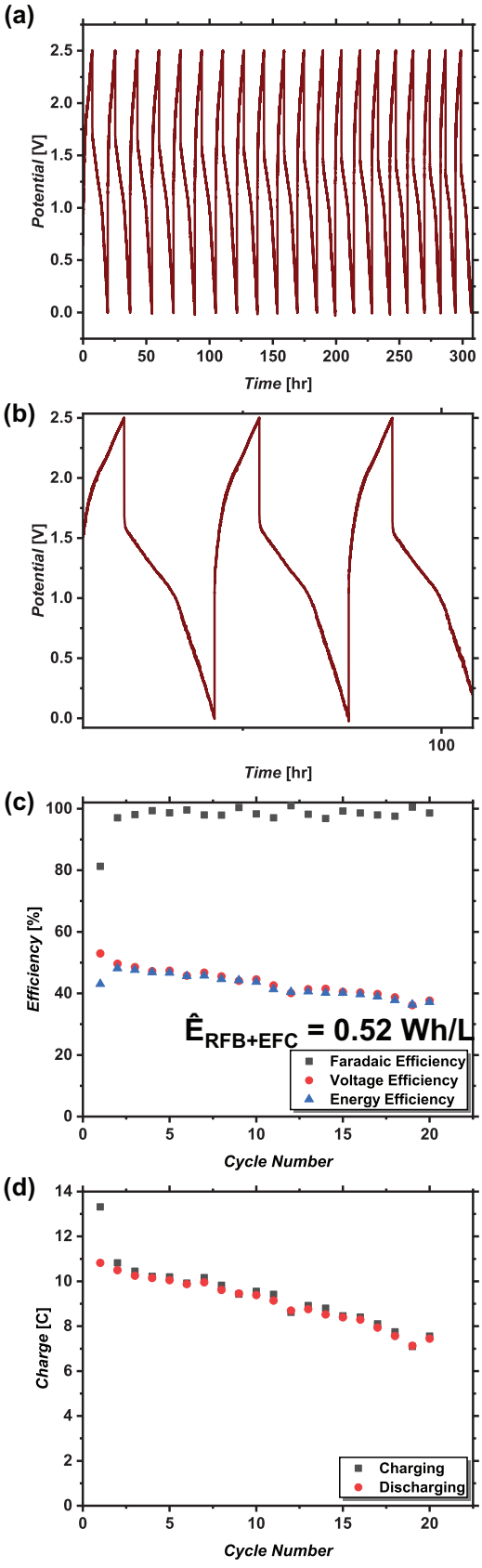
(a)
Potential [V]
Time [hr]
(b)
Potential [V]
Time [hr]
(c)
Efficiency [%]
Ê RFB+EFC = 0.52 Wh/L
Faradaic Efficiency
Voltage Efficiency
Energy Efficiency
Cycle Number
(d)
Charge [C]
Charging
Discharging
Cycle Number

Figure 4.12: (a) Galvanostatic, two-electrode charge-discharge curves of a ^{OEt}PcVO/KB slurry (b) Selected charge-discharge curves of a galvanostatically charged ^{OEt}PcVO/ KB slurry (c) Efficiency metrics of a galvanostatically charged ^{OEt}PcVO/KB slurry. Energy density inset over legend. (d) Charge transferred from a galvanostatically charged ^{OEt}PcVO/KB slurry. Conditions: taken in a glass-fritted H-cell in ACN (5mL per compartment) with [Bu_4N][PF_6] (0.2M) with 62.1mg of ^{OEt}PcVO and 101.4mg of KB per compartment, coiled Pt working electrode, and coiled Pt counter electrode. 500µA charge, -250µA discharge over 20 cycles.

The amount of charge transferred is also lower than expected with 10.8 C during cycle 1 while 15.7 C transferred were expected per cycle for 75% SOC. This is close to what is observed in the solution-state cycling data perhaps indicating instability of the **^{OEt}PcVO** in ACN. The features of the charge-discharge curves appear intermediate between those expected in a Faradaic and capacitive system, reflecting the combined contributions of the Pc and KB components.

A slurry of **^{OEt}PcNi** and KB in DMF again shows high Faradaic efficiency (>98%) that remains stable over 20 cycles as it does in the solution state cycling (Fig. 4.13). Unlike in the solution state, the voltage efficiencies are low and decrease over the course of 20 cycles (from 42% to 30%) and the charge transferred remains steady at 8.1 C per cycle.

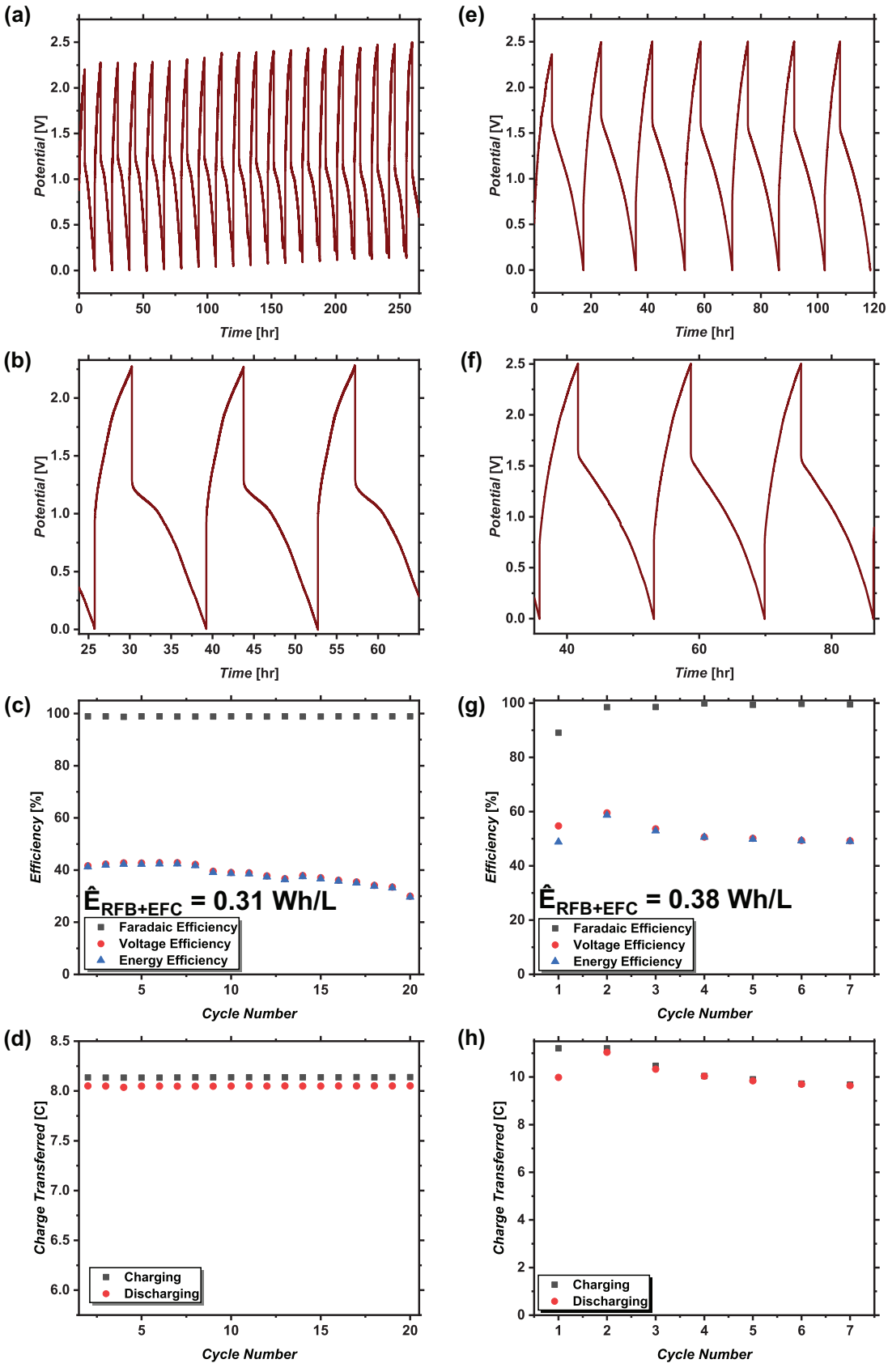
(a)
Potential [V]
Time [hr]
(e)
Potential [V]
Time [hr]
(b)
Potential [V]
Time [hr]
(f)
Potential [V]
Time [hr]
(c)
Efficiency [%]
Ê RFB+EFC = 0.31 Wh/L
Faradaic Efficiency
Voltage Efficiency
Energy Efficiency
Cycle Number
(g)
Efficiency [%]
Ê RFB+EFC = 0.38 Wh/L
Faradaic Efficiency
Voltage Efficiency
Energy Efficiency
Cycle Number
(d)
Charge Transferred [C]
Charging
Discharging
Cycle Number
(h)
Charge Transferred [C]
Charging
Discharging
Cycle Number

Figure 4.13: (a, b) Galvanostatic, two-electrode charge-discharge curves of a ^{OEt}PcNi/KB slurry. (c) Efficiency metrics of a galvanostatically charged ^{OEt}PcNi/KB slurry. Energy density inset over legend. (d) Charge transferred from a galvanostatically charged ^{OEt}PcNi/KB slurry. Conditions: taken in a glass-fritted H-cell in DMF (5mL per compartment) with [Bu_4N][PF_6] (0.2M) with 64.2mg of ^{OEt}PcNi and 101.0mg of KB per compartment, coiled Pt working electrode, and coiled Pt counter electrode. 500µA charge, -250µA discharge over 20 cycles. (e, f) Galvanostatic, two-electrode charge-discharge curves of a ^{OEt}PcNi/KB slurry. (g) Efficiency metrics of a galvanostatically charged ^{OEt}PcNi/KB slurry. Energy density inset over legend. (h) Charge transferred from a galvanostatically charged ^{OEt}PcNi/KB slurry. Conditions: taken in a glass-fritted H-cell in ACN (5mL per compartment) with [Bu_4N][PF_6] (0.2M) with 61.3mg of ^{OEt}PcNi and 105.5mg of KB per compartment, coiled Pt working electrode, and coiled Pt counter electrode. 500µA charge, -250µA discharge over 7 cycles.

The charge-discharge a ^{OEt}**PcNi** and KB slurry in ACN curves also demonstrate features of both the capacitive and Faradaic components with a Faradaic efficiency of over 98%, however, he voltage efficiency decreases(from 60% to 49%) over the first 7 cycles (Fig. 4.13 (g)) and the charge transferred lowers from 11.0C to 9.6C. To determine if this decrease is caused by voltage cutoffs that are not sufficient to allow full charging, the cycling in ACN was stopped and re-started with a change in the voltage cutoff from 2.5 to 3.5 V with the intention of the time cutoff being reached before the voltage cutoff. When cycling resumed, the potential cell continued to reach the voltage cutoff before the time cutoff with a corresponding drop in both voltage efficiency and charge transferred (Figure 4.14) indicating cell death.

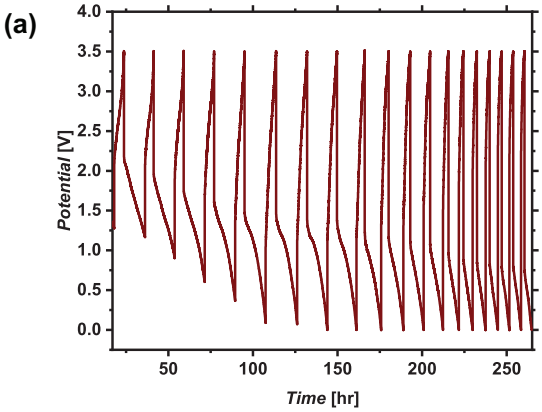
(a)
Potential [V]
Time [hr]

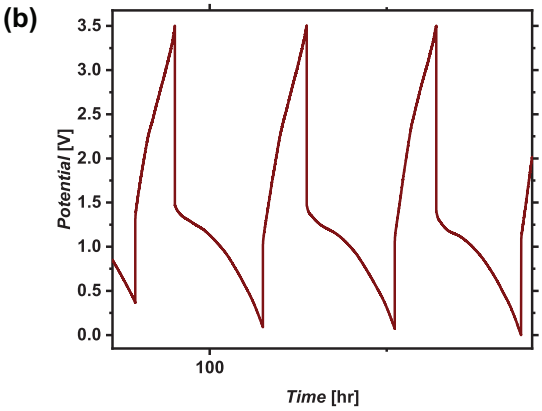
(b)
Potential [V]
Time [hr]

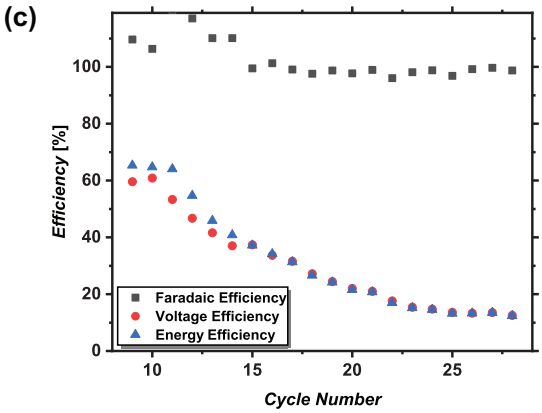
(c)
Efficiency [%]
Faradaic Efficiency
Voltage Efficiency
Energy Efficiency
Cycle Number

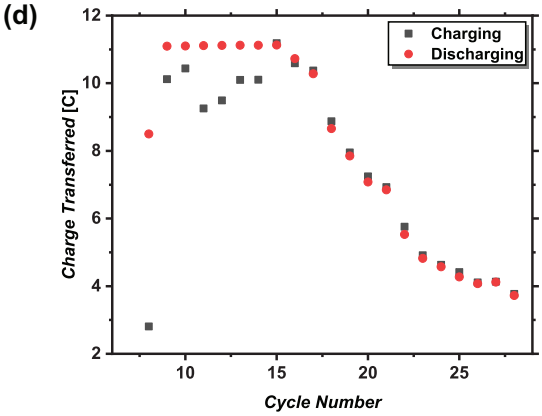
(d)
Charge Transferred [C]
Charging
Discharging
Cycle Number

Figure 4.14: (a) Galvanostatic, two-electrode charge-discharge curves of a ^{OEt}PcNi/KB slurry (b) Selected charge-discharge curves of a galvanostatically charged ^{OEt}PcNi/ KB slurry (c) Efficiency metrics of a galvanostatically charged ^{OEt}PcNi/KB slurry (d) Charge transferred from a galvanostatically charged ^{OEt}PcNi/KB slurry. Conditions: taken in a glass-fritted H-cell in ACN (5mL per compartment) with $[Bu_4N][PF_6]$ (0.2M) with 61.3mg of ^{OEt}PcNi and 105.5mg of KB per compartment, coiled Pt working electrode, and coiled Pt counter electrode. 500µA charge, -250µA discharge over 20 cycles.

These results indicate that the lowered solubility of both **^{OEt}PcVO** and **^{OEt}PcNi** limit their utility as solution state charge carriers and while combing them with KB increased the efficiencies overall there appear to be stability issues that must be addressed for long-term use as a charge carrier.

To address the need for increased stability we tested industrially manufactured unsubstituted MPcs (**PcVO**, **PcFe**, and **PcNi**) which are known to be robust to a variety of environmetns[24] while being compatible with carbon-based materials[27]. We aimed to determine their suitability as charge carriers in a slurry-based system as their low solubility would no longer be a constraint. A combination of CV and differential pulse voltammetry were used to assess their redox properties (Figure 4.15).

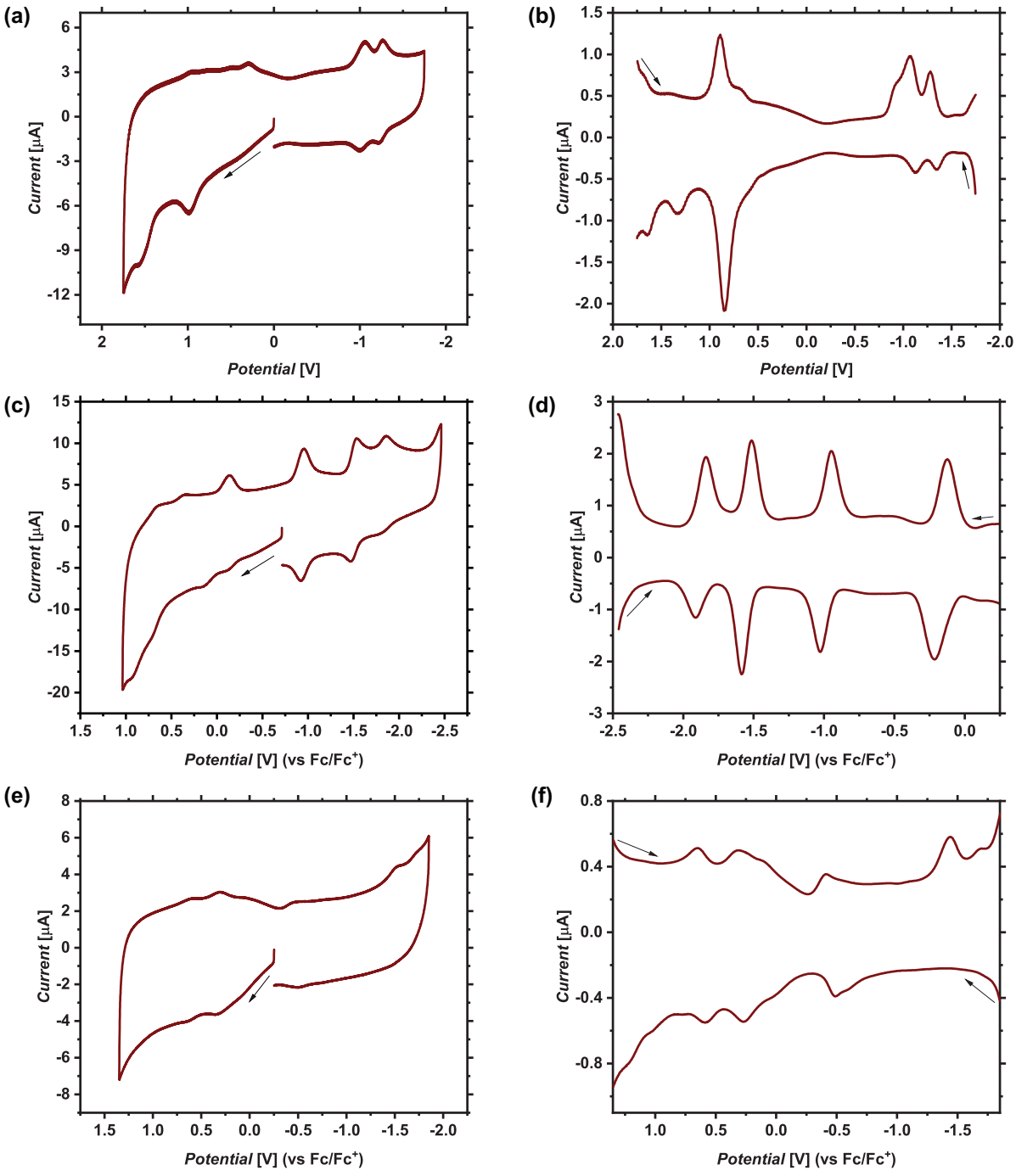

Figure 4.15: (a) CV at 0.5 V/s and (b) DPV of PcVO (0.0034g) with 5mL of $[NBu_4][PF_6]$ (0.1 M) supporting electrolyte in DCM and using a 3 mm diameter glassy carbon working electrode, Pt wire counter electrode, and Pt wire pseudo-reference electrode. Internally

referenced to ferrocene. (c) CV at 0.5 V/s and (d) DPV of PcFe (0.0029g) with 5mL of $[NBu_4][PF_6]$ (0.1 M) supporting electrolyte in DMF and using a 3mm diameter glassy carbon working electrode, Pt wire counter electrode, and Pt wire pseudo-reference electrode. Internally referenced to ferrocene. (e) CV at 0.5 V/s and (f) DPV of PcNi (0.0060g) with 5mL of $[NBu_4][PF_6]$ (0.1 M) supporting electrolyte in DCM and using a 3mm diameter glassy carbon working electrode, Pt wire counter electrode, and Pt wire pseudo-reference electrode. Internally referenced to ferrocene.

The redox potentials are listed in Table 4.2 and are similar to those reported in literature.[22, 24]

Species	R1 (V)	R2 (V)	R3 (V)	O1 (V)	O2 (V)
PcVO	-1.10	-1.31	—	0.87	1.29 (irr.)
PcFe	-0.99	-1.55	-1.87	-0.17	—
PcNi	-0.45	-1.44 (irr.)	—	0.29	0.62

Table 4.2: Electrochemical values for commercially available unsubstituted PcVO, PcFe and PcNi. R1, R2, O1, and O2 refer to successive reductions and oxidation processes. All values referenced internally to ferrocene. The note irr. indicates an irreversible process.

ACN was used as the solvent of choice for the cycling experiments of all unsubstituted MPcs as it is the most common non-aqueous solvent for RFBs. A slurry of **PcVO** and KB shows good Faradaic efficiency (>98%) as well as high voltage (58%) and energy efficiencies (57%) over the course of 20 cycles.

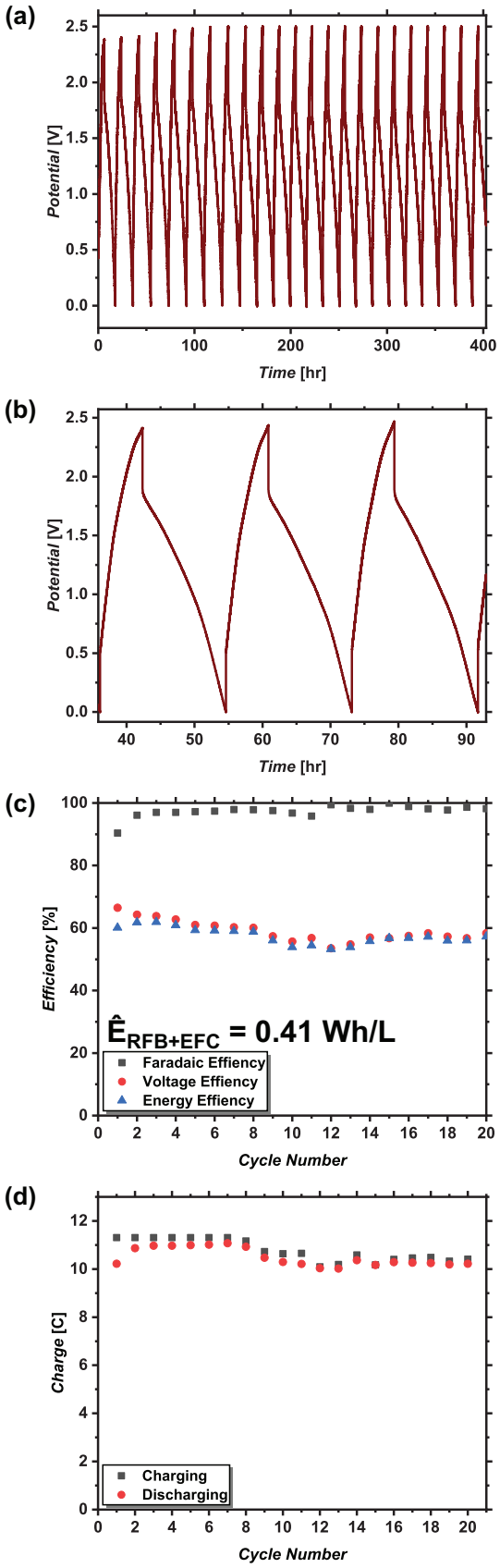
(a)
Potential [V]
Time [hr]
(b)
Potential [V]
Time [hr]
(c)
Efficiency [%]
Ê RFB+EFC = 0.41 Wh/L
Faradaic Effiency
Voltage Effiency
Energy Effiency
Cycle Number
(d)
Charge [C]
Charging
Discharging
Cycle Number

Figure 4.16: (a) Galvanostatic, two-electrode charge-discharge curves of a PcVO/KB slurry (b) Selected charge-discharge curves of a galvanostatically charged PcVO/KB slurry (c) Efficiency metrics of a galvanostatically charged ^{OEt}PcVO/KB slurry. Energy density inset over legend. (d) Charge transferred from a galvanostatically cycled PcVO/KB slurry. Conditions: taken in a glass-fritted H-cell in ACN (5mL per compartment) with $[Bu_4N][PF_6]$ (0.2M) with 39.3mg of PcVO and 106.5mg of KB per compartment, coiled Pt working electrode, and coiled Pt counter electrode. 500µA charge, -250µA discharge over 20 cycles.

The charge-discharge behavior shows some slight variability that we attribute to further mixing of the **PcVO** and KB over time which appears to stabilize at cycle 10. Once stabilized the slurry exhibits Faradaic efficiency of >98%, a voltage efficiency of 57%, energy efficiency of 57% and 10.2 C of charge transferred. It is worth noting here that the features of this curve look more capacitive than those of the substituted Pcs discussed above; however, the determined capacity exceeds that of what we would predict based on the KB contribution alone (8.5C) indicating contribution of both the **PcVO** and KB.

A slurry of **PcNi** and KB was also tested in ACN and displayed a Faradaic efficiency of 97%, voltage efficiency of 57%, energy efficiency of 55%, and 12.7 C transferred (Figure 4.17)

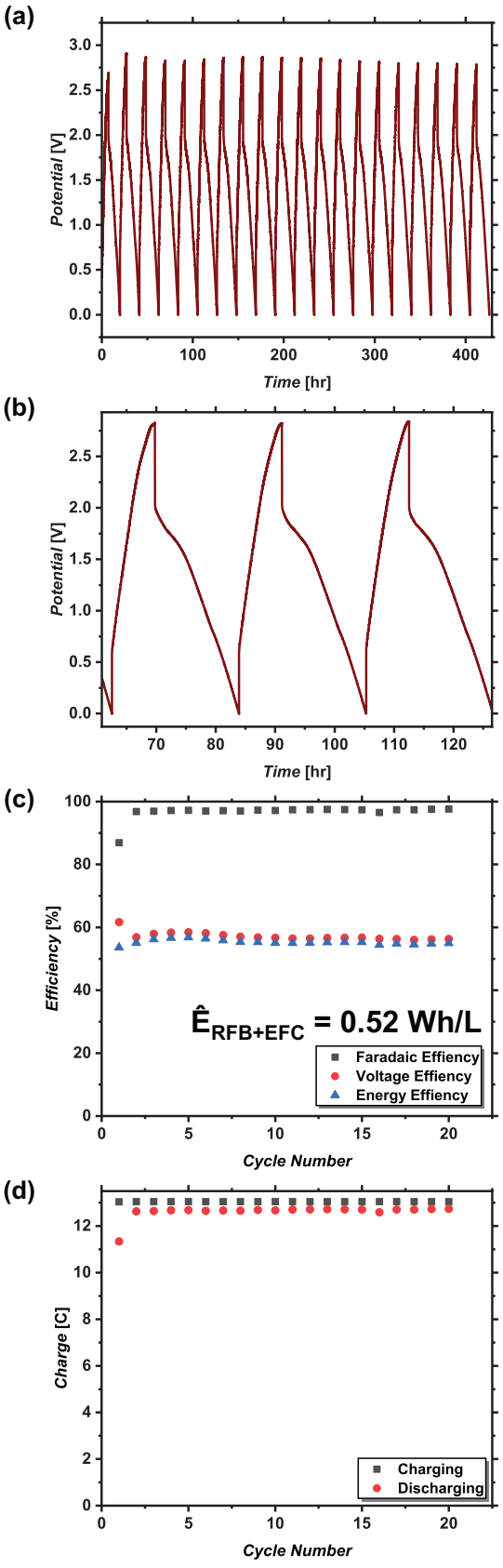
(a)
Potential [V]
Time [hr]
(b)
Potential [V]
Time [hr]
(c)
Efficiency [%]
Ê RFB+EFC = 0.52 Wh/L
Faradaic Effiency
Voltage Effiency
Energy Effiency
Cycle Number
(d)
Charge [C]
Charging
Discharging
Cycle Number

Figure 4.17: (a) Galvanostatic, two-electrode charge-discharge curves of a PcNi/KB slurry (b) Selected charge-discharge curves of a galvanostatically charged PcNi/KB slurry (c) Efficiency metrics of a galvanostatically charged ^{OEt}PcNi/KB slurry. Energy density inset over legend. (d) Charge transferred from a galvanostatically cycled PcNi/KB slurry. Conditions: taken in a glass-fritted H-cell in ACN (5mL per compartment) with $[Bu_4N][PF_6]$ (0.2 M) with 48.9 mg of PcNi and 111.7 mg of KB per compartment, coiled Pt working electrode, and coiled Pt counter electrode. 500µA charge, -250 µA discharge over 20 cycles.

The **PcNi**/KB slurry demonstrates stability over the 19 days of cycling experiments, showing no significant fade in efficiency or capacity.

As in the case of the **PcVO**/KB slurry, the charge-discharge behavior of the **PcFe**/KB slurry in ACN shows Faradaic efficiency of >98%. There is a small decline of the voltage efficiency (a decline of 3%), energy efficiency (a decline of 3%), and Faradaic capacity (declined by 2%) over the first 10 cycles. After the first 10 cycles the voltage efficiency remains at 46%, the energy efficiency at 46% and 11.0 C of charge transferred demonstrating good efficiencies and stability.

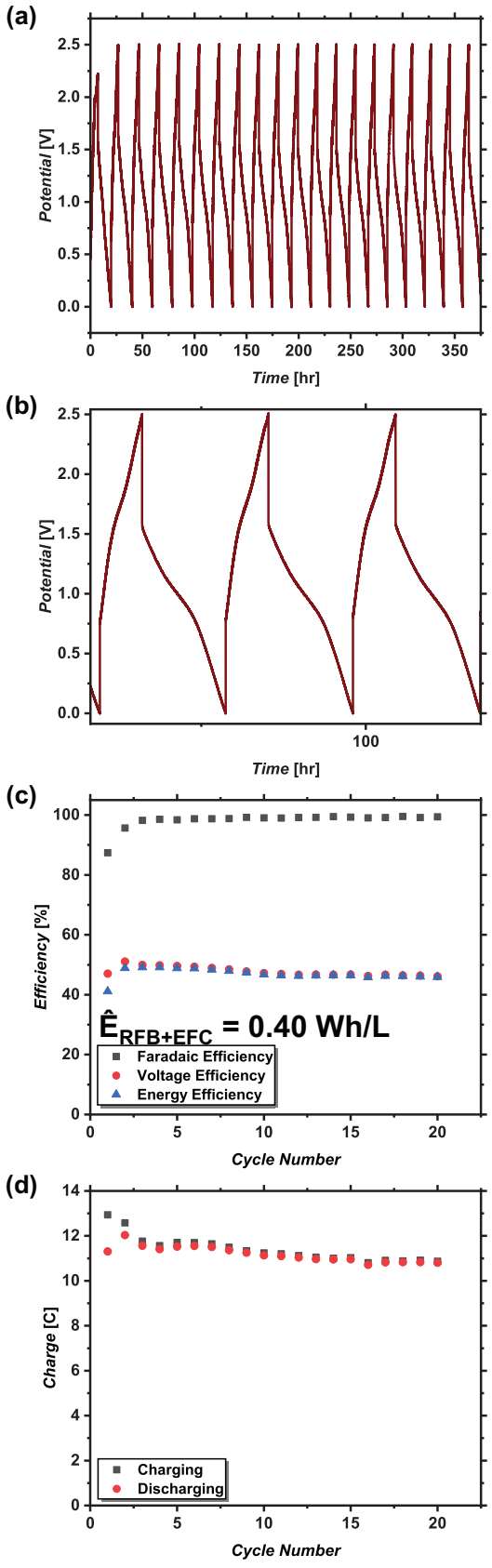
(a)
Potential [V]
Time [hr]
(b)
Potential [V]
Time [hr]
(c)
Efficiency [%]
Ê_RFB+EFC = 0.40 Wh/L
Faradaic Efficiency
Voltage Efficiency
Energy Efficiency
Cycle Number
(d)
Charge [C]
Charging
Discharging
Cycle Number

Figure 4.18: (a) Galvanostatic, two-electrode charge-discharge curves of a PcFe/KB slurry (b) Selected charge-discharge curves of a galvanostatically charged PcFe/KB slurry (c) Efficiency metrics of a galvanostatically charged ^{OEt}PcFe/KB slurry. Energy density inset over legend. (d) Charge transferred from a galvanostatically cycled PcFe/KB slurry. Conditions: taken in a glass-fritted H-cell in ACN (5 mL per compartment) with $[Bu_4N][PF_6]$ (0.2 M) with 50.0 mg of PcFe and 109.8 mg of KB per compartment, coiled Pt working electrode, and coiled Pt counter electrode. 500 µA charge, -250 µA discharge over 20 cycles.

All three Pc complexes show good efficiencies and the **PcFe** and **PcNi** show good stability over the course cycling experiments.

4.4 Summary

Here we report the changes in electrochemical behavior for **^{OEt}PcVO** and **^{OEt}PcNi** in different solvents as well as their values for D and k_0. Additionally, we then test their utility as charge carriers for use in RFBs both in the solution-state as well as a part of a hybrid slurry system with a conductive carbon additive (KB). These results show that the low solubility of both ^{OEt}PcVO and ^{OEt}PcNi limit their utility as solution-state charge carriers. While this can be improved through the use of a slurry system, there are stability issues for both complexes that must be addressed. We then demonstrated that commercially available unsubstituted Pcs may be used as charge carriers with KB in this hybrid architecture thereby reducing the cost of the charge carrier significantly while maintaining a stable system. These commercially available Pc complexes showed improved efficiencies and stability over our synthesized solubilized derivatives and offer the opportunity for significant scaling of this system.

4.5. Experimental

4.5.1 Techniques and Reagents:

Hexanes, C_6D_6, Et_2O, DCM and THF (inhibitor-free) were dried and degassed on an MBraun Solvent Purification System and stored over activated 4 Å molecular sieves. Solvents (DMF, Acetonitrile, Fluorobenzene) not degassed on the SPS were purified using modified literature methods.[28] N,N-dimethylformamide (DMF) was purchased from Fisher Scientific and dried by stirring with 4Å molecular sieves for 24 hours under nitrogen atmosphere on a Schlenk line, filtering off the sieves, and vacuum distilling followed by storage in a glovebox over 4Å molecular sieves. Acetonitrile was purchased from Alfa Aesar and dried by stirring with 4Å molecular sieves for 24 hours under nitrogen atmosphere on a Schlenk line, filtering off the sieves, and distilling over calcium hydride followed by storage in a glovebox over 4Å molecular sieves. Fluorobenzene was purchased from Alfa Aesar and dried by stirring with 4Å molecular sieves for 24 hours under nitrogen atmosphere on a Schlenk line, filtering off the sieves, and vacuum distilling followed by storage in a glovebox over 4Å molecular sieves. Tetrabutylammonium hexafluorophosphate ($[Bu_4N][PF_6]$) was purchased from Oakwood Chemical then purified by recrystallization in hot ethanol and dried at 50°C under dynamic vacuum for 24 hours before use. Ketjenblack® EC-600JD (KB) was purchased from a private supplier and ground using a mortar and pestle prior to use. PcVO and PcNi were purchased from Sigma-Aldrich and used without further purification. ^{OEt}PcVO and ^{OEt}PcNi were synthesized by previously reported methods[15] and recrystallized before use by layering either fluorobenzene/hexanes or DCM/hexanes. 4 Å molecular sieves were dried at 250°C under dynamic vacuum (<0.1 Torr) for 24 h prior to use.

4.5.2 Electrochemical Measurements:

All electrochemical measurements were performed in an atmosphere of dry, oxygen-free N_2 in an MBraun glovebox (MBRAUN UNIlab Pro SP Eco equipped with a -40°C freezer), or under an atmosphere of dry, oxygen-free Ar in a retrofitted VAC glovebox using solvents dried over 4Å molecular sieves. Cyclic voltammograms were performed on a CH Instruments 630E Electrochemical Analysis Potentiostat using either 1.5mm diameter Pt disk or 3mm diameter glassy carbon working electrodes (purchased from CH Instruments) as specified for the data set. Working electrodes were cleaned prior to each experiment and between every scan (unless otherwise specified) by polishing with a gradient of 1.0um, 0.3um, and 0.05um alumina (purchased from CH instruments) on a cloth pad, followed by rinsing with distilled water and acetone and dried under a stream of compressed air. The Pt wire pseudoreference and counter electrodes (purchased from CH Instruments) were rinsed with distilled water and acetone and heated white-hot with a butane torch. All measurements were performed on recrystallized product and referenced to the Fc/Fc^+ couple unless otherwise specified. Static cell cycling experiments were carried out using a Metrohm AutolabPGSTAT128N potentiostat/galvanostat, utilizing time cutoffs to ensure specified SOC with voltage cutoffs functioning as a back-up (the voltage cutoff for all experiments is 2.5V for charging and 0V for discharging unless otherwise specified). For all cycling calculations values for time, charge, potential, current, and resistance were exported from the Metrohm potentiostat/galvanostat and subsequently used. For cycling experiments, two coiled Pt electrodes (purchased from Bio-Logic) were used and were cleaned by rinsing with distilled water and acetone and then heating white-hot with a butane torch. All electrodes were transferred into a glovebox and subsequently rinsed with the respective electrolyte solution immediately prior to use. The H-cell was custom-made by the in-house glassblower.

4.5.3 Syntheses

3,6-Diethoxyphthalonitrile. 3,6-Diethoxyphthalonitrile was synthesized using a modified literature procedure.[29, 30] A mixture of 2,3-dicyanohydroquinone (5.20 g, 33.4 mmol, 1 equiv) and K_2CO_3 (5.00 g, 36 mmol, 1.1 equiv) in 125 mL of wet acetone was sparged with N_2 or Ar for 30 minutes then heated to reflux. Ethyl iodide (13 mL, 162 mmol, 5 equiv) was then added dropwise to the mixture. The yellow slurry was stirred under reflux for 48 h. After cooling, the yellow solid was filtered on a glass frit and subsequently transferred to a mortar and pestle where it was ground into a powder. The powder was reintroduced to the glass frit and washed successively with 500 mL of H_2O, 150 mL of EtOH, and 150 mL of Et_2O. The product was collected and dried under reduced pressure for 24 h, affording a white powder. Additional product could be recovered by evaporation of the eluent after the wash, and this additional product was similarly washed with H_2O, EtOH, and Et_2O. Yield: 5.154 g (73.4%). ^{1}H NMR (600 MHz, CD_2Cl_2): δ 7.21 (s, 2H, *C_6H_2*.), 4.16 (q, *J* = 7.0 Hz, 4H, O*CH_2*CH_3), 1.48 (t, *J* = 7.0 Hz, 6H, OCH_2*CH_3*).

^{EtO}PcHLi. This compound was synthesized following our previously reported procedure.[30] Single crystals suitable for XRD studies were obtained by vapor diffusion of Et_2O into a concentrated solution of the product in DCM. ^{1}H NMR (600 MHz, CD_2Cl_2): δ 14.75 (s, 1H, NH), 7.57-7.52 (m, 8H, *C_6H_2*), 4.97-4.89 (m, 16H, O*CH_2*CH_3), 1.82-1.75 (m, 24H, OCH_2*CH_3*). λ_{max} (ε) = 723 nm (66,552 M^{-1} cm^{-1}), 783 nm (76,897 M^{-1} cm^{-1}). MS (MALDI-TOF): Calculated 873.18(M^+) Found 873.40 (M^+).

^{EtO}PcVO. This compound was synthesized using a modified literature procedure.[29] Under an inert atmosphere, **^{EtO}PcHLi** (0.200 g, 0.23 mmol, 1 equiv), $VOSO_4 \cdot 5H_2O$ (0.200 g, 0.79 mmol, excess), and $NaHCO_3$ (0.200 g, 2.3 mmol, excess) were combined in a round-bottom flask with

15 mL of DMF, and the resulting mixture was heated to 145 °C for 4 h. H_2O (100 mL) was then added and the solution was stirred for 15 mins, and subsequently filtered through a glass frit, leaving a dark green solid. The solid was washed successively with 150 mL of H_2O, 50 mL of EtOH, and 50 mL of Et_2O and subsequently collected and dried under reduced pressure. Yield: 0.090 g (42.2%). Single crystals suitable for XRD studies were obtained by vapor diffusion of Et_2O into a concentrated solution of the product in DCM. ^{1}H NMR (600 MHz, CD_2Cl_2): δ 8.53 (bs, *C_6H_2*), 5.03 (bs, O*CH_2*CH_3), 1.86 (bs, OCH_2*CH_3*). λ_{max} (ε) = 786 nm (160,930 M^{-1} cm^{-1}). MS (MALDI-TOF): Calculated 931.30 (M^+) Found 932.39 ($M\text{-}H^+$).

^{EtO}PcNi. This compound was synthesized using a modified literature procedure.[29] In air, **^{EtO}PcHLi** (0.208 g, 0.24 mmol, 1 equiv), $NiCl_2 \cdot 6H_2O$ (0.200 g, 0.84 mmol, excess), and $NaHCO_3$ (0.200 g, 2.3 mmol, excess) were combined in a round-bottom flask with 15 mL of DMF, and the resulting mixture was heated to 145 °C for 4 h. H_2O (100 mL) was then added and the solution was stirred for 15 mins, and subsequently filtered through a glass frit, leaving a dark green solid. The solid was washed successively with 150 mL of H_2O, 50 mL of EtOH, and 50 mL of Et_2O and subsequently collected and dried under reduced pressure. Yield: 0.230 g (>100% (excluding co-crystallized CH_2Cl_2); 88.24% (including co-crystallized CH_2Cl_2)). Single crystals suitable for XRD studies were obtained by vapor diffusion of Et_2O into a concentrated solution of the product in DCM. ^{1}H NMR (600 MHz, CD_2Cl_2): δ 7.54 (s, 8H, *C_6H_2*), 4.83 (q, *J* = 7.0 Hz, 16H, O*CH_2*CH_3), 1.75 (t, *J* = 7.0 Hz, 24H, OCH_2*CH_3*). λ_{max} (ε) = 742 nm (121276.6 M^{-1} cm^{-1}). MS (MALDI-TOF): Calculated 922.29 (M^+) Found 923.40 ($M\text{-}H^+$).

4.5.4 Calculations:

The calculations were done based on the template of our previously published work.[11]

Efficiency Metrics

Faradaic efficiency was defined by Eqn. 4.3 where Q is charge transferred:

(4.3) $FE = \frac{Q_{discharge}}{Q_{charge}} \times 100\%$

Voltage efficiency was defined by Eqn. 4.4 where V_{mean} is the mean voltage over the charging and discharging periods:

(4.4) $VE = \frac{V_{mean,discharge}}{V_{mean,charge}} \times 100\%$

Energy efficiency was defined by Eqn. 4.5:

(4.5) $EE = \frac{(FE \times VE)}{100\%}$

Energy Density Calculations:

For the calculation of energy density several assumptions were necessary:

1) The number of electrons is determined from the solution state CV for each experiment
2) The V_{cell} was determined from the $V_{cell,\ discharge}$ from the experimental cycling data
3) KB provides 4.1 C for every 103 mg used which was estimated based on the experimental data obtained from Fig. 4.11.

The energy density of the solution-state Pc ($\widehat{E_{Pc}}$) cycling was defined by Eqn. 4.6:

(4.6) $\widehat{E_{Pc}} = 0.5nV_{cell}C_{active}F$

Where n is the number of electrons transferred, V_{cell} is the cell potential, C_{active} is the concentration of the active species, and F is Faraday's constant.

The energy density of the slurry-state KB ($\widehat{E_{KB}}$) contribution was defined by Eqn. 4.7:

(4.7) $\widehat{E_{KB}} = \frac{qV_{cell}}{Vol.}$

Where q is the total charge transferred and Vol. is the volume of electrolyte solution used.

In cycling experiments where both Pc and KB were used the total energy density ($\widehat{E_{total}}$) was determined using eqn. 4.8:

(4.8) $\left(\widehat{E_{total}}\right) = \widehat{E_{Pc}} + E_{KB}$

4.5.4 Electrochemical Data:

Solvent	$E_{1/2}$ (1st Ox.) [V]	$E_{1/2}$ (2nd Ox.) [V]	$E_{1/2}$ (1st Red.) [V]	$E_{1/2}$ (2nd Red.) [V]
DCM	0.05	0.48	-1.28	-1.65
DMF	1.05	0.69	-0.55	-0.97
ACN	0.02	0.434	-1.18	-1.57

Table 4.3: Electrochemical data for ^{OEt}PcVO.

Solvent	$E_{1/2}$ (1st Ox.) [V]	$E_{1/2}$ (2nd Ox.) [V]	$E_{1/2}$ (1st Red.) [V]	$E_{1/2}$ (2nd Red.) [V]
DCM	-0.05	0.676	-1.42	-1.84
DMF	-0.02	-	-1.32	-1.79
ACN	-	-	-	-

Table 4.4: Electrochemical data for ^{OEt}PcNi.

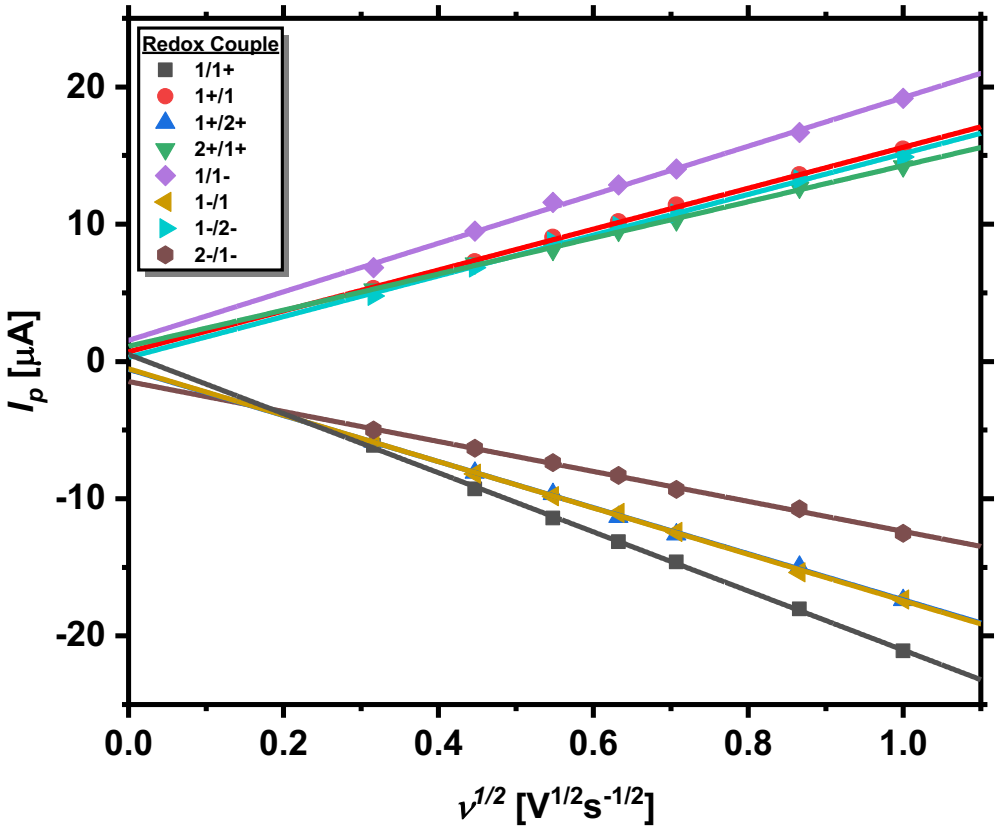

Figure 4.19: Randles-Ševčík plot for ^{OEt}PcVO.

Redox Couple	Slope ($As^{1/2}V^{-1/2}$)	R^2	Diffusion Coefficient (cm^2s^{-1})
1/1+	2.15E-05	0.999	9.87E-06
1+/1	1.49E-05	0.998	4.74E-06
1+/2+	1.68E-05	0.999	6.03E-06
2+/1+	1.32E-05	0.998	3.72E-06
1/1-	1.77E-05	0.997	6.69E-06
1-/1	1.69E-05	0.999	6.10E-06
1-/2-	1.48E-05	0.998	4.68E-06

2-/1-	1.09E-05	0.998	2.54E-06

Table 4.5: Data for the Randles-Ševčík fitting of ^{OEt}PcVO.

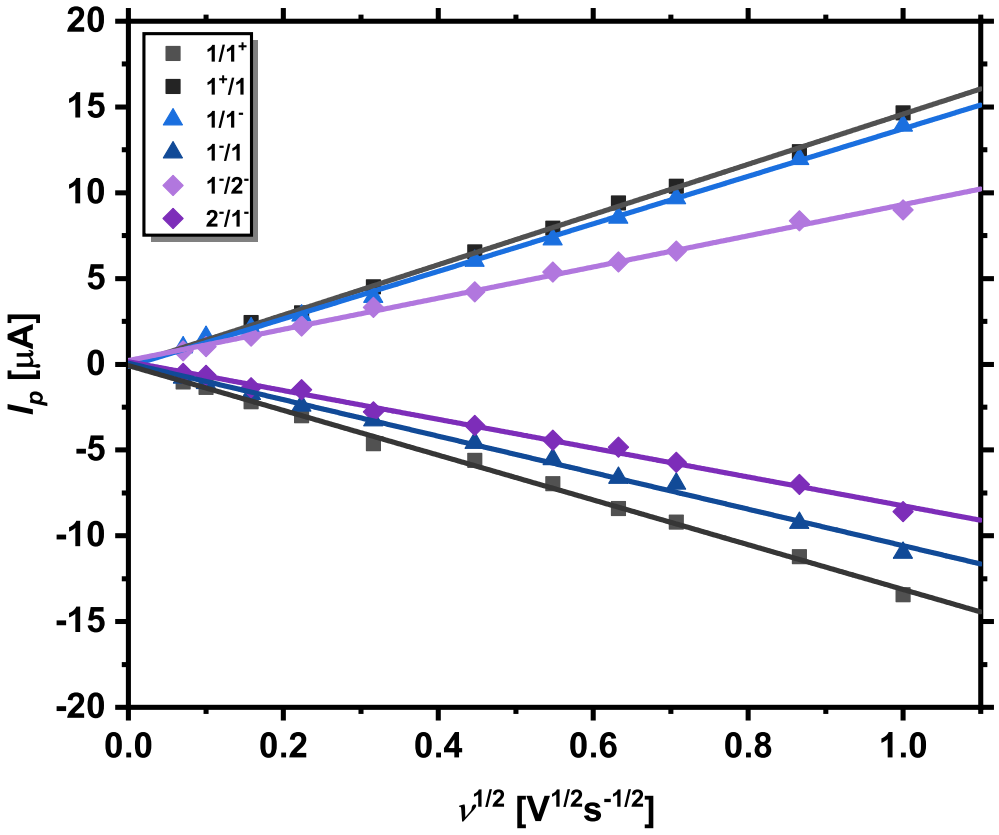

Figure 4.20: Randles-Ševčík plot for ^{OEt}PcNi.

Redox Couple	Slope ($As^{1/2}V^{-1/2}$)	R^2	Diffusion Coefficient (cm^2s^{-1})
1/1+	1.31E-05	0.997	9.08E-06
1+/1	1.46E-05	0.998	1.14E-05
1/1-	1.39E-05	0.995	1.02E-05
1-/1	1.06E-05	0.998	6.04E-06
1-/2-	9.09E-06	0.996	4.41E-06

2-/1-	8.40E-06	0.993	3.76E-06

Table 4.6: Data for the Randles-Ševčík fitting of ^{OEt}PcNi.

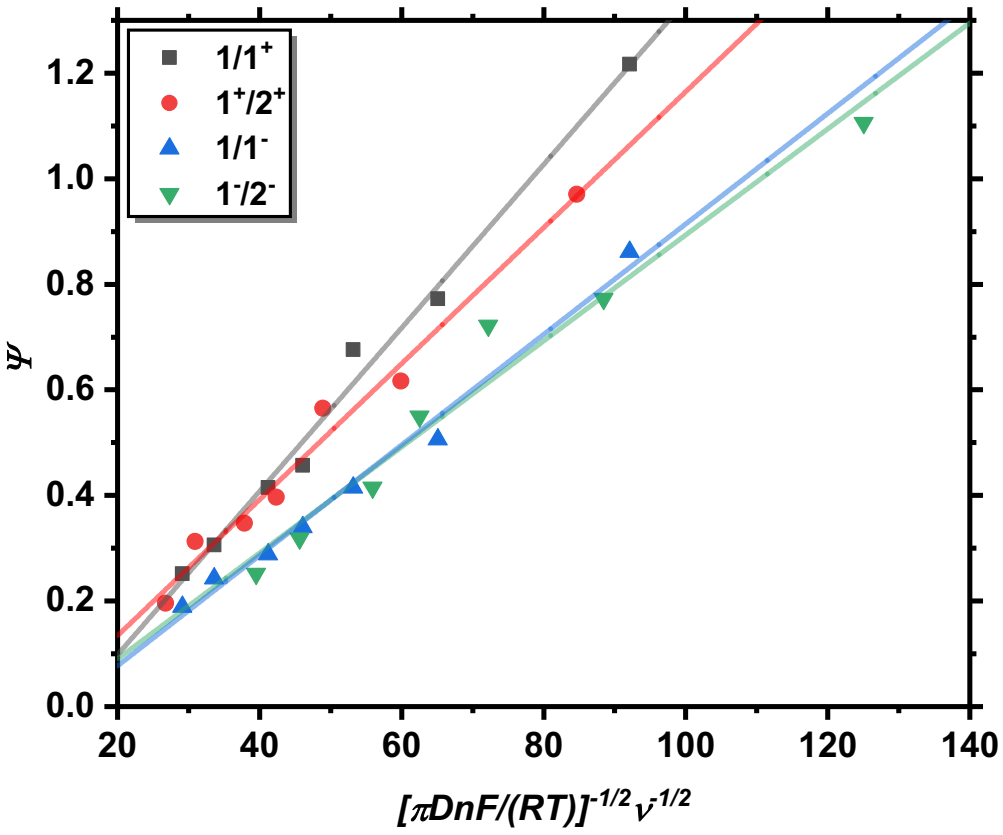

Figure 4.21: Nicholson plot for ^{OEt}PcVO.

^{OEt}PcVO Redox Couple	Slope	R^2
1/1+	0.015	0.989
1+/2+	0.012	0.981
1/1-	0.010	0.988
1-/2-	0.010	0.968

Table 4.7: Data for the Nicholson analysis fitting of ^{OEt}PcVO.

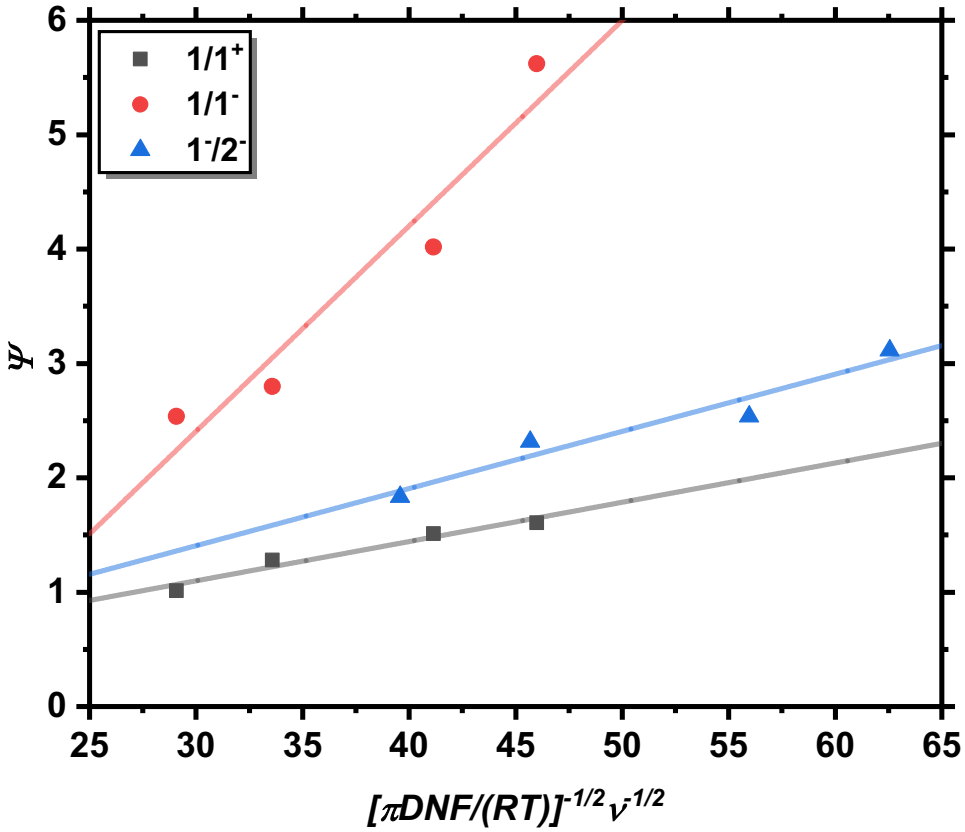

Figure 4.22: Nicholson plot for ^{OEt}PcNi.

^{OEt}PcNi Redox Couple	Slope	R^2
1/1+	0.180	0.930
1/1-	0.050	0.937
1-/2-	0.034	0.957

Table 4.8: Data for the Nicholson analysis fitting of ^{OEt}PcNi.

4.6 References

1. Denholm, P.; Hand, M., Grid flexibility and storage required to achieve very high penetration of variable renewable electricity. *Energy Policy* **2011,** *39* (3), 1817-1830.

2. Ran Fu, D. F., Robert Margolis, Mike Woodhouse, and Kridten Ardani, U.S. Solar Photovoltaic System Cost Benchmark: Q1 2017. NREL, Ed. Department of Energy: Golden, CO, 2017.

3. Lewis, N. S., Toward Cost-Effective Solar Energy Use. *Science* **2007,** *315* (5813), 798.

4. Schiermeier, Q. T., J.; Scully, T.; Witze, A.; Morton, O., Energy alternative: Electricity without carbon. *Natur* **2008,** *454*.

5. Dunn, B.; Kamath, H.; Tarascon, J.-M., Electrical Energy Storage for the Grid: A Battery of Choices. *Science* **2011,** *334* (6058), 928-935.

6. Huang, Y.; Gu, S.; Yan, Y.; Li, S. F. Y., Nonaqueous redox-flow batteries: features, challenges, and prospects. *Current Opinion in Chemical Engineering* **2015,** *8*, 105-113.

7. Weber, A. Z.; Mench, M. M.; Meyers, J. P.; Ross, P. N.; Gostick, J. T.; Liu, Q., Redox flow batteries: a review. *Journal of Applied Electrochemistry* **2011,** *41* (10), 1137.

8. Soloveichik, G. L., Flow Batteries: Current Status and Trends. *Chem. Rev.* **2015,** *115* (20), 11533-11558.

9. Duan, W.; Vemuri, R. S.; Milshtein, J. D.; Laramie, S.; Dmello, R. D.; Huang, J.; Zhang, L.; Hu, D.; Vijayakumar, M.; Wang, W.; Liu, J.; Darling, R. M.; Thompson, L.; Smith, K.; Moore, J. S.; Brushett, F. R.; Wei, X., A symmetric organic-

based nonaqueous redox flow battery and its state of charge diagnostics by FTIR. *Journal of Materials Chemistry A* **2016,** *4* (15), 5448-5456.

10. Gong, K.; Fang, Q.; Gu, S.; Li, S. F. Y.; Yan, Y., Nonaqueous redox-flow batteries: organic solvents, supporting electrolytes, and redox pairs. *Energy & Environmental Science* **2015,** *8* (12), 3515-3530.

11. Hunt, C.; Mattejat, M.; Anderson, C.; Sepunaru, L.; Ménard, G., Symmetric Phthalocyanine Charge Carrier for Dual Redox Flow Battery/Capacitor Applications. *ACS Applied Energy Materials* **2019,** *2* (8), 5391-5396.

12. Potash, R. A.; McKnoe, J. R.; Conte, S.; Abruna, H. D., On the Benefits of a Symmetric Redox Flow Battery. *Journal of The Electrochemical Society* **2016,** *163* (3), S338-A344.

13. Leznoff, C. C.; Lever, A. B. P., *Phthalocyanines: Properties and Applications*. VCH: 1989.

14. Zhou, W.; Leznoff, D. B., Phthalocyanine as a redox-active platform for organometallic chemistry. *Chemical Communications* **2018,** *54* (15), 1829-1832.

15. Peterson, M.; Hunt, C.; Wang, Z.; Heinrich, S. E.; Wu, G.; Ménard, G., Synthesis, characterization, and electrochemical properties of a first-row metal phthalocyanine series. *DTr* **2020**.

16. Alpatova, N. M.; Ovsyannikova, E. V., Electropolymerization of Phthalocyanines. In *Electropolymerization*, 2010; pp 111-132.

17. Nicholson, R. S., Theory and Application of Cyclic Voltammetry for Measurement of Electrode Reaction Kinetics. *Analytical Chemistry* **1965,** *37* (11), 1351-1355.

18. Lavagnini, I.; Antiochia, R.; Magno, F., An Extended Method for the Practical Evaluation of the Standard Rate Constant from Cyclic Voltammetric Data. *Electroanalysis* **2004,** *16* (6), 505-506.

19. DeWulf, D. W.; Leland, J. K.; Wheeler, B. L.; Bard, A. J.; Batzel, D. A.; Dininny, D. R.; Kenney, M., Isolation, spectroscopic properties, and electrochemical properties of two oligomeric silicon phthalocyanines. *Inorganic Chemistry* **1987,** *26* (2), 266-270.

20. Yu, B.; Lever, A. B. P.; Swaddle, T. W., Electrochemistry of Metal Phthalocyanines in Organic Solvents at Variable Pressure. *Inorganic Chemistry* **2004,** *43* (14), 4496-4504.

21. Schon, T. B.; McAllister, B. T.; Li, P.-F.; Seferos, D. S., Correction: The rise of organic electrode materials for energy storage. *Chemical Society Reviews* **2016,** *45* (22), 6405-6406.

22. Lever, A. B. P.; Milaeva, E. R.; Speier, G., The Redox Chemistry of Metallophthalocyanines in Solution. In *Phthalocyanines: properties and applications*, VCH: New York, NY, 1989; pp 1-69.

23. Li, H.; Guarr, T. F., Formation of electronically conductive thin films of metal phthalocyanines via electropolymerization. *J. Chem. Soc., Chem. Commun.* **1989,** (13), 832-834.

24. L'Her, M.; Pondaven, A., 104 - Electrochemistry of Phthalocyanines. In *The Porphyrin Handbook*, Kadish, K. M.; Smith, K. M.; Guilard, R., Eds. Academic Press: Amsterdam, 2003; pp 117-169.

25. Hong, J.; Fauvell, T. J.; Helweh, W.; Zhang, X.; Chen, L. X., Investigation of the photoinduced axial ligation process in the excited state of nickel(II) phthalocyanine. *Journal of Photochemistry and Photobiology A: Chemistry* **2019,** *372*, 270-278.

26. Snow, A. W., 109 - Phthalocyanine Aggregation. In *The Porphyrin Handbook*, Kadish, K. M.; Smith, K. M.; Guilard, R., Eds. Academic Press: Amsterdam, 2003; pp 129-176.

27. Wu, Y.; Jiang, Z.; Lu, X.; Liang, Y.; Wang, H., Domino electroreduction of CO2 to methanol on a molecular catalyst. *Natur* **2019,** *575* (7784), 639-642.

28. Armarego, W. L. F.; Chai, C. L. L., Chapter 4 - Purification of Organic Chemicals. In *Purification of Laboratory Chemicals (Sixth Edition)*, Armarego, W. L. F.; Chai, C. L. L., Eds. Butterworth-Heinemann: Oxford, 2009; pp 88-444.

29. Contakes, S. M.; Beatty, S. T.; Dailey, K. K.; Rauchfuss, T. B.; Fenske, D., π-Complexes of Phthalocyanines and Metallophthalocyanines. *Organometallics* **2000,** *19* (23), 4767-4774.

30. Hunt, C.; Peterson, M.; Anderson, C.; Chang, T.; Wu, G.; Scheiner, S.; Ménard, G., Switchable Aromaticity in an Isostructural Mn Phthalocyanine Series Isolated in Five Separate Redox States. *J. Am. Chem. Soc.* **2019,** *141* (6), 2604-2613.

Chapter 5 Determination of the Photochemical Properties of a Symmetrically Substituted Manganese Nitride Phthalocyanine Complex

5.1 Introduction

Atmospheric CO_2 concentrations continues to rise to alarming levels with the annual global concentration reaching 409.8ppm in 2019 with the consequence that the years between 2014-2019 were the six hottest years since global records began in the mid-1800s.[1] Globally, we are currently facing a steadily worsening climate crisis that requires major change in order to mitigate. One of the ways most commonly discussed is the need to reduce global reliance on fossil fuels, particularly in the electricity sector as it is the largest contributor to fossil fuel derived emissions.[2] This has led to increasing penetration of renewable energy sources such as hydropower[3], geothermal energy[4], wind[5], and solar[6] as well as technologies such as carbon dioxide capture[7] as a way to mitigate current CO_2 levels.

Solar power is often perceived as one of the best future power sources available to us now. An often cited fact is that 100,000 TW of solar power reach the earth's surface, enough every hour to power humanity for a year.[2] While silicon solar cells have continued to become lower in cost,[8] there is interest in developing new solar cell technologies that utilize less material, and have simpler, faster, and more tunable fabrication methods of which perovskite solar cells have emerged as prime candidates.[9, 10] Perovskites are a class of molecules, first discovered in the metal oxide mineral $CaTiO_3$, that follow a general ABX_3 structure in which A is a cation, B is a divalent metal cation and X is an anion.[11] One subset that are of interest are halide perovskites such as $CsPbX_3$ (where X =Cl, Br, I) which show semiconducting properties with high extinction coefficients and behave as excellent sensitizers in solar cells.[12] Since the first solid-state perovskite solar cell report in 2012,[13] the research into these materials has exploded and led to an increasing body of work showing this technology as a real market competitor due to their tunability (current perovskites incorporate both inorganic and organic

components as well as metals other than the traditional lead[14]), ease of processing, and rapidly increasing effiencies.[15]

One of the current limiting factors in perovskite solar cells is the material costs, in particular the cost of common hole transport materials (HTM) such as 2,2′,7,-7′-tetrakis(N,N-di-p-methoxyphenylamine)-9,9′-spirobifluorene (Spiro-MeOTAD), which limit the use at utility scale.[16] Additionally, perovskites suffer from poor stability, particularly with regards to moisture and heat which can be exacerbated by HTMs that do not sufficiently protect the perovskite active layer or themselves degrade in heat.[16] Therefore, there is interest in cheaper HTMs that can also act as protective barriers to increase the utility of perovskite solar cells.

Previously, Pcs have been used in organic photovoltaics[17], dye-sensitized solar cells[18], and organic field-effect transistors[19] and some have already shown promise as HTM for perovskite solar cells.[20-22] Our group recently published a novel 1,4,8,11,15,18,22,25-octaethoxyphthalocyanine manganese nitride (^{OEt}PcMnN) complex that displayed fast electron transfer kinetics, high stability, and relatively good solubility in common organic solvents.[23] We are interested in investigating if ^{OEt}PcMnN may be applicable as an improved HTM and herein work to characterize this material to determine its suitability.

5.2 Results and Discussion

5.2.1 Absorption and Emission of ^{OEt}PcMnN

The properties of Pcs particularly in the solid state are highly affected by their orientation and the creation of thin films can be sensitive to processing conditions. Therefore, the absorbance spectra in different solvents were measured to investigate and potential differences observed that might be of importance to selecting processing conditions (Fig. 5.1) As is typical of metalated Pcs, ^{OEt}PcMnN has a peak at 760nm, deemed Q-band of the

monomeric form, with a small shoulder centered at 685nm, typically considered a vibrational satalite[24], as well as a peak at 330 nm identified as the B-band. These bands are shifted relative to unsubstituted Pcs which is most likely a function of the ethoxy substituent's electron-donating nature.[25]

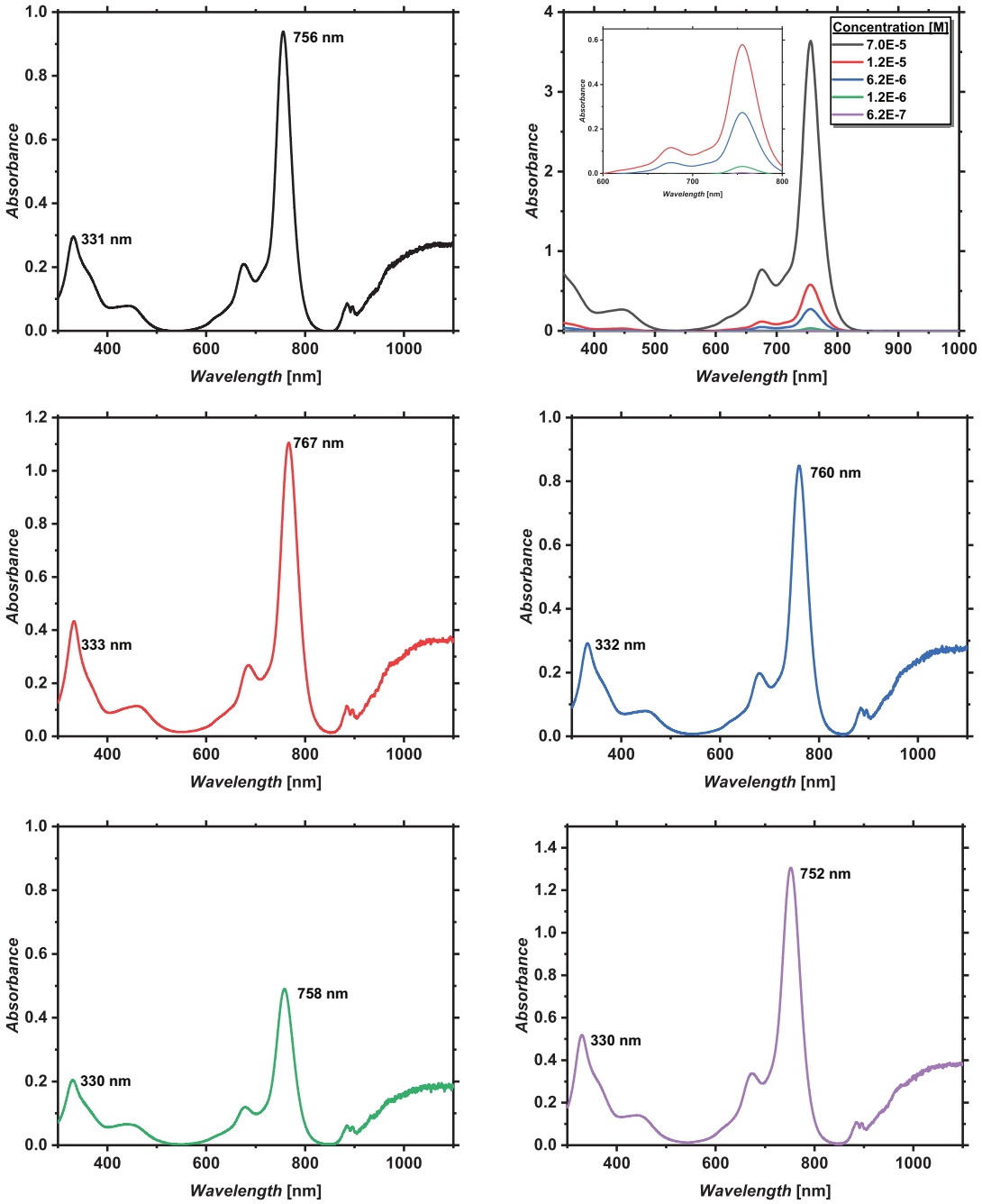

Figure 5.1: UV-vis spectra of ^{OEt}PcMnN in the following solvents taken in air: (a) Benzene (6.4 μM) (b) Benzene at different concentrations (inset) (c) DCM (4.3 μM) (d) fluorobenzene (4.3 μM) (e) glyme (4.3 μM) (f) THF (4.3 μM)

The differences observed while varying the solvents most notably manifest in a spread of 15 nm of the Q-band maxima (from 752nm in THF to 767nm in DCM) while the B-band shows a much smaller spread of 3nm (330nm in THF to 333 in DCM) (full data can be found in Figs. 5.9-5.14). The ordering from shortest to longest λ_{max} for the Q-band is: THF < Benzene < Glyme < Fluorobenzene < DCM which is relatively similar to that of the B-band order of THF ~Glyme < Benzene < Fluorobenzene < DCM. Solvent dipole moment, polarity, and coordinating ability as well as aromaticity are known to effect Pc absorption spectra but either destabilization of the HOMO or stabilization of the LUMO.[26-28] Polar, coordinating and aromatic solvents are known to give the most red-shifted spectra, although these effects can be complex. Increases in solvent polarity correspond to red-shifted Q-band but the magnitude of shift following increasing polarity is different for non-coordinating solvents (e.g., hexanes, toluene, benzene) which give more red-shifted Q-bands than for oxygen-containing solvents (e.g. glyme, THF).[29] It does appear that both of these trends hold in our data with the oxygen containing solvents showing more blue-shifted Q-band and B-band peaks and the other solvents matching what is observed in literature.

These effects can also be observed in the emission spectra for the singlet state (Fig. 5.2). It is worth noting that the fluorescence of ^{OEt}PcMnN in solution at room temperature is difficult to measure because of fluorescence quenching of our Pc with oxygen as well as the electron-donating nature of the ethoxy substituents pushing the absorption and emission to long

enough wavelengths (> 740 nm) such that non-radiative decay becomes a more dominant pathway for relaxation thus our data was collected at 77 K .[30]

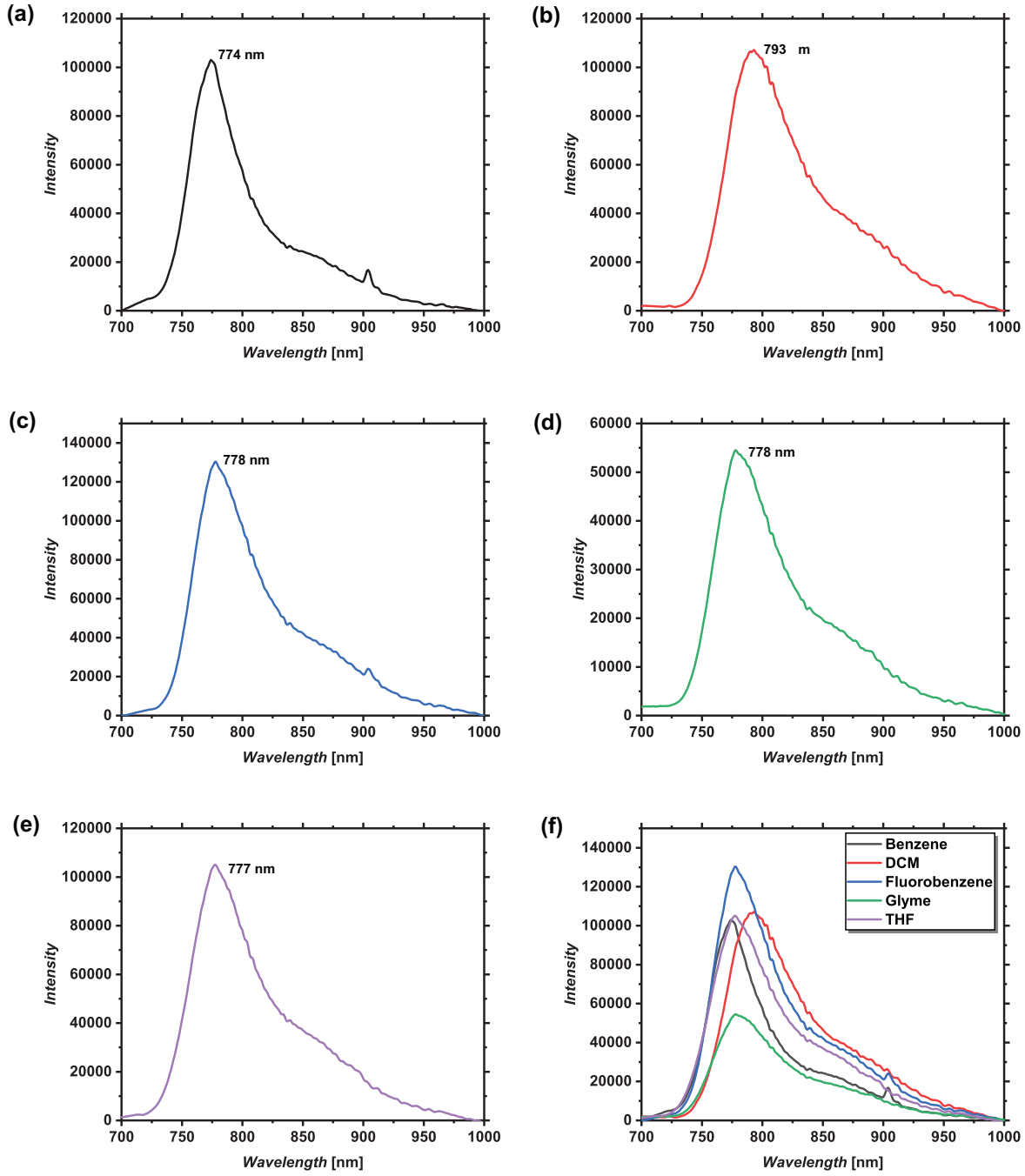

Figure 5.2: Singlet fluorescence spectra of ^{OEt}PcMnN at 77K under air atmosphere in the following solvents: (a) Benzene (b) DCM (c) fluorobenzene (d) glyme (e) THF (f) all emission spectra overlayed. The excitation pulse was at 650nm.

A similar trend to that of the absorbance data in the shortest to longest λ_{max} for the Q-band emission is seen Benzene < THF < Glyme ~Fluorobenzene < DCM. This indicates the trend discussed for the absorption spectra is consistent with what is seen in the emission spectra. The data from these experiments in summarized in Table 5.1

Solvent	Absorbance λ_{max} (nm)	Emission λ_{max} (nm)	Stokes Shift λ_{max} (nm)
Benzene	756	774	18
DCM	767	793	26
Fluorobenzene	760	778	18
Glyme	758	778	20
THF	752	777	25

Table 5.1: Metrics for the solution-state absorbance and singlet emission of ^{OEt}PcMnN in different solvents. Values taken from spectra in Figs. 5.1 and 5.2.

We observe a relatively small Stokes shift on par with other substituted Pcs which is typically ascribed to their rigidity.[31] There is an interesting deviation from the trends discussed above: the Stokes shift in benzene and fluorobenzene is smaller than might be predicted which we posit might be due to the ability of these solvents to form π-interactions with ^{OEt}PcMnN

preventing re-arrangement in the excited state and decreasing the Stokes shift. This behavior of ^{OEt}PcMnN in solution can be compared to the behavior in the solid state.

Thin films of ^{OEt}PcMnN were then fabricated through spin-coating benzene solutions onto ITO/glass substrates (Fig. 5.3, fabrication conditions as well as film thicknesses are detailed in the experimental section in Table 5.4).

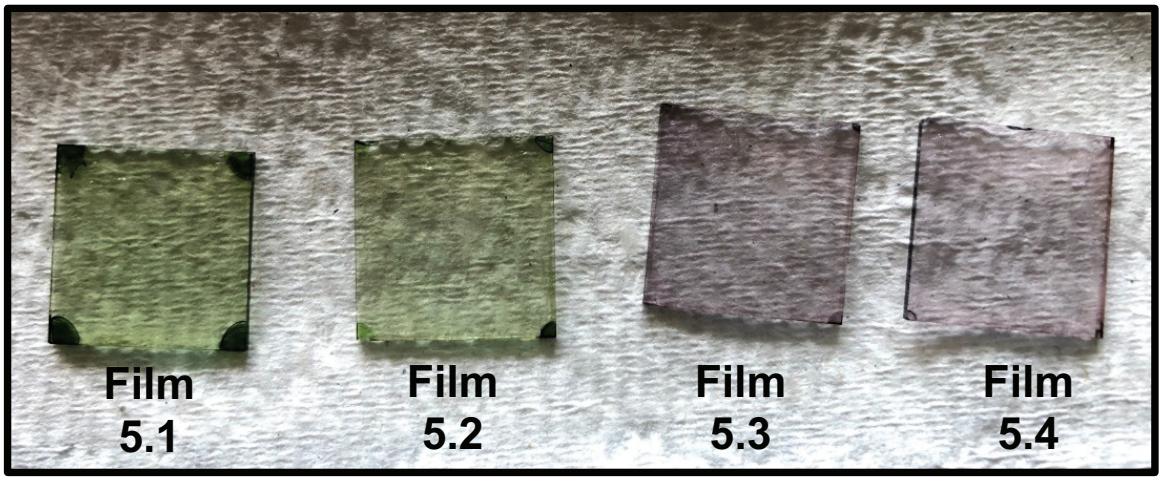

Figure 5.3: Picture of ^{OEt}PcMnN thin films.

The absorbance spectra of these films were taken in both air (Fig. 5.4 (a)) and air-free conditions (Fig. 5.4 (b)) and show minimal differences between the two (Fig. 5.4 (c)). However, there is a clear dependence of the absorption spectra on processing conditions. After fabrication, the films were dried under vacuum and subsequently stored under nitrogen atmosphere where the two thinnest films (5.3 and 5.4) changed color from green to purple (Fig. 5.3).

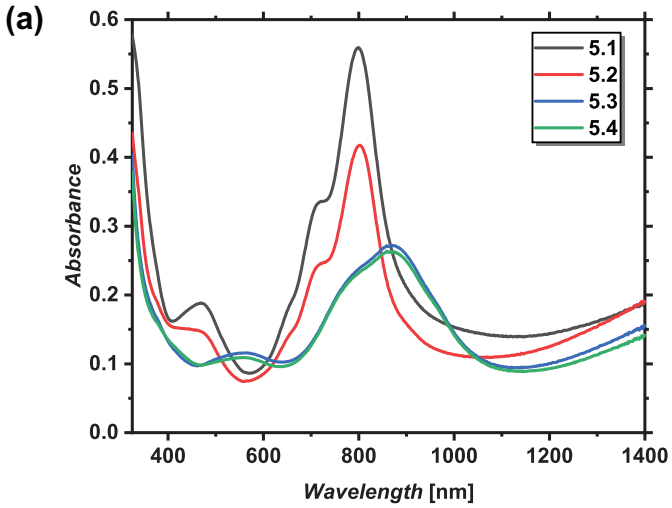
(a)
Absorbance
Wavelength [nm]
5.1
5.2
5.3
5.4

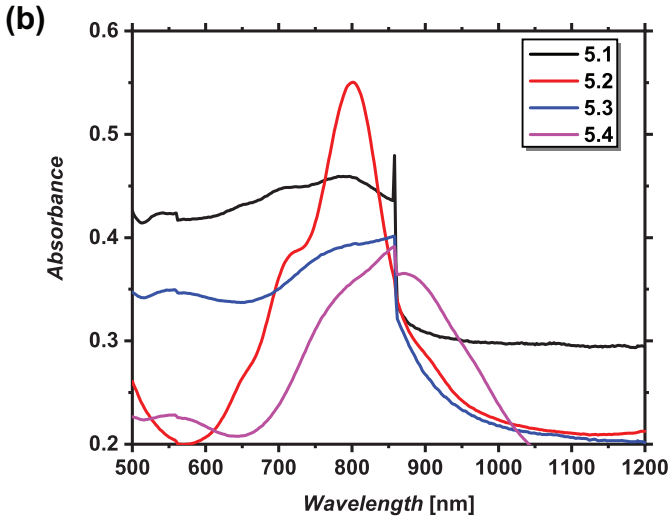
(b)
Absorbance
Wavelength [nm]
5.1
5.2
5.3
5.4

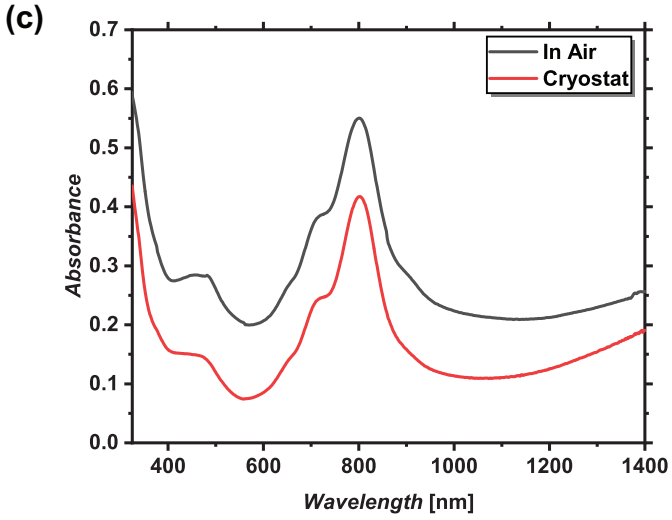
(c)
Absorbance
Wavelength [nm]
In Air
Cryostat

Figure 5.4: Absorbance spectra of ^{OEt}PcMnN thin films under (a) air atmosphere (b) N_2 atmosphere (c) comparison of air and N_2 atmospheres for film 5.2. Full details of film formation can be found in Table 5.4.

The Q-bands for all thin films were red-shifted when compared (Fig. 5.5) to the absorbance of the benzene solution shown in Fig. 5.1.

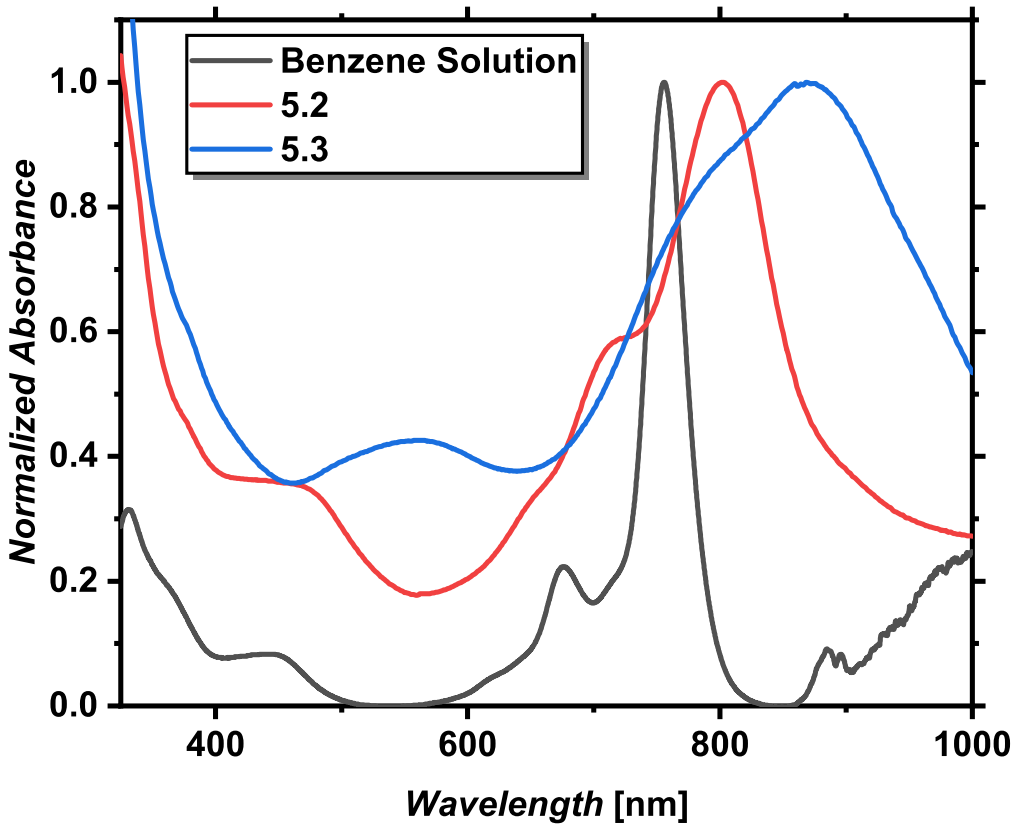

Fig 5.5: Comparison of solution-state and thin film absorbance.

X-ray crystallography experiments done previously[32] indicate that ^{OEt}PcMnN prefers to adopt a slipped stack conformation with the nitrides pointing in opposite directions. In evaporated thin films of PcM complexes with axial ligands a slipped stack conformation is

typically associated with a red-shifting of the absorbance spectrum like seen here, however, PcTiO and PcVO complexes are known to form several polymorphs in thin films which can lead to differences in the absorption spectra depending on which phase is dominant.[33-35] Additionally, PcTiO can exhibit differences in which polymorph is dominant in the initial layers versus in the bulk of thicker films.[36] Work using substituted Pcs and thin films created through spin-coating show similar evidence of shifting conformations over time.[37, 38] With this work in mind we suggest that the differences in the absorption can be attributed to differences in packing that are dependent on film thickness and that over time we observe a morphing on the packing in 5.3 and 5.4 to lower energy conformers. Additionally , the sudden broadening of the absorption bands from solution to thin films is most likely a result of interactions between adjacent ^{OEt}PcMnN molecules.[39] The combination of the axial ligation and ring substitution in ^{OEt}PcMnN should suppress aggregation in solution[40] and we observe no discernable aggregation over a range of concentrations in benzene solution (Fig. 5.1) indicating this is most likely an effect of the spin-coating process.

Evidence for different conformers in the thin films is also present in the emission spectra as there are now two emission peaks (Fig. 5.6) whose intensity changes with temperature.

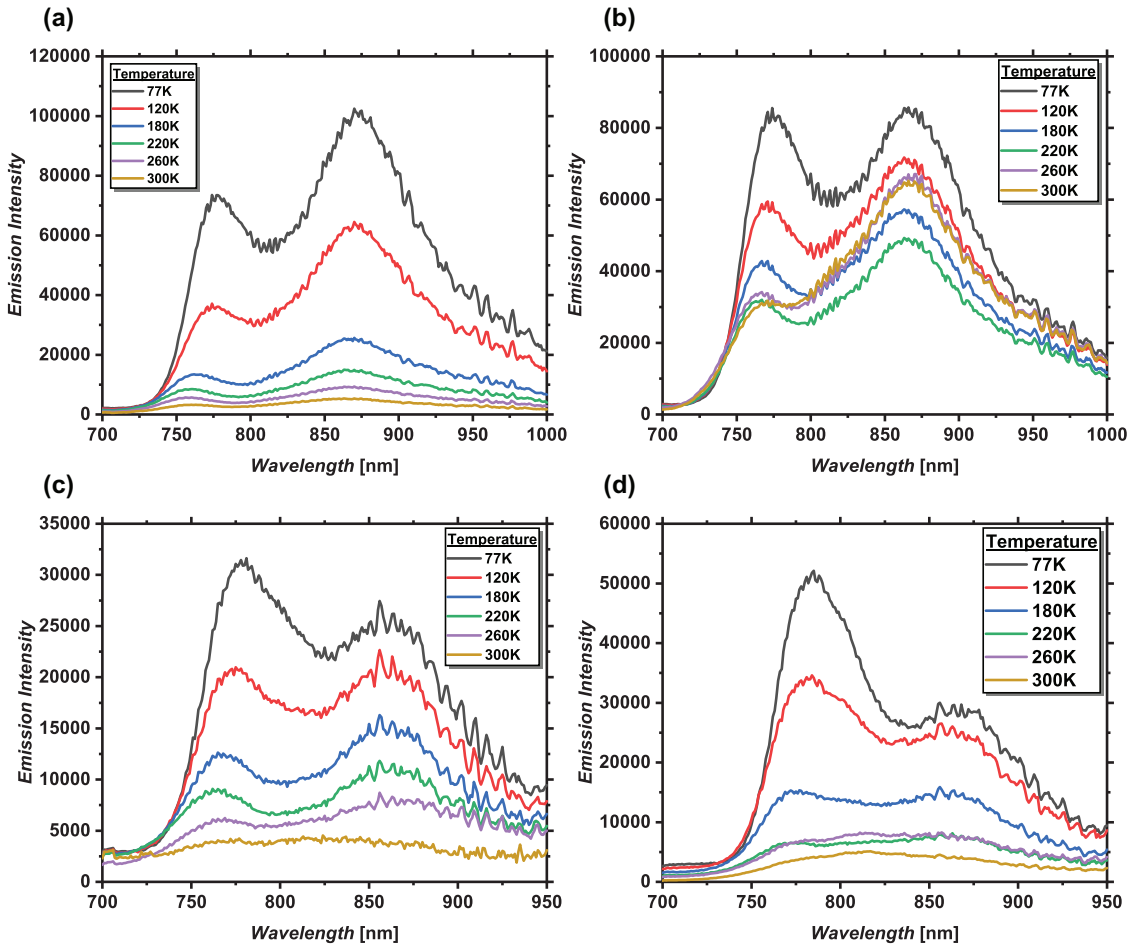

Figure 5.6: Temperature-dependent singlet emission data taken in air-free conditions for thin films (a) 5.1 (excitation at 633nm) (b) 5.2 (excitation at 633nm) (c) 5.3 (excitation at 633nm) and (d) 5.4 (excitation at 633nm).

These peaks show differing ratios between them that correlate with film thickness with the higher energy peak being more intense for thinner films and the lower energy peak being more intense for thicker films. Additionally, the intensity of the emission peaks decrease with increasing temperature which may be both attributed to increasing dominance of non-radiative decay at longer wavelengths[30] as discussed in the solution state case as well as the potential for

aggregation to quench fluorescence.[41] When the emission of the benzene solution is compared with the emission of the thin films, there is good overlap with the higher energy emission peak in all cases (Fig. 5.7, Table 5.2). This could potentially indicate conformational similarity between the higher energy peak in thin films and solution.

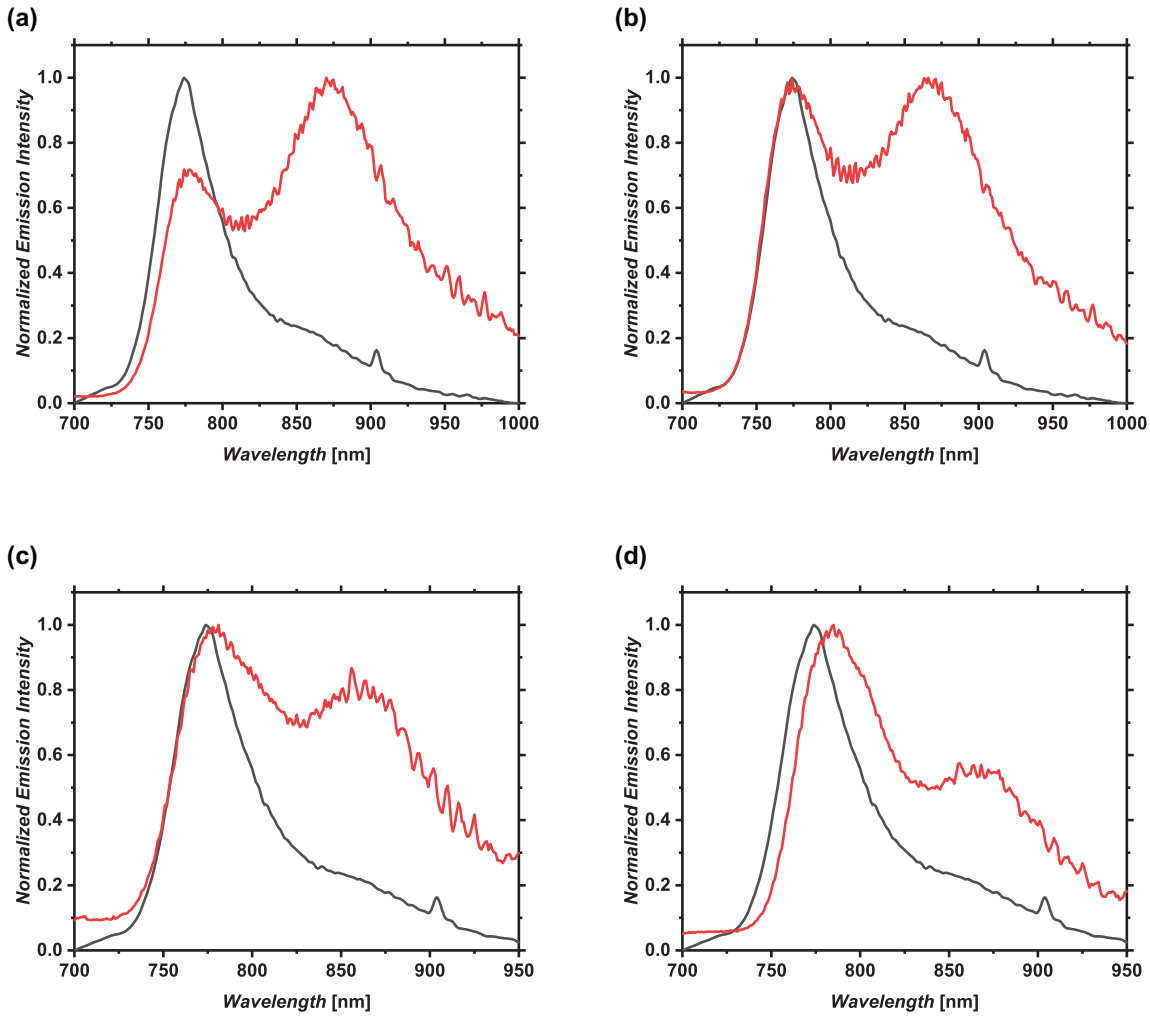

Figure 5.7: Comparison of singlet emission data in benzene solution (gray trace, excitation at 650nm) versus thin films (a) 5.1 (red trace, excitation at 633nm) (b) 5.2 (red trace, excitation at 633nm) (c) 5.3 (red trace, excitation at 633nm) and (d) 5.4 (red trace, excitation at 633nm). All measurements taken at 77K.

When comparing the λ_{max} for both emission peaks the values are largely in agreement across all samples (Table 5.2).

	Emission $\lambda_{\text{max peak 1}}$ (nm)	Emission $\lambda_{\text{max peak 2}}$ (nm)
Benzene Solution	774	-
5.1	778	870
5.2	774	866
5.3	778	864
5.4	785	864

Table 5.2: Relevant metrics for the emission of ^{OEt}PcMnN in benzene solution as well as in thin films.

Further characterization using XRD could help to elucidate the conformers responsible for the emission pattern.

5.2.2 Lifetime Measurements

To better understand the excited state dynamics, we also measured the photoluminescent lifetimes using time correlated single photon counting (TCSPC) in both the solution-state and thin films. In solution, ^{OEt}PcMnN shows a lifetime that was outside the limit of detection at room temperature. When cooled to 77K the determined lifetime was best fit with a mono-exponential decay curve (Fig. 5.8). These lifetimes are relatively consistent with those of similarly substituted Pc macrocycles however these macrocycles are fluorescent at room temperature.[30, 42]

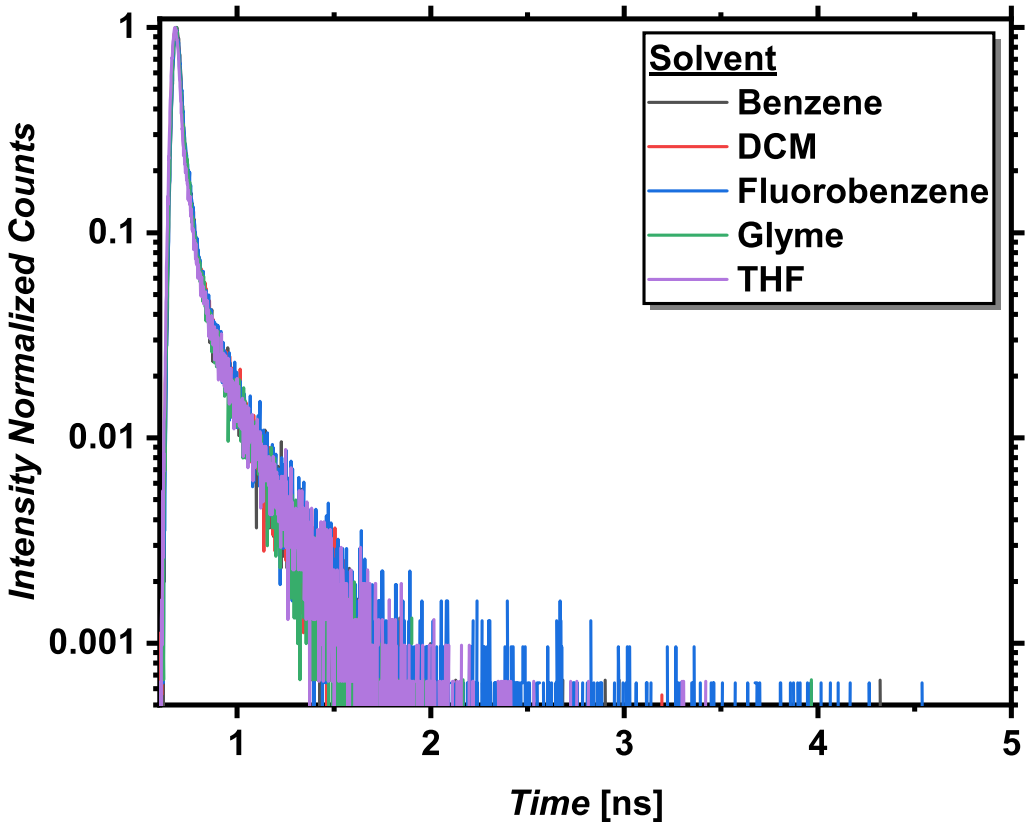

Figure 5.8: Time correlated single photon counting data for ^{OEt}PcMnN in different solvents at 77K.

The full data for all solvents is summarized in Section 5.8 Table 5.5 but it is worth noting there are no significant differences between solvents. It is possible that the relatively limited fluorescence at room temperature and the shortened lifetime could be due to quenching with oxygen and the experiment should be repeated under straight air-free conditions to test this. However, the hypothesis of oxygen quenching the fluorescent lifetime is supported as the thin film fluorescence lifetimes were collected under vacuum and showed longer lifetimes than in solution. For the thin film measurements, the lifetimes of both emission peaks were recorded

(Fig. 5.9). It was noted that the higher energy peak showed a bi-exponential decay in the fitting while the lower energy peak was best fit with a mono-exponential decay and demonstrated a longer lifetime (full details can be found in Section 5.8, Table 5.6).

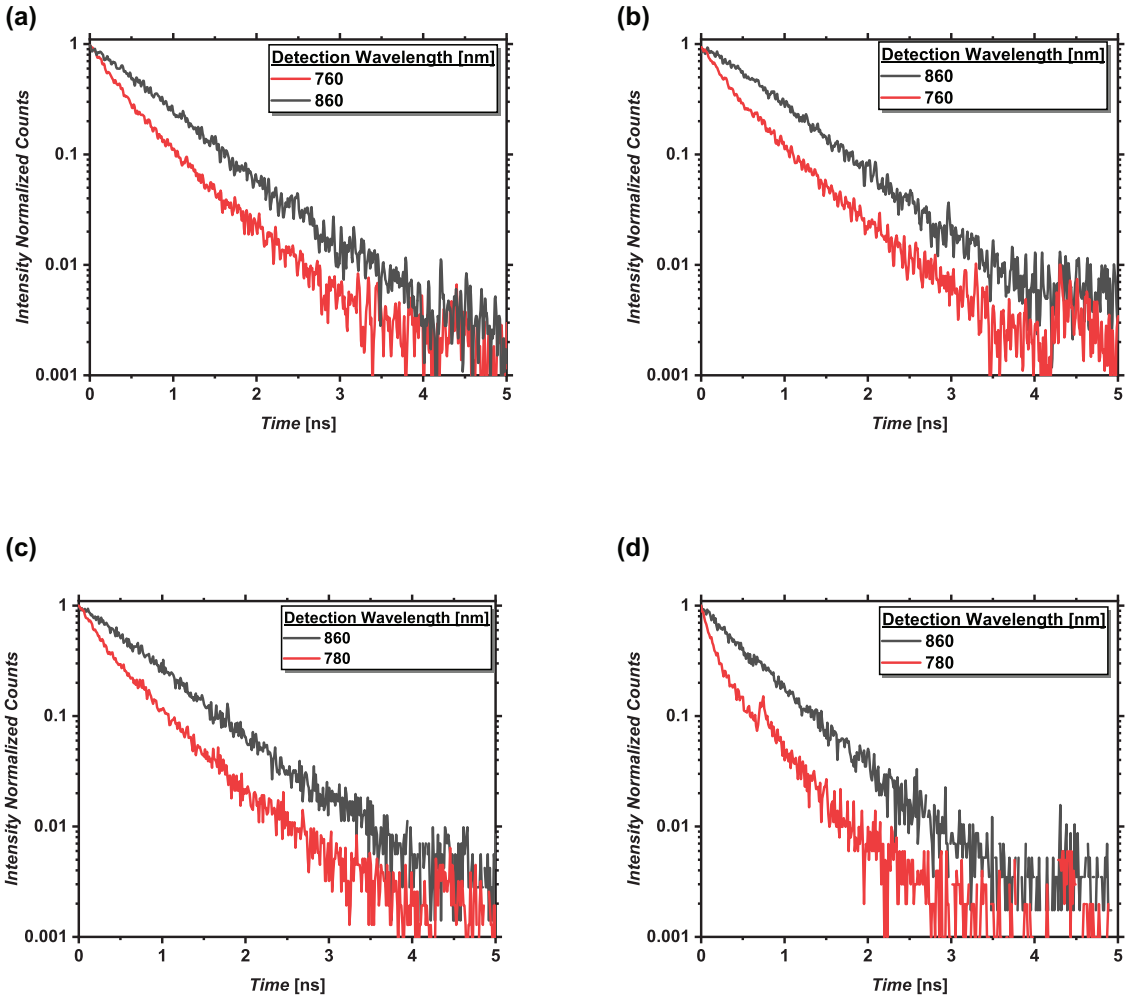

Figure 5.9: Time correlated single photon counting data for ^{OEt}PcMnN thin films (a) 5.1 (b) 5.2 (c) 5.3 (d) 5.4 at 300K in vacuum.

All four thin films show relatively similar lifetimes for both peaks although sample 5.3 (Fig 5.9 (c)) does exhibit shorter lifetimes than the other samples possibly indicative of higher levels of defects in the thin film that facilitate rapid non-radiative energy transfer.

5.2.3 Energy-level Determination

Next, we wanted to correlate our spectroscopic observation with the energy levels of our ^{OEt}PcMnN in both thin films and the solution-state. To do this we used a combination of optical band gap estimations and cyclic voltammetry (CV) to determine the positions of the HOMO and LUMO. The optical bandgap was determined using the Tauc method of analyzing the absorption spectra for both the benzene solution (Fig. 5.10 (a)) and one of the thin films (Fig. 5.10 (b)).

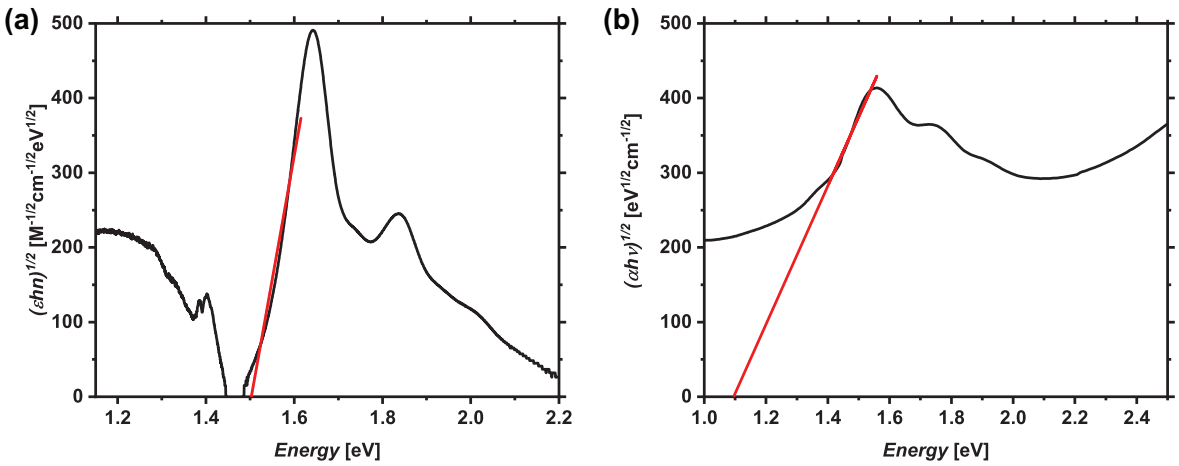

Figure 5.10: Tauc plot of (a) solution-state absorbance using data shown in Fig. 5.1. (b) thin film 5.2 using data shown in Fig. 5.5.

This analysis showed that the red-shift observed when moving from solution to thin film results in a reduction of the bandgap by 0.4 eV.[43] The energy levels of the HOMO and LUMO can also be estimated from CV in both solution-state (Section 5.9 Fig. 5.29) and thin film (Section

5.9 Fig. 5.30) by looking at the onset of the first oxidation and reduction peaks which can then be correlated to HOMO and LUMO energies versus vacuum.[44]

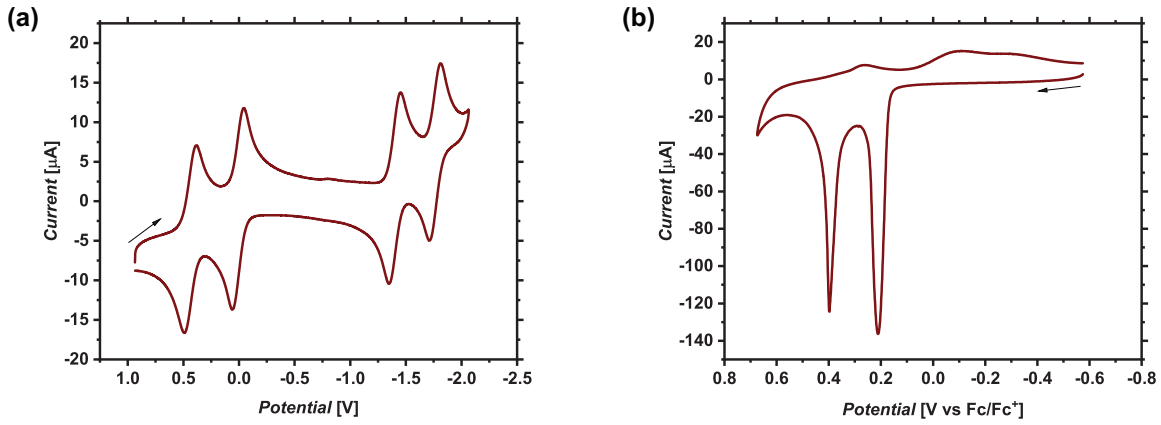

Figure 5.11: (a) CV of a DCM solution (0.29mM) solution of ^{OEt}PcMnN onto a 3mm diameter glass carbon working electrode with a Pt wire counter electrode, a Pt wire pseudo-reference electrode, and internally referenced to Fc at the end. Supporting electrolyte solution is [NBu_4] [PF_6] (0.1M) in DCM. Taken at a scan rate of 0.20V/s. (b) CV of thin film drop-cast from a DCM (0.56mM) solution of ^{OEt}PcMnN onto a 3mm diameter glass carbon working electrode with a Pt wire counter electrode, a Pt wire pseudo-reference electrode, and internally referenced to Fc at the end. Supporting electrolyte solution is KCl (0.1M) in DI water. Taken at a scan rate of 0.25V/s.

It is worth noting that the only peaks observed for the thin film CV in water were the initial two oxidative peaks. These peaks are irreversible which may be due to the dissolution of the thin film into water as well as the water sensitivity of the charge states; therefore, the bandgap and LUMO are only estimated from optical methods. It is worth nothing that for the CV measurements the solution-state CV was obtained in DCM and the thin film created for CV was drop cast from a DCM solution. This was due to the experimental difficulty of obtaining

a CV in benzene and may cause some shifts in the values since we can see there is a difference in the absorption spectra between benzene and DCM that may hint at small differences in the energy levels in these solvents. For this reason, in comparing the solution and thin film the optical method is used. From the first oxidation we can determine where the energy levels lie relative to vacuum. The values for these experiments are summarized in Table 5.3.

	λ_{max}(nm)	E_g^{opt}(eV)	E_g^{CV}(eV)	$HOMO^{CV}$(eV)	$LUMO^{CV}$(eV)	$LUMO^{opt}$(eV)
Solution	756	1.5	1.2	-5.0	-3.8	-3.5
Thin Film	800	1.1	-	-5.4	-	-4.3

Table 5.3: Data for the determination of the HOMO and LUMO energies of ^{OEt}PcMnN in solution and thin films.

The determined energy levels match with similar complexes as well as the DFT calculated HOMO energy we previously published.[30, 32] With the band gap and the energy level of the ground state we can build a picture of what our molecular energy levels look like (Fig. 5.12).

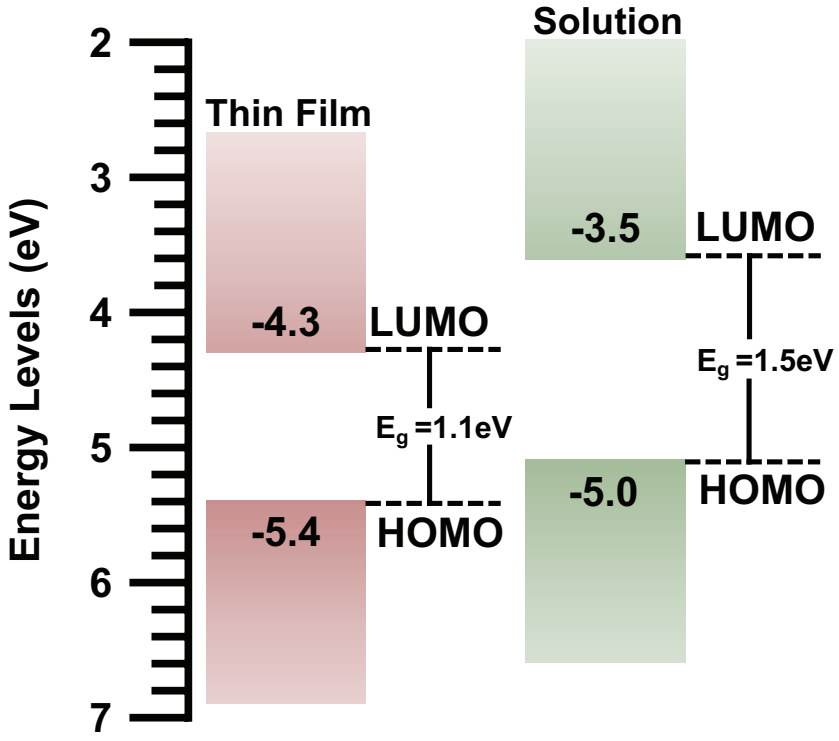

Figure 5.12: Diagram of the energy levels of ^{OEt}PcMnN in both solution state and thin films.

This data indicates that the HOMO of our complex in the solid state is stabilized relative to that of Spiro-MeOTAD[45] but still lying above that of common perovskite materials which indicates this could allow for more efficient energy transfer between our compound and perovskites.

5.3 Summary

The optical and electronic properties of ^{OEt}PcMnN in both solution and thin films were investigated in order to determine its utility as a HTM. ^{OEt}PcMnN showed similar absorbance behavior in both solution- and solid-state although the thin films showed band broadening as

well as a red-shift, indicative of the increasing electronic overlap between adjacent Pc rings. While both solution and solid state showed one emission peak around 780 nm, thin films showed an additional peak at 860-870 nm most likely due to different conformations of ^{OEt}PcMnN in thin films. Additionally the emission at room temperature was relatively low, common for Pcs with long emission wavelengths.[30] The energy levels were determined to be sufficiently close to that of perovskites for use as HTM. Further work is needed to optimize the thin film fabrication conditions in order to reduce the variation in morphology observed. Additionally, this material should undergo further testing to determine if its experimental hole mobility is suitable for use in solar cells. Finally, testing this material along with a suitable perovskite in a solar cell along with atmospheric testing could be used to show this material offers protection against perovskite degradation.

5.4 Experimental

5.4.1 General Considerations

Techniques and Reagents. All air-free manipulations were performed under an atmosphere of dry, oxygen-free N_2 within an MBraun glovebox (MBRAUN UNIlab Pro SP Eco equipped with a −40°C freezer), or by standard Schlenk techniques. Pentane, hexanes, benzene, diethyl ether, DCM, and THF (inhibitor-free) were dried and degassed on an MBraun Solvent Purification System and stored over activated 4 Å molecular sieves. All other solvents (chloroform, DMF) were degassed by freeze-pump-thaw and stored on activated 4 Å molecular sieves prior to use. $MnCl_2$ were purchased from Strem Chemicals, Li metal, 2,3-dicyanohydroquinone from Acros Organics, and ethyl iodide from Alfa Aesar and all were used without further purification. All other reagents were obtained from Sigma-Aldrich, Fisher Scientific, or VWR and used without further purification. **^{OEt}PcMnCl** and **^{OEt}PcMnN** were

synthesized following our previous report.[32] Celite® and 4 Å molecular sieves were dried at 250 °C under dynamic vacuum (<0.1 Torr) for 24 h prior to use. All water used in syntheses was de-ionized.

5.4.2 Syntheses

^{OEt}PcMnN was synthesized following the procedure outlined in Scheme 5.1. 3,6-Diethoxyphthalonitrile (Scheme 5.1, ^{OEt}Pn) and ^{OEt}PcLiH were synthesized as detailed in Chapter 2. ^{OEt}PcMnCl and ^{OEt}PcMnN were synthesized according to modified procedures from our previous work.[32]

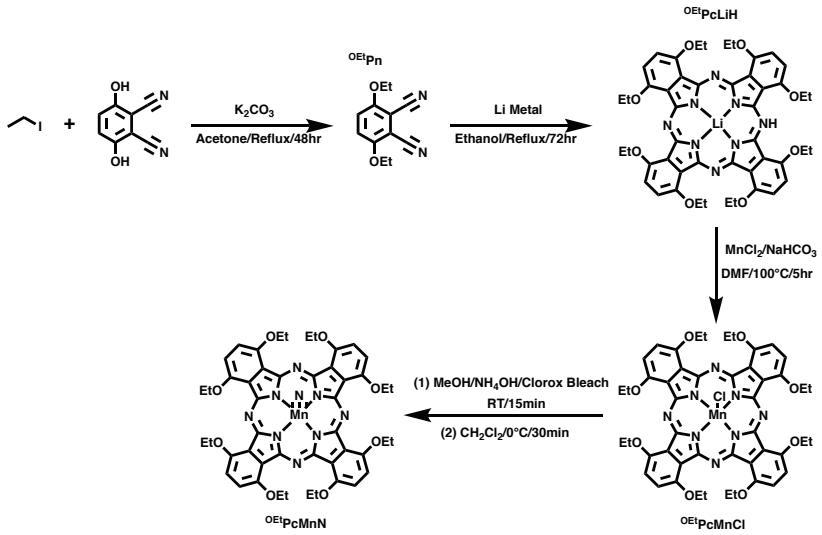

Scheme 5.1: Synthetic scheme of ^{OEt}PcMnN from a phthalonitrile precursor.

^{OEt}PcMnCl. ^{OEt}PcLiH (2.118g, 2.4mmol, 1 eq.) was slurried with $MnCl_2$ (2.115g, 16.8mmol, 7eq.) and $NaHCO_3$ (1.016g, 12.1mmol, 5 eq.) in DMF (23mL). The mixture was heated in open air to 100°C for 5.5 hours, during which time the solution changed from green to purple. After cooling to room temperature water (150mL) was added and allowed to stir for 1 hour.

The solution was then filtered over a glass frit, washed with water (150mL) and OEt_2 (150mL). The result red powder was dried under vacuum and then recrystallized for further use layer DCM/hexanes. Yield: 1.86g (80%). ^{1}HNMR (600MHz, CD_2Cl_2) **δ** 6.66 (bs), 1.76 (bs).

^{OEt}PcMnN. ^{OEt}PcMnCl (2.439g, 2.6mmol, 1eq.) was stirred in MeOH (200mL) at room temperature. While stirring, concentrated NH_4OH (2.6mL, 36.4mmol, 14 eq.) was slowly added dropwise. After the addition of NH_4OH was complete, Clorox Bleach® (22mL, ~6 eq.) was added dropwise during which time the solution turned from deep red to green. The solution was stirred at room temperature for 5 minutes then cooled in an ice bath and stirred for an additional 10 minutes. Once cool, DCM (150mL) was slowly poured into the solution, allowed to stir for 5 minutes, then water (100mL) was added, and stirred for an additional 5 minutes in the ice bath. Separation of the biphasic solution was done using a separatory funnel at room temperature. The organic layer was washed with water until the aqueous layer was clear and colourless, organic layer was then washed with brine, and isolated. The DCM was removed under vacuum, the solid dissolved in benzene, filtered over a celite plug, and the benzene was removed under vacuum. The solid was recrystallized from layer DCM/pentane. Yield: 2.00g (83.9%). ^{1}HNMR (600MHz, $CDCl_3$) **δ** 7.63 (s, 8H), 4.96 (q, J= 7Hz, 16H), 1.83 (t, J=7Hz, 24H).

5.4.3 Thin Film Fabrication

Thin films of ^{OEt}PcMnN were fabricated using the following procedure. First the ITO/glass substrates were cleaned in detergence then sonicated in DI water, rinsed in DI water, sonicated in acetone, rinsed with acetone, sonicated in isopropyl alcohol, rinsed with isopropyl alcohol

and dried with compressed air. The slides were then covered and dried in an oven overnight at 100℃

The active layer was spin-coated in air using a solution of ^{OEt}PcMnN in benzene (10mg/mL) utilizing the spin-coating parameters and sample aliquots shown below in Table 5.4. The thicknesses were measured using a profilometer (Ambios).

Film ID	Spin Speed (rpm)	Spin Time (s)	Aliquot Vol. (µL)	Thickness (nm)
5.1	700	30	25	100
5.2	1000	30	25	-
5.3	1310	30	25	30
5.4	1310	30	25	20

Table 5.4: Spin coating parameters for creation of thin films.

5.4.4 Electronic Spectra Measurements

Absorbance spectra were collected on a Perkin-Elmer Lambda 750 UV/Vis spectrometer using a quartz cuvette (Starna Cells) for solution state measurements and ITO-coated glass slides (MSE supplies). Optical bandgaps were determined by absorption onset using the Tauc method. Air-free and temperature dependent solid-state measurements were taken by mounting samples in a closed-cycle nitrogen cryostat, pumping down to vacuum (10^{-5} Torr), and using a LakeShore autotuning temperature controller. Photoluminescence spectra were taken using an Acton Research SPC-500 monochromator and a charge-coupled device camera (Princeton Instruments PIXIS: 400). For the steady-state temperature-dependent measurements a HeNe laser was used coupled with a long pass filter (650nm, Thor Labs).

Photoluminescence decays were taken using the TCSPC method with a Ti:Sapphire tunable laser (Coherent Mira 900) with 1020fs pulses with 50ns between pulses using a CCD detector

set to detect the wavelength of maximum emission intensity. The repetition rate of the laser was reduced by a homemade acousto-optical pulse picker.

5.8 Lifetime Measurement Data

Solvent	A_1	τ_1 (ns)
Benzene	3.69	0.035
DCM	8.28	0.038
Fluorobenzene	4.46	0.039
Glyme	1.38	0.037
THF	3.06	0.039

Table 5.5: Relevant metrics from the fitting of solution state lifetime data for ^{OEt}PcMnN.

Sample ID	Detection Wavelength (nm)	A_1	τ_1 (ns)	A_2	τ_2 (ns)
5.1	860	1.02	0.79	-	-
	760	0.46	0.24	0.51	0.65
5.2	860	0.97	0.75	-	-
	760	0.54	0.26	0.46	0.64
5.3	860	0.96	0.58	-	-
	780	0.65	0.12	0.32	0.55
5.4	860	1	0.76	-	-
	780	0.49	0.22	0.54	0.62

Table 5.6: Relevant metrics from the fitting of thin film lifetime data for ^{OEt}PcMnN.

5.4.5 Electrochemical Measurements

CV was performed on a CH Instruments 630E Electrochemical Analysis Potentiostat. Unless otherwise noted, the working electrode was a 3mm diameter glassy carbon (CH Instruments) and was cleaned prior to each experiment by sequentially polishing with a gradient of 1.0 μm, 0.3 μm, and 0.05 μm alumina (CH Instruments) on a cloth pad, followed by rinsing with distilled water and acetone. The Pt wire pseudo-reference and counter electrodes were rinsed with distilled water and acetone and heated white-hot with a butane torch. All measurements were performed on recrystallized product and referenced to the Fc/Fc^+ redox couple unless otherwise stated.

5.5 References

1. Blunden, J.; Arndt, D. S., State of the Climate in 2019. *Bulletin of the American Meteorological Society* **2020,** *101* (8), S1-S429.

2. Schiermeier, Q. T., J.; Scully, T.; Witze, A.; Morton, O., Energy alternative: Electricity without carbon. *Natur* **2008,** *454*.

3. IEA, Climate Impacts of Latin America. IEA: Paris, 2021.

4. Kulasekara, H.; Seynulabdeen, V. In *A Review of Geothermal Energy for Future Power Generation*, 2019 5th International Conference on Advances in Electrical Engineering (ICAEE), 26-28 Sept. 2019; 2019; pp 223-228.

5. Li, G.; Zhi, J., Chapter 2 - Analysis of Wind Power Characteristics. In *Large-Scale Wind Power Grid Integration*, Wang, N.; Kang, C.; Ren, D., Eds. Academic Press: Oxford, 2016; pp 19-51.

6. Hayat, M. B.; Ali, D.; Monyake, K. C.; Alagha, L.; Ahmed, N., Solar energy—A look into power generation, challenges, and a solar-powered future. *IJER* **2019,** *43* (3), 1049-1067.

7. Leung, D. Y. C.; Caramanna, G.; Maroto-Valer, M. M., An overview of current status of carbon dioxide capture and storage technologies. *Renewable and Sustainable Energy Reviews* **2014,** *39*, 426-443.

8. Ran Fu, D. F., Robert Margolis, Mike Woodhouse, and Kridten Ardani, U.S. Solar Photovoltaic System Cost Benchmark: Q1 2017. NREL, Ed. Department of Energy: Golden, CO, 2017.

9. Palmstrom, A. F.; Eperon, G. E.; Leijtens, T.; Prasanna, R.; Habisreutinger, S. N.; Nemeth, W.; Gaulding, E. A.; Dunfield, S. P.; Reese, M.; Nanayakkara, S.; Moot, T.; Werner, J.; Liu, J.; To, B.; Christensen, S. T.; McGehee, M. D.; van Hest, M. F. A. M.; Luther, J. M.; Berry, J. J.; Moore, D. T., Enabling Flexible All-Perovskite Tandem Solar Cells. *Joule* **2019,** *3* (9), 2193-2204.

10. Lee, T. D.; Ebong, A. U., A review of thin film solar cell technologies and challenges. *Renewable and Sustainable Energy Reviews* **2017,** *70*, 1286-1297.

11. Jena, A. K.; Kulkarni, A.; Miyasaka, T., Halide Perovskite Photovoltaics: Background, Status, and Future Prospects. *Chem. Rev.* **2019,** *119* (5), 3036-3103.

12. Ponseca, C. S.; Savenije, T. J.; Abdellah, M.; Zheng, K.; Yartsev, A.; Pascher, T.; Harlang, T.; Chabera, P.; Pullerits, T.; Stepanov, A.; Wolf, J.-P.; Sundström, V., Organometal Halide Perovskite Solar Cell Materials Rationalized: Ultrafast Charge Generation, High and Microsecond-Long Balanced Mobilities, and Slow Recombination. *Journal of the American Chemical Society* **2014,** *136* (14), 5189-5192.

13. Lee, M. M.; Teuscher, J.; Miyasaka, T.; Murakami, T. N.; Snaith, H. J., Efficient Hybrid Solar Cells Based on Meso-Superstructured Organometal Halide Perovskites. *Science* **2012,** *338* (6107), 643.

14. Lakhdar, N.; Hima, A., Electron transport material effect on performance of perovskite solar cells based on CH3NH3GeI3. *Optical Materials* **2020,** *99*, 109517.

15. Yang, S.; Fu, W.; Zhang, Z.; Chen, H.; Li, C.-Z., Recent advances in perovskite solar cells: efficiency, stability and lead-free perovskite. *Journal of Materials Chemistry A* **2017,** *5* (23), 11462-11482.

16. Wang, R.; Mujahid, M.; Duan, Y.; Wang, Z.-K.; Xue, J.; Yang, Y., A Review of Perovskites Solar Cell Stability. *Adv. Funct. Mater.* **2019,** *29* (47), 1808843.

17. Singh, V. P.; Singh, R. S.; Parthasarathy, B.; Aguilera, A.; Anthony, J.; Payne, M., Copper-phthalocyanine-based organic solar cells with high open-circuit voltage. *Applied Physics Letters* **2005,** *86* (8), 082106.

18. Ragoussi, M.-E.; Ince, M.; Torres, T., Recent Advances in Phthalocyanine-Based Sensitizers for Dye-Sensitized Solar Cells. *Eur. J. Org. Chem.* **2013,** *2013* (29), 6475-6489.

19. Melville, O. A.; Grant, T. M.; Lessard, B. H., Silicon phthalocyanines as N-type semiconductors in organic thin film transistors. *Journal of Materials Chemistry C* **2018,** *6* (20), 5482-5488.

20. Cheng, M.; Li, Y.; Safdari, M.; Chen, C.; Liu, P.; Kloo, L.; Sun, L., Efficient Perovskite Solar Cells Based on a Solution Processable Nickel(II) Phthalocyanine and Vanadium Oxide Integrated Hole Transport Layer. *Advanced Energy Materials* **2017,** *7* (14), 1602556.

21. Duong, T.; Peng, J.; Walter, D.; Xiang, J.; Shen, H.; Chugh, D.; Lockrey, M.; Zhong, D.; Li, J.; Weber, K.; White, T. P.; Catchpole, K. R., Perovskite Solar Cells Employing Copper Phthalocyanine Hole-Transport Material with an Efficiency over 20% and Excellent Thermal Stability. *ACS Energy Letters* **2018,** *3* (10), 2441-2448.

22. Guo, J.-J.; Meng, X.-F.; Niu, J.; Yin, Y.; Han, M.-M.; Ma, X.-H.; Song, G.-S.; Zhang, F., A novel asymmetric phthalocyanine-based hole transporting material for perovskite solar cells with an open-circuit voltage above 1.0V. *Synthetic Metals* **2016,** *220*, 462-468.

23. Hunt, C.; Mattejat, M.; Anderson, C.; Sepunaru, L.; Ménard, G., Symmetric Phthalocyanine Charge Carrier for Dual Redox Flow Battery/Capacitor Applications. *ACS Applied Energy Materials* **2019,** *2* (8), 5391-5396.

24. Krichevsky, D. M.; Zasedatelev, A. V.; Tolbin, A. Y.; Luchkin, S. Y.; Karpo, A. B.; Krasovskii, V. I.; Tomilova, L. G., Highly transparent low-symmetry zinc phthalocyanine-based monolayers for NO2 gas detection. *Thin Solid Films* **2017,** *642*, 295-302.

25. Kobayashi, N.; Sasaki, N.; Higashi, Y.; Osa, T., Regiospecific and Nonlinear Substituent Effects on the Electronic and Fluorescence Spectra of Phthalocyanines. *Inorganic Chemistry* **1995,** *34* (7), 1636-1637.

26. Harazono, T.; Takagishi, I., Solvent Effects on Electronic States of Phthalocyanines. *Bull. Chem. Soc. Jpn.* **1993,** *66* (4), 1016-1023.

27. Rauf, M. A.; Hisaindee, S.; Graham, J. P.; Nawaz, M., Solvent effects on the absorption and fluorescence spectra of Cu(II)-phthalocyanine and DFT calculations. *J. Mol. Liq.* **2012,** *168*, 102-109.

28. Ogunsipe, A.; Maree, D.; Nyokong, T., Solvent effects on the photochemical and fluorescence properties of zinc phthalocyanine derivatives. *Journal of Molecular Structure* **2003,** *650* (1), 131-140.

29. Law, W.-F.; Liu, R. C. W.; Jiang, J.; Ng, D. K. P., Synthesis and spectroscopic properties of octasubstituted (phthalocyaninato)titanium(IV) complexes. *Inorg. Chim. Acta* **1997,** *256* (1), 147-150.

30. Kobayashi, N.; Ogata, H.; Nonaka, N.; Luk'yanets, E. A., Effect of Peripheral Substitution on the Electronic Absorption and Fluorescence Spectra of Metal-Free and Zinc Phthalocyanines. *Chemistry – A European Journal* **2003,** *9* (20), 5123-5134.

31. Ishii, K.; Kobayashi, N., 102 - The Photophysical Properties of Phthalocyanines and Related Compounds. In *The Porphyrin Handbook*, Kadish, K. M.; Smith, K. M.; Guilard, R., Eds. Academic Press: Amsterdam, 2003; pp 1-42.

32. Hunt, C.; Peterson, M.; Anderson, C.; Chang, T.; Wu, G.; Scheiner, S.; Ménard, G., Switchable Aromaticity in an Isostructural Mn Phthalocyanine Series Isolated in Five Separate Redox States. *J. Am. Chem. Soc.* **2019,** *141* (6), 2604-2613.

33. Cook, M. J.; Chambrier, I., 108 - Phthalocyanine Thin Films: Deposition and Structural Studies. In *The Porphyrin Handbook*, Kadish, K. M.; Smith, K. M.; Guilard, R., Eds. Academic Press: Amsterdam, 2003; pp 37-127.

34. Chau, L. K.; England, C. D.; Chen, S.; Armstrong, N. R., Visible absorption and photocurrent spectra of epitaxially deposited phthalocyanine thin films: interpretation of exciton coupling effects. *The Journal of Physical Chemistry* **1993,** *97* (11), 2699-2706.

35. Chau, L. K.; Chen, S. Y.; Armstrong, N. R.; Collins, G. E.; England, C. D.; Williams, V. S.; Anderson, M. L.; Schuerlein, T. J.; Lee, P. A.; Nebesny, K. W.; Parkinson, B. A.; Arbour, C., Organic/Inorganic Molecular Beam Epitaxy (O/I-MBE): Formation and Characterization of Ordered Phthalocyanine Thin Films –

Photoelectrochemical Processes. *Molecular Crystals and Liquid Crystals Science and Technology. Section A. Molecular Crystals and Liquid Crystals* **1994,** *252* (1), 67-77.

36. Ueda, Y.; Watanabe, M.; Yamaguchi, H., Enhancement of Photoelectrochemical Properties of Phthalocyanine Thin Films by the Control of Molecular Orientation. *Molecular Crystals and Liquid Crystals Science and Technology. Section A. Molecular Crystals and Liquid Crystals* **1995,** *267* (1), 175-180.

37. Michael J. Cook, I. C., Phthalocyanine Thin Films: Deposition and Structural Studies. In *The Porphyrin Handbook: Phthalocyanines: Properties and Materials*, K.M. Kadish, K. M. S., R. Guilard, Ed. Elsevier Science: 2003; Vol. 17, p 37.

38. Critchley, S. M.; Willis, M. R., Deposition of thin phthalocyanine films by spin coating. *IJE* **1994,** *76* (5), 809-814.

39. Dini, D.; Hanack, M., 107 - Physical Properties of Phthalocyanine-based Materials. In *The Porphyrin Handbook*, Kadish, K. M.; Smith, K. M.; Guilard, R., Eds. Academic Press: Amsterdam, 2003; pp 1-36.

40. Tai, S.; Hayashi, N.; Katayose, M., Unique molecular aggregation of novel naphthalocyanine (near IR absorbing dye). *Progress in Organic Coatings* **1994,** *24* (1), 323-339.

41. Snow, A. W., 109 - Phthalocyanine Aggregation. In *The Porphyrin Handbook*, Kadish, K. M.; Smith, K. M.; Guilard, R., Eds. Academic Press: Amsterdam, 2003; pp 129-176.

42. Hong, J.; Kelley, M. S.; Shelby, M. L.; Hayes, D. K.; Hadt, R. G.; Rimmerman, D.; Zhang, X.; Chen, L. X., The Nature of the Long-Lived Excited State in a NiII Phthalocyanine Complex Investigated by X-Ray Transient Absorption Spectroscopy. *ChemSusChem* **2018,** *11* (14), 2421-2428.

43. Sánchez-Vergara, M. E.; Alonso-Huitron, J. C.; Rodriguez-Gómez, A.; Reider-Burstin, J. N., Determination of the Optical GAP in Thin Films of Amorphous Dilithium Phthalocyanine Using the Tauc and Cody Models. *Molecules* **2012,** *17* (9), 10000.

44. Cardona, C. M.; Li, W.; Kaifer, A. E.; Stockdale, D.; Bazan, G. C., Electrochemical Considerations for Determining Absolute Frontier Orbital Energy Levels of Conjugated Polymers for Solar Cell Applications. *Adv. Mater.* **2011,** *23* (20), 2367-2371.

45. Pham, H. D.; Jain, S. M.; Li, M.; Manzhos, S.; Feron, K.; Pitchaimuthu, S.; Liu, Z.; Motta, N.; Wang, H.; Durrant, J. R.; Sonar, P., Dopant-free novel hole-transporting materials based on quinacridone dye for high-performance and humidity-stable mesoporous perovskite solar cells. *Journal of Materials Chemistry A* **2019,** *7* (10), 5315-5323.